

Compound Coaxial Helicopter Modelling, Control and Assessment

Master of Science Thesis

Ynias J.E. Prencipe



Compound Coaxial Helicopter Modelling, Control and Assessment

Master of Science Thesis

Control and Simulation Department

by

Ynias J.E. Prencipe

to obtain the degree of Master of Science
at the Delft University of Technology
to be defended publicly on August 30, 2024 at 10:00

Thesis committee:

Chair:	Dr. Ir. M.M. van Paassen
Supervisors:	Dr. Ir. M.D. Pavel Ir. G. Tzanetos Alevras
External examiner:	Dr. O.A. Sharpans'kykh
Place:	Faculty of Aerospace Engineering, Delft
Project Duration:	December, 2023 - August, 2024
Student number:	4777158

An electronic version of this thesis is available at <http://repository.tudelft.nl/>.



Copyright © Ynias J.E. Prencipe, 2024
All rights reserved.

Preface

This thesis summarises and concludes the past 11 months of hard work, thereby also concluding the past 6 years of my university career. It has been an extremely rewarding, insightful, but also challenging journey, for which I will forever be grateful. In this document I will study the modelling, control and handling quality assessment of a modern-day compound coaxial helicopter, and apply these very principles myself.

As is customary in a preface, I would like to express my sincere gratitude towards various people who have supported me throughout this entire journey, who'm without, this thesis, and especially the entire academic training, would have gone very differently. Firstly, I would like to thank my supervisor Marilena Pavel for her efforts and motivation in guiding me throughout this thesis. I looked forward to all of our meetings in which she always provided me with key insights, but also took the opportunity to talk about everyday things on a more personal level, which is something I highly appreciated and enjoyed (also the chocolates and coffee's in the office). Secondly, I would like to thank the entire NLR team for providing me with this thesis assignment, fruitful working environment, and friends made along the way. Thank you Richard Bakker, Stefan van 't Hoff, Laurent Declerck, and Peter Booij (one more peppermint Mr Creosote?). Of course, I would like to express my greatest gratitude towards George, who besides mentoring me at NLR, has become a great friend who was always willing to help and listen throughout all of the thesis ups and downs. I will cherish our long drives to and from the office (even with the hours of traffic jams), library sessions, and tosti's at Koffiehuys Koning.

Probably the most influential people throughout my university career were my friends in Delft. We not only shared our journeys, but also great memories and struggles. Thank you Ihab for supporting me throughout my most difficult (first) year in Delft and drilling the library grind in me, Andrea, Francesco, Walid and Martino for being great friends, if I were to write out all the things I appreciate, this preface would become even longer. Our Gnocchi Monday's were one of the fondest memories I have from Delft. Lastly I would like to thank all the other many friends I made along the way.

As anyone who slightly knows me in Delft knows, I went home to Belgium very often, for good reason. Thank you to all my hometown friends who have always supported me throughout many years - thank you Jorden, Rob, Jelle, and Mathias, Yven, Michael, Theo, Marnic and Ben for the great friendship and DnD games. Thank you to everyone from GWC, who provided me with many years of great memories and evenings as a board member. Thank you Thibaut for everything, you are simultaneously a great inspiration and a great friend. Lastly, thank you Georgios, after more than 22 years of being friends you have become like a brother, and your family a second home.

On the topic of family, for whom I saved the best for last. This entire journey would not have been possible without them. Thank you Nonkel Philip, Tante Evelyne, Nonkel Steven, Tante Tinne, Frederiek and Kirsten, and all my nieces and nephews. I greatly appreciate the work you have contributed to my thesis, by helping me with the 3D CAD model, and many many hours of proofreading. Thank you to Thea en Geert for the indescribable impact on my life, without them none of this would have happened. Thank you to my mother for being my greatest motivation throughout all of this, and all the (almost) weekly dinners we enjoyed together. Marie, I am the luckiest person alive to have, and have had you as my girlfriend for the past 5 years, thank you for all the support, patience, and comfort. Thank you also to Denise and Mark, for also supporting me throughout all these years. Lastly, thank you Nonno, for being like a father to me, having provided me with everything, and supporting me throughout all my endeavours. Words fall short to describe my gratitude.

Contents

List of Figures	vi
List of Tables	x
1 Introduction	1
1.1 Research Motivation	1
1.2 Research Scope	1
1.3 Research Formulation	2
1.4 Document Outline	4
I Scientific Paper	5
2 Flight Dynamics Modelling, Control and Handling Quality Assessment of a Compound Coaxial Helicopter in Transition Flight	6
2.1 Abstract	6
2.2 Introduction.	7
2.3 Compound Coaxial Helicopter Modelling	8
2.4 Stability Analysis.	9
2.5 Flight Controller Design	10
2.6 Handling Quality Assessment	11
2.7 Conclusions	12
2.8 Recommendations	13
2.9 Appendices	14
II Literature Study	30
3 Historical Overview of Coaxial Rotorcraft	31
3.1 Early Developments of Coaxial Rotorcraft	31
3.2 Rigid Rotors Technology	32
3.3 Modern (Compound) Coaxial Rotorcraft Designs.	33
4 Advances in Compound Helicopter Designs	35
4.1 Advancing Blade Concept (ABC) Rotors	35
4.2 Control System Description	38
5 Modelling Approaches for Coaxial Compound Helicopters	43
5.1 Coaxial Rotor Modelling	43
5.2 Pusher Propeller Modelling	61
5.3 Fuselage Modelling	61
5.4 Empennage Modelling	62
6 Control System Strategies in a Compound Coaxial Rotorcraft	63
6.1 Challenges of Compound Rotorcraft FCS Design	63
6.2 Classical Control Techniques.	64
6.3 Modern Control Techniques	66
7 Control Allocation of a Compound Coaxial Rotorcraft	70
7.1 Control Allocation Techniques	70
7.2 Implementation Considerations in Compound Coaxial Rotorcraft	74



8	Handling Quality Assessment in High-Speed Helicopter Design	79
8.1	Objective Handling Quality Metrics	79
8.2	Subjective Handling Quality Metrics	80
9	Results and Discussion	84
9.1	Research Gap	84
9.2	Research Questions Results	85
9.3	Summary	87
III	Main Analysis	89
10	Compound Coaxial Helicopter Modelling – Nonlinear Model	90
10.1	General Modelling Overview	90
10.2	Body Axes and Forces Definitions	92
10.3	Coaxial Rotor Modelling	94
10.4	Pusher Propeller Modelling	107
10.5	Empennage Modelling	109
10.6	Fuselage Modelling	112
10.7	Lateral Lift-Offset Considerations	114
11	Trimming the Model	117
11.1	Trim Problem and Choice of Trim Variables	117
11.2	Newton-Raphson Trim Algorithm	118
11.3	Trim Results	121
12	Stability Analysis of the Compound Coaxial Helicopter	123
12.1	Linearisation Algorithm	123
12.2	Stability Derivatives	124
12.3	Control Derivatives	127
12.4	Open-Loop System Response	129
12.5	Longitudinal Natural Modes of Motion	136
13	Flight Controller Design	138
13.1	Controller Architecture.	138
13.2	Multi-Stage Control Allocation	139
13.3	Inner-Loop Attitude Controller	142
13.4	Outer-Loop Velocity Controller	145
13.5	Controller Tuning.	145
13.6	Manoeuvre Simulation	148
14	Objective Handling Quality Assessment	155
14.1	Bandwidth and Phase Delay	155
14.2	Attitude Quickness	157
14.3	Further Handling Quality Considerations	159
IV	Closure	162
15	Conclusion	163
15.1	Research Objectives	163
15.2	Research Conclusions.	163
16	Recommendations	166
	References	171
A	Algorithms	172
A.1	Nonlinear Simulation	172
B	Linearisation Results	174
B.1	Stability Derivatives	174



B.2 Control Derivatives 176

List of Figures

3.1	de la Cierva's C-1 Autogiro (1920). [4]	32
3.2	d'Asciano's Prototype Coaxial D At3 Helicopter (1930). [4]	32
3.3	Kamov A-8 coaxial helicopter (1947). [4]	32
3.4	Kamov Ka-52 "Alligator" (2008). [5]	32
3.5	Lockheed AH-56A Cheyenne Advanced Mechanical Control System Featuring Mechanical Feedback Gyro. [7]	33
3.6	Sikorsky X2 Technology Demonstrator (2008).	34
3.7	Sikorsky S-97 Raider X (2023).	34
4.1	Lateral moment equilibrium comparison between a single main rotor (left) and the ABC concept (right). [13]	36
4.2	X2TD and XH-59A general main rotor blade parameters - length dimensions normalized by rotor radius. [13]	36
4.3	$C_L M^2$ (upper) and $C_D M^2$ (lower) contours at $V=265\text{kts}$ with $\text{LOS}=30\%$ (left) and 20% (right) for a single coplanar rotor. [13]	37
4.4	Variation of rotor lift-to-drag efficiency with rotor lift-offset, normalized by the maximum efficiency achieved with 30% LOS. [13]	38
4.5	Ganged Coaxial Helicopter Controls on the Ka-52.	39
4.6	Rotor System Response To Cyclic Control Inputs for Various Types of Rotors. [6]	39
4.7	Rotor Control System Definitions and (Non-)Coplanarity Effect. [6] (Edited)	40
4.8	XH-59A Control System. [6]	41
4.9	Independent FBW Control Scheme on the X2 Technology Demonstrator and S-97 Raider.	41
5.1	Modelling fidelity levels. [18]	43
5.2	Blade element aerodynamic environment with accompanying induced velocities. [19]	44
5.3	Perturbation velocities on the blade resulting from blade flapping velocity about a hinge and blade coning. [19]	45
5.4	Rotor flow conditions in axial flight: hover (a), climb (b), descent (c). [18]	48
5.5	Momentum theory solutions for axial flight rotor inflows.	49
5.6	Local momentum theory visualisation on a single rotor disc. [18]	50
5.7	Linear inflow approximation over the rotor disc, approximating the non-linear, non-uniform physical distribution.	51
5.8	Typical rotor skew angles in function of advance ratio for various thrust coefficients. [19]	52
5.9	BEMT flow model used for the analysis of a coaxial rotorcraft with the lower rotor operating in the wake of the upper rotor. [30]	53
5.10	Variation of inflow interference with advance ratio from the CFD simulation results by Zhou et al. [37]	54
5.11	Wake vortex geometry as used in Castles. [38]	56
5.12	Wake contraction of the upper rotor, and its influence on the lower rotor. [39]	57
5.13	Visualisation of the rotor wake structure during hover. [40]	57
5.14	Coriolis force visualisation on a rotor blade during flapping motion.	58
5.15	Equivalent blade flapping model. [26]	58
5.16	Flapping and feathering motions in the longitudinal plane for the upper (left) and lower (right) rotor. [39]	60
5.17	Flapping and feathering motions in the lateral plane for the upper (left) and lower (right) rotor. [39]	60
5.18	Propeller angles and velocities in the propeller blade element reference frame. [28]	61
6.1	Structure of a PID controller. [45]	64



6.2	Outer loop PID control architecture for a compound coaxial helicopter.	65
6.3	Top level control architecture for an EMF control system.	66
6.4	Inner loop control law architecture using EMF for a compound coaxial helicopter. [26] . . .	66
6.5	State results in a compound coaxial helicopter during a bob-down manoeuvre using a PID or DATC controller architecture. [26]	67
7.1	Solution domain for the desired control effort $2u_1 + u_2 = \nu$	71
7.2	Control strategy for a compound coaxial helicopter. [26]	74
7.3	Control efficiency for pitch and yaw channels. [26]	76
7.4	Trim results with propeller allocation strategy only accounting for minimum power requirements. [41]	77
7.5	Propeller control strategy design flowchart. [41]	78
8.1	ADS-33E-PRF definitions for frequency response gain and phase stability margins. [51] . .	80
8.2	ADS-33E-PRF bandwidth/phase delay handling quality criteria for pitch (right) and roll (left). [51]	81
8.3	Pitch-roll cross-coupling requirements for aggressive agility according to ADS-33E standards. [18] [51]	82
8.6	Cooper-Harper rating scale definition. [51]	82
8.4	Attitude quickness requirements according to ADS-33E for target acquisition and tracking (left) and all other MTEs (right). [51]	83
8.5	Definition of quickness criterion parameters. [51]	83
10.1	Top-level model architecture diagram.	91
10.2	Right view of the compound coaxial helicopter.	93
10.3	Top view of the compound coaxial helicopter.	93
10.4	Front view of the compound coaxial helicopter.	94
10.5	Rotor system depicting reference planes and definition of angles.	95
10.6	Equivalent blade flapping model using equivalent hinge-offset and spring-stiffness. [26] . . .	97
10.7	Blade mode fan diagram depicting the hinge and spring model, hinge only model, and validation data from Berger [60].	98
10.8	Flow-diagram of the discrete time-step inflow calculation.	100
10.9	Actuator disk theory model during hover.	100
10.10	Actuator disk theory model during forward flight.	101
10.11	Variation of inflow interference with advance ratio from the CFD simulation results by Zhou et al. [37]	102
10.12	Wake contraction from upper to lower rotor in an ABC rotor configuration.	104
10.13	Forces acting on the rotor blade. (Illustrated for the upper rotor, same principle applies to lower rotor)	104
10.14	Aerodynamic interference over the propeller and empennage caused by rotor wakes.	108
10.15	Upward shift in lift curve with positive airsurface deflection.	110
10.16	Lookup table used for lift coefficient calculation for horizontal and vertical tail, including stall effect.	111
10.17	Summed equivalent flat plate coefficient $\sum(C_D S)_S$ in function of gross weight. [19]	113
10.18	Lateral moment equilibrium comparison between a single main rotor (left) and the ABC concept (right). [33]	114
10.19	LOS in function of flight velocity as per Ferguson. [28]	115
10.20	Effect on LOS due to differential collective input. [17]	116
11.1	Newton-Raphson trim algorithm flowchart.	118
11.2	Number of iterations until threshold ϵ has been reached, using the last trim point's trim vector, or starting from the very first initial conditions respectively.	120
11.3	Trim results for the compound coaxial model without and with RPM scheduling, with validation from Qiu [26] and Berger [46] respectively.	121
11.4	Rotor angles throughout the trim regime using a rotor blade twist angle $\theta_{tw} = -10$ deg for both rotors.	122



11.5 Rotor angles throughout the trim regime using a rotor blade twist angle $\theta_{tw} = -3$ deg for both rotors.	122
12.1 Main stability derivatives under analysis.	125
12.2 Component contribution to M_w	126
12.3 Control derivatives - collective.	127
12.4 Control derivatives - differential collective.	128
12.5 Control derivatives - longitudinal cyclic.	129
12.6 Control derivatives - lateral cyclic.	130
12.7 Control derivatives - differential lateral cyclic.	131
12.8 Control derivatives - pusher propeller collective.	132
12.11 Nonlinear response at hover.	132
12.12 Nonlinear response at 40 m/s.	132
12.9 Control derivatives - elevator.	133
12.13 Nonlinear response at 65 m/s.	133
12.14 Nonlinear response at 100 m/s.	133
12.10 Control derivatives - rudder.	134
12.15 Linear response at hover.	134
12.16 Linear response at 40 m/s.	134
12.17 Linear response at 65 m/s.	135
12.18 Linear response at 100 m/s.	135
12.19 Longitudinal natural modes of motion.	136
12.20 Spring term result of Equation 12.10.	137
13.1 Top-level controller architecture.	138
13.2 Control effectiveness for pitch and yaw throughout flight range.	140
13.3 Control allocation weights for the pitch channel.	140
13.4 Inner loop controller design based on EMF control.	143
13.5 Step input reference command and EMF model response.	144
13.6 Outer loop controller design based on EMF control. [26]	145
13.7 Pitch attitude tracking performance at 40 m/s.	146
13.8 Decoupled manual gain tuning approach for the CCH control system.	147
13.9 Coupled attitude step input tuning results at 40 m/s.	147
13.10 Reference 3-2-1-1 signal with an attitude command of 3 degrees.	149
13.11 Tracked attitude commands during the 3-2-1-1 roll manoeuvre.	150
13.12 Inputs commands during the 3-2-1-1 roll manoeuvre.	150
13.13 Tracked attitude commands during the 3-2-1-1 pitch manoeuvre.	150
13.14 Inputs commands during the 3-2-1-1 pitch manoeuvre.	150
13.15 Tracked attitude commands during the 3-2-1-1 yaw manoeuvre.	151
13.16 Inputs commands during the 3-2-1-1 yaw manoeuvre.	151
13.17 Commanded velocities V_x and V_y during the ADS-33 bob-up/bob-down with acceleration and deceleration manoeuvre.	152
13.18 State results comparing the commanded values and EMF values during the bob-up/bob-down with acceleration and deceleration manoeuvre.	153
13.19 Control inputs results resulting from the EMF controller during the bob-up/bob-down with acceleration and deceleration manoeuvre.	154
14.1 Definitions of bandwidth and phase delay as in ADS-33E PRF. [51]	156
14.2 ADS-33E-PRF Standards for bandwidth and phase delay during pitch target acquisition and tracking.	157
14.3 ADS-33E-PRF Standards for bandwidth and phase delay during roll target acquisition and tracking.	157
14.4 Pitch attitude quickness results from 5-30 deg commands, compared to ADS-33 requirements.	158
14.5 Pitch response for $\theta_{cmd} = 5$ deg.	159
14.6 Pitch response for $\theta_{cmd} = 20$ deg.	159
14.7 Roll attitude quickness results from 10-50 deg commands, compared to ADS-33 requirements.	160
14.8 Roll response for $\phi_{cmd} = 10$ deg.	160



14.9	Roll response for $\phi_{cmd} = 20$ deg.	160
14.10	Yaw attitude quickness results from 10-60 deg commands, compared to ADS-33 requirements.	161
14.11	Yaw response for $\psi_{cmd} = 10$ deg.	161
14.12	Yaw response for $\psi_{cmd} = 20$ deg.	161
B.1	Stability derivatives - longitudinal.	174
B.2	Stability derivatives - lateral.	175
B.3	Stability derivatives - lateral into longitudinal.	175
B.4	Stability derivatives - longitudinal into lateral.	176
B.5	Control derivatives - collective.	176
B.6	Control derivatives - differential collective.	177
B.7	Control derivatives - longitudinal cyclic.	177
B.8	Control derivatives - lateral cyclic.	178
B.9	Control derivatives - differential lateral cyclic.	178
B.10	Control derivatives - pusher propeller collective.	179

List of Tables

6.1	Modern Control Strategies. [44]	69
9.1	Main research paper domain exploration applicable to research topic.	84
10.1	Main aiframe parameters.	94
10.2	Blade Flapping Model Parameters.	98
10.3	Upper and lower rotor planform parameters.	106
10.4	Pusher propeller planform parameters.	109
10.5	Empennage parameters.	112
10.6	Fuselage parameters.	113
11.1	Initial guesses of the trim variables at the first trim point.	119
12.1	Longitudinal eigenvectors throughout the trim range.	137
13.1	Compound coaxial helicopter control strategy throughout flight regime. [26]	142
13.2	Explicit model parameters.	143
13.3	Actuator limit and rate constraints.	144
13.4	Performance values for the pitch, roll and yaw channels after coupled inner-loop tuning.	148
13.5	Final controller gains used in the inner- and outer- loop at 40m/s.	148
14.1	Bandwidth and phase delay results on the inner-loop control during the transition region for the linear system.	156

Introduction

1.1. Research Motivation

In 2009, the US Army officially issued a modernisation program in order to modernise the current combat rotorcraft platforms in the U.S. Inventory - the Chinook, Black Hawk, Apache and Kiowa Warrior dating from the 1960's and 1970's. This program was coined the 'Future Vertical Lift (FVL) program, serving as an effort to implement new technologies that improve manoeuvrability, speed, range, survivability and reduced logistical footprint compared to current rotorcraft.

The FVL program aims to fulfil developments in five basic categories, or 'capability sets', of various aircraft sizes, but the initial focus is set onto two categories. The first category being a medium transport aircraft, able to succeed the Army UH-60 Blackhawk, and the Marine H-1 "Huey" under the term of Future Long-Range Assault Aircraft (FLRAA). The second category aims to provide a novel solution for a scout platform in roughly the same role as the AH-64 Apache under the term Future Attack and Reconnaissance Aircraft (FARA). [1]

Based on the facts that the FLRAA contract was recently (2022) awarded to Bell in favour of the Sikorsky-Boeing SB-1 Defiant [2], it would have been a fair assumption to predict the 2024 FARA contract to go to Sikorsky in order to maintain a competitive landscape between the two manufacturers for the years to come. This prediction is further backed up by the fact that the coaxial Raider X helicopter is based on the continuous development of previous variants of the rotorcraft, such as the Raider, X2 Technology Demonstrator, and XH-59A dating back to the 1970's. Meanwhile, Bell has yet to finish the construction of the first Invictus prototype. However, in early 2024, the U.S. Army decided to cancel the FARA program, with reasons still open to speculation. Critics have however stated that the cancellation of FARA would leave unfilled gaps in the Army inventory, with drones not being the solution to them. [3]

Apart from the U.S. Army, European industry and research and development branches such as the Netherlands Aerospace Center (NLR)¹ have taken up interest in future concepts as well. Recently, NLR has started cooperation with industry partners to develop a high-speed compounded coaxial rotorcraft. Based on these current industry events and shifts in rotorcraft doctrine, an interest was sparked for a master thesis project combining the interests of TU Delft, NLR and industry partners.

1.2. Research Scope

This thesis shall focus on the preliminary modelling, high-level control law and architecture development, control allocation architecture designs, and handling quality metric selection and evaluation for a compound coaxial rotorcraft. The thesis and accompanying literature study serve as an effort to map and demonstrate the current advancements in compound coaxial rotorcraft control & simulation field, while simultaneously providing insights into these aspects for stakeholders such as NLR and industry partners.

The modelling efforts will prioritise achieving the necessary fidelity to accurately capture the flight dynamics of the helicopter. The primary focus will be on the dynamic behaviour and simulation manoeuvres in the longitudinal plane, while still accounting for lateral cross-coupling effects. The control and handling quality assessments will concentrate on the aircraft's transition region, specifically between 20 and 65 m/s, utilising a control allocation algorithm.

¹Netherlands Aerospace Centre: <https://www.nlr.nl>



1.3. Research Formulation

In this section, the research gap, objectives and questions are stated. The research is split up over three topics: modelling, control and handling quality assessment. These will each have their own sub-objectives and sub-questions. While the literature study covers, and the thesis will cover modelling and handling quality analysis, the main focus is and will be on the design and implementation of a high-level control law & control allocation architecture. The modelling of the helicopter is a necessary step to complete this goal and to gain physical understanding of the system being worked with. Handling quality criteria selection and evaluation then serves as a way to evaluate the control design, while being the driver for the control design itself.

1.3.1. Research Objectives

The research objectives serve as goals to be accomplished during the thesis work. They are meant to be specific and demarcate the project scope, such that clear project objectives can be fulfilled. The main research objective incorporates three topics: (i) modelling, (ii) control and (iii) handling quality assessment.

Modelling

Research Objective

Construct and validate a compound coaxial helicopter flight dynamics model capable of supporting the development of a control system during the conceptual design phase.

The first part of the research focuses on the modelling of the compound coaxial rotorcraft. In order to obtain a solid foundational knowledge on the research topic, a 3 degrees-of-freedom model flight dynamics model, accompanied by a coaxial inflow model will be developed in Matlab and MATLAB Simulink. After this model has been developed and a thorough understanding of the physics at play has been conceived, a previously developed 6 degrees-of-freedom model will be extended and modified in order to provide an Advancing Blade Concept compound coaxial rotorcraft model. The goal of the model is not to provide a high level of fidelity for higher order analyses, but rather aims to serve as a model suitable for the analysis of flight dynamics and design of a flight control system.

Control

Research Objective

Construct a high-level control law architecture, suitable for the conceptual design phase, which leverages the use of control allocation, in order to assess the identified handling quality criteria.

The development of the control system is the main goal of this thesis. As a helicopter is a naturally unstable vehicle in some parts of envelope, the resulting handling qualities are poor at best, which drives the need for a stability and control augmentation system. Therefore, the control system aims to provide improved, and preferably Level 1 handling qualities. However, due to the helicopter design being in the conceptual phase, the control system has to reflect this in terms of flexibility and practical implementability.

Handling Quality Assessment

Research Objective

Identify and implement suitable objective handling quality criteria, and methods to assess these criteria, which are applicable to the high-speed helicopter configuration during the conceptual design phase.

The main driver of the flight mechanics model and flight control system are the handling qualities. Due to the high-speed capability and compound design of the helicopter, typical handling quality criteria do not cover all aspects applicable to such a configuration. Therefore, an analysis must be conducted to identify the applicable handling qualities. After the identification of the handling qualities, they will be



assessed accompanied by the control system. The assessment of the handling qualities will be limited to the objective criteria, since the assessment of subjective criteria require the use of additional simulation efforts such as inverse simulation or piloted simulation experiments, which is beyond the scope of this thesis.

1.3.2. Research Questions

The research questions serve as a guideline throughout the literature study. Therefore, the research questions posed here are to be addressed in this document. As in the research objectives, the main research question incorporates three topics: (i) modelling, (ii) control and (iii) handling quality assessment. Each topic will have its own sub-questions. Although these topics are split, it must be noted that they are intertwined and all influence each other due to the multidisciplinary nature of the project.

Main Research Question

Research Question Main

What type of control architecture, accompanying model structure, and handling quality criteria are practically implementable during the conceptual design phase of a high-speed compound coaxial helicopter configuration in order to execute a high-level flight dynamics analysis and objective handling quality assessment?

Modelling

Research Question M.1

What model fidelity-level is required for the design of a helicopter controller during conceptual design?

Research Question M.2

How will the rotor inflow, rotor interference, wake contraction, pusher propeller, fuselage, and empennage be modelled for a compound coaxial rotorcraft?

Research Question M.3

What trim strategy will be employed in order to trim the compound coaxial helicopter model?

Control

Research Question C.1

What control architectures are most suitable for the design of a high-level controller of a compound coaxial helicopter during the conceptual design phase in order to attain desirable handling qualities?

Research Question C.2

What methods are most suitable for the control allocation of a compound coaxial helicopter during the conceptual design phase?

Research Question C.3

How are the control actuators for a compound coaxial helicopter allocated during the various flight phases?



Handling Quality Assessment

Research Question HQ.1

What objective handling quality assessment criteria should be considered during the conceptual design of a compound coaxial helicopter?

Research Question HQ.2

How will the selected handling quality criteria be enforced such that they have desirable results in the compound coaxial helicopter configuration?

1.4. Document Outline

A broad literature study, aiming to map the current advancements in compound coaxial rotorcraft modelling, control and handling quality assessment, was the start of this thesis. Apart from the mapping of advancements, various research questions and a plan of attack for the thesis development was developed. This is all outlined in Chapter 3-Chapter 15. The core of the report then starts in Chapter 10, in which a 9-dof nonlinear helicopter model is constructed, and further considerations such as more advanced inflow modelling methods, lateral lift-offset and RPM-scheduling are discussed. After the construction of the nonlinear model, it is trimmed using the Newton-Raphson trim algorithm in Chapter 11. The model is linearised and its stability and control derivatives, along with the analysis of the open-loop system and longitudinal natural modes of motion are discussed in Chapter 12. After the compound coaxial helicopter has been modelled and its stability analysed, a controller in order to improve the stability and fly mission task elements is designed in Chapter 13. In this chapter, the aspects of the control allocation are discussed as well. Lastly, an objective handling quality assessment is performed in terms of bandwidth and phase delay, and attitude quickness in Chapter 14. This chapter also concludes with some closing remarks on further handling quality selection considerations.

Part I

Scientific Paper

Flight Dynamics Modelling, Control and Handling Quality Assessment of a Compound Coaxial Helicopter in Transition Flight

Ynias J.E. Prencipe*
Aerospace Engineering
Delft University of Technology
Delft, Netherlands
Y.J.E.Prencipe@student.tudelft.nl

Marilena D. Pavel†
Aerospace Engineering
Delft University of Technology
Delft, Netherlands
M.D.Pavel@tudelft.nl

George Tzanetos Alevras°
Vertical Flight & Aeroacoustics
Netherlands Aerospace Centre
Amsterdam, Netherlands
George.Tzanetos.Alevras@nlr.nl

* Msc Student, † Supervisor, ° External Supervisor

Keywords: Compound Coaxial Helicopter, Flight Dynamics, Mathematical Modelling, Control, Handling Qualities, Explicit Model Following, Weighted Pseudo Inverse, Control Allocation

Abstract

This research focuses on developing a control system for a compound coaxial helicopter (CCH) similar to the SB-1 Defiant, capable of both hovering and high-speed forward flight. The study introduces a 9 degrees of freedom mathematical model with 3 inflow states for the upper rotor, lower rotor, and pusher propeller, accounting for mutual rotor interference. The model undergoes a trim and stability analysis, revealing instability during transitional flight, necessitating a stability and control augmentation system. This system is implemented using an Explicit Model-Following (EMF) method, stabilized by a PID controller and a Weighted Pseudo-Inverse (WPI) control allocation algorithm. The controller effectively manages various flight controls through transition, as tested in a bob-up/bob-down mission task. While it performs well, there is room for improvement in input coupling and jitter behavior. Finally, an objective handling quality assessment based on ADS-33E metrics shows that the control system meets Level 1 handling quality criteria in the transition region for attitude and bandwidth, though some inefficiencies in control allocation during large attitude maneuvers were identified.

Nomenclature

Symbols

α Angle of attack [rad]

β Sideslip angle [rad]

δ Interference factor [-]

δ_e Elevator deflection [rad]

δ_r Rudder deflection [rad]

ϵ Small non-zero constant [-]

ϵ_0 Average downwash angle [rad]

ϵ_β Flapping hinge offset ratio [-]

γ Lock number [-]

γ_s Rotor shaft angle [rad]

λ Permeability [-]

λ_0 Induced inflow ratio [-]

μ Real part of eigenvalue [-]

μ_x Advance ratio [-]

ν Virtual control signal [-]

Ω Rotational velocity [rad/s]

ω Bandwidth [rad/s]

ω Imaginary part of eigenvalue [-]

ω Natural frequency [rad/s]

ϕ Attitude roll angle [rad]

Ψ Blade azimuth position [rad]

ψ Attitude yaw angle [rad]

ρ Air density [kg/m³]

ρ Control weight [-]

σ Rotor Solidity [-]

τ Phase delay [s]

τ Time constant [s]

θ Attitude pitch angle [rad]

θ_0 Collective pitch [rad]

θ_c Lateral cyclic pitch [rad]

θ_d Differential collective pitch [rad]

θ_p Propeller collective pitch [rad]

θ_s Longitudinal cyclic pitch [rad]

ζ	Damping coefficient [-]
K_β	Equivalent flapping spring stiffness [N/m]
M	EMF transfer function [-]
N	Amount of rotor blades per rotor [-]
p	Body roll rate [rad/s]
q	Body pitch rate [rad/s]
r	Body yaw rate [rad/s]
u	X-axis velocity component [m/s]
v	Y-axis velocity component [m/s]
w	Z-axis velocity component [m/s]

Subscripts

c	Commanded signal after EMF model
cmd	Commanded signal
fus	Fuselage
h	Horizontal tail surface
l	Lower rotor
l2u	Lower to upper
p	Pusher propeller
u	Upper rotor
u2l	Upper to lower
v	Vertical tail surface

Superscripts

BEM	Blade Element Method
Gl	Glauert theory

Abbreviations

ABC	Advancing Blade Concept
CCH	Compound Coaxial Helicopter
EMF	Explicit Model Following
WPI	Weighted Pseudo-Inverse

1 Introduction

In 2009, the US Army officially issued a modernisation program in order to modernise the current combat rotorcraft platforms in the U.S. Inventory - the Chinook, Black Hawk, Apache and Kiowa Warrior dating from the 1960's and 1970's. This program was coined the 'Future Vertical Lift (FVL) program, serving as an effort to implement new technologies that improve manoeuvrability, speed, range, survivability and reduced logistical footprint compared to current rotorcraft.

Apart from the U.S. Army, European industry and research and development branches such as the Netherlands Aerospace Center (NLR)¹ have taken up interest in future concepts as well. Recently, NLR has started cooperation with industry partners to develop a high-speed compounded coaxial rotorcraft. Based on these current industry events and shifts in rotorcraft doctrine, an interest was sparked for a master thesis project combining the interests of TU Delft, NLR and industry partners.

This research focuses on the preliminary modelling, high-level control law and architecture development, control allocation architecture design, and handling quality metric evaluation for a Compound coaxial rotorcraft (CCH). The research serves as an effort to demonstrate the current advancements in compound coaxial rotorcraft control & simulation field, while simultaneously providing insights into these aspects for stakeholders such as NLR and industry partners.

The modelling efforts will prioritise achieving the necessary fidelity to capture the flight dynamics of the CCH including a collective control, differential collective, longitudinal cyclic, lateral cyclic, elevator, rudder, and pusher propeller. The primary focus will be on the dynamic behaviour and simulation manoeuvres in the longitudinal plane, while still accounting for lateral cross-coupling effects. The control and handling quality assessments will concentrate on improving the stability and control inside the CCH transition region, specifically between 20 and 65 m/s, utilising a control allocation algorithm.

The research paper is outlined as follows. First, the CCH mathematical model will be discussed in section 2, including the planform analysis, equations of motion description, coaxial rotor modelling where the special inflow dynamics and flapping dynamics are discussed, empennage and fuselage modelling, and the overall contribution of these parts. Following the construction of the model, the model is trimmed and validated in subsection 2.6. In section 3, the model will be linearised and a longitudinal dynamic stability analysis is performed, assessing the need for a stability and control augmentation system. An EMF flight controller design, including a control allocation algorithm, and assessment by means of a bob-up/bob-down with acceleration and deceleration manoeuvre, is described fully in section 4. section 5 covers the ADS-33 handling quality parameters bandwidth and phase delay, and attitude quickness. The paper is concluded by the conclusion and recommendations in section 6 and section 7 respectively.

¹Netherlands Aerospace Centre: <https://www.nlr.nl>

2 Compound Coaxial Helicopter Modelling

In this section, a nonlinear analytical model of the compound coaxial helicopter is developed which will be used for stability analysis, flight control design, and handling quality assessment. The helicopter under analysis is depicted in Figure 1- Figure 3. The configuration is based on the SB-1 defiant and previous generations of the ABC family [1] [2] [3] and features a coaxial rotor based on the ABC rotors [4], fuselage, elevator, rudder, and pusher propeller. The coaxial rotor features 4 controls: the mean collective θ_0 , differential collective θ_d , longitudinal cyclic θ_s , and lateral cyclic θ_c . The rudder and elevator bring their respective controls δ_r and δ_e , and the pusher propeller features variable pitch by means of the propeller collective θ_p . The airframe planform parameters are listed in subsection A.1.

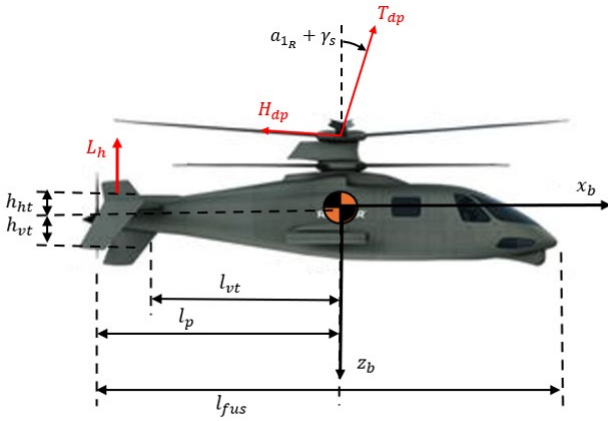


Figure 1: Right view of the compound coaxial helicopter.

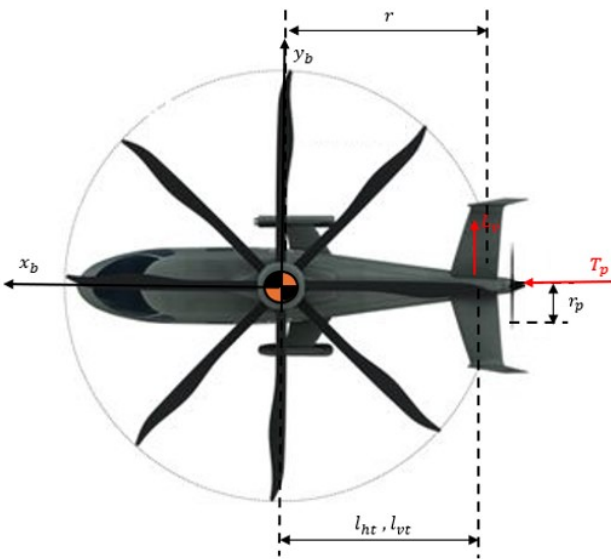


Figure 2: Top view of the compound coaxial helicopter.



Figure 3: Front view of the compound coaxial helicopter.

2.1 Equations of Motion

A total of 9 states are part of the model's system of equations:

- The body velocities: $\vec{u} = [u \ v \ w]^T$
- The body angular velocities: $\vec{\omega} = [p \ q \ r]^T$
- The quasi-dynamic inflow states of the upper rotor, lower rotor and pusher propeller: $\vec{\lambda}_0 = [\lambda_{0_u} \ \lambda_{0_l} \ \lambda_{0_p}]^T$

The positional vector $[x \ y \ z]^T$ and the Euler angles $[\phi \ \theta \ \psi]^T$ are not part of the system states. Rather, when used in the control system detailed in section 4, their values are calculated by time integration of the body velocities and angular velocities respectively, with their initial position as starting condition. The generalised notation of the body velocity and angular velocity states is stated in Equation 1 and are well known throughout literature. Here, g denotes the gravitational constant, J the moment of inertia matrix, M the helicopter mass, $\vec{u} = [u, v, w]^T$ the body-fixed linear velocity, $\vec{\omega} = [p, q, r]^T$ the body-fixed angular velocity, and \mathbb{T}_n^b the transformation matrix from the navigational to the body frame.

$$\begin{aligned} \dot{\vec{u}} &= \frac{1}{M} F_{tot} + \mathbb{T}_n^b [0 \ 0 \ g]^T - \vec{\omega} \times \vec{u} \\ \dot{\vec{\omega}} &= J^{-1} [M_{tot} - \vec{\omega} \times J \vec{\omega}] \end{aligned} \quad (1)$$

Expanding these equations, one can find the total system equations of motion using the default 6-dof equations of motion, joined by the quasi-dynamic inflow states [5]:

$$\begin{aligned} \dot{u} &= \frac{X_{tot}}{m} - g \sin \theta - qw + rv \\ \dot{v} &= \frac{Y_{tot}}{m} - g \cos \theta \sin \phi - ru + pw \\ \dot{w} &= \frac{Z_{tot}}{m} - g \cos \theta \cos \phi - pv + qu \end{aligned} \quad (2)$$

$$\begin{aligned}
\dot{p} &= \frac{(I_{yy}I_{zz} - I_{zz}^2 - I_{xz}^2)r q + (I_{xx} - I_{yy} + I_{zz})I_{xz}pq}{I_{xx}I_{zz} - I_{xz}^2} \\
&+ \frac{I_{zz}L_{tot} + I_{xz}N_{tot}}{I_{xx}I_{zz} - I_{xz}^2} \\
\dot{q} &= \frac{M_{tot} + (I_{zz} - I_{xx})pr - I_{xz}(r^2 - p^2)}{I_{yy}} \\
\dot{r} &= \frac{(I_{xx}^2 - I_{xx}I_{yy} + I_{xz}^2)pq}{I_{xx}I_{zz} - I_{xz}^2} \\
&+ \frac{-(I_{xx} - I_{yy} + I_{zz})I_{xz}qr + I_{xz}L_{tot} + I_{xx}N_{tot}}{I_{xx}I_{zz} - I_{xz}^2} \\
\dot{\lambda}_{0_u} &= \frac{C_{T_u}^{BEM} - C_{T_u}^{Gl}}{\tau_{\lambda_0}} \\
\dot{\lambda}_{0_l} &= \frac{C_{T_l}^{BEM} - C_{T_l}^{Gl}}{\tau_{\lambda_0}} \\
\dot{\lambda}_{0_p} &= \frac{C_{T_p}^{BEM} - C_{T_p}^{Gl}}{\tau_{\lambda_0}}
\end{aligned} \tag{3}$$

where m is the aircraft mass, X , Y , Z the forces in positive x -, y - and z -axis directions, ϕ , θ , and ψ the attitude roll, pitch and yaw angles, L , M , and N the aerodynamic moments around the x -, y , and z -axis respectively, C_T^{BEM} the blade element thrust coefficient, C_T^{Gl} the Glauert thrust coefficient, and τ_{λ_0} a small non-zero time constant for the quasi-dynamic inflow, as will be elaborated upon in the following subsection.

2.2 Coaxial rotor modelling

The most complex aspect on any coaxial helicopter model are the coaxial rotor blades. The main aspects on this are the manners in which the thrust is calculated, more specifically, the inflow dynamics and flapping dynamics.

2.2.1 Rotor Forces and Moments

The thrust of the upper and lower rotors are calculated by means of Glauert's theory of thrust which is based on momentum theory.[6] This results in the thrust coefficients as calculated by Equation 5 where both coefficients are a result of the advance ratio μ , their mean inflow coefficient λ_0 , the disk plane angle α^{dp} , and an interference factor δ_{u2l} and δ_{l2u} for the upper to the lower and lower to the upper rotor respectively, taking into account the inflow of the other rotor. [7]

$$\begin{aligned}
C_{T_u}^{Gl} &= 2\lambda_0^u \sqrt{\left(\mu \cos \alpha_u^{dp}\right)^2 + \left(\mu \sin \alpha_u^{dp} + \lambda_0^u + \delta_{l2u}\lambda_0^l\right)^2} \\
C_{T_l}^{Gl} &= 2\lambda_0^l \sqrt{\left(\mu \cos \alpha_l^{dp}\right)^2 + \left(\mu \sin \alpha_l^{dp} + \lambda_0^l + \delta_{u2l}\lambda_0^u\right)^2}
\end{aligned} \tag{5}$$

As clear from the equation above, both rotors are modelled to include mutual interference effects by means of the factors δ_{u2l} and δ_{l2u} . However, wake contraction effects are not taken into account due to the close rotor spacing of the ABC rotors.

[4] The interference factors are a function of advance ratio μ due to the wake skew angle. [8] These effects were linearly approximated, resulting in the interference factors:

$$\begin{cases} \delta_{l2u} = -2.15\mu + 0.68 & \text{for } 0 \leq \mu \leq 0.316 \\ \delta_{l2u} = 0 & \text{for } \mu > 0.316 \\ \delta_{u2l} = -3.81\mu + 1.45 & \text{for } 0 \leq \mu \leq 0.381 \\ \delta_{u2l} = 0 & \text{for } \mu > 0.381 \end{cases} \tag{6}$$

Using these interference factors, the mean inflow of the upper and lower, λ_{0_u} and λ_{0_l} , are calculated by

$$\begin{aligned} \lambda_{0_u} &= \lambda'_{0_u} + \delta_{l2u}\lambda'_{0_l} \\ \lambda_{0_l} &= \lambda'_{0_l} + \delta_{u2l}\lambda'_{0_u} \end{aligned} \tag{7}$$

where λ'_0 denotes the mean inflow before interference effects.

There are many ways to calculate this inflow [9] [10] [11] [12], with varying degrees of fidelity. In this research, use is made out of a quasi-dynamic inflow for both rotors, calculated by

$$\dot{\lambda}_0 = \frac{C_T^{BEM} - C_T^{Gl}}{\tau_{\lambda_0}} \tag{8}$$

where τ_{λ_0} is a small non-zero time constant. It becomes clear that λ_0 is calculated by means of a difference between the Glauert thrust coefficient and the BEM thrust coefficient C_T^{BEM} . Based on the small angle approximation, the thrust coefficient in the disk plane can be approximated to be equal to the thrust coefficient in the control plane, and according to Pavel [13] [14] can be calculated, together with the horizontal and sideway forces $C_{H_{dp}}$ and $C_{S_{dp}}$, and the torque moment $C_{Q_{dp}}$ coefficients, by

$$C_{T_{dp}} = \frac{\sigma C_{L\alpha}}{2} \left[\left(\frac{1}{3} + \frac{\mu_x^2}{2} \right) (\theta_0 \pm \Delta\theta_0) + \frac{1 + \mu_x^2}{8} \theta_{tw} + \frac{\mu_x \bar{p}}{4} + \frac{\lambda}{2} \right]$$

$$C_{H_{dp}} = \sigma C_D \frac{\mu_x}{4} + \frac{\sigma C_{L\alpha}}{4} \left[(a_1 \frac{\mu_x^2}{2} + \mu_x \lambda) (\theta_0 \pm \Delta\theta_0) + \frac{\mu_x \lambda}{2} \theta_{tw} + \bar{q} \left(\frac{b_1 \mu_x}{4} - \frac{a_0}{3} \right) - \frac{a_0 b_1}{3} + (a_0^2 + a_1^2) \frac{\mu_x}{2} + \frac{\bar{p} \lambda}{2} \right]$$

$$C_{S_{dp}} = \frac{\sigma C_{L\alpha}}{4} \left[-\frac{1}{2} \mu_x a_0 (\theta_0 \pm \Delta\theta_0) + \left(-a_0 \frac{\mu_x}{3} + b_1 \frac{\mu_x^2}{4} - \frac{\bar{q}}{4} \right) \theta_{tw} - 3a_0 \mu_x (\mu_x a_1 - \lambda) + b_1 \frac{\mu_x a_1 - \lambda}{2} + a_0 a_1 \frac{\mu_x^2 + 1}{3} \right]$$

$$C_{Q_{dp}} = \sigma \left[\frac{C_D}{8} (1 + 4.7\mu_x^2) - C_{T_{dp}} \lambda_{dp} - C_{H_{dp}} \mu_x \right] \tag{9}$$

2.2.2 Flapping Dynamics

In order to calculate the flapping coefficients, an equivalent blade flapping model is used, which utilises hinge-offset and spring-stiffness, as depicted in Figure 4. Here, K_β denotes the spring stiffness, and ϱ the equivalent hinge offset. These parameters are tuned in order to achieve realistic moments and achieve a normalised flapping frequency at nominal rotor speed

of 1.4, similar to the results in Berger [15]. Note that due to the use of the ABC rotor, the lead/lag and feathering dynamics can be neglected. [16]

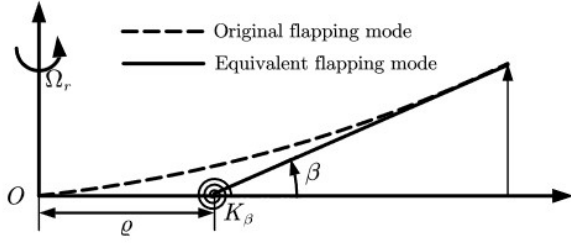


Figure 4: Equivalent blade flapping model. [17]

In order to calculate the flapping angles produced by this system, use is made of the Bramwell flapping angles [5]:

$$\begin{aligned}
 a_0 &= \frac{\gamma}{8\nu_\beta^2} [\theta_0 (1 + \mu_x^2) + \frac{4}{3}\lambda + \frac{2}{3}\mu_x\bar{p} + \theta_{tw} \left(\frac{4}{5} + \frac{2}{3}\mu_x^2 \right) - \frac{4}{3}\mu_x\theta_s] \\
 a_1 &= \frac{8}{\gamma} \frac{\nu_\beta^2 - 1}{1 - \frac{1}{2}\mu_x^2} b_1 \\
 &+ \frac{\frac{8}{3}\mu_x\theta_0 + 2\mu_x\lambda + \bar{p} - \frac{16}{\gamma}\bar{q} + 2\theta_{tw}\mu_x - (1 + \frac{3}{2}\mu_x^2)\theta_s}{1 - \frac{1}{2}\mu_x^2} \\
 b_1 &= -\frac{8}{\gamma} \frac{\nu_\beta^2 - 1}{1 + \frac{1}{2}\mu_x^2} a_1 \\
 &+ \frac{\frac{4}{3}\mu_x a_0 + \bar{q} - \frac{16}{\gamma}\bar{p} + (1 + \frac{1}{2}\mu_x^2)\theta_c}{1 + \frac{1}{2}\mu_x^2}
 \end{aligned} \tag{10}$$

where γ is the rotor Lock number, λ the rotor permeability, calculated by $\lambda = \frac{\mu_x - \lambda_0}{2}$, \bar{p} , and \bar{q} the normalised angular rates ($\bar{q} = \frac{q}{\Omega R}$), and θ_{tw} the rotor blade twist angle. In these equations, only the hinge-offset is taken into account by $\nu_\beta = 1 + \frac{3}{2} \frac{\epsilon_\beta}{1 - \epsilon_\beta}$, and not spring stiffness. In an effort to overcome this problem, the hinge offset ϵ_β used in the flapping equations, and thus not during force and moment calculations, is tuned in order to produce a normalised flapping frequency at nominal rotor speed of 1.4 as well. It must be stressed that this ϵ_β value is not used in the body dynamics, but only for flapping angle calculations. In order to take the moments produced by the hinge-offset and spring stiffness into account, use is made of the equations for the L and M moment produced by the hinge offset, L_e and M_e :

$$\begin{aligned}
 L_e &= (\Omega R)^2 \epsilon_\beta m_{bl} \sin b_{1r} \\
 M_e &= (\Omega R)^2 \epsilon_\beta m_{bl} \sin (a_{1r} + \gamma_s)
 \end{aligned} \tag{11}$$

where m_{bl} the blade mass, Ω the rotational frequency of the rotor blades, R the rotor radius, $a_{1R} = \theta_{1s} - a_{1u}$ the resulting longitudinal flapping angle after control inputs, $b_{1R} = \theta_{1c} + \Delta\theta_{1c} + b_{1u}$ the resulting lateral flapping angle after con-

rol inputs, and γ_s the rotor shaft angle.

The spring-stiffness moments L_k and M_k are calculated by:

$$\begin{aligned}
 L_k &= \frac{1}{2} N K_b \sin (b_{1r}) \\
 M_k &= \frac{1}{2} N K_b \sin (a_{1r} + \gamma_s)
 \end{aligned} \tag{12}$$

where N is the number of blades per rotor.

2.2.3 Global Rotor Contribution

The total resulting forces of one rotor \vec{F}_{mr} can be transformed from the control plane to the body frame by

$$\vec{F}_{mr} = \begin{bmatrix} X_{mr} \\ Y_{mr} \\ Z_{mr} \end{bmatrix} = \begin{bmatrix} c(a_{1R} + \gamma_s) & s(a_{1R} + \gamma_s) s(b_{1R}) & s(a_{1R} + \gamma_s) c(b_{1R}) \\ 0 & c(b_{1R}) & -s(b_{1R}) \\ -s(a_{1R} + \gamma_s) & c(a_{1R} + \gamma_s) s(b_{1R}) & c(a_{1R} + \gamma_s) c(b_{1R}) \end{bmatrix} \begin{bmatrix} -H_{dp} \\ S_{dp} \\ -T_{dp} \end{bmatrix} \tag{13}$$

where s denotes \sin and c \cos . Again use is made of the small angle approximation. The final forces and torque can then be dimensionalised by

$$\begin{aligned}
 T &= \rho A (\Omega R)^2 C_T \\
 H &= \rho A (\Omega R)^2 C_H \\
 S &= \rho A (\Omega R)^2 C_S \\
 Q &= \rho A (\Omega R)^2 R C_Q
 \end{aligned} \tag{14}$$

where ρ is the air density, and A the disc area.

These rotor force components are summed for the upper and lower rotor to form the total main rotor force vector $\vec{F}_{mr_{tot}}$.

The total moments produced by one rotor, \vec{M}_{mr} , can be calculated by

$$\vec{M}_{mr} = \begin{bmatrix} L_{mr} \\ M_{mr} \\ N_{mr} \end{bmatrix} = \begin{bmatrix} L_e + L_k + hY_{mr} - l_1 Z_{mr} \\ M_e + M_k - hX_{mr} + l_2 Z_{mr} \\ Q_{dp} + l_1 X_{mr} - lY_{mr} \end{bmatrix} \tag{15}$$

where again the total main rotor moment vector $\vec{M}_{mr_{tot}}$ is formed by the sum of the individual rotor moments.

2.3 Pusher propeller modelling

The pusher propeller thrust is modelled by means of a similar approach to that of the coaxial rotor setup. The propeller thrust is calculated by means of

$$T_p = C_{T_p}^{BEM} \rho (\Omega_p R_p)^2 \pi R_p^2 \tag{16}$$

where Ω_p is the propeller rotational speed, R_p the propeller radius, and $C_{T_p}^{BEM}$ the propeller thrust coefficient calculated by means of Blade Element Theory, as per [5]

$$C_{T_p}^{BEM} = \frac{\sigma_p c_{\alpha_p}}{2} \left(\left(\frac{1}{3} + \frac{\mu_x^{p2}}{2} \right) \theta_p + \frac{1 + \mu_x^{p2}}{8} \theta_{twist}^p + \frac{\lambda_p}{2} \right) \quad (17)$$

where μ_x^p is the propeller advance ratio, and is calculated by

$$\mu_x^p = \frac{\sqrt{v^2 + (w + K_p \Omega R (\delta_{l2u} \lambda_0^u + \delta_{u2l} \lambda_0^l) + ql_p)^2}}{\Omega_p R_p} \quad (18)$$

which takes into account the aerodynamic velocities of the airframe, angular accelerations and an aerodynamic interference factor K_p from the rotor wakes. λ_p is the rotor permeability, and is calculated by

$$\lambda_p = -\frac{u + qh_p - rd_p}{\Omega_p R_p} - \lambda_0^p \quad (19)$$

which compensates the airflow for the angular rates and corresponding moment arms, and takes into account the mean propeller inflow, which is also calculated by a quasi-dynamic inflow λ_{0_p} , similar to Equation 8. The required Glauert thrust coefficient for the quasi-dynamic inflow is calculated by means of

$$C_{T_p}^{Gl} = 2\lambda_0^p \sqrt{\mu_x^p \sin \alpha_p^{sp2} + \mu_x^p \cos \alpha_p^{sp} + \lambda_0^{p2}} \quad (20)$$

The torque moment produced by the propeller, Q_p , was calculated in a similar manner to that of the rotor.

Subsequently, the total forces and moments generated by the propeller are calculated by:

$$\vec{F}_p = \begin{bmatrix} X_p \\ Y_p \\ Z_p \end{bmatrix} = \begin{bmatrix} T_p \\ 0 \\ 0 \end{bmatrix} \quad (21)$$

$$\vec{M}_p = \begin{bmatrix} L_p \\ M_p \\ N_p \end{bmatrix} = \begin{bmatrix} Q_p \\ T_p h_p \\ T_p d_p \end{bmatrix} \quad (22)$$

2.4 Empennage modelling

The aerodynamic forces of the horizontal tail, vertical tail, elevator and rudder are modelled by simple aerodynamic lookup tables, for which a simple stall model is included by means of truncation of the lift coefficient at the positive and negative stall angle of attack. The lift coefficient of the tail surfaces are calculated by means of

$$C_{l_h} = C_{l_{\alpha_h}}(\alpha_h) + \frac{dC_{l_{\alpha_h}}}{d\delta_e} \delta_e \quad (23)$$

$$C_{l_h} = C_{l_{\beta_v}}(\beta_v) + \frac{dC_{l_{\beta_v}}}{d\delta_r} \delta_r$$

where C_{l_h} is the lift coefficient of the horizontal tail, and C_{l_v} that of the vertical tail. By using the elevator or rudder, the lift curve is essentially 'shifted' upwards by a factor $\frac{dC_{l_{\alpha_h}}}{d\delta_e}$ or $\frac{dC_{l_{\beta_v}}}{d\delta_r}$. The airspeed components, as seen by the horizontal and vertical tail, are calculated by [18]

$$\begin{aligned} V_h &= \sqrt{u^2 + (w + ql_h)^2} \\ V_v &= \sqrt{u^2 + (v + ph_v - rl_v)^2} \end{aligned} \quad (24)$$

which takes into account the airspeeds and angular rates. The angle of attack as seen by the surfaces is calculated by

$$\begin{aligned} \alpha_h &= \tan^{-1} \left(\frac{w + ql_h}{u} \right) + \alpha_{h_0} - K_h \epsilon_0 \\ \beta_v &= \tan^{-1} \left(\frac{v + ph_v - rl_v}{u} \right) + \beta_{v_0} \end{aligned} \quad (25)$$

which also takes into account the airspeeds and angular rates, while accounting for the tail incidences α_{h_0} and β_{v_0} . K_h is a factor taking into account the main rotor wake, where $\epsilon_0 = \nu_0/V$. Here ν_0 is the inflow velocity of the main rotor, which is the sum of the lower and upper inflow velocities.

The lift produced by the empennage surfaces can then simply be calculated by the lift equation.

$$\begin{aligned} L_h &= \frac{1}{2} \rho V_h^2 S_h C_{l_h} \\ L_v &= \frac{1}{2} \rho V_v^2 S_v C_{l_v} \end{aligned} \quad (26)$$

The total force and moment contributions are then calculated by means of [5]

$$\begin{aligned} \vec{F}_{emp} &= \begin{bmatrix} X_{emp} \\ Y_{emp} \\ Z_{emp} \end{bmatrix} = \begin{bmatrix} X_h + X_v \\ Y_h + Y_v \\ Z_h + Z_v \end{bmatrix} = \\ &= \begin{bmatrix} -L_h * \sin(\alpha_h + \alpha_{h_0}) \\ 0 \\ -L_h * \cos(\alpha_h + \alpha_{h_0}) \end{bmatrix} + \begin{bmatrix} -L_v * \cos(\beta_v + \beta_{v_0}) \\ L_v * \cos(\beta_v + \beta_{v_0}) \\ 0 \end{bmatrix} \end{aligned} \quad (27)$$

$$\begin{aligned} \vec{M}_{emp} &= \begin{bmatrix} L_{emp} \\ M_{emp} \\ N_{emp} \end{bmatrix} = \begin{bmatrix} L_h + L_v \\ M_h + M_v \\ N_h + N_v \end{bmatrix} = \\ &= \begin{bmatrix} Z_h * d_h + Y_h * h_h \\ Z_h * l_h - X_h * h_h \\ -Y_h * l_h - X_h * d_h \end{bmatrix} + \begin{bmatrix} Z_v * d_v + Y_v * h_v \\ Z_v * l_v - X_v * h_v \\ -Y_v * l_v - X_v * d_v \end{bmatrix} \end{aligned} \quad (28)$$

2.5 Fuselage modelling

The fuselage model is represented by a drag model which uses an equivalent flat plate drag area, calculated in Leishman [19]. This produces a total drag force of

$$D_{fus} = \frac{1}{2} \rho V^2 \sum (C_{DS})_S \cos(\alpha_{fus}) \quad (29)$$

where $\alpha_{fus} = \tan^{-1}(w/u)$, V the total airspeed, and $\Sigma(C_{DS})_S$ the total flat plate drag coefficient from Leishman [19]. The fuselage also creates a pitching moment, for which the coefficient is calculated by

$$C_{M_{fus}} = \left(\frac{V}{\Omega R}\right)^2 \frac{1}{AR} K_{fus} V_{fus} (\alpha_{fus} - \alpha_{fus M=0} - \epsilon_0) \quad (30)$$

where A is the fuselage cross-sectional area, assumed to be a perfect circle, and thus equal to πR^2 , R the radius of that circle, K_{fus} a correction factor for the assumed fuselage volume V_{fus} , α_{fus} the fuselage angle of attack, calculated by $-\tan^{-1}(w/u)$, and $\alpha_{fus M=0}$ the angle of attack for which the fuselage pitching moment coefficient is zero. Lastly, ϵ_0 equals the same wake correction factor as for the empennage, this time assumed to be central on the fuselage, and thus not needing a correction factor.

The fuselage rolling moment can be calculated using the rolling moment coefficient $C_{N_{fus}}$:

$$C_{N_{fus}} = \left(\frac{V}{\Omega R}\right)^2 \frac{1}{AR} K_{fus} V_{fus} \beta_{fus} \quad (31)$$

where β_{fus} equals the sideslip angle of the fuselage, equal to $\sin^{-1}(v/V)$. The resulting forces from the fuselage still have to be expressed in the body-fixed reference frame, and thus transformed using α_{fus} and β_{fus}

$$\vec{F}_{fus} = \begin{bmatrix} X_{fus} \\ Y_{fus} \\ Z_{fus} \end{bmatrix} = -D_{fus} \begin{bmatrix} \cos \beta_{fus} \cos \alpha_{fus} \\ \sin \beta_{fus} \\ \cos \beta_{fus} \sin \alpha_{fus} \end{bmatrix} \quad (32)$$

The fuselage moments can simply be calculated using:

$$\vec{M}_{fus} = \begin{bmatrix} L_{fus} \\ M_{fus} \\ N_{fus} \end{bmatrix} = \rho A (\Omega R)^2 R \begin{bmatrix} 0 \\ C_{M_{fus}} \\ C_{N_{fus}} \end{bmatrix} \quad (33)$$

2.6 Model Trimming

In order to get an idea of the validity of the model, the model is validated by means of a trim comparison to literature results of [20] and [17]. It is difficult to get a formal validation by means of flight test data, as the developed model is generic in nature and data is not readily available due to the novelty of this configuration.

In order to trim the developed nonlinear model, use was made of a Newton-Raphson trim algorithm [16], and the following conditions were applied:

1. The coaxial rotor controls: θ_0 , θ_d , θ_s and θ_c , and pusher propeller pitch θ_p were used to trim the aircraft
2. The fuselage pitch angle θ , elevator deflection δ_e and rudder deflection δ_r were pre-scheduled and set to zero throughout the entire trim routine.
3. Use was made of the roll angle ϕ as an extra trim variable

The trim results are depicted in Figure 5. The collective θ_0 can be seen to have a maximum value at hover, which decreases with airspeed. This is in contrast with the behaviour of conventional helicopters, which after reaching a minimum at a certain airspeed, increase the collective required due to the use of longitudinal cyclic. In the compound coaxial helicopter however, the cyclic is unloaded for forward speed by the pusher propeller, and is only used for compensation of the flapping angle. The longitudinal cyclic can be seen to be different compared to the validation data, this is due to the use of different twist angles, and a different approach to the flapping angle calculation. The other controls, θ_d , θ_c and θ_p can be seen to follow a similar trend as the validation data and thus indicate proper functioning of the model, capable of capturing the salient flight dynamics characteristics of the helicopter. This brings confidence that the mathematical model can be used for subsequent analysis.

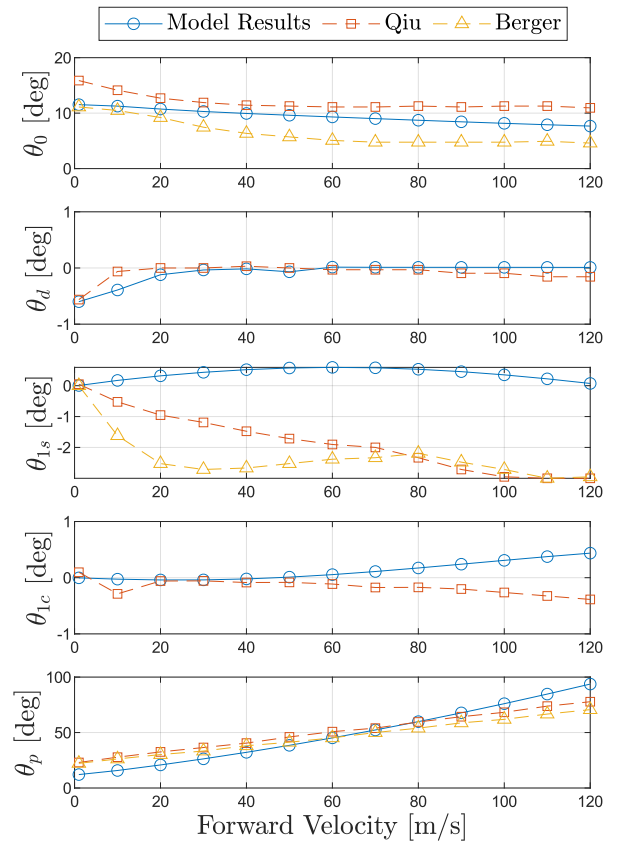


Figure 5: Trim results for the compound coaxial model.

3 Stability Analysis

In order to verify the dynamic behaviour of the modelled compound coaxial helicopter, a stability analysis is performed. This will give a general insight of the effects of thrust and lift compounding on the dynamic characteristics of the helicopter.

3.1 Model Linearisation

In order to find the stability and control derivatives, and compute the linear models, the nonlinear model has to be linearised. This linearisation is achieved by expressing the forces and moments as Taylor-series expansion and perturbing the states by a certain input, which by means of a central-difference approximation results in the stability and control derivatives. These can in turn be used to form the A and B matrices at a certain trim speed. This procedure was repeated for every trim speed, and for variables falling between any of the trim speeds during simulation, the closest trim speed is selected for trim variables and stability/control derivatives.

3.1.1 Longitudinal Dynamic Stability

The longitudinal stability of the aircraft was studied more closely, since the manoeuvres to be performed in section 4 are all within the longitudinal planes. By means of the stability derivatives, the longitudinal modes of motion can be calculated according to the approximatory equations in Padfield [9], resulting in the longitudinal natural modes of motion depicted in Figure 6 where ω and μ denote the imaginary and real parts of the eigenvalues respectively. The results are plotted for 0 to 120 m/s.

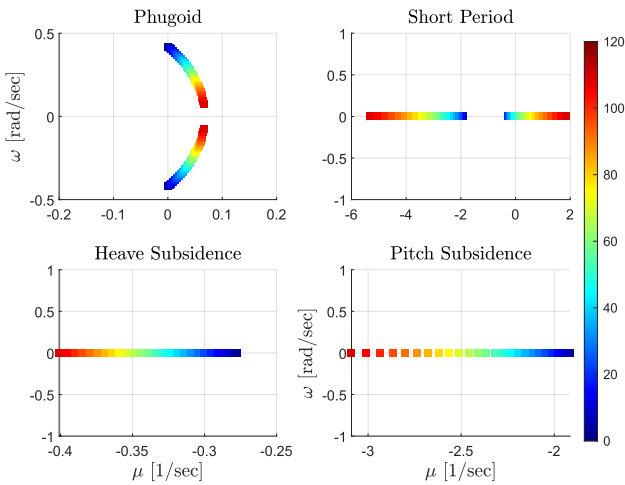


Figure 6: Longitudinal natural modes of motion.

It can be seen that the phugoid is close to stability at hover, but diverges more into the unstable region, with decreasing oscillation. This result is in line with Ferguson [16]. The main reason for this instability is the use of a hingeless rotor, where the stiff rotors create large moments around the rotor hub due to the large hinge-offset and spring-stiffness moments. When the coaxial rotor system is perturbed in forward speed, there is a pitch-up moment due to the rotor blades flapping back, which is confirmed by the positive M_u derivative. As the fuselage pitches up, the main rotors provide a pitch down moment due to the negative M_q value, causing an oscillatory motion which steadily increases in magnitude. Due to a similar perturbation in forward speed, the blade incidence of the rotor reduces, pro-

viding an extra drag force [16], decreasing X_u . However, this appears to be insufficient to stabilise the aircraft. Note that the model behaviour, and consequently its derivatives and open-loop behaviour, highly depend on the rotor characteristics such as hinge offset and spring stiffness.

The short period can be seen to be non-oscillatory and stable at low speeds, while decreasing with increasing speed. This is the result of the spring term $Z_w M_q - M_w (Z_q + U_e)$, which greatly impacts the short period stability, and was found to become unstable around 55 m/s.

Both the pitch and heave subsidence are non-oscillatory and damped throughout the entire flight envelope, which was clear from their longitudinal stability derivative values M_q and Z_w .

Due to the presence of right-half plane poles, resulting in the instability of the system, and the presence of overactuation, results in a clear need for a stability and control augmentation system.

4 Flight Controller Design

As mentioned in the previous paragraph, there is a clear need for a stability and control augmentation system in the transition region. This will be evaluated in this section, in which the controller architecture, control allocation algorithms, inner- and outer-loop control laws and a bob-up/bob-down manoeuvre with acceleration/deceleration will be designed and analysed.

4.1 Controller Architecture

The top-level controller architecture is visualised in Figure 7, based on the works of Qiu [17]. It can be seen that the controller is split into an outer-loop controller, inner-loop controller, actuators and the nonlinear CCH model.

Firstly, the outer-loop controller receives velocity tracking commands, which it feeds a virtual control for the outer-loop controller v_{out} into an outer-loop control allocation algorithm. The outer-loop then outputs the collective θ_0 , and propeller collective θ_p , together with the roll and pitch commands ϕ_{cmd} and θ_{cmd} respectively. The roll and pitch commands are fed, together with a pre-specified yaw command ψ_{cmd} to the inner-loop controller, which similarly feeds a virtual control signal v_{in} into the inner-loop control allocation algorithm. The inner-loop control then outputs the rest of the controls: $[\theta_d, \theta_s, \theta_c, \delta_e, \delta_r]^T$. All the control inputs are lumped together in \vec{u}_c which are added to the trim input vector \vec{u}_{trim} , and fed into the actuators. Note that the actuator block does not contain any actuator dynamics in this specific research, but only limits the position and rate constraints of the actuators according to These inputs are then fed into the nonlinear model which in turn calculates the airspeeds $[u, v, w]^T$, attitudes $[\phi, \theta, \psi]$ and angular rates $[p, q, r]^T$. Note that due to the decoupling of the outer and inner loop, the inner loop controls and outer loop controls are decoupled. This reduces the influence of the inner loop on altitude and velocity control.

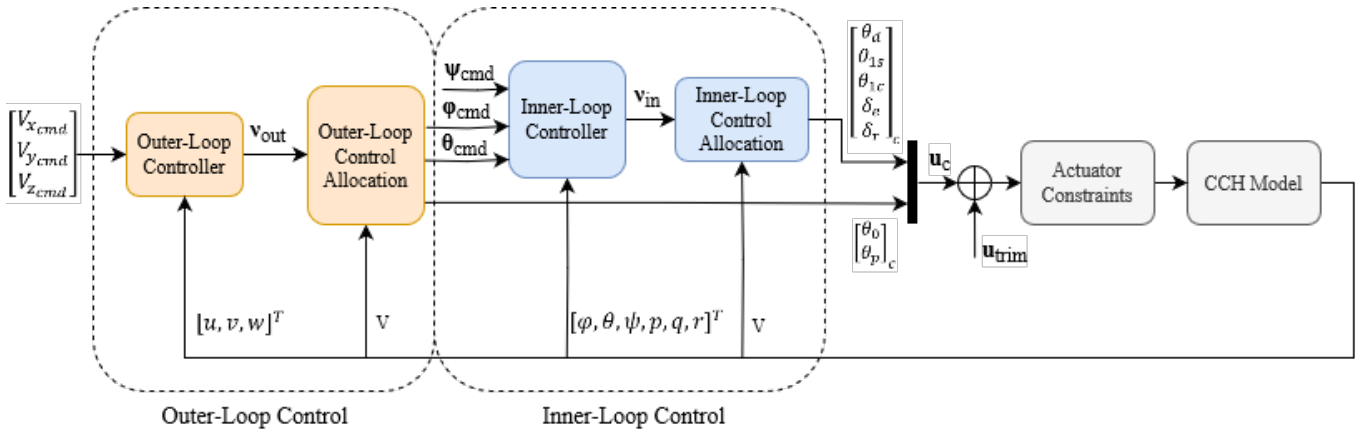


Figure 7: Top-level controller architecture.

4.2 Multi-Stage Control Allocation

To address the control redundancy and control cross-coupling, a multi-stage control allocation algorithm will be developed. Given the drastic changes in actuator effectiveness throughout the flight envelope, these must be considered during the allocation process. The allocation procedure will be based on the weighted pseudo-inverse method and is designed to compute the seven actuator commands using inner- and outer-loop virtual control laws.

4.2.1 Inner-Loop Control Allocation

The first stage of the algorithm design involves inner loop allocation to control the aircraft's attitude angles: pitch, roll, and yaw. Pitch is controlled by the longitudinal cyclic θ_s and elevator δ_e , roll by the lateral cyclic θ_c , and yaw by the differential collective θ_d and rudder δ_r . The control effectiveness of these actuators, M_{θ_s} and M_{δ_e} varies throughout the flight range, with transition regions indicated at 20 m/s and 65 m/s, as shown in Figure 8. These regions mark where one control becomes more effective than another. Similarly, the yaw-channel control effectiveness N_{θ_d} and N_{δ_r} are depicted, which follow a similar trend. However, it can be seen that a low control authority region is present around 40 m/s.

A linear distribution for control weights is established within these transition regions. This decreases the use of θ_s and θ_d while increasing the use of δ_e and δ_r . The control weights for pitch are calculated by Equation 34. Those for yaw are based on the same weighting scheme and speeds.

$$\rho_{\theta_{1s}} = \begin{cases} 1, & V \leq 20 \text{ m/s} \\ 1 - \frac{1}{40}(V - 20), & 20 < V < 65 \text{ m/s} \\ \epsilon, & V \geq 65 \text{ m/s} \end{cases} \quad (34)$$

$$\rho_{\delta_e} = \begin{cases} \epsilon, & V \leq 20 \text{ m/s} \\ \frac{1}{40}(V - 20), & 20 < V < 65 \text{ m/s} \\ 1, & V \geq 65 \text{ m/s} \end{cases}$$

Next, using the inner-loop virtual control signal $\vec{v}_{in} = [\nu_\phi, \nu_\theta, \nu_\psi]^T$, a pseudo-inverse allocation algorithm can be ap-

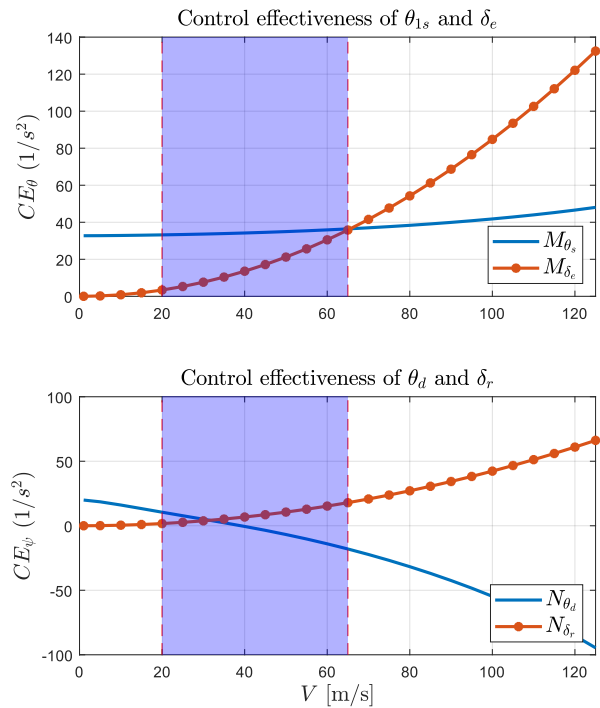


Figure 8: Control effectiveness for pitch and yaw throughout flight range.

plied, resulting in the allocation for roll, pitch, and yaw as per Equation 35. [17] Here, Here, L_{θ_s} , M_{δ_e} , θ_d , and N_{δ_r} are the control derivatives calculated in subsection 3.1. Notably, a significant advantage of this design is its inherent ability to account for cross-coupling between the primary control axes of the helicopter.

$$\left\{ \begin{array}{l} \phi: [\theta_{1c}]_c = \frac{\nu_\phi}{L_{\theta_{1c}}} \\ \theta: [\theta_{1s}, \delta_e]_c^T = \mathbf{W}_\theta^{-1} \mathbf{B}_\theta^T (\mathbf{B}_\theta \mathbf{W}_\theta^{-1} \mathbf{B}_\theta^T)^{-1} \nu_\theta, \\ \quad \mathbf{W}_\theta = \text{diag} \left[\frac{1}{\rho_{\theta_{1s}}}, \frac{1}{\rho_{\delta_e}} \right], \mathbf{B}_\theta = [L_{\theta_{1s}}, M_{\delta_e}] \\ \psi: [\theta_d, \delta_r]_c^T = \mathbf{W}_r^{-1} \mathbf{B}_r^T (\mathbf{B}_r \mathbf{W}_r^{-1} \mathbf{B}_r^T)^{-1} \nu_r, \\ \quad \mathbf{W}_r = \text{diag} \left[\frac{1}{\rho_{\theta_d}}, \frac{1}{\rho_{\delta_r}} \right], \mathbf{B}_r = [N_{\theta_d}, N_{\delta_r}] \end{array} \right. \quad (35)$$

4.2.2 Outer-Loop Control Allocation

The second stage of the allocation process is the outer loop, which manages airspeed tracking. The longitudinal velocity V_x is controlled by the pitch angle θ_{cmd} and pusher propeller θ_p , vertical velocity V_z by collective θ_0 and pitch angle θ , and lateral velocity by the roll angle ϕ . This allocation process is based on the transition from hover (helicopter) mode to high-speed (fixed wing) mode. The transition region will also range from 20-65 m/s, similar to the inner-loop control allocation, leading to similar weighting schemes as in Equation 34.

Next, using the inner-loop virtual control $v_{in} = [v_\phi, v_\theta, v_r]^T$, a pseudo-inverse allocation algorithm can be applied, resulting in the allocation for roll, pitch, and yaw as follows [17]: Similarly to the inner-loop, the outer loop control $\nu_{out} = [\nu_x, \nu_y, \nu_z]^T$ can be used in a pseudo-inverse algorithm, resulting in the outer-loop control outputs θ_{cmd} , θ_p , θ_0 , and ϕ :

$$\left\{ \begin{array}{l} V_x: [\theta_{cmd}^x, \theta_p]_c^T = \mathbf{W}_x^{-1} \mathbf{B}_x^T (\mathbf{B}_x \mathbf{W}_x^{-1} \mathbf{B}_x^T)^{-1} \nu_x \\ \quad \mathbf{W}_x = \text{diag} \left[\frac{1}{\rho_{\theta_{cmd}^x}}, \frac{1}{\rho_{\theta_p}} \right], \mathbf{B}_x = [-1, 1] \\ V_y: \phi_{cmd} = \nu_y \\ V_z: [\theta_0, \theta_{cmd}^z]_c^T = \mathbf{W}_z^{-1} \mathbf{B}_z^T (\mathbf{B}_z \mathbf{W}_z^{-1} \mathbf{B}_z^T)^{-1} \nu_z \\ \quad \mathbf{W}_z = \text{diag} \left[\frac{1}{\rho_{\theta_0}}, \frac{1}{\rho_{\theta_{cmd}^z}} \right], \mathbf{B}_z = [1, 1] \end{array} \right. \quad (36)$$

4.2.3 Control Strategy

Due to the demonstrated changing control effectiveness, and by implementing the control allocation procedure outlined before, a control strategy throughout the flight regime can be constructed, and is outlined in Table 1.

4.3 Inner-Loop Attitude Controller

The inner-loop control law is based on EMF control [21], as depicted in Figure 9. The commanded attitudes are fed into a pre-defined model, which are defined by a second order transfer function, as per Equation 37. Here, the natural frequency ω_m equals 4 rad/s, and the damping ratio ζ 0.707. These values are chosen based achieving a desirable transient behaviour according, providing good compromise between agility and stability.

$$M(s) = \frac{\omega_n^2}{s^2 + 2\zeta\omega_n s + \omega_n^2} \quad (37)$$

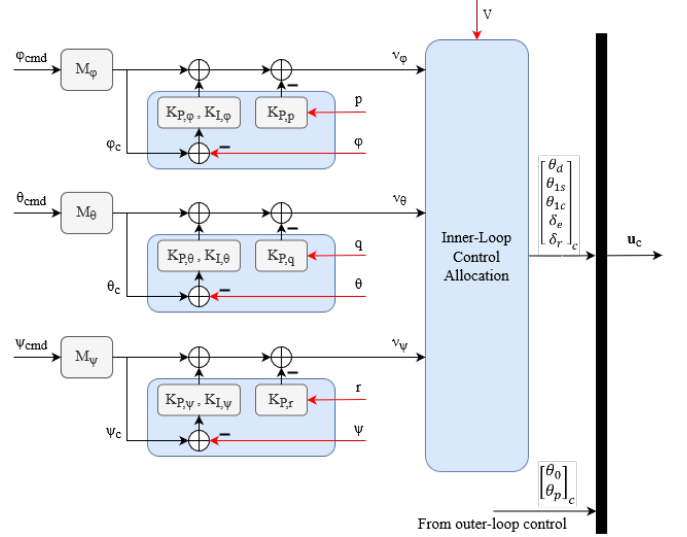


Figure 9: Inner loop controller design based on EMF control. [17]

The controller then uses the EMF model command, ϕ_c , θ_c , and ψ_c in a PID controller in order to track this value. It achieves this by using the control laws listed in Equation 38.

$$\left\{ \begin{array}{l} \nu_\phi = K_P, \phi (\phi_c - \phi) + K_I, \phi \int (\phi_c - \phi) dt - K_P, pp \\ \nu_\theta = K_P, \theta (\theta_c - \theta) + K_I, \theta \int (\theta_c - \theta) dt - K_P, qq \\ \nu_\psi = K_P, \psi (r_c - r) + K_I, \psi \int (r_c - r) dt - K_P, rr \end{array} \right. \quad (38)$$

4.4 Outer-Loop Velocity Controller

Similar to the inner-loop controller, the outer loop controller is based on EMF control, with the same transient response characteristics according to Equation 37. The outer-loop control architecture is depicted in ... , and also uses a PID controller in order to provide feedback stabilisation for the commanded velocity signals $V_{x,c}$, $V_{y,c}$, and $V_{z,c}$. The outer-loop control law is denoted in Equation 39.

$$\left\{ \begin{array}{l} v_x = K_P, x (V_{xc} - V_x) + K_I, x \int (V_{xc} - V_x) dt \\ v_y = K_P, y (V_{yc} - V_y) + K_I, y \int (V_{yc} - V_y) dt \\ v_z = K_P, z (V_{zc} - V_z) + K_I, z \int (V_{zc} - V_z) dt \end{array} \right. \quad (39)$$

Table 1: Compound coaxial helicopter control strategy throughout flight regime. [17]

Flight Mode	Control Method				
	Roll	Pitch	Yaw	Height	Forward Velocity
Helicopter Mode (0-20 m/s)	θ_{1c}	θ_{1s}	θ_d	θ_0	θ
Transition Mode (20-65 m/s)	θ_{1c}	$\theta_{1c} \rightarrow \delta_e$	$\theta_d \rightarrow \delta_r$	$\theta_0 \rightarrow \theta$	$\theta \rightarrow \theta_p$
Fixed Wing Mode (>65 m/s)	θ_{1c}	δ_e	δ_r	θ	θ_p

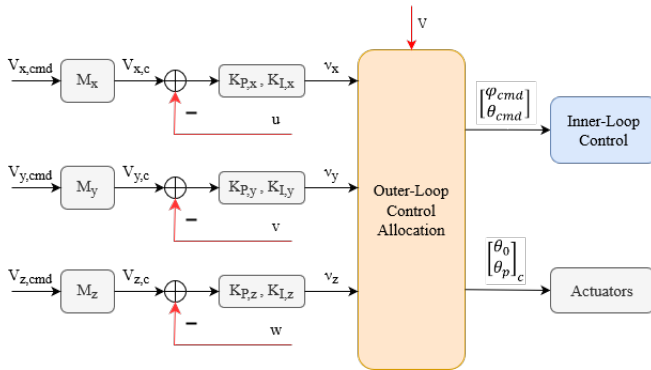


Figure 10: Outer loop controller design based on EMF control. [17]

4.5 Bob-Up Bob-Down with Acceleration and Deceleration

In order to demonstrate the performance of the helicopter control system, a bob-up bob-down with acceleration and deceleration manoeuvre is simulated, a limited agility, precise manoeuvring mission task element from ADS-33. It combines the commands of both vertical and horizontal velocities which serves as an evaluation for the developed outer- and inner-loop control allocation. Using the manually tuned control system discussed before, the results depicted in Figure 11-Figure 12 are found.

These findings offer valuable insights into the overall model, control system, and control allocation. The discussion will focus on the forward velocity command, vertical velocity command, and cross-coupling effects, with the corresponding control mechanisms forming the basis of this analysis:

- **Forward velocity:** It can be seen that the forward velocity is tracked well with respect to the commanded signal. During the transition region, a combination of the aircraft pitch and pusher propeller setting set the forward velocity. The pitch is allocated in the inner-loop to both to longitudinal cyclic and elevator. Figure 12 shows the propeller collective θ_p changes in the same manner as the forward velocity, with altering trim values and with very little oscillations. In Figure 11 it becomes clear that the control system commands a pitch up with deceleration, and a pitch down with acceleration, as expected. Looking again at Figure 12, the allocation to θ_{1s} and δ_e can be seen. It can be seen that there is some jittery behaviour for the longitudinal cyclic, which is due to the a

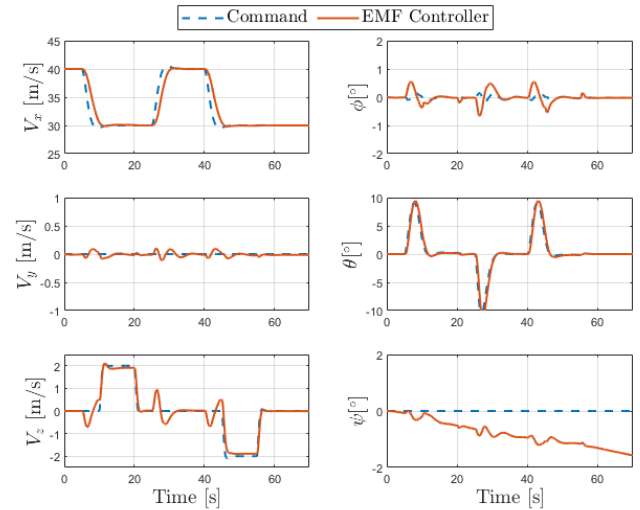


Figure 11: State results for the bob-up/bob-down with acceleration and deceleration manoeuvre for the EMF controller.

combination of the limitation of the PID controller and imperfect tuning. It should also be noted that there is an unexpected use of the longitudinal cyclic during the pitch commanding, instead of pulling the longitudinal cyclic backwards, to raise the nose, the controller momentarily pitches nose up, quickly followed by nose down. It appears that the combination with the elevator results in a proper pitch angle. Most likely, this is the result due to the pitch coupling of the collective and lateral cyclic. It appears that the EMF controller with PID has a tough time with the highly coupled, simultaneous control requests.

- **Vertical Velocity:** The vertical velocity is also tracked well as soon as the command is given. However, a clear coupling between the pitch angle and the vertical velocity can be seen. The vertical velocity can be seen to be controlled by the collective and the pitch angle. However, since collective is much more dominant at this speed than the pitch angle, it can be seen that almost solely the collective is used. One can observe the cross-coupling effect of the loss of lift due to a cyclic input, requiring a compensation in collective, and the altering low/high state of the collective, depending on the required vertical velocity.
- **Cross-Coupling Effects:** These encompass the lateral

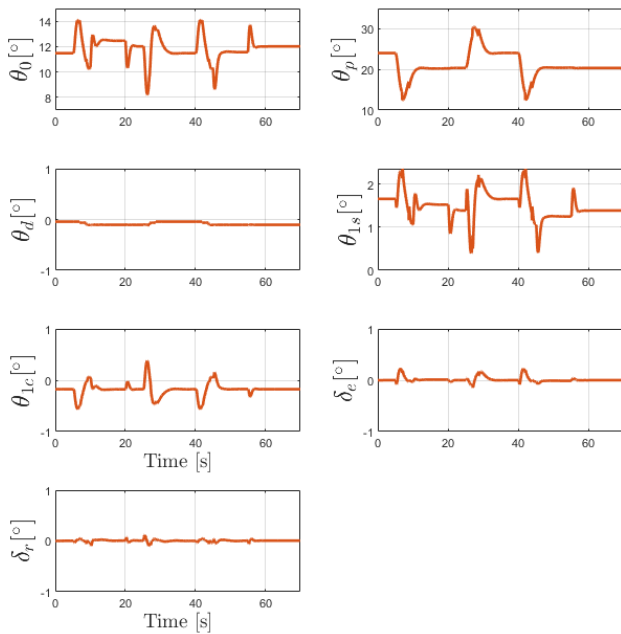


Figure 12: Control inputs for the bob-up/bob-down with acceleration and deceleration manoeuvre for the EMF controller.

axis states, such as the roll and yaw. It can be seen that there is a clear cross-coupling between pitch and roll, which the lateral cyclic is able to compensate for. The yaw on the other hand is observed to have a slight drift, with the rudder and differential collective being only very slightly active. It is thought that this is a combination between a modelling discrepancy and the chosen control law for yaw. Upon closer analysis, it was seen that there was a very small steady-state error of the yaw rate r , which a yaw-rate controller might be able to solve, instead of a yaw-angle controller.

5 Handling Quality Assessment

Apart from the mission task element that was flown in previous section, an objective handling quality assessment is performed in order to quantify various aspects of the CCH. The handling qualities analysed in this research are the bandwidth and phase delay, and the attitude quickness.

5.1 Bandwidth and Phase Delay

The flight velocities at which the ADS-33 [22] metrics bandwidth and phase delay are assessed are at 20, 40, and 65 m/s, since these are the velocities inside the transition region and are of special interest. The attitude commands were evaluated for 1 degree step inputs for all 3 attitudes and evaluated in MATLAB Simulink. The results are summarised in Table 2. All airspeeds fell within Level 1 handling quality criteria with increasing responsiveness with speed. However, it must be noted that the

delays are very small, this is most likely to be attributed to the fact that the actuators dynamic are not accounted for, which are the largest source of command delays.

5.2 Attitude Quickness

The ADS-33E standards specify attitude quickness requirements for combat helicopters, which are especially interesting to consider in a coaxial helicopter configuration, since they are well known to be more manoeuvrable and agile than their single rotor counterparts. With the added compound features for attitude changes, such as the elevator and the rudder, this quickness is expected to be even more powerful. With the current allocation algorithm however, a maximum moment set is not analysed. However, with the compounding, it is a logical conclusion that this large moment set brings the possibility for some very large attitude rates to be achieved. The attitude quickness will be analysed at 40 m/s due to the positioning within the transition region.

Indeed, it was found that all 3 attitudes fell within Level 1 handling qualities, as visualised in Figure 23, Figure 26 and Figure 29 in subsection A.4. A similar trend could be noticed that as soon as one of the controls reached its maximal deflection, the attitude quickness started to degrade. Another finding was that during the control allocation algorithm, priority was not given to attaining a large moment set, hindering the attitude quickness. Rather, one control was deflected at maximal deflection for an extended period while not maximally using the other control. This is especially clear in the pitch attitude quickness response for $\theta_{cmd} = 20$ deg, shown in Figure 25 in subsection A.4. Lastly, it was noticed, as expected from Figure 8, that a low control authority for the yaw axis was present, requiring considerable control effort. However, the aircraft still achieved Level 1 handling quality criteria.

It must be stressed that these results are heavily dependent on the rotor parameters, especially equivalent hinge offset and spring stiffness, and airframe parameter data, with an emphasis on the moment of inertia estimates. Different results, although with equivalent conclusions, are expected with more refined parameter data.

6 Conclusions

The goal of this research was to construct and evaluate a mathematical model for flight dynamics analysis, construct an initial controller able to stabilise the system and track an ADS-33E manoeuvre, and perform an objective handling quality assessment.

The constructed nonlinear compound coaxial helicopter model featured 4 main rotor controls: the collective θ_0 for altitude control, differential collective θ_d for yaw control, longitudinal cyclic θ_s for pitch control, and lateral cyclic θ_c for roll control. Compounding was achieved by the inclusion of an elevator and rudder for pitch and yaw control, and a pusher propeller for longitudinal velocity control. The main rotors blade dynamics were modelled by an equivalent hinge and spring model, with a quasi-dynamic, mutually interfering inflow mod-

Table 2: Bandwidth and phase delay results on the inner-loop control during the transition region for the linear system.

Metric	20 m/s			40 m/s			65 m/s		
	Roll	Pitch	Yaw	Roll	Pitch	Yaw	Roll	Pitch	Yaw
Response Bandwidth [rad/s]	3.52	4.8	5.23	3.72	4.91	5.23	3.91	5.17	5.23
Response Phase Delay [s]	0.02	0.04	0.05	0.02	0.04	0.05	0.02	0.04	0.05
Handling Qualities Level	Level 1			Level 1			Level 1		

elling. Due to the usage of the ABC rotor a very stiff and highly responsive rotor system was achieved, which did not require the inclusion of wake contraction. The model was trimmed and resulted in comparable trim schemes compared to literature. The dynamic stability analysis of the CCH concluded that the helicopter became longitudinally unstable around 50 m/s due to the stiff hingeless rotors, and thus required a stability and control augmentation system.

The control system featured an Explicit Model-Following controller with PID stabilisation, and was decoupled by an outer-loop velocity controller and inner-loop attitude controller. Each loop included a Weighted Pseudo-Inverse control allocation algorithm with a linear distribution in weights according to the transition region between 20 and 65 m/s. This transition region was based on the control effectiveness of the CCH's controls. The controller was able to stabilise the helicopter and performed good tracking performance, although there was still a strong cross-coupling between controls, which caused some jittery control input behaviour. Further analysis of the flight controller performance by means of the handling quality assessment proved Level 1 performance in bandwidth and phase delay, and attitude quickness, at 40 m/s, for all attitudes. This analysis revealed an inefficient use of the controls during allocation when large moments are commanded, and a high dependency on several used model parameters such as hinge-offset, spring stiffness and moment of inertias.

7 Recommendations

It is believed that this research holds good potential to form a solid foundation for researched to be based off. In order to guide future iterations of this research, the most important recommendations in the domains of modelling, control, and handling quality assessments are provided.

- Use different flapping coefficient equations which utilise both the hinge offset and spring stiffness, instead of having to rely on the spring frequency values. This would remove some inaccuracies for the flapping angles, which carry through in the resulting rotor angles and thus trim and control.
- Include a non-uniform inflow distribution, such as a linear inflow distribution, in order to be able to model and schedule for the LOS effects using the differential lateral cyclic.
- Re-iterate the planform sizing parameters such as the horizontal and vertical tail size, by performing a more

detailed sizing study in order to improve the realism of the design. The design parameters now are deduced from comparable helicopters in literature and sometimes roughly estimated by an educated guess.

- Use sophisticated tuning methods beyond manual tuning. Examples include MATLAB Simulink options and the industry-standard CONDUIT for handling quality requirements.
- Incorporate an inverse model, as in [17], to enhance system robustness and reduce dependence on PID tuning, using it only for stabilisation. Consider advanced controllers like NDI.
- Develop a sophisticated control allocation scheme using multi-objective optimization, targeting minimal power consumption, handling qualities, and secondary control usage during saturation, especially in high attitude maneuvers.
- Implement Pseudo-Control Hedging (PCH) to address actuator saturation, working well with NDI control and enhancing EMF control with an inverse model.
- Extend the controller to cover hover and high-speed flight domains.
- Include actuator dynamics beyond rate and position constraints.
- Address the low authority zone for yaw control around 40 m/s by exploring additional controls like monocyclic propeller pitch, despite potential increased design costs and complexity, and optimise sizing metrics for consistent control effectiveness during transition.
- Assess a broader range of handling qualities, focusing on the worst-performing ones deemed crucial to the system.
- For high-speed flight, analyse fixed-wing handling quality requirements, including high-speed manoeuvres as discussed in the control recommendations.

References

- [1] Rely Victoria Petrescu. Defiant, a today unique helicopter in the world. *Journal of Aircraft and Spacecraft Technology*, 3:92–106, 2019.

- [2] R. Blackwell and T. Millott. Dynamic design characteristics of the sikorsky x2 technology demonstrator aircraft. *American Helicopter Society*, Forum 64, 2008.
- [3] Ashish Bagai and J Gordon Leishman. Rotor free-wake modeling using a pseudo-implicit technique—including comparisons with experimental data. *Journal of the American Helicopter Society*, 40(3):29–41, 1995.
- [4] J. Ruddell et al. Advancing blade concept (abc) technology demonstrator - final report for period 1972 - june 1980. Technical report, Sikorsky Aircraft Division United Technologies Corporation, 1981.
- [5] P Simplício, MD Pavel, E Van Kampen, and QP Chu. An acceleration measurements-based approach for helicopter nonlinear flight control using incremental nonlinear dynamic inversion. *Control Engineering Practice*, 21(8):1065–1077, 2013.
- [6] Hermann Glauert. A general theory of the autogyro. Technical report, HM Stationery Office, 1926.
- [7] G-Y Zhou, J-Z Hu, Y-H Cao, and J-J Wang. Research on a mathematical model for coaxial helicopter flight dynamics. *Acta Aeronautica et Astronautica Sinica*, 24(4):293–295, 2003.
- [8] Anton J Landgrebe. The wake geometry of a hovering helicopter rotor and its influence on rotor performance. *Journal of the American Helicopter society*, 17(4):3–15, 1972.
- [9] G. Padfield. Helicopter flight dynamics. In *The Theory and Application of Flying Qualities and Simulation Modelling*. Blackwell Publishing, 2013.
- [10] W. Johnson. Rotorcraft aeromechanics. Cambridge, 2007.
- [11] S. Saito and A. Azuma. A numerical approach to co-axial rotor aerodynamics. 1981.
- [12] D. Pitt and D. Peters. Theoretical prediction of dynamic-inflow derivatives. *European Rotorcraft and Powered Lift Aircraft Forum*, 16(47), 1980.
- [13] Marilena Domnica Pavel. On the necessary degrees of freedom for helicopter and windturbine low-frequency mode modeling. 2001.
- [14] Marilena Pavel. Memorandum m-756: Six degrees of freedom linear model for helicopter trim and stability calculation.
- [15] Tom Berger, Chris L Blanken, Mark B Tischler, and Joseph Francis Horn. Flight control design and simulation handling qualities assessment of high-speed rotorcraft. In *Vertical Flight Society's 75th Annual Forum and Technology Display*, 2019.
- [16] K. Ferguson. Towards a better understanding of the flight mechanics of compound helicopter configurations. Technical report, University of Glasgow, 2015.
- [17] Q. Yuqing and L. Yan. Dynamics analysis and control of coaxial high-speed helicopter in transition flight. *Aerospace Science and Technology*, (137), 2023.
- [18] George Tzanetos. Flight dynamics modelling and trim optimization for a hybrid compound helicopter in forward flight.
- [19] J. Gordon Leishman. *Principles of Helicopter Aerodynamics, 2nd Ed.* Cambridge University Press, 2006, 2006.
- [20] Tom Berger, Chris L Blanken, Jeff A Lusardi, Mark B Tischler, and Joseph F Horn. Coaxial-compound helicopter flight control design and high-speed handling qualities assessment. *Journal of the American Helicopter Society*, 67(3):98–113, 2022.
- [21] K Hilbert and Gerhard Bouwer. The design of a model-following control system for helicopters. In *17th Fluid Dynamics, Plasma Dynamics, and Lasers Conference*, page 1941, 1984.
- [22] C. Blanken et al. Proposed revisions to aeronautical design standard - 33e (ads-33-e-prf) towards ads-33f-prf. Technical report, U.S. Army, 2019.

A Appendices

A.1 Planform Data

A.1.1 Airframe Parameters

Table 3: Main airframe parameters.

Dimension	Symbol	Value	Unit
Length Fuselage	l_{fus}	12.2	m
MOI X-axis	I_x	6800	$kg \cdot m^2$
MOI Y-axis	I_y	40000	$kg \cdot m^2$
MOI Z-axis	I_z	12000	$kg \cdot m^2$
Product MOI XZ	I_{xz}	5000	$kg \cdot m^2$
X-pos. Propeller	l_p	7.66	m
X-pos. Vertical Tail	l_{vt}	6.8	m
X-pos. Horizontal Tail	l_{ht}	6.8	m
Height Upper Rotor	h_u	1.66	m
Height Lower Rotor	h_l	0.89	m
Height Vertical Tail	h_{vt}	0.5	m
Height Horizontal Tail	h_{ht}	0	m
Main Rotor Radius	r	5.49	m

A.1.2 Rotor Flapping Parameters

Table 4: Blade Flapping Model Parameters.

Parameter	Value	Unit
K_β	900 000	[N/m]
M_β	500	[kg m ²]
I_β	502	[kg m ²]
ϱ	0.04	[-]

A.1.3 Coaxial Rotor Parameters

Table 5: Upper and lower rotor planform parameters.

Main Rotor Parameters	Symbol	Value	Unit
Lift curve slope	c_{l_α}	5.7	-
Blade chord	c	0.257	m
Rotational velocity	ω	207	rad/s
Radius	R	1.1	m
Amount of blades - Upper, lower	N_u, N_l	4, 4	-
Lock number	γ	6.57	-
Solidity Ratio	σ_p	0.153	-
Aerodynamic Interference Factor	K_p	0.4	-
X-distance from C.G. - Upper, lower	l_u, l_l	0, 0	m
Z-distance from C.G. - Upper, lower	h_u, h_l	1.66, 0.77	m
Y-distance from C.G. - Upper, lower	d_u, d_l	0, 0	m
Blade twist	θ_{twist}^p	-10	deg
Shaft angle	γ_s	0	deg

A.1.4 Pusher Propeller Parameters

Table 6: Pusher propeller planform parameters.

Pusher Propeller Parameters	Symbol	Value	Unit
Lift curve slope	$c_{l_{\alpha_p}}$	5.7	-
Drag coefficient	c_{d_p}	0.19	-
Rotational velocity	ω_p	207	rad/s
Radius	R_p	1.1	m
Amount of blades	N_p	6	-
Blade chord	c_p	0.2	m
Solidity Ratio	σ_p	0.142	-
Aerodynamic Interference Factor	K_p	0.4	-
Location on x-axis	l_p	7.66	m
Location on z-axis	h_p	0	m
Location on y-axis	d_p	0	m
Blade twist	θ_{twist}^p	-30	deg

A.1.5 Empennage Parameters

Table 7: Empennage planform parameters.

Empennage Parameters	Symbol	Value	Unit
<i>Horizontal Tail</i>			
Lift curve slope	$dC_{l_{\alpha_h}}$	3.4	-
Lift elevator slope	$dC_{l_{\alpha_h}}/d\delta_e$	0.7	rad ⁻¹
Incidence angle	α_{h_0}	0	deg
Surface Area	S_h	5	m ²
Downwash factor	K_h	1.5	-
X-distance from C.G.	l_h	6.8	m
Y-distance from C.G.	d_h	0	m
Z-distance from C.G.	h_h	0	m
<i>Vertical Tail</i>			
Lift curve slope	$dC_{l_{\beta_v}}$	4	-
Lift elevator slope	$dC_{l_{\beta_v}}/d\delta_r$	0.3	rad ⁻¹
Incidence angle	β_{v_0}	0	deg
Surface Area	S_v	1.197	m ²
X-distance from C.G.	l_v	6.8	m
Y-distance from C.G.	d_v	0	m
Z-distance from C.G.	h_v	0.5	m

A.1.6 Fuselage Parameters

Table 8: Fuselage parameters.

Fuselage Parameters	Symbol	Value	Unit
Equivalent flat plate drag	$dC_{l_{\alpha_h}}$	2.5	m ²
Volume correction factor	K_{fus}	0.7	-
Fuselage radius	R	4	m
Zero moment fuselage angle of attack	$\alpha_{fus M=0}$	-1	deg

A.2 Stability Derivatives

A.2.1 Longitudinal Stability Derivatives

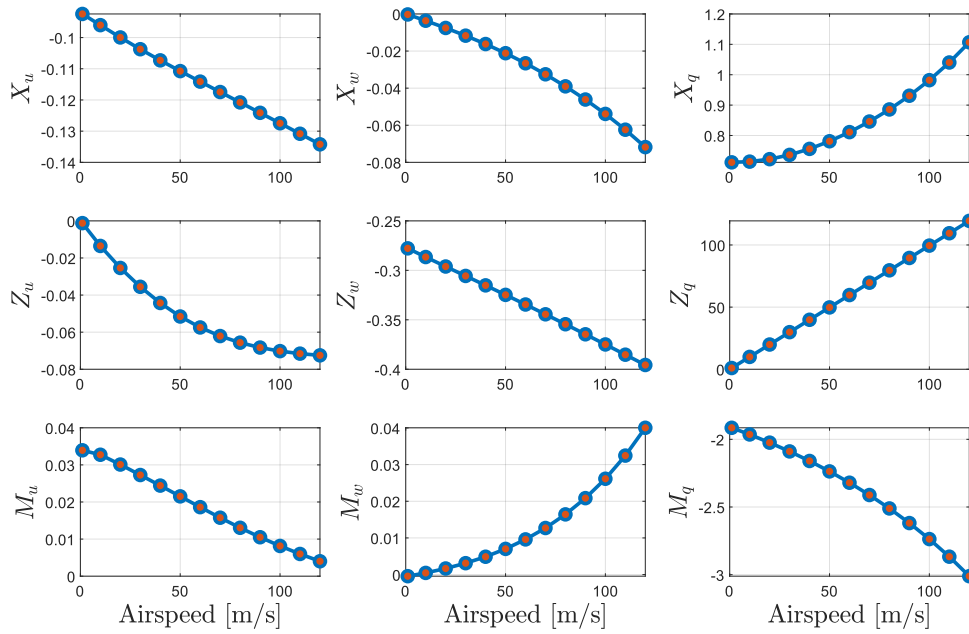


Figure 13: Stability derivatives - longitudinal.

A.2.2 Lateral Stability Derivatives

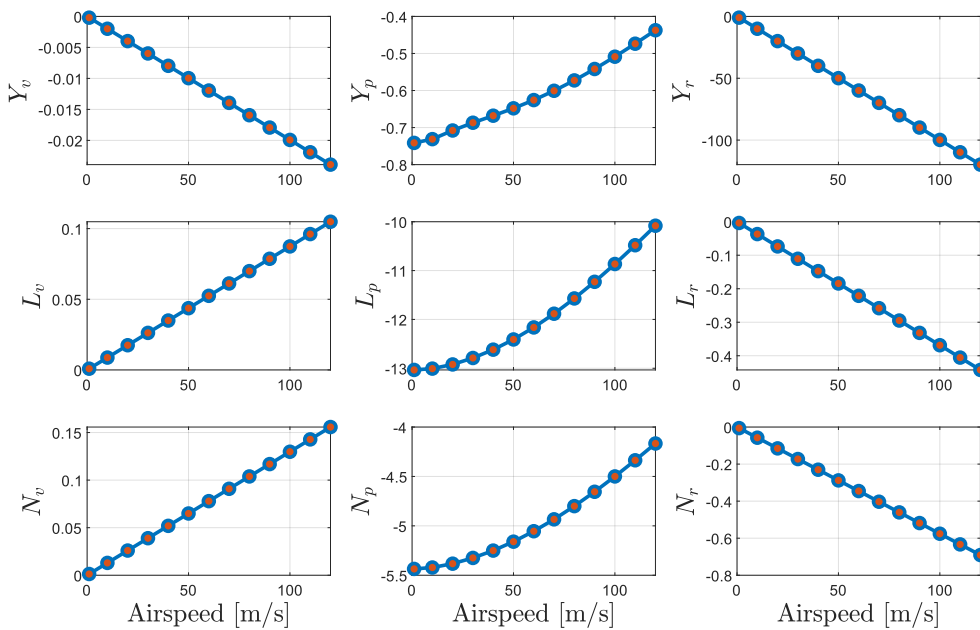


Figure 14: Stability derivatives - lateral.

A.2.3 Lateral into Longitudinal Stability Derivatives

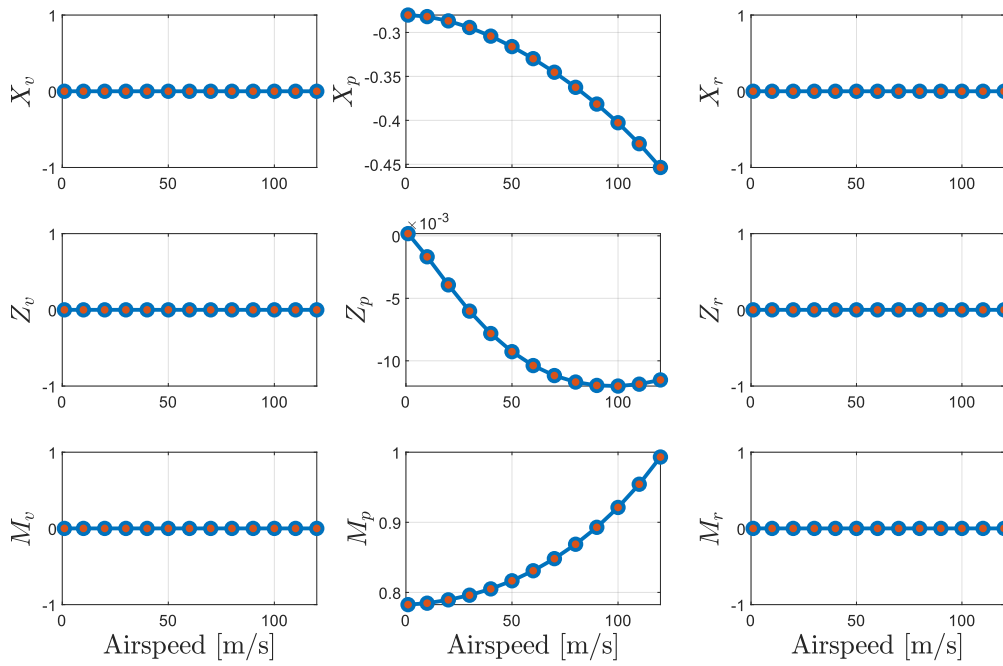


Figure 15: Stability derivatives - lateral into longitudinal.

A.2.4 Longitudinal into Lateral Stability Derivatives

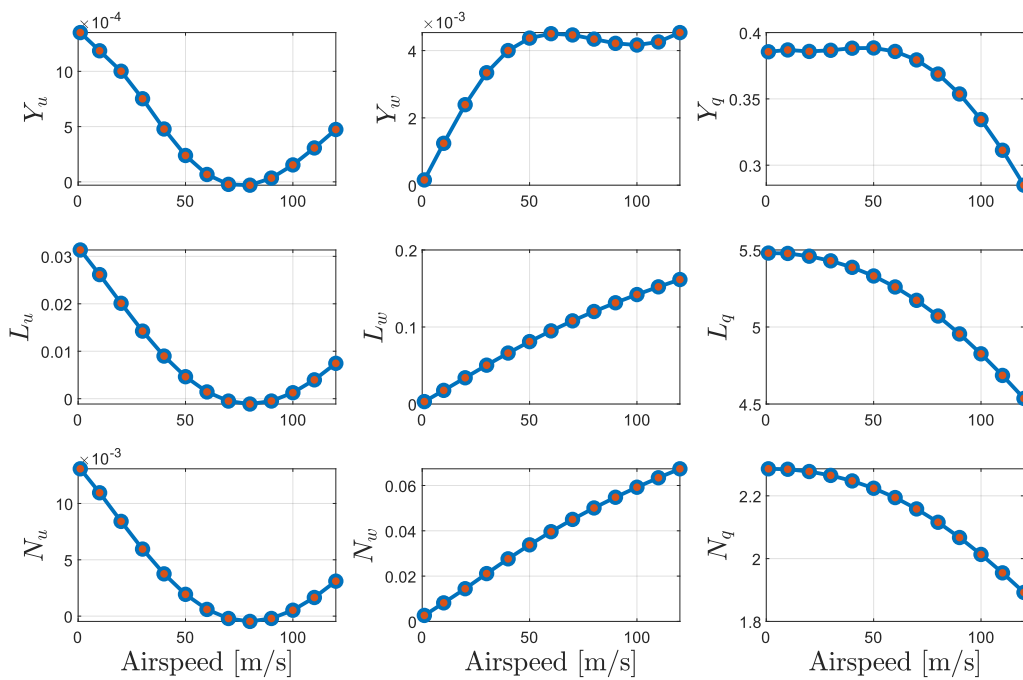


Figure 16: Stability derivatives - longitudinal into lateral.

A.3 Control Derivatives

A.3.1 Collective Control Derivatives

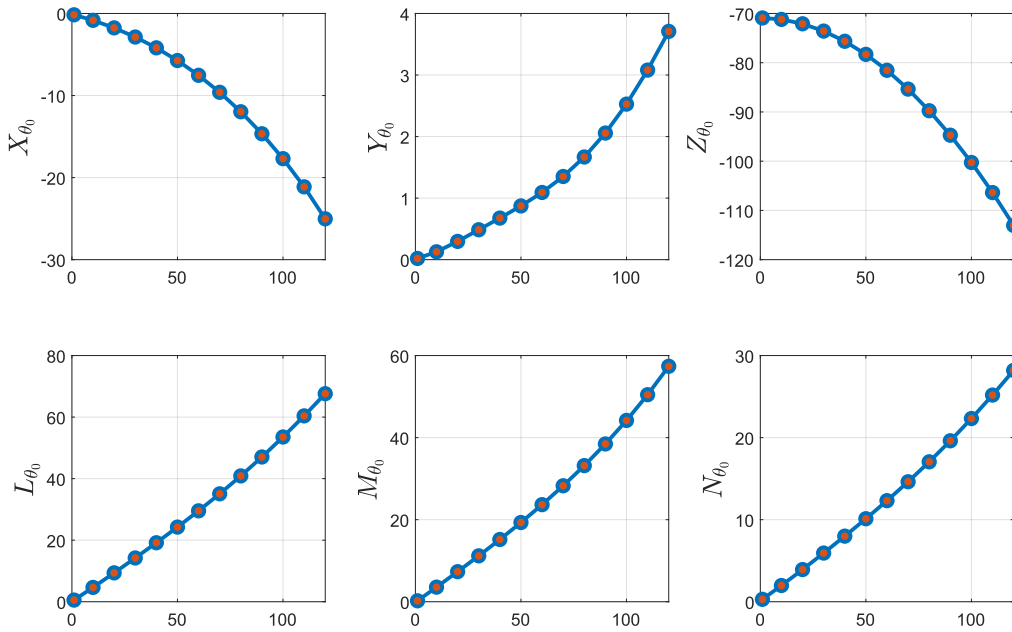


Figure 17: Control derivatives - collective.

A.3.2 Differential Collective Control Derivatives

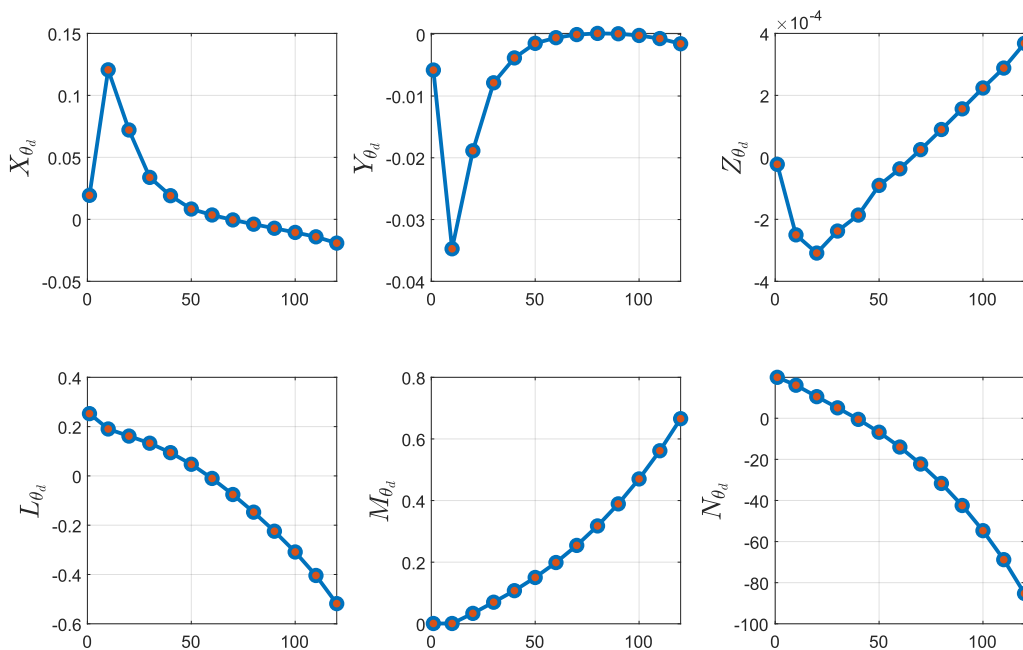


Figure 18: Control derivatives - differential collective.

A.3.3 Longitudinal Cyclic Control Derivatives

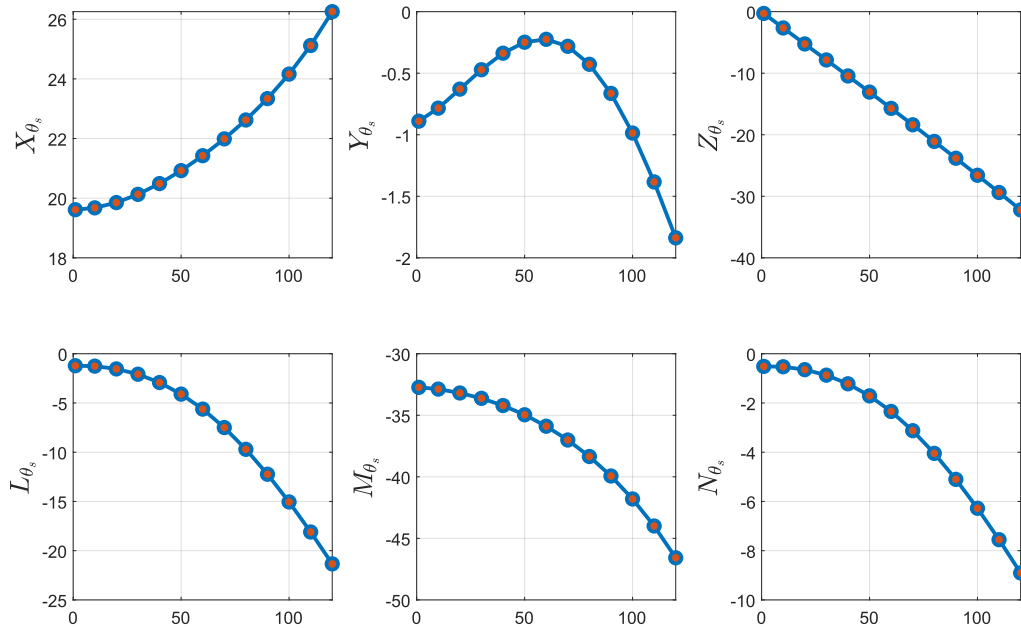


Figure 19: Control derivatives - longitudinal cyclic.

A.3.4 Lateral Cyclic Control Derivatives

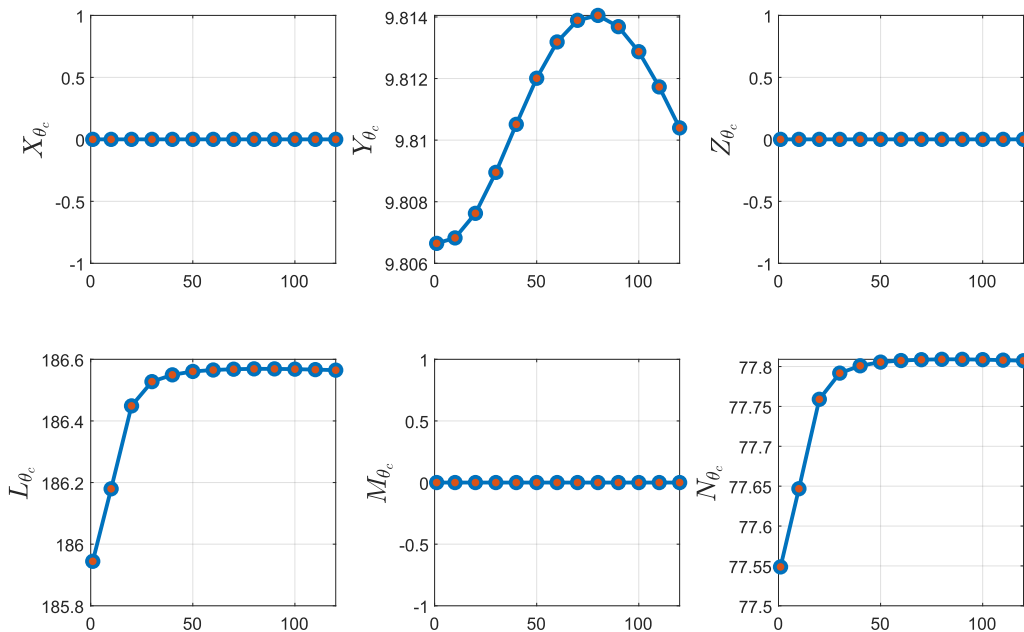


Figure 20: Control derivatives - lateral cyclic.

A.3.5 Differential Lateral Cyclic Control Derivatives

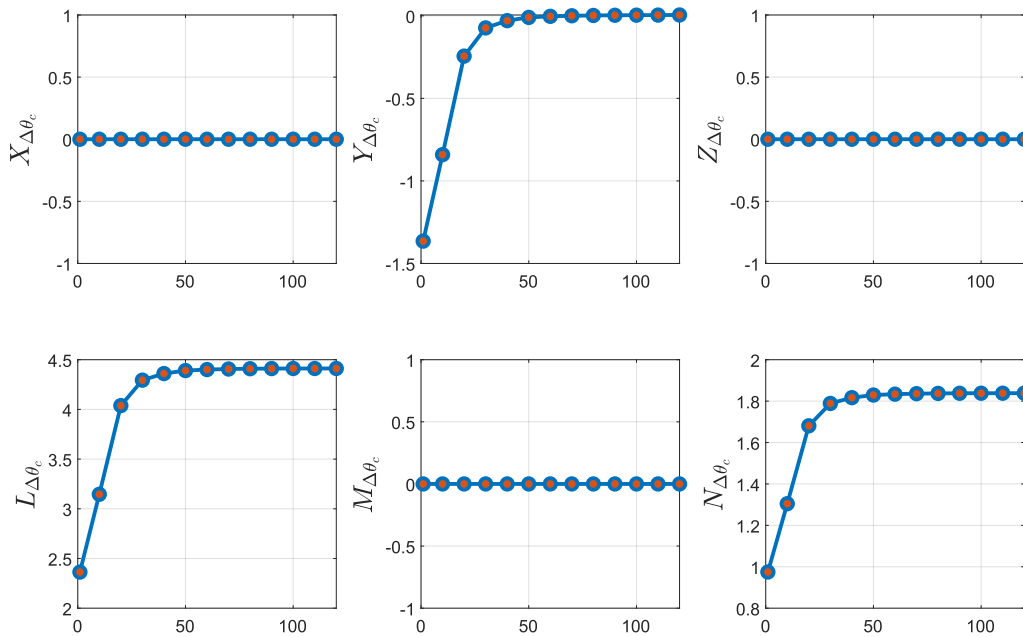


Figure 21: Control derivatives - differential lateral cyclic.

A.3.6 Pusher Propeller Collective Control Derivatives

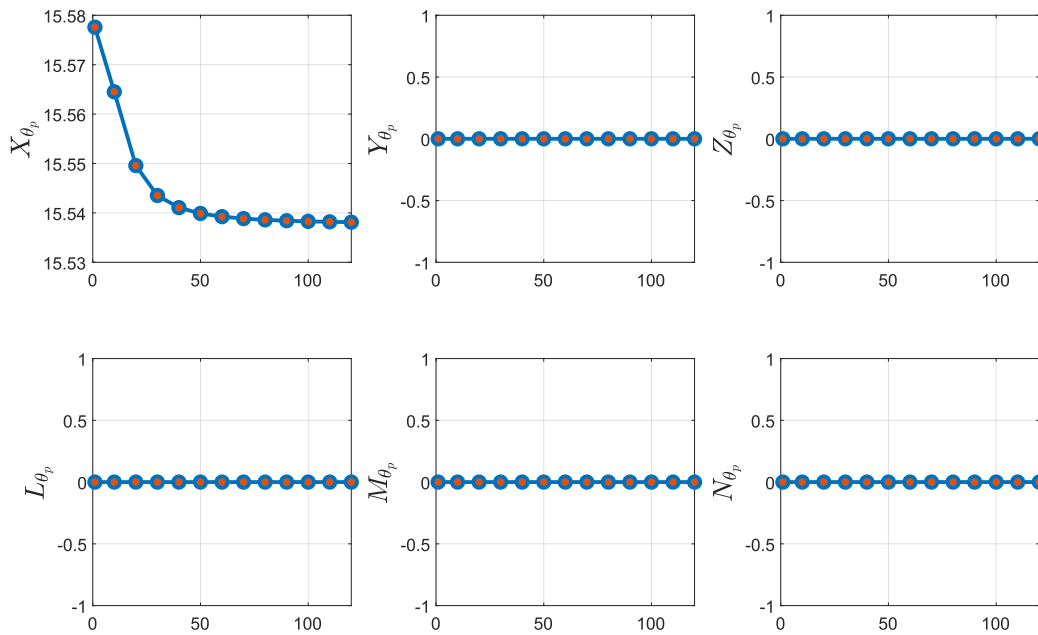


Figure 22: Control derivatives - pusher propeller collective.

A.4 Attitude Quickness Results

A.4.1 Pitch Attitude Quickness

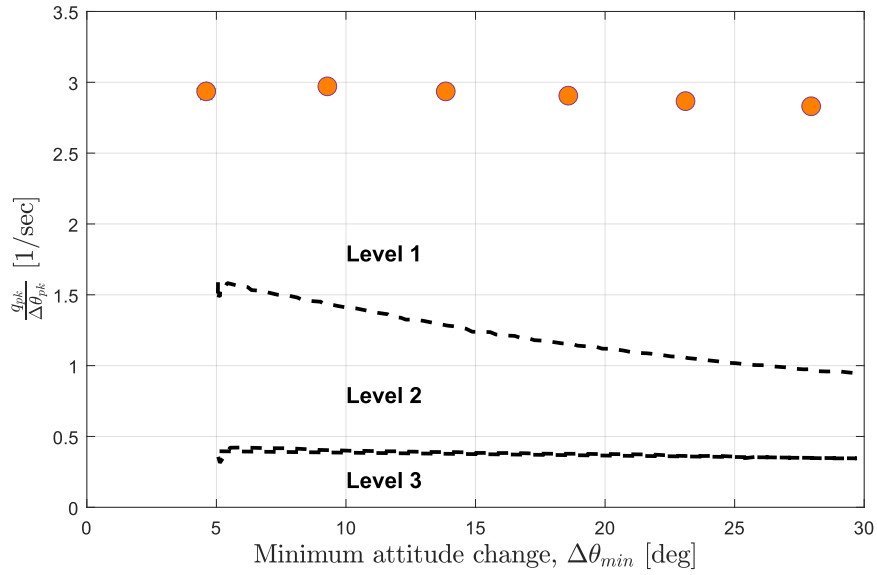


Figure 23: Pitch attitude quickness results from 5-30 deg commands, compared to ADS-33 requirements.

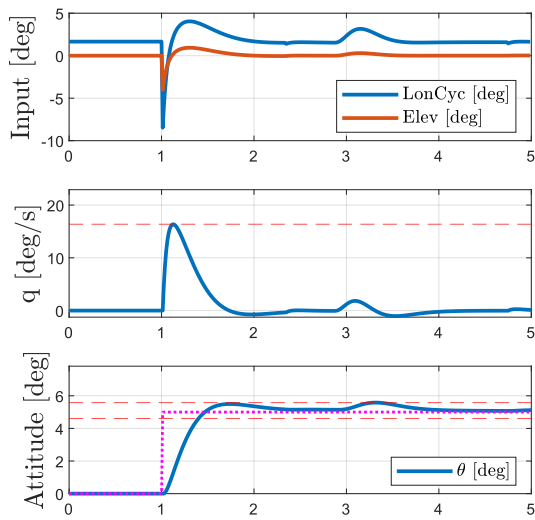


Figure 24: Pitch response for $\theta_{cmd} = 5$ deg.

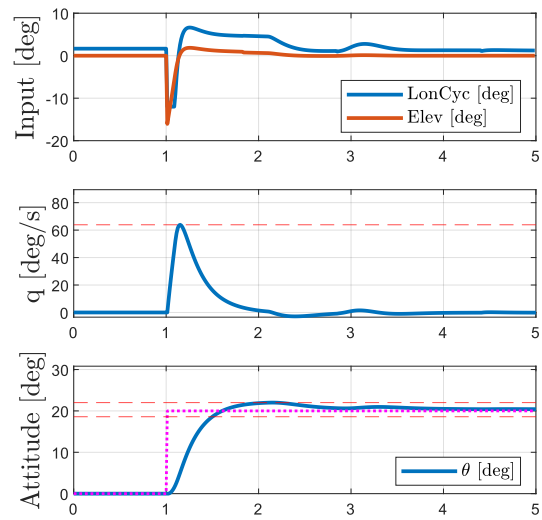


Figure 25: Pitch response for $\theta_{cmd} = 20$ deg.

A.4.2 Roll Attitude Quickness

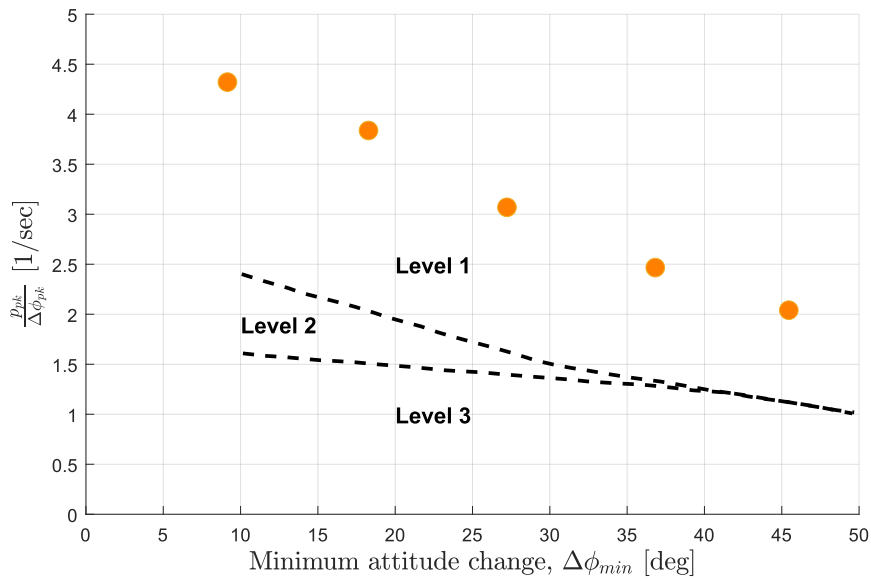


Figure 26: Roll attitude quickness results from 10-50 deg commands, compared to ADS-33 requirements.

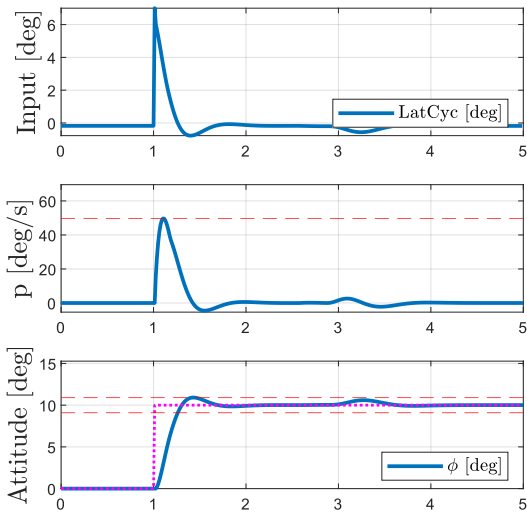


Figure 27: Roll response for $\phi_{cmd} = 10$ deg.

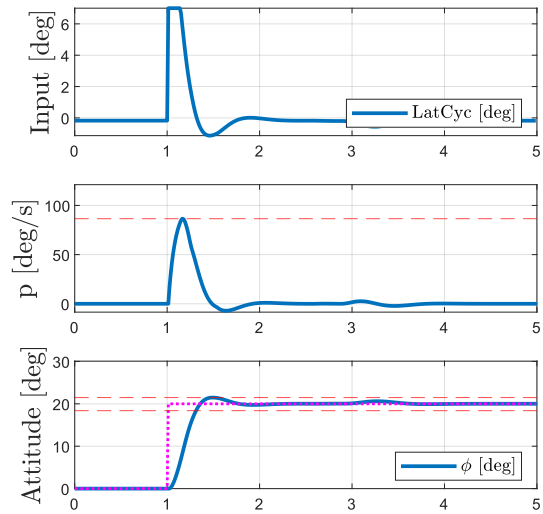


Figure 28: Roll response for $\phi_{cmd} = 20$ deg.

A.4.3 Yaw Attitude Quickness

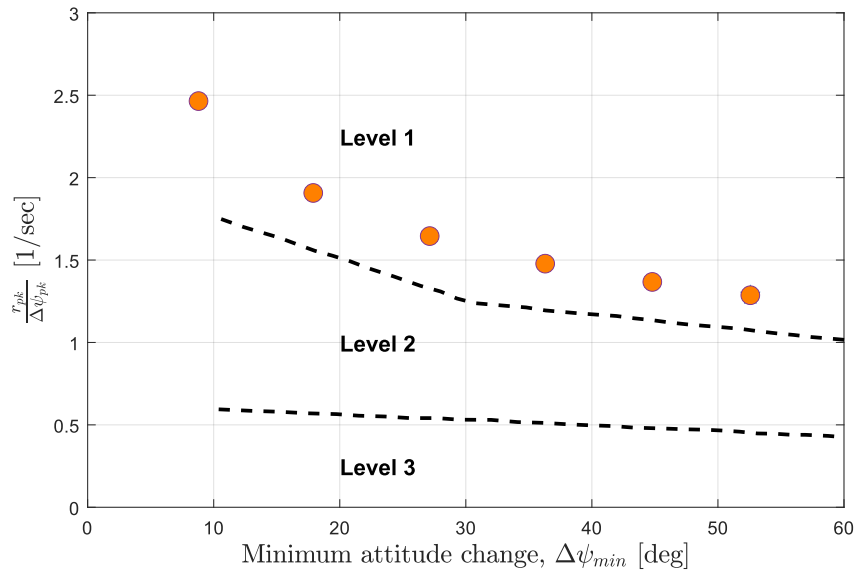


Figure 29: Yaw attitude quickness results from 10-60 deg commands, compared to ADS-33 requirements.

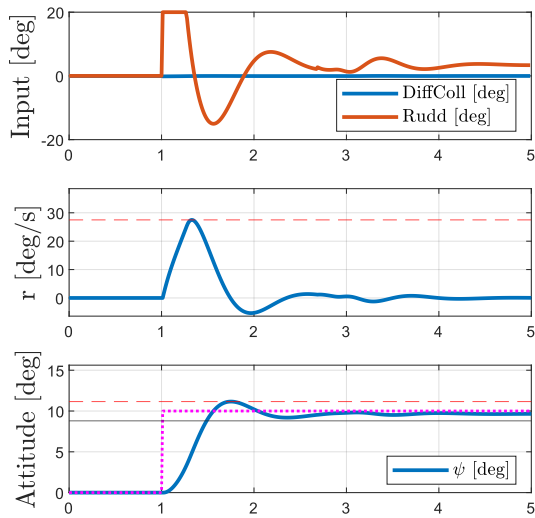


Figure 30: Yaw response for $\psi_{cmd} = 10$ deg.

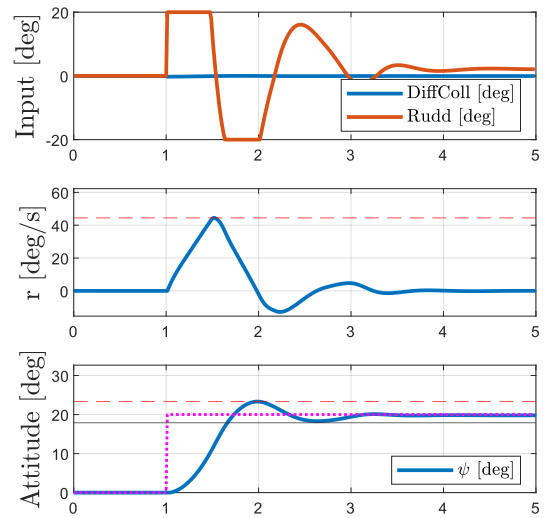


Figure 31: Yaw response for $\psi_{cmd} = 20$ deg.

Part II

Literature Study

*This part has been assessed for the course AE4020 Literature Study.

Historical Overview of Coaxial Rotorcraft

In this chapter, a brief outline on the historical development of coaxial helicopters will be given. Firstly, the early days of coaxial rotorcraft and several pioneering inventors and their designs will be discussed in Section 3.1, together with their contribution to helicopter technology in general. Secondly, the technological development of rigid rotors, and their contributions to helicopter technology development is discussed in Section 3.2. Lastly, modern coaxial helicopter designs are discussed in Section 3.3 in light of the FVL program, with specific attention to compound coaxial helicopter designs.

3.1. Early Developments of Coaxial Rotorcraft

Coaxial helicopters feature a design which places two contra-rotating rotors above each other. This results in a net-zero torque, eliminating the need of a tailrotor and creating very stable hover conditions due to the counteraction of asymmetric lift, where the lower rotor would counteract the rolling moment produced by the upper rotor, resulting in a net zero situation [4]. However, building and controlling two separate rotors requires extra engineering and piloting efforts. This however did not stop several pioneers and manufacturers from pursuing the benefits of coaxial helicopter flight.

One of the first true coaxial helicopters that achieved flight were the designs of Juan de la Cierva in the early 1920's. De la Cierva's C-1 autogiro, depicted in Figure 3.1, (a term which Cierva coined, and became widespread as 'autogyro') featured coaxial blades which produced a net zero rolling moment as described before. However, due to aerodynamic interference between the two rotorblades, the rotors were turning at different speeds, spoiling the required aerodynamic roll balance which ultimately resulted in a crash of the vehicle. In later designs, Cierva implemented articulated hinges featuring flapping (C-4 autogiro) and lead/lag (C-6 autogiro) degrees of freedom. Although it were Charles Renard and Louis Brueget who respectively founded the idea of the flapping hinge and patented the design, it was Cierva who first successfully implemented this concept in a rotating-wing aircraft. [4]

Cierva went on to produce many more iterations of his C-series. However, the aircraft was ultimately still not able to achieve hovering flight, a challenge that soon would be solved by Corradino d'Ascanio 1930 D At3 design, shown in Figure 3.2. Control of this coaxial helicopter was achieved by the ingenious use of small servo-tabs on the trailing edge of the blades, and auxiliary wings below the blades. The servo-tabs could be actuated by a contraption of cables and pulleys, resulting in a cyclically changing lift distribution. It also featured three small auxiliary propellers, mounted to the airframe, which provided extra yaw, pitch and roll controls. d'Ascanio's invention held several records at the time, including speed and altitude records. Ultimately, these pioneering designs formed the foundation of coaxial helicopter advancements, even though much progress could be made to improve their stability and control. [4]

In 1929, Nicolai Kamov started his legacy by building the first soviet Autogiro, based on the Cierva models, the KaSkr-I Gyrocraft, together with N.K. Skrzhinskij. Kamov then went on to produce the only armed autogiro ever built, which even saw limited combat action, the Kamov A-7. However, Kamov's first true coaxial helicopter, able to achieve stable hovering flight, was the 1947 Ka-8 Vertolet (Figure 3.3). Kamov went on to produce many more unconventional helicopter types, emphasising the coaxial helicopter class. [4] Later on, he built a series of very successful light and medium weight coaxial rotor helicopter designs, suited for armed combat. The most notable designs were the Ka-15 and Ka-18 in 1956, followed by the Ka-20 in 1961, which were still piston-engine driven. The Ka-25, and most types after, were all gas-turbine



Figure 3.1: de la Cierva's C-1 Autogiro (1920). [4]

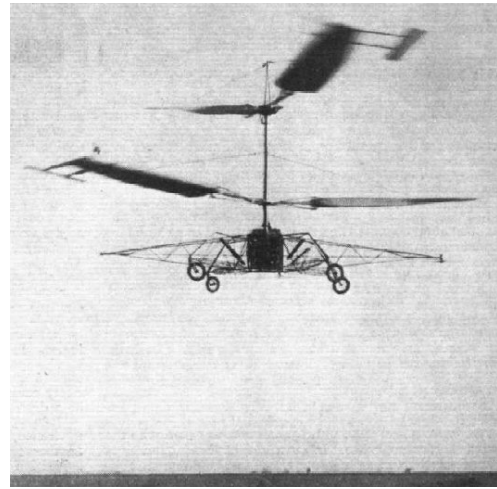


Figure 3.2: d'Asciano's Prototype Coaxial D At3 Helicopter (1930). [4]

powered. The Ka-32, which was originally built in 1972, is still in production. The same goes for the Ka-50 "Black Shark" which has been in production since 1990, and its evolution: the Ka-52 "Alligator" (Figure 3.4), which had its first flight in 1997 and entered production in 2008. [5]



Figure 3.3: Kamov A-8 coaxial helicopter (1947). [4]



Figure 3.4: Kamov Ka-52 "Alligator" (2008). [5]

An important note of the previously mentioned coaxial helicopter designs, is that they feature flexible, articulated rotors, which are able to feather, lead/lag, and flap. Even though the resulting articulated rotors became widely used on various rotorcraft, with few exceptions, it has its drawbacks. One of the main drawbacks of the articulated coaxial rotorblade that applies to the study concerning high-speed rotorcraft, is the effect of retreating-blade stall. Due to the flapping dynamics which were introduced by Cierva to provide lateral rolling moment stability, the retreating blades experience an increase in angle of attack to provide the additional lift required for this net zero moment. The higher the advance ratio of the helicopter, the larger this compensation becomes, whereby at some point the retreating blade angle of attack encounters stall conditions. Concluding this thought process, it can be stated that the articulated rotor limits the advance ratio of high-speed rotorcraft because of its inherent retreating blade stall characteristics. This brings the analysis towards the use of rigid rotors in high-speed helicopter configurations. [6]

3.2. Rigid Rotors Technology

The use of rigid rotors drastically reduces the amount of flapping the rotor blades experience due to the rigid connection of the blades to the rotor hub, omitting the hinge connection. The only flapping degree of freedom that is allowed within these designs comes from the inevitable bending of the rotor blades. Although this effect is small, it is not negligible. In order to overcome the problems that come with having



almost no flapping, (a problem why flapping was invented in the first place) the rolling moment must be balanced in other ways. This has been done by using an additional rotor (such as a coaxial, tandem, or intermeshing configuration), or by offloading the main rotor by use of an auxiliary wing and trimming the roll moment by a combination of cyclic and aileron control. In this study, the focus is put on the coaxial solution to achieve helicopter rolling balance.

The use of rigid rotors dives in a history of itself, spawning various designs such as the XH-44 coaxial rigid rotor helicopter in 1944, designed by Stanley Hiller [4], followed by the X-2-235, which ultimately did not progress into free flight. The rigid rotor concept was quite rare until the 1960's due to various problems concerning vibrations, control cross-coupling (for single rigid rotors) and rotor weight. Various attempts were made to improve these issues in the Lockheed CL-475, and the AH-56A Cheyenne (which also used compounded wings to offload the stiff rotor). Lockheed ultimately improved control cross-coupling behaviour by implementing a mechanical gyro, depicted in Figure 3.5 between the rotor and the controls. [7] This helicopter program, however promising, was ultimately canceled due to a fatal crash due to a 'half P-hop'¹, causing vibrations so bad the pilot started giving large involuntary inputs to the collective, causing the rotor blades to strike through the canopy roof. Ironically, most of these issues were solved or well on their way to being solved. It is said that politics and changing army doctrine played a large part in the utmost promising Cheyenne development. [8]

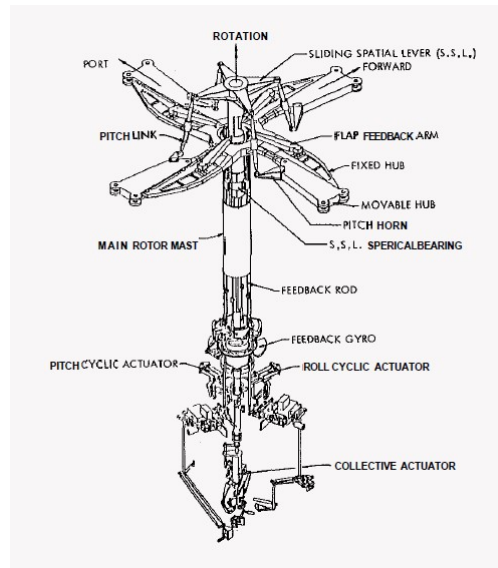


Figure 3.5: Lockheed AH-56A Cheyenne Advanced Mechanical Control System Featuring Mechanical Feedback Gyro. [7]

Similar cockpit strike incidents due to P-hop excitation still occur, with a similar incident on the Bell 525 prototype in 2016. [9] The next iteration and promising development in rigid rotor helicopters was the MBB BO-105, which had its maiden flight in '67. It featured a rigid main rotor system without flap and lead/lag hinges, creating a success story and spawning many variations later on. The BO-105 marked a milestone in the development of practical rigid rotor helicopter concepts, which could be applied to coaxial helicopter concepts. [10]

3.3. Modern (Compound) Coaxial Rotorcraft Designs

Continuing the advancement of the coaxial rotor, we arrive at the development of the Sikorsky XH-59A, which flew between 1973 and 1981. This coaxial helicopter came in two versions, a pure coaxial configuration which had its first flight in 1973, and a twin turbojet J-60 engines augmented version for auxiliary thrust, which had its first flight in 1987, enabling the helicopter to achieve speeds of up to 238 KTAS. [11] The

¹A half P-hop, or 0.5P hop, is a type of vibration that happens once per two main rotor revolutions, where P is the rotor rotational speed.



XH-59A was designed as a technology demonstrator for the Advancing Blade Concept (ABC), which will be elaborated upon in subsequent chapters. Ultimately, the XH-59A had several issues such as low aerodynamic efficiency and payload-range characteristics, alongside severe vibration levels, intense pilot workload, heavy weight and fuselage volumetric shortcomings. Despite these (non-fatal) shortcomings, the ABC concept proved very promising. The XH-59A concept was further developed, forming the XH-59B which removed the J-60 turbojet engines in favour of a compound ducted pusher propeller in the tail section. The XH-59B was proposed but not selected for the army's search for a new light attack helicopter (LHX) [4] in favour of the RAH-66 Comanche in 1990, which was also canceled in 2004. [12]

Because of the promising nature of the XH-59A, a follow-up program was funded and resulted in the first flight of the Sikorsky X2 Technology Demonstrator in 2008 (Figure 3.6). The X2 featured an Active Vibration Control (AVC) system, Fly-By-Wire (FBW) technology, and a newly designed rigid rotor (including rotor hub), featuring advanced structural and aerodynamic properties. [13] Load alleviating strategies have been implemented under the X2 Load Alleviating Controls (LAC) which use a suite of sensors, control laws, and independent rotor controls to automatically reduce rotor loads which in turn can reduce vibratory stresses, and increase rotor tip clearances. [14]

Due to a renewed interest in coaxial helicopter development, originating from the United States Army's Future Vertical Lift (FVL) program, Sikorsky went on to develop the S-97 Raider, which had its maiden flight in 2015. Using the lessons learned from the 136 flight test hours of the Raider, Sikorsky wanted to decrease the helicopter weight, and started development of the S-97 Raider X (Figure 3.7), which is in its final stages of construction at the time of writing, and planned to have its first flight early 2024. [15] The Raider X program aims to provide the army with a successor for the OH-58A Kiowa in the Armed Scout Helicopter category, under the Future Attack Reconnaissance Aircraft (FARA) [1] program, for which it shall be competing against the Bell 360 Invictus. [16].



Figure 3.6: Sikorsky X2 Technology Demonstrator (2008).



Figure 3.7: Sikorsky S-97 Raider X (2023).

This history provides some background knowledge on the development of coaxial rotor helicopters, including a brief discussion on the use of rigid rotors. In order to gain more insight into how these designs can be controlled, which is the ultimate goal of this thesis, a deeper look into the control system and rotor dynamics shall be given.

4

Advances in Compound Helicopter Designs

In this chapter, several design aspects which are featured in modern coaxial helicopters are discussed. Firstly, the principle of the Advancing Blade Concept (ABC) rotor is discussed in Section 4.1, which is prominently featured in helicopters such as the XH-59A, X2TD, Raider, Raider X, and SB-1 Defiant. Secondly, an overview of the control system of a rigid ABC rotor helicopter, with particular interest to the rotor head mechanism and control actuators, is given in Section 4.2.

4.1. Advancing Blade Concept (ABC) Rotors

As described in Chapter 3, the Sikorsky XH-59A was developed and had its maiden flight to serve as the demonstrator aircraft to show off the Advancing Blade Concept (ABC) rotor system. As discussed, this design was improved upon by the X2 Technology Demonstrator, and now being incorporated by the Sikorsky Raider X and Sikorsky-Boeing SB-1 Defiant. Because of the nature of the helicopter being discussed in this literature study, a deeper look into the ABC rotor system will be given.

The ABC rotor system fundamentally works by producing more lift on the advancing side of the blade than on the retreating side. A comparison to a conventional single-rotor design is shown in Figure 4.1. For both a single-rotor and coaxial helicopter, moment equilibrium must be achieved to avoid a large net rolling moment caused by the rotor lift. In a single-rotor system, this is achieved by maintaining lateral moment equilibrium $M_R = -M_A$ by also creating lift on the retreating side of the blade. As discussed before, relying on the lift generated by the retreating side of the blade limits the helicopter speed due to retreating blade stall at high speeds, which causes the net rolling moment to become non-zero, causing a roll.

In a coaxial rotor system, the lateral moment equilibrium is achieved by maintaining balance in the moments generated by the advancing blades of the upper and lower rotors $M_{RU} = -M_{RL}$. Because this design omits the requirement for retreating blade lift generation to maintain lateral moment equilibrium, the designers now get the freedom to shift the lift generation towards the advancing side, completely omitting the importance of retreating blade stall, allowing the helicopter to achieve much higher speeds. This also has the added benefit of significantly reducing the high drag and torque associated with retreating blade stall. [13]

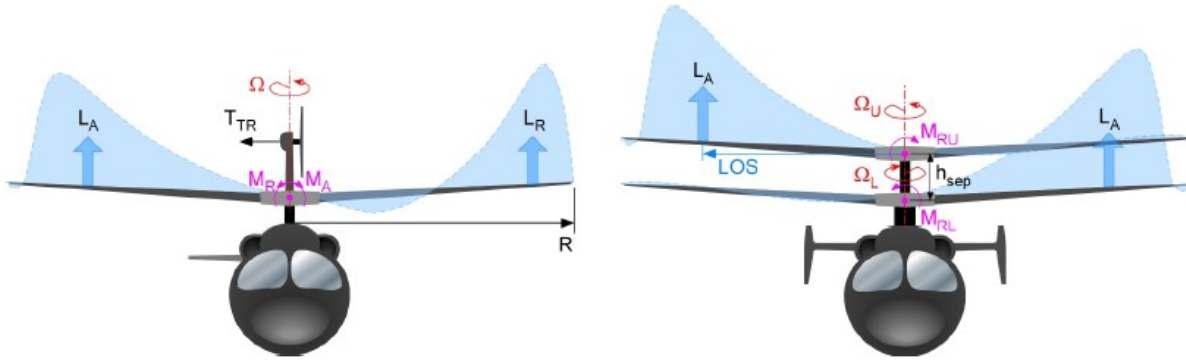


Figure 4.1: Lateral moment equilibrium comparison between a single main rotor (left) and the ABC concept (right). [13]

In order to achieve such a advancing/retreating rotor lift distribution, the X2TD incorporates several unconventional design characteristics such as a non-uniform blade planform, both positive and negative twist gradients and a complex distribution of modern airfoils and thicknesses [13], as shown in Figure 4.2.

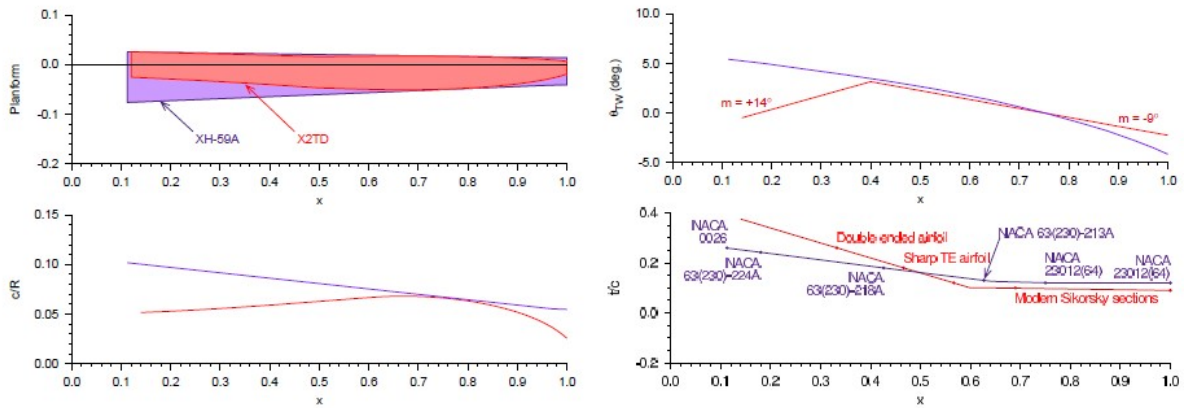


Figure 4.2: X2TD and XH-59A general main rotor blade parameters - length dimensions normalized by rotor radius. [13]

An important parameter in the use of ABC rotors is the lift-offset (LOS) of the rotor. LOS is a measure of the magnitude of lateral rolling moment compared to lift, caused by the concentration of lift on the advancing side, given by Equation 10.67, where M_X is the rotor individual rotor roll moment, T the individual rotor's thrust, and R the rotor radius. This value is typically given in terms of % and in proportion to rotor radius. [13]

$$LOS = \frac{M_X}{TR} \quad (4.1)$$

Varying the LOS can be achieved by differential lateral cyclic inputs, and can be scheduled to achieve an optimal lift-to-drag ratio of the rotorblades. In the X2TD, LOS values up to 20% were tested [14], which were limited due to the large structural bending stresses in the rotorshaft that come with increased LOS values. However, values of up to 30% are designed for and analysed [13]. In Figure 4.3, two contour plots of $C_L M^2$ and $C_D M^2$ are plotted for an LOS value of 30% (left) and 20% (right), from which several conclusions can be drawn.

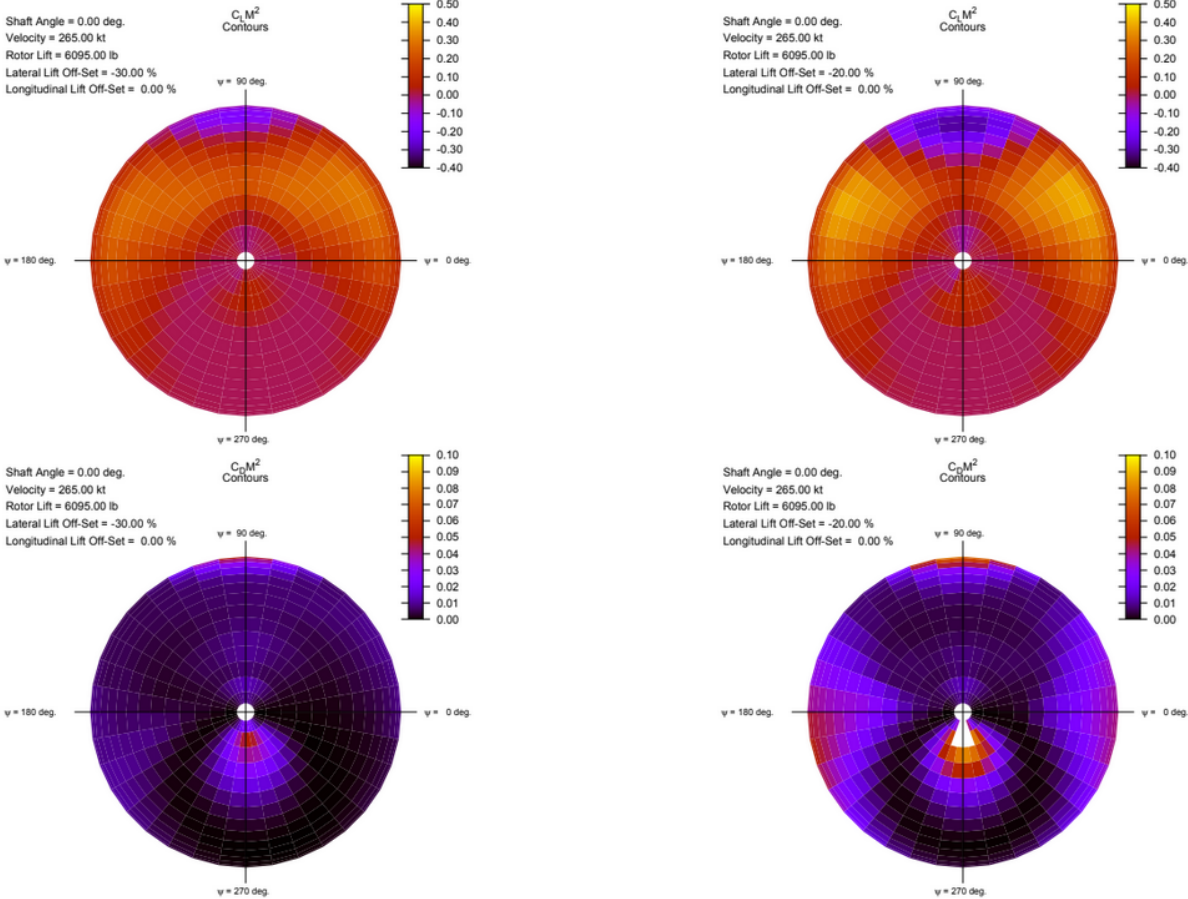


Figure 4.3: $C_L M^2$ (upper) and $C_D M^2$ (lower) contours at $V=265$ kts with LOS=30% (left) and 20% (right) for a single coplanar rotor. [13]

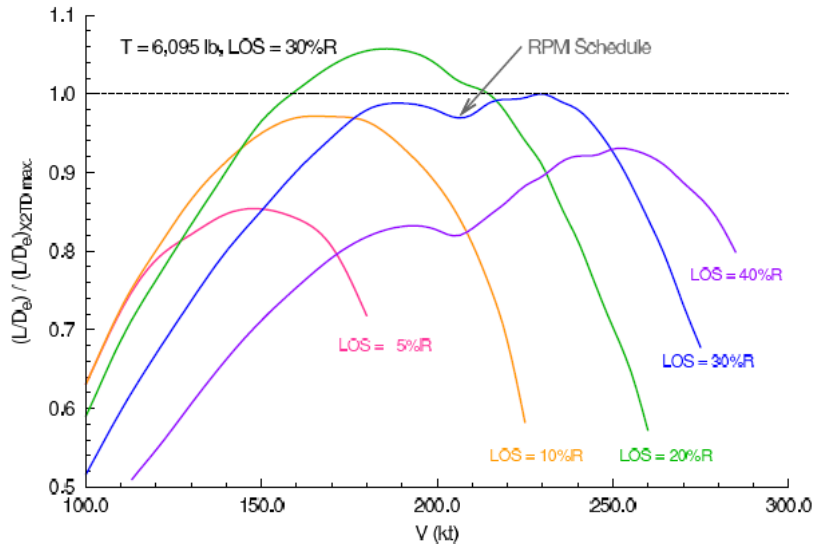


Figure 4.4: Variation of rotor lift-to-drag efficiency with rotor lift-offset, normalized by the maximum efficiency achieved with 30% LOS. [13]

Firstly, a region of negative lift can be found in the 90° azimuth area, which can be explained by the fact that due to the low dynamic pressure and low roll moment compensation, the advancing blade tips become sub-optimally loaded and can produce negative lift. This region can be pushed out (and thus become smaller) or even removed by increasing LOS, at the expense of increased shaft bending stresses. [13] Secondly, pockets of high drag can be found in two locations: near the retreating blade root, where reversed flow conditions occur, and at the advancing blade tips where compressibility effects are dominant. [13] By comparing the contour plots of 30% and 20% LOS, one can observe the increase of the contour areas of both previously mentioned effects, namely the regions of negative lift on the advancing side, and the high drag pocket sizes. This is to be expected due to the innate design nature of the ABC rotor system, which takes advantage by moving out (increasing) the LOS. If one were to decrease the LOS to small values such as 5% or even 0%, the advantageous effect of increased rotor performance for an ABC would (almost) completely disappear, only providing the advantage of omitting the importance of retreating blade stall, but increasing lift-to-drag penalties. A variation of rotor lift-to-drag efficiency with rotor lift-offset is depicted in Figure 4.4, from which the required LOS schedule to fly the rotor at for best efficiency can be ascertained. [13] According to Yuan [17], an equation in function of velocity can be set to determine the quasi-optimal LOS value at various speeds, which is formulated in Equation 4.2 below.

$$LOS = 0.0002V^2 \quad (4.2)$$

4.2. Control System Description

In an articulated coaxial rotor, such as that of the Kamov Ka-52, a 'ganged' control system is used. In such a system, the swashplates of the upper and lower rotor are mechanically linked together, as shown in Figure 4.5. This works for an articulated rotor because the control phase angle¹ Γ is close to 90° , which with the articulated rotor's flapping response results in an (almost) coplanar upper/lower rotor swashplate tilt. However, for a hingeless rigid² coaxial rotor helicopter, such as the XH-59A which employs the ABC rotor concept (more on this later), the phase angle is typically around 30 to 40 degrees. For an infinitely stiff rotor (a true 'rigid' rotor) the phase lag is essentially zero (Figure 4.6). [6].

¹Due to gyroscopic precession, the point of maximum displacement lags the point of maximum applied force by 90 degrees

²The term 'rigid' is in fact often used while incorrect in reality, due to finite stiffness of a real stiff rotorblade. Nonetheless, a 'rigid' rotor is used to describe a 'semirigid' rotor.

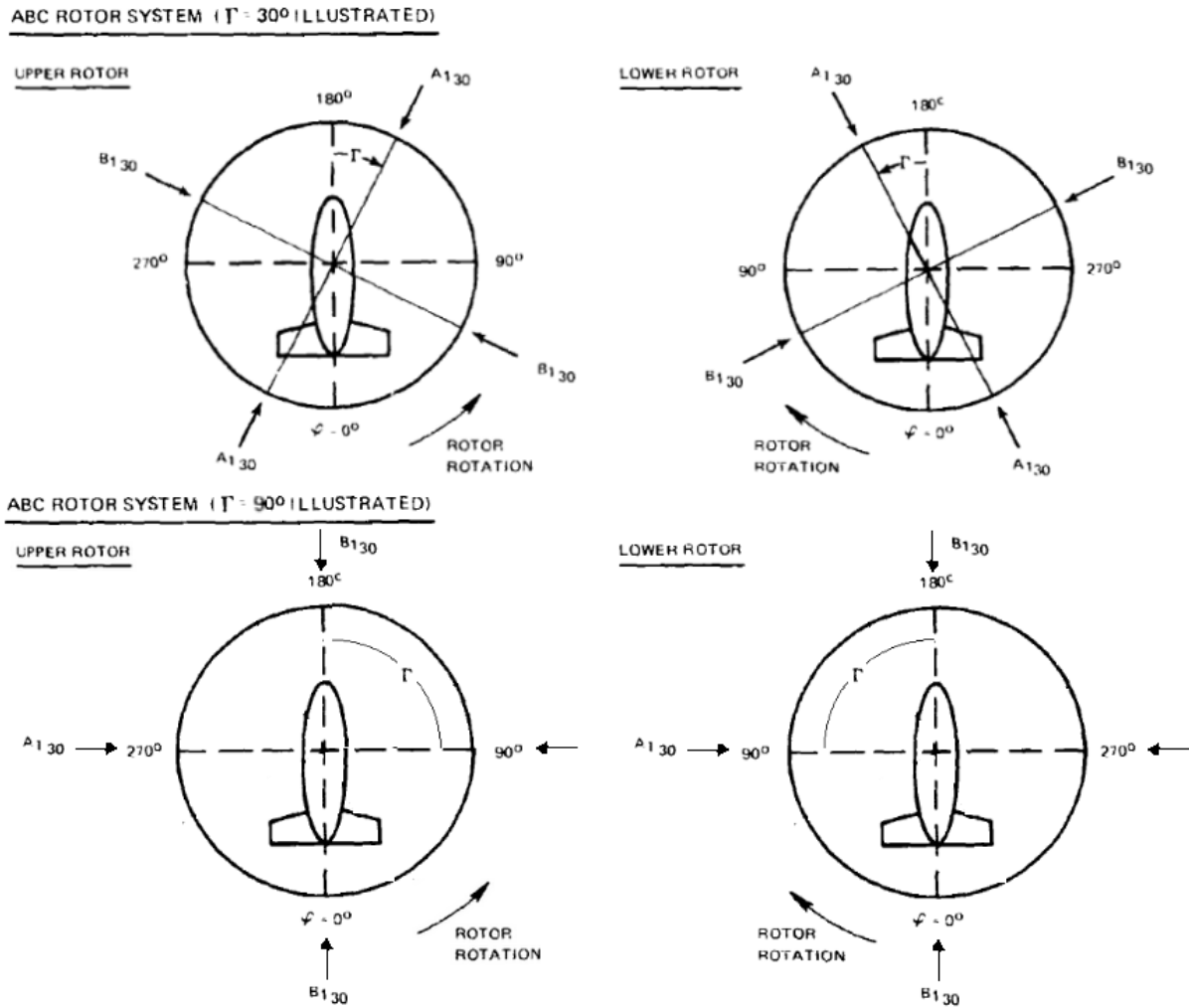


Figure 4.7: Rotor Control System Definitions and (Non-)Coplanarity Effect. [6] (Edited)

An important conclusion can be drawn from Figure 4.7. A keen observer can notice that for a rotor system with a phase lag close to 90° (lower part of figure), the lines connecting the 90° and 180° azimuth angles (representing the orientation in which the swashplate is oriented), are parallel between the upper and lower rotor. This means that their swashplates are always parallel, i.e. coplanar, which allows for direct linking between the two swashplates, removing the need for separate swashplate controls. This concept is known as control "ganging" and is used in all articulated rotor configurations. For a rotorsystem with a phase lag between 3° and 87° (assuming small phase lag differences from 90° still allow coplanarity of the swashplates), one can observe that the swashplates are no longer coplanar, and thus need separate controls.

In order to be able to control each rotor (i.e. the rotor swashplate) independently, differential controls are implemented. Differential cyclic (longitudinal for pitch, or lateral for roll) generates differential (and opposing) rotor moments, while differential collective produces a differential in thrust between the upper and lower rotor, causing different coning and a net difference in torque, providing low-speed yaw control. In the early days of differential control implementation, as used in the XH-59A, a plethora of servos, stationary swashplates, bearings, control rods, mixers, etc. were used. An illustration of the complicated, yet elegant control system of the XH-59A is depicted in Figure 4.8. In the X2 Technology Demonstrator, a Fly-By-Wire (FBW) control system was implemented, eliminating a large part of the control rods etc. Besides this, specialised coaxial (and even compound coaxial) control laws can be implemented, reducing pilot workload by scheduling differential controls, as well as rotor speed. A top-level view depicting the architecture of this FBW scheme used in the X2 Technology Demonstrator and S-97 Raider [14] is depicted in Figure 4.9.

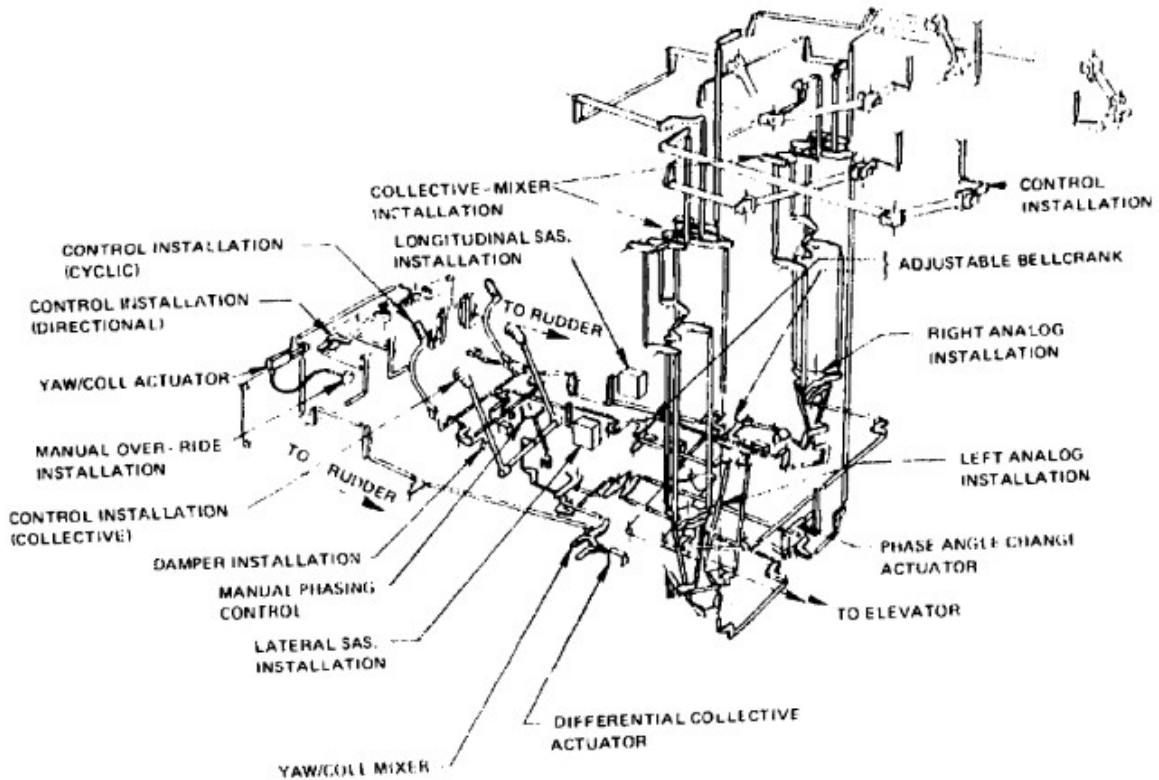


Figure 4.8: XH-59A Control System. [6]

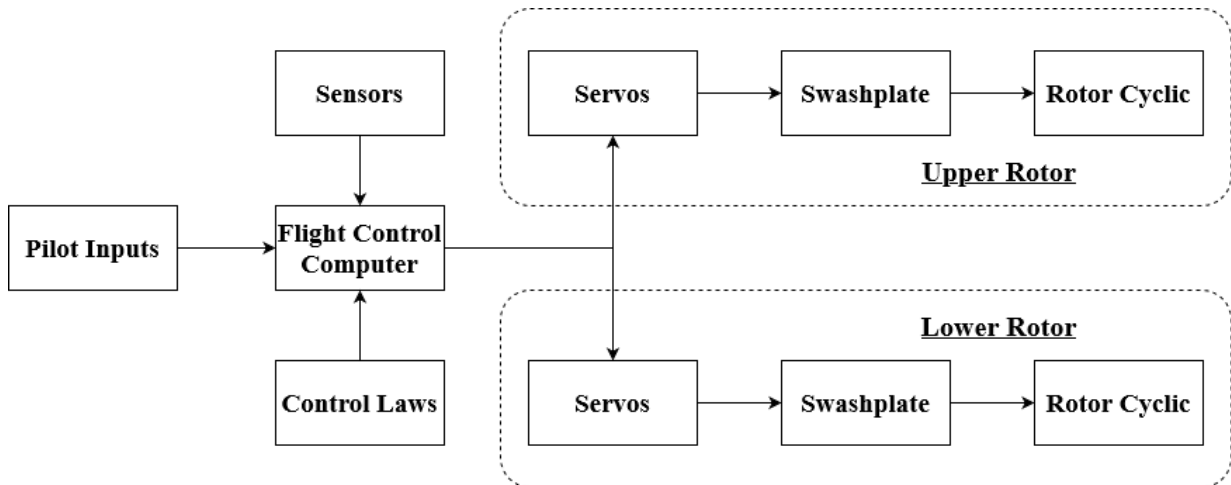


Figure 4.9: Independent FBW Control Scheme on the X2 Technology Demonstrator and S-97 Raider.

In order to be able to design a control system for a compound helicopter of using differential controls in a coaxial configuration, it is useful to define the angles defining these control deflections. The angles are split into the differential angles between the upper and lower rotor, and an average value between the two rotor control angles, known as the "ganged" angles. The former are used to generate opposite aerodynamic rotor moments, while the latter are used to generate the manoeuvring-loads. The three ganged and differential angles are defined in Equation 4.3, which are dictated by the sign convention for blade angle as a function of azimuth $\theta(\psi) = \theta_0 - B_1 \sin \psi - A_1 \cos \psi$. Here, A_1 and B_1 are the longitudinal and lateral cyclic pitch



coefficients respectively, θ_0 the collective angle and the values with a ' indicating the differential.

$$\begin{aligned} A_1 &= \frac{A_{1U} + A_{1L}}{2} \\ B_1 &= \frac{B_{1U} - B_{1L}}{2} \\ \theta_0 &= \frac{\theta_{0U} + \theta_{0L}}{2} \\ A'_1 &= \frac{A_{1U} - A_{1L}}{2} \\ B'_1 &= \frac{B_{1U} + B_{1L}}{2} \\ \Delta\theta_0 &= \frac{\theta_{0U} - \theta_{0L}}{2} \end{aligned} \tag{4.3}$$

Modelling Approaches for Coaxial Compound Helicopters

In this chapter, the modelling of a compound coaxial rotorcraft is discussed. In Section 5.1, the mathematical principles required to model a coaxial rotor are discussed. Firstly, the blade-element theory and its use is discussed, followed by various approaches to probably the largest modelling challenge, the rotor inflow modelling. This is followed by a discussion on the simple and local momentum theories, after which rotor interference and wake contraction effects in a coaxial rotor are discussed, concluded by a discussion on the blade dynamics such as flapping and lead-lag mechanics. Hereafter, the pusher propeller, fuselage and empennage modelling are discussed in Section 5.2, Section 5.3, and Section 5.4 respectively.

Throughout the modelling part, the fidelity levels described by Padfield [18], listed in Figure 5.1, are taken into account. Due to the nature of the thesis, with the goal of developing a control system and evaluating handling qualities and performance trends during conceptual design, a Level 1 fidelity level is chosen as appropriate.

	Level 1	Level 2	Level 3
<i>Aerodynamics</i>	linear 2-D dynamic inflow/local momentum theory analytically integrated loads	nonlinear (limited 3-D) dynamic inflow/local momentum theory local effects of blade vortex interaction unsteady 2-D compressibility numerically integrated loads	nonlinear 3-D full wake analysis (free or prescribed) unsteady 2-D compressibility numerically integrated loads
<i>Dynamics</i>	rigid blades (1) quasi-steady motion (2) 3 DoF flap (3) 6 DoF flap + lag (4) 6 DoF flap + lag + quasi-steady torsion	(1) rigid blades with options as in Level 1 (2) limited number of blade elastic modes	detailed structural representation as elastic modes or finite elements
<i>Applications</i>	parametric trends for flying qualities and performance studies well within operational flight envelope low bandwidth control	parametric trends for flying qualities and performance studies up to operational flight envelope medium bandwidth appropriate to high gain active flight control	rotor design rotor limit loads prediction vibration analysis rotor stability analysis up to safe flight envelope

Figure 5.1: Modelling fidelity levels. [18]

5.1. Coaxial Rotor Modelling

In this section, the modelling of the most complex part of the helicopter, the coaxial rotor, is discussed. First, an overview of the blade element theory is given, followed by a discussion on the existing literature



on rotor inflow modelling. The most promising methods in order to achieve the inflow modelling during the conceptual design phase within the time-frame of the thesis are then discussed. An overview of the global and local momentum theories is provided, after which these concepts are further explored for a coaxial rotor system. This is done by discussing the rotor interference and wake contraction effects. Lastly, the modelling of the blade dynamics is discussed.

5.1.1. Blade Element Theory

A classical analytical approach to calculating the forces produced by a rotating blade, such as a fixed wing propeller, or the rotor of a helicopter, is the blade element theory. This theory provides a way to calculate the separate forces per infinitesimal rotor span and azimuth angle. In a situation where the flow is non-uniform, such as at the lower rotor of a coaxial helicopter due to the influence of the upper rotor, the blade element theory (BET) becomes essential, since uniform inflow methods cannot be used anymore.

Figure 5.2 shows a sketch of a rotor blade with accompanying blade element. The flow environment and aerodynamic forces on the rotor are depicted. It is assumed that the radial velocity component U_R only affects the drag on the blade in forward flight, and is ignored for lift. In forward flight a number of complications occur to the aerodynamics. These include the effects of blade flapping, compressibility effects, stall, reverse flow, unsteady aerodynamics, nonlinear aerodynamics and so forth. The only effect that is modelled in Section 5.1.7 is that of blade flapping. Using BET while neglecting the other effects still results in the obtainment of the leading terms of the rotor aerodynamic forces which are very instructive and provide adequate results. [19]

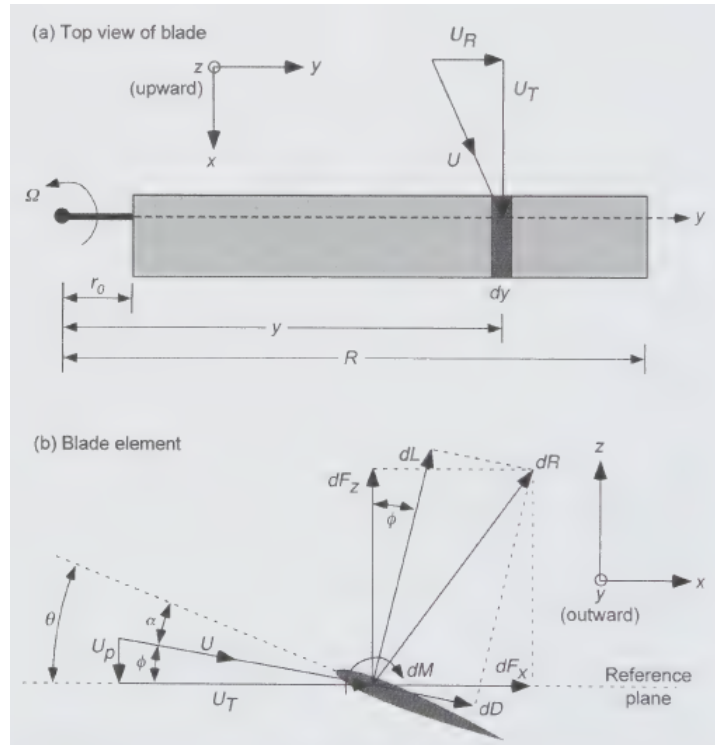


Figure 5.2: Blade element aerodynamic environment with accompanying induced velocities. [19]

The velocity at a certain blade pitch angle θ is split into two parts: the local tangential velocity U_T and the local perpendicular velocity U_P . The total velocity of a certain blade element is calculated as in Equation 5.1. In general, $U_T \gg U_P$ which simplifies the equation as shown. Note that the radial velocity component along the blade element U_R is omitted in the BET. This is due to the independence principle of sweep, which states that an aerodynamic force only results from velocity components perpendicular to the leading edge of the blade. [19]

$$U = \sqrt{U_T^2 + U_P^2} \approx U_T \quad (5.1)$$



In forward flight, the tangential (in-plane) blade element velocity U_T can be calculated by four components as shown in Equation 5.2. The first component is that caused by the blade rotation around the rotor shaft. The second and third components are those caused by the free-stream velocity component, decomposed in the longitudinal velocity u and the lateral velocity v . In hover, this free-stream component is in fact 0. The fourth and last component is the effect of the yaw rate of the rotorcraft on the tangential velocity. [19]

$$U_T(y, \psi) = \Omega y + u \cdot \sin \psi + v \cdot \cos \psi + r \cdot y \quad (5.2)$$

The perpendicular (out-of-plane) velocity U_P consists of three components as shown in Equation 5.3. The first part comprises the vertical velocity w , and the inflow velocities λ_c coming from a climbing velocity V_c and λ_i . The second group of components, which is not present in straight and level flight, is that caused by the rolling and pitching rates of the rotorcraft, which affect the local out-of-plane velocities. The last two components, which are not present in hover and are caused by the forward velocity, are the result of blade flapping motions. The blade flapping references are displayed in Figure 5.3. The first flapping motion component $y\dot{\beta}$ is produced by the result of of the blade flapping velocity about a hinge. The second flapping motion component group are those caused by the local longitudinal and lateral velocities on the blade, produced because of blade coning. [19]

$$U_{Pu}(y, \psi) = \underbrace{-w + (\lambda_c + \lambda_i) \cdot \Omega R}_{\text{Vertical velocity inflow}} + \underbrace{\dot{\beta} y}_{\text{Hinge flapping}} - \underbrace{p \cdot y \cdot \sin(\psi) - q \cdot y \cdot \cos(\psi)}_{\text{Rotational rate effect}} + \underbrace{u \sin(\beta) \cdot \cos(\psi) + v \sin(\beta) \cdot \sin(\psi)}_{\text{Blade coning}} \quad (5.3)$$

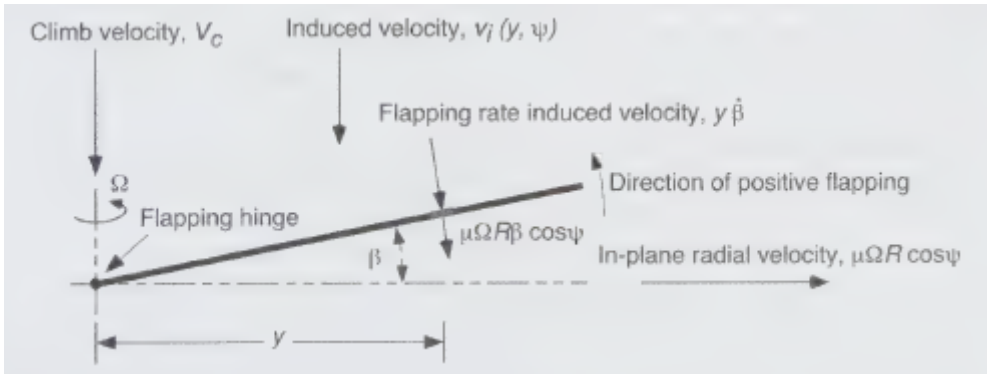


Figure 5.3: Perturbation velocities on the blade resulting from blade flapping velocity about a hinge and blade coning. [19]

The relative inflow angle is calculated as per Equation 5.4 , which can be simplified as well for small angles.

$$\phi = \tan^{-1} \left(\frac{U_P}{U_T} \right) \approx \frac{U_P}{U_T} \quad (5.4)$$

Which results in the angle of attack of the blade α given by Equation 5.5:

$$\alpha = \theta - \phi \quad (5.5)$$

The resultant incremental lift force for a certain blade element per unit span is given by Equation 5.6:

$$\begin{aligned} dL &= \frac{1}{2} \rho U^2 c C_l dy = \frac{1}{2} \rho U^2 c C_{l_\alpha} (\theta - \phi) dy \\ &= \frac{1}{2} \rho U^2 c C_{l_\alpha} \left(\theta - \frac{U_P}{U_T} \right) dy = \frac{1}{2} \rho U^2 c C_{l_\alpha} (\theta U_T^2 - U_P U_T) dy \end{aligned} \quad (5.6)$$



And the resultant incremental drag is given by Equation 5.7:

$$dD = \frac{1}{2}\rho U^2 c C_d dy \quad (5.7)$$

From these equations, the forces in X, Y and Z direction can be decomposed. When applying the blade element theory to the upper and lower rotor, these can be combined to calculate the total coaxial rotor forces and moments which can be used in the total model force and moment calculations.

In order to calculate the perpendicular and tangential velocity components for the blade-element theory, the inflow on the blade sections need to be available. This is the topic of the next subsection.

5.1.2. Rotor Inflow Modelling

In rotor wake modelling, there are two main requirements as stated in Chen [20]: accuracy and computational efficiency. The accuracy of the rotor wake model heavily influences the level of validity of the model in various points throughout the envelope, while the computational efficiency dictates the practical applicability of the model in (real-time) simulations. High computational times limit the ability of the model to generate results for control responses and handling quality assessment. Increased levels of accuracy almost always come at the cost of decreased computational efficiency.

Various methods to calculate rotor wake models for evaluating induced velocity distributions along rotor blade spans have been discussed over the years in literature. In the following, an attempt is given to summarize the currently existing methods, with various levels of accuracy and complexity. We will start by discussing basic momentum theory, discussed in Johnson [21] and Padfield [18], among others, followed by local momentum theory (LMT), explained in Padfield [18] and numerically applied in Saito and Azuma's work [22]. More complex and recent rotor wake modelling techniques which utilize prescribed wake and free wake, or implement vortex theories, are shortly discussed as well. However, due to their complex and in-depth nature, they will not be analysed further to limit the scope of this literature study and thesis.

Simple momentum theory provides an overall adequate result for general performance calculations. The simple momentum theory assumes a uniform inflow of the rotor, allowing a high degree of computational efficiency. However, a good accuracy level is limited for specific flight cases. Due to the assumption of an instantaneous velocity change across the rotor disc in the simple momentum theory, which results in a discrepancy in the modelling of the dynamic lag of the induced velocity, some aerodynamic accuracy is lost. [23] During forward flight, the rotor inflow also becomes non-uniform due to the wake being tilted backwards. In order to combat this problem, Coleman [24] built a linear model based on momentum theory which took into account the wake correction, which enabled him to calculate the induced velocity distribution in the mid-high speed ranges. However, his model lost accuracy for the low speed range. Furthermore, these models were designed to be used on single-rotor rotorcraft, thus not analysing the effect on coaxial rotorcraft.

Simple momentum theory can also be expanded to local momentum theory, allowing it to be used for non-uniform flowfields, as described by Padfield [18]. The local momentum theory considers the one-per-rev components of the load and inflow, instead of averaging the load around the disk. [18] This allows for an expression of non-uniform inflow, capable of evaluating timewise (and thus dynamic) variations of airloading, aerodynamic moments and most importantly, induced velocity distributions along the rotor blade span. These dynamic inflows are given in the form of first-order ordinary differential equations. One of the most widely used and accepted applications of the local momentum theory is the model developed by Pitt and Peters [25], commonly known as the Pitt-Peters inflow model. Numerous works [26] [27] have used the inflow model provided by these researches, who provided a means to find a compromise between accuracy and computational efficiency for calculating induced velocity distributions. Nevertheless, for this type of model to work, the inflow velocity must be much larger than the induced velocity of the rotor disk. Therefore, this model is only applicable for low disk loading rotorcraft, or mid-high forward flight speeds. [20] This however, due to the inherent lower disk loading of a coaxial rotorcraft, might make the local momentum theory a good solution for the coaxial rotorcraft class. Indeed, several works have been done using this type of model on coaxial rotorcraft. [26][28] Leishman and Syal [29] and Leishman and Ananthan [30] developed a steady coaxial inflow model by slightly adapting the classical blade element momentum theory.



In 1981, Saito and Azuma [22] developed a numerical approach to calculate the non-uniform rotor inflows for a steady aerodynamic system using local momentum theory. They concluded that the lower rotor had a better performance compared to normal momentum theory, alongside the fact that this approach also enables the possibility to calculate instantaneous airloading of the blades in a complex wake system. With the addition of the effect of radial shrinkage of the upper rotor wake in their analysis, the accuracy was further improved. Wind tunnel tests in both forward and hovering flight showed good agreement with theoretical predictions, although the results did not differ significantly for hovering flight compared to normal momentum theory.

In his PhD thesis, Ferguson [28] applies an adapted simple momentum theory based on Leishman's work, assuming that the rotors are close enough so that the wake from the upper rotor does not contract radially inward, and that the inflow of the lower rotor does not affect the upper rotor's thrust generating ability. The former assumption is justifiable for the ABC rotor, which features very stiff blades which allows for a very small separation distance, as explained in Section 4.1. However, in his analysis which goes up to advance ratios of 0.25, Ferguson omitted the effects of skew angle, which accounts for the part of the upper rotor wake not to be ingested in the lower rotor during forward flight. He found that omitting the wake skew angle from the model still results in a good fit with experiments. This assumption however, might not be valid for high-speed rotorcraft such as the X2TD which can reach advance ratio's of around 0.75. Therefore, wake skew angle will most likely have to be incorporated in the model.

Lastly, a short discussion on more advanced modelling techniques is covered. Prescribed and free vortex wake models are aerodynamically more accurate, but are much more complex and thus computationally much more intensive. However, they do allow for nonlinear analysis of the flow-field and vortex interactions. Therefore, they are typically only used for high fidelity aerodynamic analyses, such as that used for the rotor aerodynamic design. [18] Prescribed vortex wake models, developed by several researchers such as Barocela [31], Krothapalli [32] and numerous others, typically use a pre-scheduled curvature of the wake distortion, using a parameter K_{re} [20] which reflects the proportional relationship between induced velocity of the rotor and the wake curvature gradient. Because the prescribed-wake vortex models are not able to fully reflect the distortion caused by vortex interactions, they cannot be used to precisely simulate the flow interactions between multi-rotor configurations. Therefore, the free-wake method was developed, which is based on rotor vortex theory. [33] The free-wake vortex theory method received many iterations and improvements to suit the needs for several applications.

In recent years, many researchers tried to refine the principles of the vortex wake theories, achieving models capable of including airflow separation, dynamic stalling, and shock wave implementation. However, a lot of these solutions either suffer from numerical instabilities or convergence issues in certain regions, or are extremely computationally intensive. [20]

5.1.3. Simple Momentum Theory

As described above, the simplest way to calculate the rotor inflow is by means of the simple momentum theory, also referred to as the global momentum theory. In the case of flight dynamics analysis, Padfield [18] states that it is sufficient to consider the normal component inflow, i.e. the rotor-induced downwash. In the analysis to calculate the rotor inflows, a number of assumptions concerning the rotor and fluid motion characteristics can be made to simplify the downwash analytical expressions. These encompass the flow to be steady, inviscid and incompressible, with a well-defined slipstream between the flowfield generated by the actuator-disc (the rotor) and the external flow. The last assumptions are an atmospheric pressure in the far wake and a uniform-inflow. [18] The simplest representation of the rotor wake is based on the so-called actuator disk-theory. In this representation, the rotor is assumed to have an infinite amount of blades, forming a disc through which the air is instantaneously accelerated. A large shortcoming of the actuator-disk theory is the assumption of a uniform flow field. This assumption will not be valid for the lower rotor as discussed before, but will provide suitable results for the upper rotor, as demonstrated in Ferguson [28]. In the next subsection, the blade-element momentum, or local momentum theory, will consider a finite number of blades, able to analyse non-uniform flow fields, which can be applied for the lower rotor inflow calculations.

First consider Figure 5.4, which depicts three possible scenario's for the momentum theory applied in axial flight: stationary hover (a), climbing (b) and descending (c) flight. Here, T is the rotor thrust, v the velocity at various stations in the streamtube, v_i the disc inflow, V_c the climb velocity, and V_d the descent velocity. The momentum theory starts by considering a mass flow rate \dot{m} (constant at each station)



through a rotor disc area A_d , which is calculated per:

$$\dot{m} = \rho A_d (V_c + v_i) \quad (5.8)$$

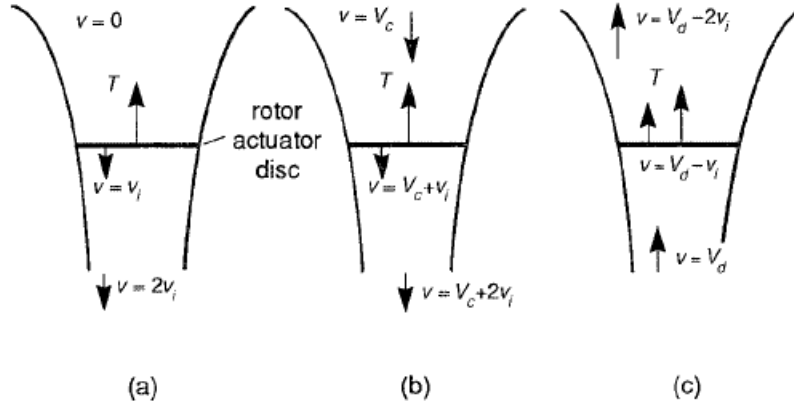


Figure 5.4: Rotor flow conditions in axial flight: hover (a), climb (b), descent (c). [18]

The law of conservation of momentum can be applied by equating the undisturbed upstream conditions and the far wake conditions to the rotor. This results in Equation 5.9 as an expression for T , where $V_{i\infty}$ is the induced flow velocity in the fully developed wake.

$$T = \dot{m}(V_c + v_{i\infty}) - \dot{m}V_c = \dot{m}v_{i\infty} \quad (5.9)$$

The kinetic energy of the flow can be deduced from the work done by the disc:

$$T(V_c + v_{i\infty}) = \frac{1}{2}\dot{m}(V_c + v_{i\infty})^2 - \frac{1}{2}\dot{m}V_c^2 = \frac{1}{2}\dot{m}(2V_cv_{i\infty} + v_{i\infty}^2) \quad (5.10)$$

From Equation 5.9 and Equation 5.10 we can conclude that the induced velocity in the far wake of the flowfield is accelerated to twice the rotor inflow, as per Equation 5.11. The induced velocity is often used in its normalized form, which can be calculated by normalizing as shown in

$$v_{i\infty} = 2v_i \quad (5.11)$$

$$\lambda_i = \frac{v_i}{\Omega R} \quad (5.12)$$

Implementing Equation 5.8 and Equation 5.11 in Equation 5.9, we obtain an expression for thrust directly in terms of the induced velocity at the rotor disc:

$$T = 2\rho A_d (V_c + v_i) v_i \quad (5.13)$$

The inflow from the hover and climb situations can be written by Equation 5.14 and Equation 5.15 respectively, where $\mu_c = \frac{V_c}{\Omega R}$.

$$\lambda_{ih} = \sqrt{\left(\frac{C_T}{2}\right)} \quad (5.14)$$

$$\lambda_i = -\frac{\mu_c}{2} + \sqrt{\left[\left(\frac{\mu_c}{2}\right)^2 + \lambda_{ih}^2\right]} \quad (5.15)$$



The inflow during descent is more complicated however. Physically, the momentum theory conditions are only satisfied for the conditions where the wake is fully established above the rotor, and where the flow is upwards throughout the entire streamtube. This condition is called the windmill brake state, whose name originates from the operation of a windmill which extracts energy (or momentum) from the air, as depicted in Figure 5.4(c). In this case, the air performs work on the rotor, or in other words, the work done by the rotor on the air is negative, which results in Equation 5.16 for the rotor thrust. The inflow during the windmill brake state can be written as Equation 5.17, where $\mu_d = \frac{V_d}{\Omega R}$. [18]

$$T = 2\rho A_d (V_d - v_i) v_i \quad (5.16)$$

$$\lambda_i = \frac{\mu_d}{2} - \sqrt{\left[\left(\frac{\mu_d}{2}\right)^2 - \lambda_{ih}^2\right]} \quad (5.17)$$

Figure 5.5 depicts the momentum theory solutions for axial flight rotor inflows. The physical solutions for hovering, climbing and windmill brake state are plotted in full lines. The dashed lines represent the vortex ring states. In and around these conditions, vortices are (being) formed on the rotor tips, which are caused by the equalling of the rotor inflow and descent rate, the so called 'ideal autorotation' condition. The flow in these torroidal-shaped vortex rings is very non-uniform and unsteady. Therefore, momentum theory falls short in the analysis of this condition. However, Young [34] derived a semi-empirical relation which describes the mean inflow at the rotor disc between hover and the windmill brake state, as depicted by the dotted lines in Figure 5.5.

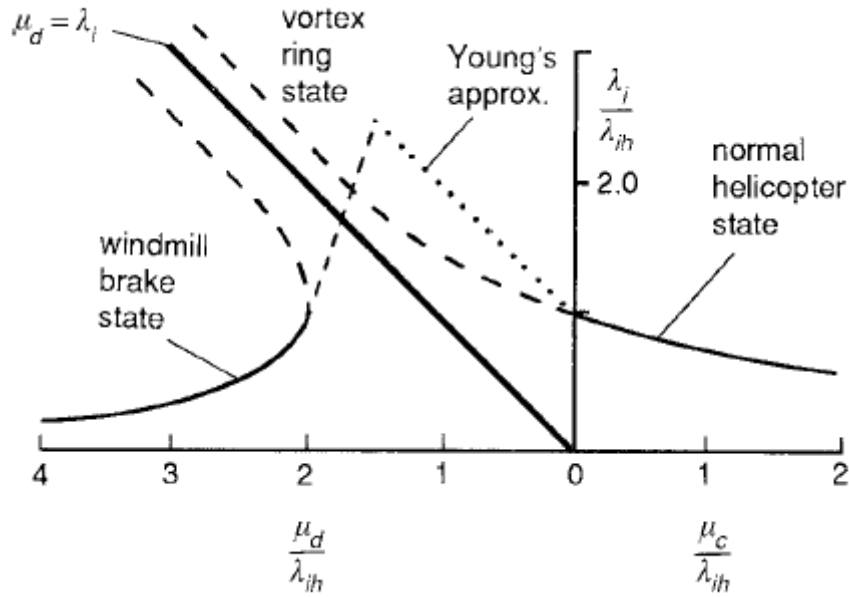


Figure 5.5: Momentum theory solutions for axial flight rotor inflows.

The solutions formed by Young intersect at $\frac{\mu_d}{\lambda_{ih}} = 1.5$ and is therefore split into two region. The solutions take the form as shown in Equation 5.18 and Equation 5.19, and enable an approximation for the induced velocity in the region between hover and the windmill brake state for descending flight.

$$\lambda_i = \lambda_{ih} \left(1 + \frac{\mu_d}{\lambda_{ih}}\right) \quad 0 \leq -\mu_d \leq -1.5\lambda_{ih} \quad (5.18)$$

$$\lambda_i = \lambda_{ih} \left(7 - 3\frac{\mu_d}{\lambda_{ih}}\right) \quad -1.5\lambda_{ih} < -\mu_d \leq -2\lambda_{ih} \quad (5.19)$$

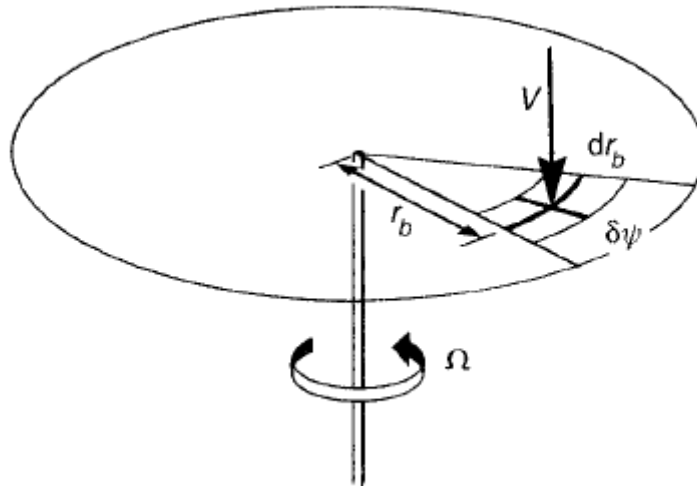


Figure 5.6: Local momentum theory visualisation on a single rotor disc. [18]

In forward flight, the induced downwash field is pushed back with a certain skew angle χ , which is elaborated upon in Section 5.1.4. Following a similar reasoning as for axial flight, applying the law of conservation of momentum, calculating mass flow and thrust, the normalized induced velocity λ_i can be calculated using Equation 5.20, where μ and μ_z are calculated using Equation 5.21 and Equation 5.22 respectively. α_d is the rotor disc incidence angle.

$$\lambda_i = \frac{C_T}{2\sqrt{[\mu^2 + (\lambda_i - \mu_z)^2]}} \quad (5.20)$$

$$\mu = \frac{V \cos \alpha_d}{\Omega R} \quad (5.21)$$

$$\mu_z = -\frac{V \sin \alpha_d}{\Omega R} \quad (5.22)$$

Strictly speaking, Equation 5.20 is only applicable to conditions where the flight velocity is much greater than the induced velocity. However, for the limit cases where $\mu = 0$ such as in hover or axial flight, the forward flight induced velocity equation still provides a reasonable approximation. [18] In fact, this equation holds for a wide range of flight conditions, including steep descent, and can also be used to estimate the induced power required.

5.1.4. Local Momentum Theory

As discussed before, the local momentum theory, also known as the blade-element momentum theory (BEMT), expands the global momentum theory by considering local annuli, or sections, of the blade in function of radial and azimuthal position. The goal is to calculate a non-uniform inflow distribution for each position on the rotor disc plane. A visualisation of this approach is shown in Figure 5.6.

The equations for mass flow and incremental thrust are given in Equation 5.23 and Equation 5.24.

$$d\dot{m} = \rho V_{r_b} dr_b d\psi \quad (5.23)$$

$$dT = d\dot{m} 2v_i \quad (5.24)$$

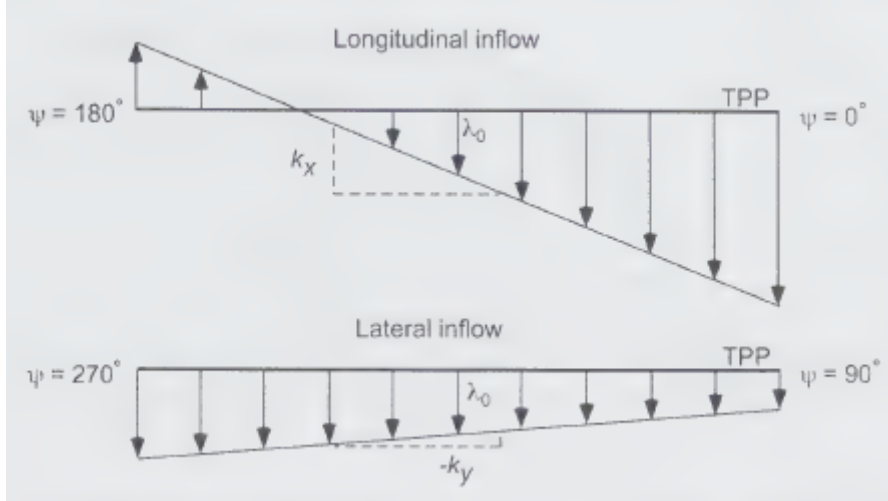


Figure 5.7: Linear inflow approximation over the rotor disc, approximating the non-linear, non-uniform physical distribution.

Using the two-dimensional blade element theory as discussed before, these two equations can be combined to result in the following form:

$$\frac{N_b}{2\pi} \left(\frac{1}{2} \rho a_0 c (\theta \bar{U}_T^2 + \bar{U}_T \bar{U}_p) dr_b d\psi \right) = 2\rho r_b \left(\mu^2 + (\lambda_i - \mu_z)^2 \right)^{1/2} \lambda_i dr_b d\psi \quad (5.25)$$

If one integrates this expression along the disc and along the blades, the expression leading to the solution for the mean uniform component of inflow is derived, as shown in Equation 5.20. When applying Equation 5.25 to the one-per-rev components of the load and inflow, a non-uniform inflow expression is found as expressed in Equation 5.26 using only the fundamental and first harmonics of the inflow (which is deemed sufficient for the analysis of flight dynamics [18]).

$$\lambda_i(\psi, r_b) = \lambda_0 + \bar{r}_b (\lambda_{1c} \cos \psi + \lambda_{1s} \sin \psi) \quad (5.26)$$

Deriving the longitudinal and lateral inflows λ_{1c} and λ_{1s} can require intensive modelling effort, as elaborated upon in Padfield [18], who restricts his analysis to the solutions for the inflows in the case of hover. Simplifications can be made by assuming a linear non-uniform distribution of the longitudinal and lateral inflow, as explained in Leishman [19]. He explains that during the transition from hover to forward flight, i.e. within the range of $0.0 \leq \mu \leq 0.1$, the non-uniformity of the inflow is strongest due to the presence of tip vortices sweeping downstream near the rotor plane. In higher speed forward flight ($\mu > 0.15$), the time (or azimuthal) averaged inflows become almost linear. This effect was first suggested by Glauert [35] from which a variation was derived, splitting the longitudinal and lateral linear inflow distributions, resulting in Equation 5.27 and depicted in Figure 5.7.

$$\lambda_l = \lambda_0 \left(1 + k_x \frac{x}{R} + k_y \frac{y}{R} \right) = \lambda_0 (1 + k_x r \cos \psi + k_y r \sin \psi) \quad (5.27)$$

Here, λ_0 represents the mean inflow at the center of the rotor disc as found by the uniform momentum theory as per Equation 5.20. Glauert's approach received various iterations, of which the one described by Drees [36] is frequently implemented [19]. Drees obtained the coefficients k_x and k_y from a variation of vortex theory, resulting in the simple expression as given by Equation 5.28. Pitt & Peters also obtained their own estimates for k_x and k_y , and are shown in Equation 5.29. Other researchers have come up with additional estimates for the two parameters, but the ones from Pitt & Peters and Drees are the most commonly used. [19]

$$k_x = \frac{4}{3} \left(\frac{1 - \cos \chi - 1.8\mu^2}{\sin \chi} \right) \quad \text{and} \quad k_y = -2\mu \quad (5.28)$$

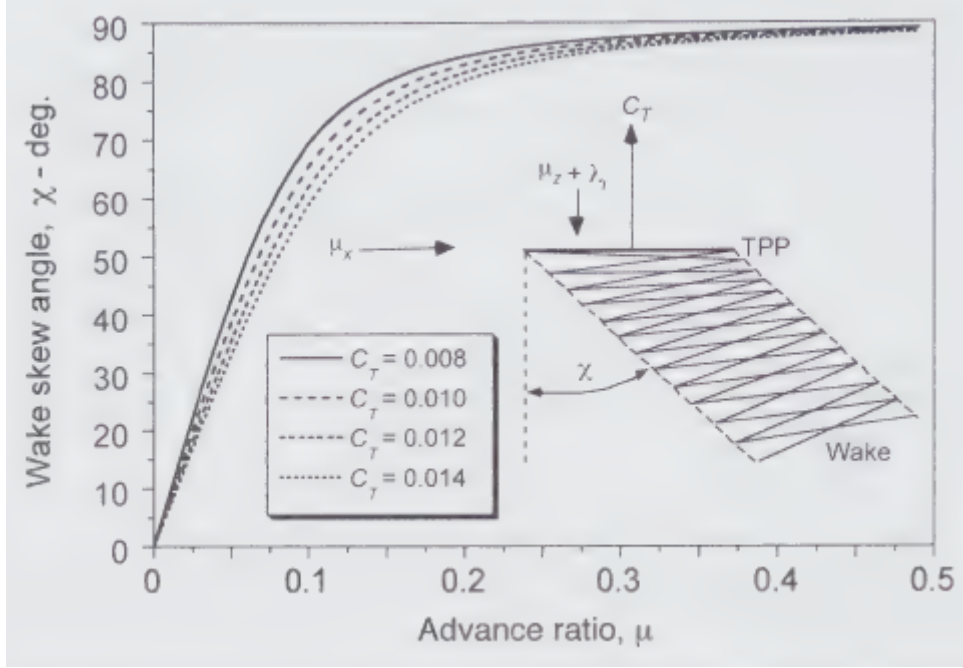


Figure 5.8: Typical rotor skew angles in function of advance ratio for various thrust coefficients. [19]

$$k_x = \frac{15\pi}{32} \tan\left(\frac{\chi}{2}\right) \quad \text{and} \quad k_y = 0\mu \quad (5.29)$$

χ is defined as the rotor wake skew angle, calculated by Equation 5.30. Here, μ_x and μ_z are the parallel and perpendicular advance ratio's respectively. Various typical rotor skew angles are plotted for several thrust coefficients for a single rotor rotorcraft in function of advance ratio in Figure 5.8, together with the graphical definitions of χ , μ_x and μ_z .

$$\chi = \tan^{-1}\left(\frac{\mu_x}{\mu_z + \lambda_i}\right) \quad (5.30)$$

Leishman [19] mentions that there are various other suggestions offered by different authors in order to estimate the values of k_x and k_y , but that those of Drees [36] and Pitt & Peters [25] offer the best results when compared to experimental evidence, at practically the same computational efficiency.

In their paper on 'An Optimum Coaxial Rotor System for Axial Flight' [30], Leishman and Ananthan developed a numerical computation scheme applying the blade element momentum theory to a coaxial rotorcraft in axial and hovering flight. They assumed a non-uniform flow field, with a azimuthal-averaged inflow over a specific annular element, as depicted in Figure 5.9.

Their model includes the effect of a contracting wake from the upper rotor, resulting in a vena contracta on the lower rotor, where the inflow is accelerated by the upper rotor. The solutions for the inflows in the upper rotor, lower rotor inside the vena contracta, and lower rotor outside the vena contracta can be calculated by equations Equation 5.31, Equation 5.32 and Equation 5.33 respectively. Leishman and Ananthan recommend using fixed-point iteration by first calculating λ using $F=1$, and then finding F from Equation 5.34 and recalculating λ from their respective formulae. Convergence is said to be rapid and achievable within 5-10 iterations. Further insights in calculating the required parameters for the aforementioned equations, and the upper and lower rotor thrust and power coefficients are described in Leishman and Ananthan [30].

$$\lambda(r, \lambda_\infty) = \sqrt{\left(\frac{\sigma_u C_{l_\alpha}}{16F} - \frac{\lambda_\infty}{2}\right)^2 + \frac{\sigma_u C_{l_\alpha}}{8F} \theta_u r} - \left(\frac{\sigma_u C_{l_\alpha}}{16F} - \frac{\lambda_\infty}{2}\right) \quad (5.31)$$

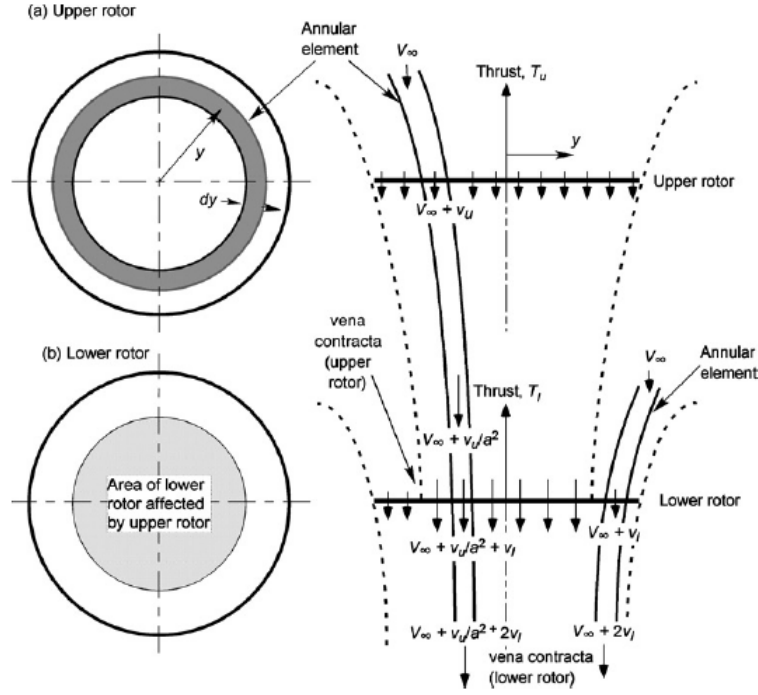


Figure 5.9: BEMT flow model used for the analysis of a coaxial rotorcraft with the lower rotor operating in the wake of the upper rotor. [30]

$$\lambda(r, \lambda_\infty) = \sqrt{\left(\frac{\sigma_l C_{l\alpha}}{16F} - \frac{\lambda_\infty + \lambda_u/a^2}{2}\right)^2 + \frac{\sigma_l C_{l\alpha}}{8F} \theta_l r} - \left(\frac{\sigma_l C_{l\alpha}}{16F} - \frac{\lambda_\infty + \lambda_u/a^2}{2}\right) \quad \text{for } r \leq a \quad (5.32)$$

$$\lambda(r, \lambda_\infty) = \sqrt{\left(\frac{\sigma_l C_{l\alpha}}{16F} - \frac{\lambda_\infty}{2}\right)^2 + \frac{\sigma_l C_{l\alpha}}{8F} \theta_l r} - \left(\frac{\sigma_l C_{l\alpha}}{16F} - \frac{\lambda_\infty}{2}\right) \quad \text{for } r > a \quad (5.33)$$

$$F = \left(\frac{2}{\pi}\right) \cos^{-1}(\exp(-f)) \quad (5.34)$$

The axial flight theory proposed by Leishman and Ananthan can be further expanded to forward flight conditions by inclusion of the skew angle and advance ratio's by means of Equation 5.27.

5.1.5. Rotor Interference Effects

Saito and Azuma [22] created a numerical approach in which they applied the local momentum theory for a coaxial rotor system in hovering and forward flight. Their wake model in forward flight disregarded the wake contraction for simplicity, an effect that is investigated further in the next subsection. They also assumed constant attenuation coefficients, which dictate how much the upper rotor wake influences the lower rotor as represented in Equation 5.35, where λ_l is the lower rotor inflow, λ_{0l} the mean lower rotor inflow, and λ_{0u} the mean upper rotor inflow. The distinction between upper and inner wake caused by the vena contracta is omitted in this equation, following the approach of Saito and Azuma [22].

$$\lambda_l = \lambda_{0l} + C_{att} \lambda_{0u} \quad (5.35)$$

The interference equation in Equation 5.35 from Saito [22] can be expanded to a coaxial rotor system, as shown in Equation 5.36 below. δ_{l2u} and δ_{u2l} are the interference from the lower and upper rotor on the upper and lower rotor respectively.

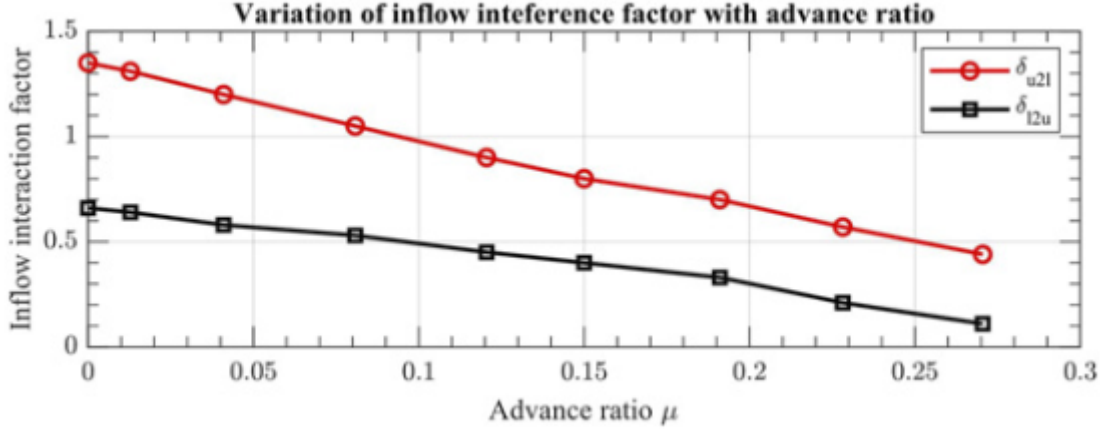


Figure 5.10: Variation of inflow interference with advance ratio from the CFD simulation results by Zhou et al. [37]

$$\begin{cases} v_{i,u}(\psi) = v'_{i,u}(\psi) + \delta_{l2u}v'_{i,l}(\psi) \\ v_{i,l}(\psi) = v'_{i,l}(\psi) + \delta_{u2l}v'_{i,u}(\psi) \end{cases} \quad (5.36)$$

If the rotors were to have no interference on each other, both δ_{l2u} and δ_{u2l} would be 0. Obviously, this is not the case, since the lower rotor is in the downwash area below the upper rotor. This means that $\delta_{l2u} < \delta_{u2l}$. As previously mentioned, various studies such as those based on Ferguson [28], assume that the wake is not yet fully developed before reaching the lower rotor, meaning the wake did not yet contract. In this case $\delta_{l2u} = 0$ and $\delta_{u2l} = 1$.

This gives rise to two discussion points concerning the interference factors:

- Concerning constant interference/attenuation factors: The use of constant attenuation coefficients across the rotor disc by Saito, was justified by three statements: (i) counter-rotating rotors will tend to have a homogeneous velocity distribution, (ii) at high advance ratio's, a constant attenuation coefficient is not improper in the single rotor, and may be similar in the co-axial rotor, and (iii) the reduced computational effort and programming simplifications will be appreciable. Saito and Azuma [22] concluded that this assumption is valid, except at low advance ratio's.
- Concerning the assumption of no wake contraction: Through their CFD simulations, Zhou et al. [37] found that δ_{l2u} and δ_{u2l} are not constantly 0 and 1, but change as a function of advance ratio.

Following the second point, a higher fidelity approach to the calculation of δ_{l2u} and δ_{u2l} is to model the interference factors as a function of advance ratio using the results from Zhou et al. [37] as depicted in Figure 10.11. A linear approximation from these results can be made, accounting for the fact that the interference goes to 0 with increasing advance ratio, resulting in Equation 5.37. This can be explained by the fact that the skew angle χ is almost 90 degrees at high advance ratio's, therefore not influencing the lower rotor at all.

$$\begin{cases} \delta_{l2u} = -2.15\mu + 0.68 & \text{for } 0 \leq \mu \leq 0.316 \\ \delta_{l2u} = 0 & \text{for } \mu > 0.316 \\ \delta_{u2l} = -3.81\mu + 1.45 & \text{for } 0 \leq \mu \leq 0.381 \\ \delta_{u2l} = 0 & \text{for } \mu > 0.381 \end{cases} \quad (5.37)$$

The attenuation coefficient can also be calculated manually in function of skew angle (i.e. advance ratio) as a function of radial and azimuthal position, as demonstrated by the analysis by Castles [38]. Castles defined the ratio of the normal component of the induced velocity to the normal component of the induced velocity at the rotor centre. As previously stated, the upper rotor can be assumed to have a uniform inflow,



which makes the normal component of the induced velocity of the upper rotor the induced velocity of the whole upper rotor; λ_{0u} . Therefore, the ratio's calculated by Castles are exactly the attenuation coefficients C_{att} needed to determine the lower rotor inflow. The attenuation coefficient C_{att} can be calculated by Equation 5.38.

$$C_{att} = \frac{1}{2\pi} \int_0^{2\pi} \frac{A - B\sqrt{C}}{\sqrt{C}(\sqrt{C} - D)} d\theta \quad (5.38)$$

With coordinate system as shown in Figure 5.11 and

$$\begin{aligned} A &= 1 + r_0 \cos(\psi - \theta) \\ B &= m \cos \theta / \sqrt{1 + m^2} \\ C &= 1 + r_0^2 + z_0^2 + 2r_0 \cos(\psi - \theta) \\ D &= (z_0 + mr_0 \cos \psi + m \cos \theta) / \sqrt{1 + m^2} \\ m &= \tan(\chi) \end{aligned} \quad (5.39)$$

5.1.6. Wake Contraction Effects

As explained in the previous subsection, wake contraction effects might impact the required fidelity of the rotor inflow model. This effect is illustrated in Figure 5.12, from which two distinct regions can be identified. The region which is not affected by the upper rotor wake only requires the induced velocity of the lower rotor. The region which is affected by the upper rotor requires the lower rotor induced velocity to be summed with the upper rotor induced velocity at the position of the lower rotor.

In order to determine whether or not wake contraction effects have to be taken into account, the wake contraction at a vertical position equal to the rotor separation of the coaxial rotorcraft is calculated using the approach formulated by Landgrebe [40] is followed. Landgrebe states that the vortex tip path can be modeled by Equation 5.40 for the z location, and Equation 5.41 for the y location for various wake azimuth angles ψ_w , also known as the wake age. \bar{z}_T and \bar{y}_T denote the x- and y-locations of the vortex tip path normalized by the rotor radius R . The contracting vortex sheet which is formed by a spinning rotor blade during hover (hence without wake skew) is depicted in Figure 5.13.

$$\bar{z}_T = \begin{cases} k_1 \psi_w & \text{for } 0 \leq \psi_w \leq \frac{2\pi}{N_b} \\ (\bar{z}_T)_{\psi_w = \frac{2\pi}{N_b}} + k_2 \left(\psi_w - \frac{2\pi}{N_b} \right) & \text{for } \psi_w \geq \frac{2\pi}{N_b} \end{cases} \quad (5.40)$$

$$\bar{y}_T = A + (1 - A) \exp(-\Lambda \psi_w) \quad (5.41)$$

N_b denotes the number of blades on one rotor, A and Λ both denote empirical coefficients which are found using Equation 5.42. The coefficients k_1 and k_2 are found using Equation 5.43. In these equations, C_T is the thrust coefficient of one rotor, σ is the rotor solidity, and θ_{1deg} is the linear twist angle of the blade in degrees. k_2 should only be taken into account if $(\bar{z}_T)_{\psi_w = \frac{2\pi}{N_b}} < \bar{z}_T$, of which the latter is simply taken to equal the normalized axial spacing between the rotorcraft, i.e. H/R where H is the rotor spacing and R the rotor radius.

$$\begin{aligned} A &= 0.78 \\ \Lambda &= 0.145 + 27C_T \end{aligned} \quad (5.42)$$

$$\begin{aligned} k_1 &= -0.25 (C_T / \sigma + 0.001 \theta_{1deg}) \\ k_2 &= - (1.41 + 0.0141 \theta_{1deg}) \sqrt{C_T / 2} \end{aligned} \quad (5.43)$$

The wake age ψ_w at the location of the lower rotor, i.e. $\bar{z}_T = H/R$, can be calculated by rearranging Equation 5.40, resulting in Equation 5.44. Using this value for ψ_w , \bar{y}_T can be calculated using Equation 5.41.

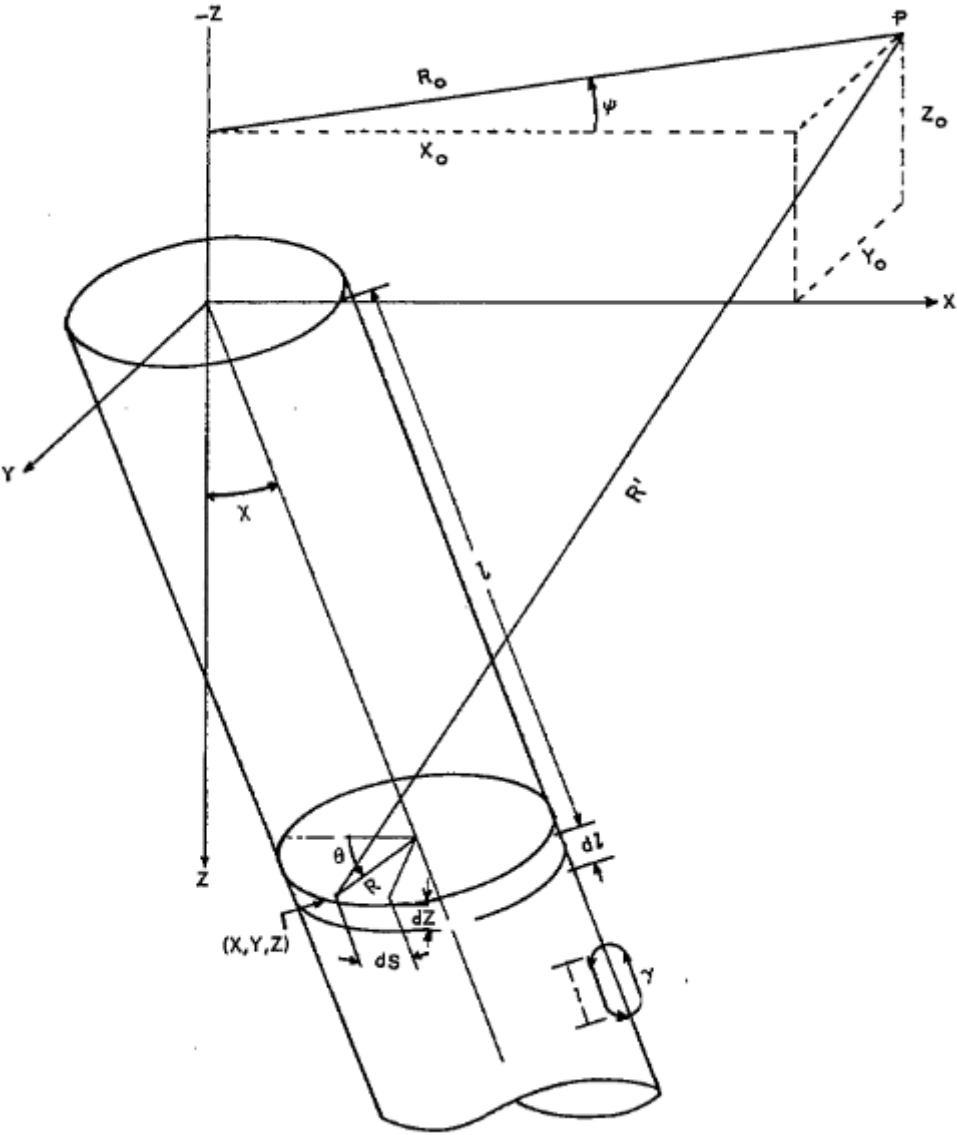


Figure 5.11: Wake vortex geometry as used in Castles. [38]

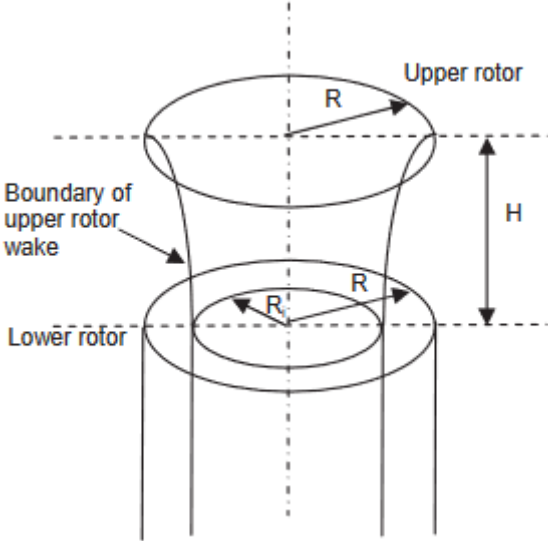


Figure 5.12: Wake contraction of the upper rotor, and its influence on the lower rotor. [39]

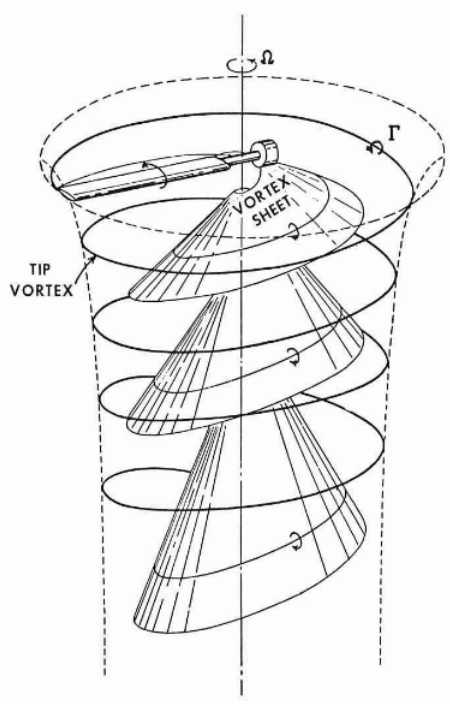


Figure 5.13: Visualisation of the rotor wake structure during hover. [40]



Depending on this value, the wake contraction should be taken into account or not. For the ABC coaxial rotor of the XH-59A, this value is found to be 0.873, which means only 87.3% of the radius of the lower rotor is affected by the upper rotor at the location of the lower rotor. This means that only 76% of the lower rotor radius is influenced by the upper rotor, which is quite significant. Hence, it can be concluded that for an ABC type rotorcraft such as the XH-59A, wake contraction effects could be taken into account. For simplicity, it is assumed that the wake contraction does not vary with forward speed. In reality however, the wake contraction decreases with forward speed [19], hence the upper rotor influences the lower rotor slightly more as a result.

$$\psi_w = \frac{\bar{z}_T - (\bar{z}_T)_{\psi_w=2\pi/N_b} + k_2 \frac{2\pi}{N_b}}{k_2} \quad (5.44)$$

5.1.7. Blade Dynamics Modelling

The last part essential in any rotor modelling, including that of a coaxial rotor, are the blade dynamics. In this study, only the flapping motion of the blade is taken into account. Various studies, such as that by Yuan [41], Ferguson [28], and Yuqing [26], assumed that the lead-lag motion of the blade is negligible. Yuan and Thomson explained that due to the high rigidity of the ABC rotor system, which decreases the flapping motion of the blades and thus decreases the Coriolis force provided by this flapping motion, visualised in Figure 5.14. Due to this decreased Coriolis force, the relative amplitude of the lead-lag motion also decreases, and is said to contribute little to the overall flight dynamic characteristics of the coaxial helicopter.

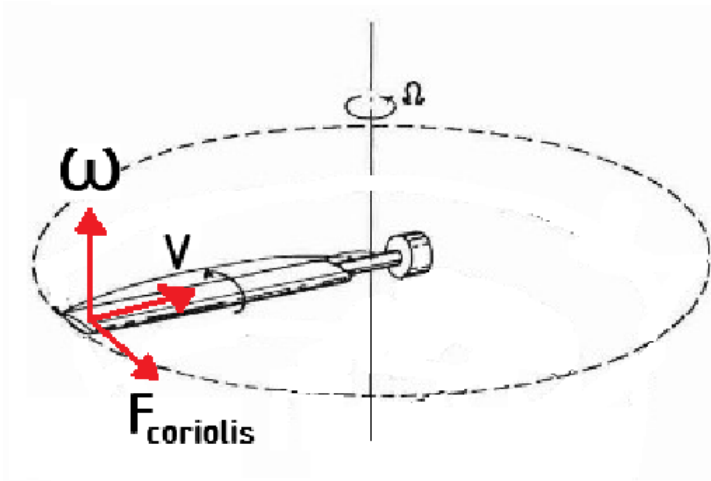


Figure 5.14: Coriolis force visualisation on a rotor blade during flapping motion.

The stiff rotors of the ABC can be modeled by means of an equivalent model, depicted in Figure 10.6, which uses an infinitely stiff blade with hinge offset and spring. Both Yuan [41] and Yuqing [26] used the same model.

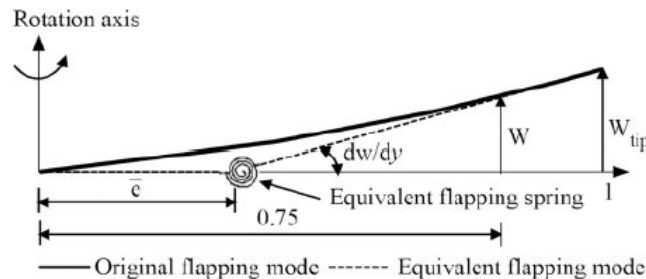


Figure 5.15: Equivalent blade flapping model. [26]



Assuming the flapping motion can be represented by means of a Fourier series, as represented in Equation 5.45, for both the upper and lower rotor. Three factors can be distinguished: the coning angle a_0 , and the longitudinal and lateral flapping angles, denoted by a_1 and b_1 respectively. The calculation of these factors is not yet covered in this literature study, but can be found in literature.

$$\begin{aligned}\beta_u(\psi) &= a_{0u} - a_{1u} \cos(\psi) - b_{1u} \sin(\psi) \\ \beta_l(\psi) &= a_{0l} - a_{1l} \cos(\psi) - b_{1l} \sin(\psi)\end{aligned}\quad (5.45)$$

In the equivalent blade model, \bar{e} equals the flapping hinge offset, which is calculated using Equation 5.46. Here, W_{tip} is the blade tip deflection, $W'_{0.75}$ the blade deflection at 75% blade radius, and R the blade radius.

$$\bar{e} = 1 - \frac{W_{tip}}{R \cdot W'_{0.75}} \quad (5.46)$$

The blade flapping frequency can be calculated by means of Equation 10.15 [26], where ω_n is the flapping frequency, M_β the mass moment of the blade, I_β the inertia of the blade, K_β the equivalent spring stiffness. β the flapping angle, and Ω the rotor rotational speed.

$$\omega_n = \sqrt{1 + \frac{\bar{e}M_\beta}{I_\beta} + \frac{K_\beta}{I_\beta\Omega^2}} \cdot \Omega \quad (5.47)$$

The equivalent spring stiffness K_β can be calculated using [41]

$$K_\beta = \left(\bar{\omega}_n^2 - 1 - \frac{\bar{e}RM_\beta}{I_\beta} \right) I_\beta \Omega^2 \quad (5.48)$$

The second order differential equation, representing the blade flapping motion according to the equivalence method is then represented by

$$\ddot{\beta} + (1 + \bar{e}RM_\beta/I_\beta) \dot{\beta} + K_{10}\beta/I_\beta\Omega^2 + M_A = 0 \quad (5.49)$$

where M_A represents the summation of the aerodynamic, Coriolis, inertia and gravity moments.

The feathering motion of the blade, also known as the pitch motion, is influenced by two factors: the control inputs of the rotorcraft, and the predetermined twist in the rotor blades. In an articulated rotor, the control phase angle Γ is almost 90 degrees. This results in a well defined separation between the longitudinal and lateral cyclic inputs on the longitudinal and lateral pitch angles. However, as discussed in the ABC subsection, the control phase angle for a rigid rotor such as the ABC is much lower, typically in the range of 40-60 degrees. This results in Equation 5.50 describing the feathering motion of the upper and lower rotor respectively.

$$\begin{aligned}\theta_u(y, \psi, \Gamma) &= (\theta_0 + \theta_d) + (\theta_{1c} + \Delta\theta_{1c}) \cos(\psi_u - \Gamma) + (\theta_{1s} + \Delta\theta_{1s}) \sin(\psi_u - \Gamma) + \frac{\theta_{twisty}}{R} \\ \theta_l(y, \psi, \Gamma) &= (\theta_0 - \theta_d) - (\theta_{1c} - \Delta\theta_{1c}) \cos(\psi_l - \Gamma) + (\theta_{1s} - \Delta\theta_{1s}) \sin(\psi_l - \Gamma) + \frac{\theta_{twisty}}{R}\end{aligned}\quad (5.50)$$

The following differences between the two equations can be elaborated:

- The differential collective θ_d , differential lateral cyclic θ_{1c} , and differential longitudinal cyclic θ_{1s} are defined to be applied positively in the upper rotor, and negatively in the lower rotor. This is essential since an equal sign would result in a net zero collective difference.
- The effect of the phase angle is taken into account by subtracting it from the azimuth angle, which dictates at what azimuthal position the force is applied, controlling the point of maximum control deflection due to gyroscopic precession.

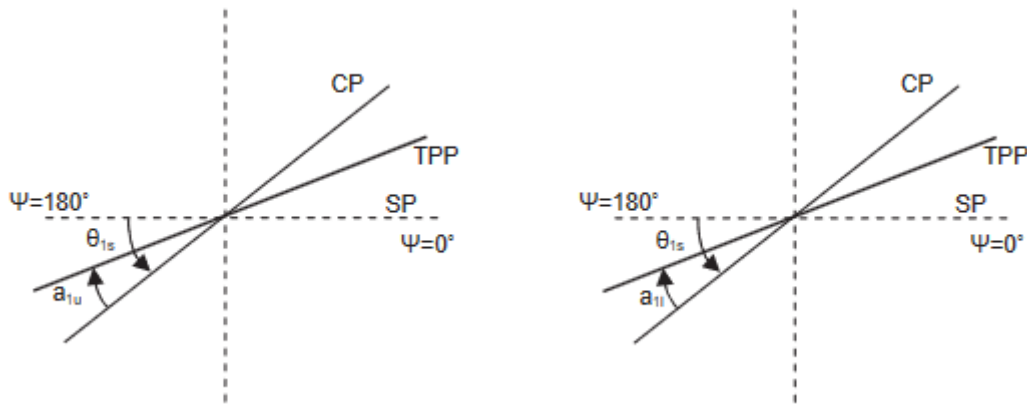


Figure 5.16: Flapping and feathering motions in the longitudinal plane for the upper (left) and lower (right) rotor. [39]

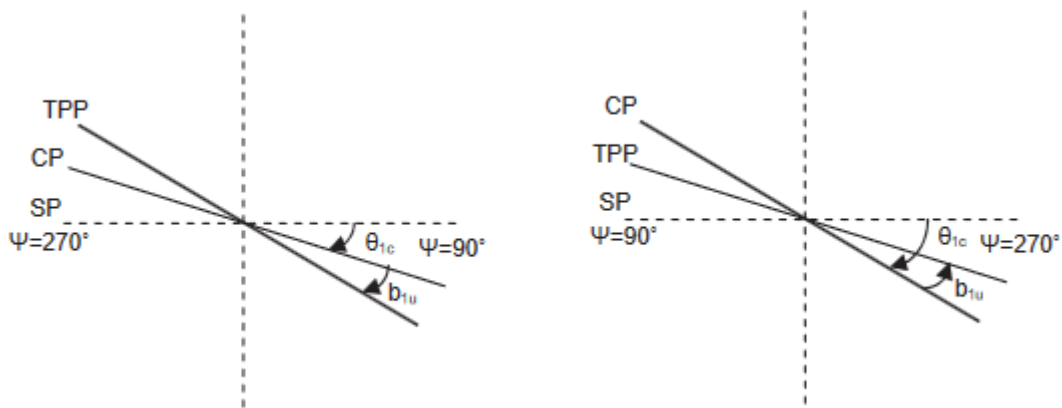


Figure 5.17: Flapping and feathering motions in the lateral plane for the upper (left) and lower (right) rotor. [39]

- The sign for the lateral cyclic pitch is multiplied by -1 for the lower rotor. This is due to the fact that by controlling the lateral cyclic, the pilot in fact controls the roll angle at $\psi = 90 \pm \Gamma$. If the sign for the upper and lower rotor would be the same, a positive applied lateral cyclic pitch would result in a lateral left tilt in the upper rotor, and a lateral right tilt in the lower rotor. This can be visualized in Figure 4.7 in Chapter 4. Since this would result in a net zero tilt, essentially making the aircraft uncontrollable in roll, the lateral tilt direction is matched by multiplying the lateral cyclic input of the lower rotor by -1 . Note that the lateral cyclic pitch of both the upper and lower rotor in a rigid rotor with Γ other than 90 degrees also result in longitudinal components, however, these are cancelled out when multiplying by -1 .
- A similar analogy can be followed for the longitudinal cyclic pitch. This time however, the pitch angle of the helicopter is controlled by the pilot at the angles $\psi = 180 \pm \Gamma$. As can be visualized on Figure 4.7, a positive pitch input would result in a backward tilt of the rotor disk for the upper rotor, but now also results in a backward tilt for the lower rotor. Therefore, the longitudinal cyclic input is not multiplied by -1 . Note that a lateral control input is also commanded by a pitch input in a rigid rotor. However, as with the previous point, these are cancelled out between the upper and lower rotor.

The total cyclic motion of the upper and lower rotor rotors is depicted in Figure 5.16 and Figure 5.17 for the longitudinal and lateral plane respectively. The motion consists of the blade flapping motion, represented by the longitudinal and lateral flapping coefficients a_1 and b_1 , and the feathering motion, represented by the longitudinal and lateral cyclic θ_{1s} and θ_{1c} .



5.2. Pusher Propeller Modelling

The tail pusher propeller featured in a compound coaxial helicopter such as the XH-59A or X2TD provides the rotorcraft with extra thrust during high-speed flight to reach higher speeds while offloading the main rotors and to overcome fuselage drag.

Flapping dynamics of the propeller blades is often neglected due to the stiff blades, and the high rotational speed (in the range of 2000-2500rpm [13]) [26]. Therefore, the only factor controlling the blade incidence relative to the airflow is the propeller collective pitch θ_p . The thrust dT_p and torque dQ_p per blade element can be calculated as per Equation 5.51 using the blade element theory. Details on the aerodynamic model including propeller kinematics, forces and moments and coordinate transformations can be found in Ferguson [28].

$$\begin{aligned}dT_p &= l_p \cos \phi_{ip} - d_p \sin \phi_{ip} \\dQ_p &= (l_p \sin \phi_{ip} + d_p \cos \phi_{ip}) r_p\end{aligned}\quad (5.51)$$

Here, ϕ_{ip} denotes the propeller inflow angle, r_p the radial position of the blade element, and l_p and d_p the lift and drag forces per unit span of each blade element respectively. The resulting propeller force $\mathbf{F}_p = [X_p, 0, 0]^T$ and moment $\mathbf{\Sigma}_p = [L_p, 0, 0]^T$ in the body frame can be obtained by coordinate transformation. [26] The blade element lift and drag per unit span can be obtained via the familiar form of Equation 5.52, from which the lift and drag coefficients can be found in look-up-tables. [13] The propeller angle of attack is found using Equation 5.53, where $\tan^{-1} \frac{v_n}{v_{tan}}$ equals the inflow angle ϕ_i . Generally, the propeller has significant twist (in the range of -30deg) so that each blade element operates at an efficient angle of attack, similar to propeller fixed wing aircraft. The definitions of all angles and velocities are shown in Figure 5.18 where the subscript *p.bl.* denotes the propeller blade element reference frame.

$$\begin{aligned}\bar{l} &= \frac{1}{2} \rho v_{res}^2 c_l C_l(\alpha, M) \\ \bar{d} &= \frac{1}{2} \rho v_{res}^2 c_d C_d(\alpha, M)\end{aligned}\quad (5.52)$$

$$\alpha = \theta_p + \tan^{-1} \left(\frac{v_n}{v_{tan}} \right) + \theta_{twist} \left(\frac{r_i}{R_{prop}} \right)\quad (5.53)$$

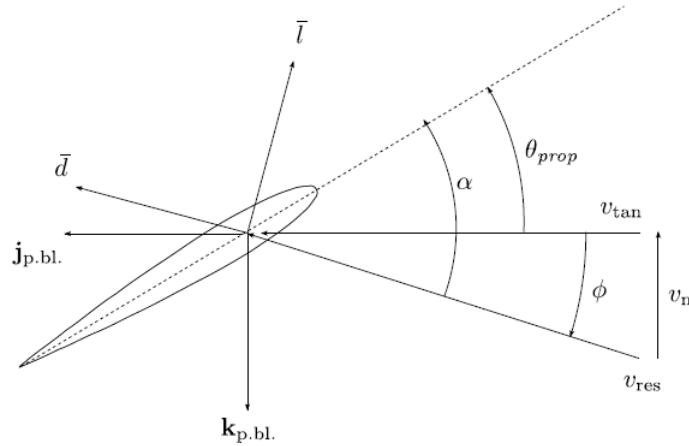


Figure 5.18: Propeller angles and velocities in the propeller blade element reference frame. [28]

5.3. Fuselage Modelling

The fuselage constitutes a significant part of the drag, especially at high speeds, and affects the dynamic performance of the rotorcraft. The fuselage drag forces in the body frame $\mathbf{F}_p = [X_f, Y_f, Z_f]^T$ are calculated using Equation 5.54.



$$\begin{aligned}
X_f &= -\frac{1}{2}\rho V^2 f \cos(\alpha_{fus}) \cos(\beta_{Ls}) \\
Y_f &= -\frac{1}{2}\rho V^2 f \sin(\beta_{fus}) \\
Z_f &= -\frac{1}{2}\rho V^2 f \sin(\alpha_{fus})
\end{aligned} \tag{5.54}$$

f denotes the equivalent flat plate area, which is the frontal area of a flat plate with a drag coefficient equal to that of the fuselage that has to be estimated. The equivalent flat plate area can be estimated by using wind tunnel test data look-up tables from other helicopters, such as the CH-47 tandem helicopter as in [39]. The angle of attack α_f and sideslip β_f of the fuselage are given by Equation 5.55. [18]

$$\begin{aligned}
\alpha_f &= \tan^{-1}(w/u) \\
\beta_f &= \tan^{-1}(v/u)
\end{aligned} \tag{5.55}$$

The moment calculation and transformation matrices to the aerodynamic reference frame are detailed in Yuqing Qiu [26]. Assuming that the only offset between the aerodynamic center (aerodynamic frame) and centre of gravity (body frame) is the vertical distance, reduces the body frame moment of the fuselage to a single component around the y-axis.

5.4. Empennage Modelling

Lastly, the horizontal stabilizer, vertical stabilizer, elevator and rudder are modelled using conventional strip theory for which the details covered Yuan [42] and Ferguson [28]. The theory incorporates a simple 2D representation of the wing surfaces, for which the lift and drag coefficients can be obtained from 2D airfoil aerodynamic look-up tables, such as the wind-tunnel data on the XH-59A [43] based on α_h , β_h , and δ_e for the horizontal stabilizer including the effects of the elevator, and α_v , β_v , and δ_r for the vertical stabilizer including the effects of the rudder.

The horizontal tail forces $\mathbf{F}_h = [X_h, Y_h, Z_h]^T$, and moments $\mathbf{\Sigma}_h = [L_h, M_h, N_h]^T$ are calculated using Equation 5.56 and Equation 5.57. The vertical tail forces $\mathbf{F}_v = [X_v, Y_v, Z_v]^T$, and moments $\mathbf{\Sigma}_v = [L_v, M_v, N_v]^T$ are calculated using Equation 5.58 and Equation 5.59. [41]

$$\begin{bmatrix} X_h \\ Y_h \\ Z_h \end{bmatrix} = \begin{bmatrix} \cos \beta_h \cos \alpha_h & -\sin \beta_h \cos \alpha_h & -\sin \alpha_h \\ \sin \beta_h & \cos \beta_h & 0 \\ \cos \beta_h \sin \alpha_h & -\sin \beta_h \sin \alpha_h & \cos \alpha_h \end{bmatrix} \bullet \begin{bmatrix} -q_h S_h C_{D,h} \\ 0 \\ -q_h S_h C_{L,h} \end{bmatrix} \tag{5.56}$$

$$\begin{bmatrix} L_h \\ M_h \\ N_h \end{bmatrix} = \begin{bmatrix} y_h Z_h - z_h Y_h \\ z_h X_h - x_h Z_h \\ x_h Y_h - y_h X_h \end{bmatrix} \tag{5.57}$$

$$\begin{bmatrix} X_v \\ Y_v \\ Z_v \end{bmatrix} = \begin{bmatrix} \cos \beta_v \cos \alpha_v & -\sin \alpha_v & -\sin \beta_v \cos \alpha_v \\ \cos \beta_v \sin \alpha_v & \cos \alpha_v & -\sin \beta_v \sin \alpha_v \\ \sin \beta_v & 0 & \cos \beta_v \end{bmatrix} \bullet \begin{bmatrix} -q_v S_v C_{D,v} \\ -q_v S_v C_{L,v} \\ 0 \end{bmatrix} \tag{5.58}$$

$$\begin{bmatrix} L_v \\ M_v \\ N_v \end{bmatrix} = \begin{bmatrix} y_v Z_v - z_v Y_v \\ z_v X_v - x_v Z_v \\ x_v Y_v - y_v X_v \end{bmatrix} \tag{5.59}$$

where q equals the dynamic pressure, calculated using:

$$q = \frac{1}{2}\rho V^2 \tag{5.60}$$

Control System Strategies in a Compound Coaxial Rotorcraft

This chapter aims to provide an overview on the existing control strategies, their practical engineering implementation and theoretical development. Firstly, a brief overview of the need for advanced control systems in rotorcraft is discussed in Section 6.1, followed the discussion on classical control techniques such as PID and Explicit Model Following (EMF) and the use of gain scheduling in Section 6.2. In Section 6.3, a brief overview is given on modern control methods such as H_∞ optimal control, (I)NDI, and various others.

6.1. Challenges of Compound Rotorcraft FCS Design

As discussed in Chapter 4, early helicopters were primarily controlled through mechanical linkages. Throughout time, advancements on the control systems were made in order to decrease pilot workload, improve handling qualities, increase flight safety and flight efficiency. The first enhancement of the control system was the implementation of analog electronic feedback. As electronics and computational techniques and power developed, more advanced digital systems started to replace the analog feedback. These digital systems had increased flexibility, reduced power consumption and could provide more complex task support. [44] The most recent development of flight control systems is digital Fly-By-Wire (FBW) control and has been adopted in many modern rotorcraft such as the JUH-60A, AH-64D, CH-47B, RAH-66, NH-90, Raider X, etc. [44]

With the increased capabilities of flight control systems, and improvement of helicopter multirole capability, requirements have gone up as well. New flight control systems are often expected to execute multitasks in adverse flying conditions. In order to meet these expectations, more advanced control methodologies (specifically designed for aviation control, or from other fields) are developed, which in turn provides a direct contribution to helicopter simulation, advancing practically implementable control laws. It can be concluded that a highly reliable control methodology greatly improves helicopter stability and control, improving handling qualities and safety throughout the flight envelope, although a reliable controller is not necessarily a complex controller.

Helicopters are, by nature, highly nonlinear, coupled, and time-varying dynamic systems, which makes the design of helicopter flight control systems difficult due to the following reasons [44]:

1. **Complicated Dynamic Response.** The highly-coupled nature of the helicopter dynamics increase FCS design complexity due to one control input not only affecting the state variables, but also leading to secondary, and sometimes even tertiary system responses. The nonlinearity of the helicopter system is also non-affine with control inputs, which can lead to unwanted controller responses.
2. **Multiple Flight Modes.** Due to the requirement in ADS-33E of military helicopters having to be capable of achieving different flight modes, the controller design becomes more complex. The different flight modes could be attitude command attitude hold (ACAH), rate command (RC), or translational rate command (TRC). The controller design is especially challenging due to the transitional period between the various flight modes, which can lead to unsmooth transitions and/or controller saturation.
3. **System Uncertainties.** The controller becomes less accurate due to the inherent modelling uncertainties compared to real life flight physics. Model uncertainties such as in the rotor dynamics, and high



frequency dynamics associated with actuators make the controller less accurate. Other effects such as ground effect, near ground wind gusts and atmospheric turbulence also impact controller efficiency.

4. Rapidly Varying Flight Conditions. Due to the inherent flexibility of flight manoeuvring and flight mode transitions of a helicopter within the envelope, the flight parameters and dynamic states undergo intensive change. Conventional linear controllers are not able to stabilize the helicopter throughout certain flight regimes.
5. Control Redundancy. The added actuators in a compound coaxial helicopters add the extra challenge of control redundancy. The controller should be amended with extra laws and allocation schemes in order to efficiently take use of these extra control actuators, while taking into account physical actuator rate and deflection constraints.

Compounding of a helicopter results in various challenges and opportunities. Due to the inherent redundancy of controls, the controls have to be allocated, which is elaborated upon in Chapter 7. However, these redundant controls also enable the control system engineers to tailor the distribution of control actuator usage for specific goals. This could be improving flight efficiency, expand the flight envelope, decrease the loading on the main rotor(s), etc.

6.2. Classical Control Techniques

In this section, two classical controllers are discussed: PID control and Explicit Model Following (EMF) control. This is followed by a discussion on gain scheduling.

6.2.1. PID Feedback Control

PID based feedback control is a linear controller which is often used in primary flight control law design due to its easiness of realization and application. The structure of the classical PID controller is depicted in Figure 6.1. In this figure, K_P denotes the proportional gain, which is directly proportional to the error of the reference ($r(t)$) and the output ($f(t)$) signal. K_I denotes the integral gain, which is proportional to the integral of the error. Lastly, K_D denotes the differential gain, proportional to the derivative of the error with respect to time.

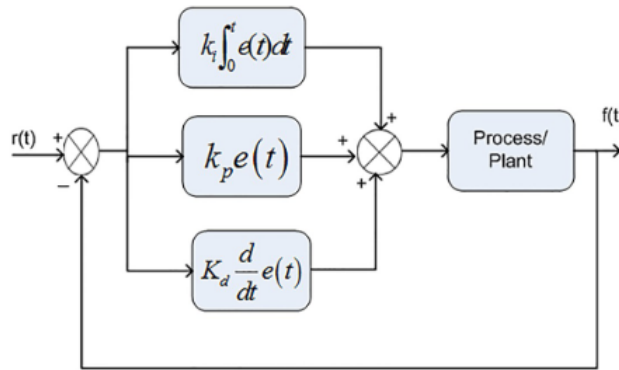


Figure 6.1: Structure of a PID controller. [45]

An application of a PID architecture in outer loop autopilot control of a compound coaxial helicopter can be found in Qiu [26], as shown in Figure 6.2. In this controller structure, the reference trajectory of the outer loop is the longitudinal, lateral and vertical velocities $[V_{xcmd}, V_{ycmd}, V_{zcmd}]^T$. The outer loop autopilot tries to track the ground velocity commands and calculate the desired pitch and roll angles for the inner loop (SAS) to use. Define the measured velocities as the controlled states as V_x , V_y and V_z , resulting in the outer loop virtual PID control law $\nu_{out} = [\nu_x, \nu_y, \nu_z]^T$ as defined in:



$$\begin{aligned}
 v_x &= K_P^x (V_{xc} - V_x) + K_I^x \int (V_{xc} - V_x) dt \\
 v_y &= K_P^y (V_{yc} - V_y) + K_I^y \int (V_{yc} - V_y) dt \\
 v_z &= K_P^z (V_{zc} - V_z) + K_I^z \int (V_{zc} - V_z) dt
 \end{aligned} \tag{6.1}$$

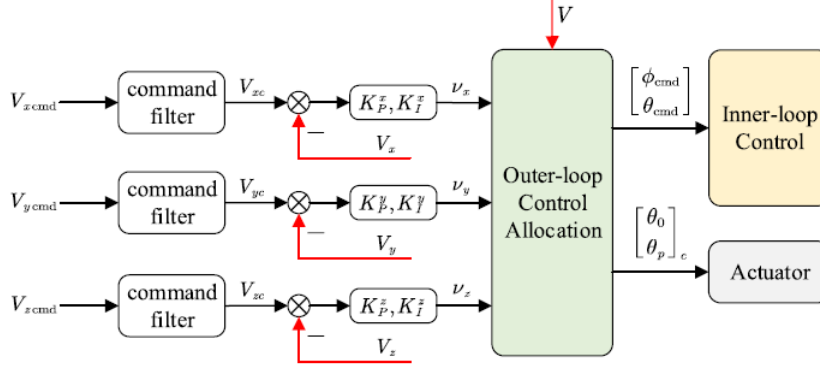


Figure 6.2: Outer loop PID control architecture for a compound coaxial helicopter.

where V_{xc} , V_{yc} and V_{zc} are command-filtered reference values according to a specific second-order transfer function, as described in [26]. In his paper, Yuqing shows the results for the PID controller as depicted in Figure 6.2, from which it can be concluded that the PID controller shows adequate but not ideal results. This is due to the limited operation range of PID control. When applying it to multivariable, time-varying and highly coupled helicopter dynamics, it falls short. This is due to neglecting high frequency characteristics and disturbance rejections. [44]

6.2.2. Explicit Model Following Control

Explicit model following, commonly referred to as EMF, is a widely adopted control architecture used in designing helicopter flight control systems. It offers good command tracking and decoupling properties. [44] In general, an EMF architecture has three distinct features, depicted in Figure 6.3: a command model, an inverse plant, and feedback compensation. The command model transforms pilot inputs to desired attitudes, from which the attitude sensor data is provided by gyros. The inverse plant serves to cancel internal helicopter dynamics, and the feedback compensation serves to provide dynamic stabilization and disturbance rejection. In general EMF provides excellent command tracking and control input decoupling, which is highly appreciable in helicopter flight control. However, the inverse plant is often linear, of low order and invariant with flight conditions. Therefore, the architecture is unable to cancel high-frequency dynamics such as those produced by the main-rotor and actuators. To combat this issue, either high-frequency dynamics can be incorporated in the FCS directly, or by including command delays τ_{cmd} which account for the high-frequency dynamics. Command delay values typically are in the range of $\tau_{cmd} = 0.04 - 0.14s$. [46] Specific values are given in Berger. [47]

An implementation of an EMF scheme on a compound coaxial helicopter is shown in Figure 6.4 from Yuqing [26]. Analogous to Figure 6.3, $M_\phi(s)$, $M_\theta(s)$, and $M_r(s)$ denote the command models, $\frac{\phi}{\delta_{lat}}$, $\frac{\theta}{\delta_{lon}}$, and $\frac{r}{\delta_{ped}}$ the inverse models, and the gains K the PI gains for feedback. The command delays are accounted for by the term $e^{-\tau s}$ where the time delay τ is different for every axis as described above. Apart from the normal EMF scheme, this control architecture also takes into account control allocation, and Pseudo-Control Hedging (PCH) by means of the α_{PCH} terms being fed into the command models.

The state results for the implemented EMF control architecture for the example in Yuqing [26] are depicted and compared to the PID results in Figure 6.5. It can be seen that the EMF improves command tracking performance, despite the lack of high-frequency dynamics inclusion.

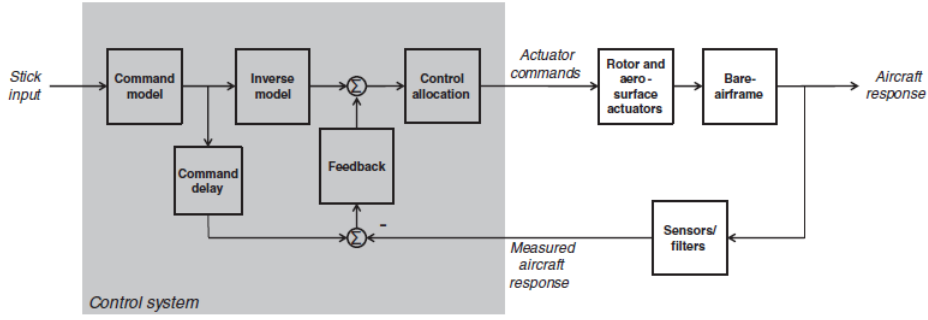


Figure 6.3: Top level control architecture for an EMF control system.

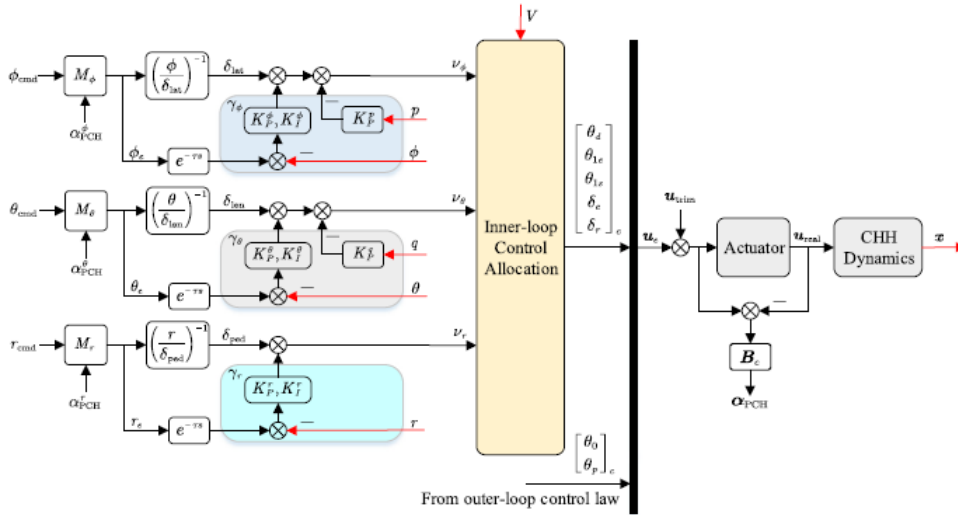


Figure 6.4: Inner loop control law architecture using EMF for a compound coaxial helicopter. [26]

6.2.3. Gain Scheduling

As stated before, the design of helicopter FCS features high nonlinearities and shows different behaviour throughout the wide flight envelope, resulting in a nonuniform desired controller. Therefore, the discrete operating-point-parameters at a certain position in the flight envelope are required to be optimal in order to keep the dynamic response as desired, at and around the operating point.

In order to cope with the nonlinear process over the entire flight regime of a helicopter, the gain-scheduling policy is introduced. Herein, the flight envelope is gridded into several operating points, for which a linear controller such as a PID or EMF controller is tuned at each region. Hence, the system must be linearized at each of these operating points, and an interpolation algorithm, such as a TS-Fuzzy scheme as used in Yuqing [26], is used such that a smooth transition between operating points can be achieved.

The tuning of these controllers can be a work-intensive endeavour if done manually, since each operating point has to be tuned for desired handling quality criteria for a specific flight condition (speed, altitude, dynamic pressure, etc.). Therefore, specific engineering tools that automate this process such as CONDUIT (discussed in Chapter 8) are developed. These tools automatically tune the controller after the user specifies the desired handling qualities.

6.3. Modern Control Techniques

In this section, a brief discussion on modern and intelligent control systems is given. Because these control methods are beyond the scope of the thesis due to time limitations, only their most important characteristics are covered. A possible expansion on the thesis could therefore be the implementation of a more advanced and modern control system. Firstly, H_∞ optimal control and INDI control is discussed. These two modern control techniques have been thoroughly tested and INDI is even implemented in the F-35 control system.

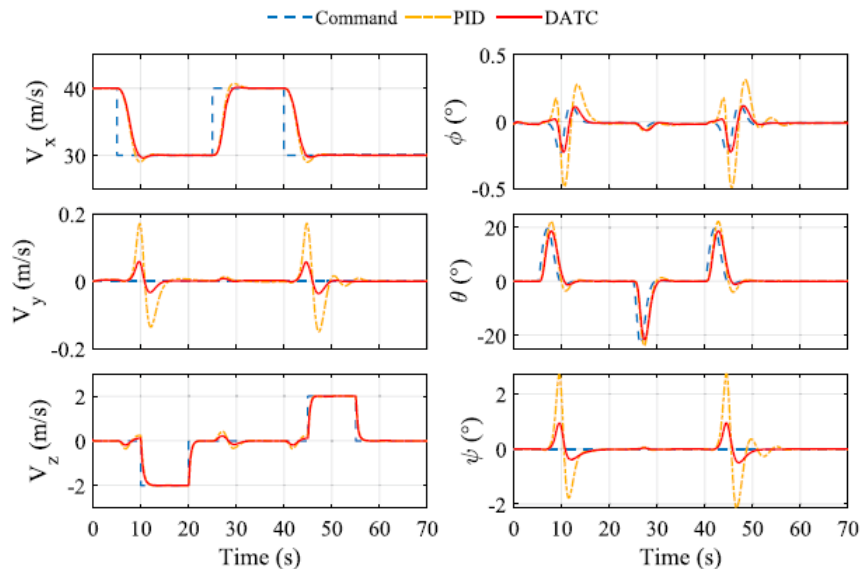


Figure 6.5: State results in a compound coaxial helicopter during a bob-down manoeuvre using a PID or DATC controller architecture. [26]

This is followed by a brief discussion on other control techniques (still under development or in early stages of implementation) and a brief word on intelligent control systems.

6.3.1. H_∞ Optimal Control

H_∞ optimal control is designed to minimize the infinity norm of weighted transfer function in order to achieve appropriate frequency response characteristics, commonly referred to as loop shaping. The H_∞ controller is mainly known for its great robustness properties. However, it could be said that the H_∞ in of itself is too conservative of a controller due to several reasons. Firstly, the controller generates slow responses, especially in yaw. Secondly, interaxis coupling was a problem, especially pitch-yaw and heave-yaw coupling. Lastly, large undershoot in acceleration responses can be found in non-minimum phase regions of the dynamic system (the helicopter). Therefore, H_2 control is often combined with H_∞ control. H_2 enjoys the benefits of a good dynamic response, but with reduced robustness. A mixed H_2/H_∞ controller combines the advantages of both worlds, and has been applied in several studies and real air vehicles [44]. Because H_∞ and H_2/H_∞ still are linear-model-based controllers, significant effort still has to be put in gain-scheduling, linear model interpolation and model switches. Even after these efforts, the linear assumption still assumes that the deviations from the nominal condition are small, which might not always be the case, resulting in degraded controller responses. Therefore, a closer look to nonlinear controllers should be taken.

6.3.2. INDI Control

Nonlinear controller designs provide a great contribution to helicopter flight control due to their innate ability to use a nonlinear model, without the need of linearization and interpolation. However, their applicability in real applications is still a challenge due to the increased order and nonlinear structure of the controller [44].

During a cooperative endeavour to improve the handling qualities of the Apache AH-64D Longbow, TU Delft and Boeing Mesa underwent a joint adventure and developed an INDI control scheme which succeeded in exactly that, successfully testing the control approach in the SIMONA research simulator. They concluded that the strength of the INDI based approach is the omission of the need of a detailed helicopter model, as the INDI architecture only requires control effectiveness parameters and estimates of the real-time helicopter accelerations. [48]

The drawback of an INDI approach however, is the sensitivity to measurement and actuator delays, which demands additional model parameter estimations and control effectiveness tuning. This in turn requires the design of additional compensators and filters. Full order observers can also be integrated, however, this



may degrade stability robustness properties of the controller. These technical concerns bring difficulties to the implementation of INDI controllers. Nonetheless, while practically complex controllers, they show promising results in e.g. the F-35.

6.3.3. Other Modern Control Strategies

Apart from the previously mentioned modern control methods, many more exist. However, these methods are less widely incorporated in practice, or have only seen academic usage. Most common methods are listed and shortly discussed, in Table 6.1, coming directly from [44]. Apart from these methods, the use of intelligent control systems is also interesting. These have seen an increase in usage in especially drones. However, due to the low technology readiness level of these techniques, they have not yet been implemented in practice. Two major intelligent control techniques are those based on fuzzy control and artificial neural networks.

**Table 6.1:** Modern Control Strategies. [44]

Control Strategies	Advantages	Disadvantages
LQR/LQG Control	Guaranteed stability margins for state feedback LQR Good transient response and disturbance rejection	Full state feedback requires significant use of sensors Kalman filters degrades frequency domain properties
Eigenstructure Assignment Control	Close-loop performance index can be designed directly Relatively simple to implement without higher order dynamic compensators	Analytical linear plant is required Stability and robustness is not guaranteed Dynamic cross-coupling between inputs and outputs cannot be cancelled
Adaptive Control	Control gains can be adjusted automatically using an on-line adaptation Robustness is achieved within bounded system uncertainties Regulated output dynamics are allowed to be non-minimum phase	Parameter drift is caused by process noise High frequency flexible modes are difficult to control Large rates of adaption are practically non-realizable
LPV Control	Nonlinear natures of the planet are captured accurately using LPV modelling Controller robustness is improved over conventional gain-scheduled controllers	The complexity is significantly increased System uncertainties caused by rapid varying flight parameters cannot be completely eliminated
Sliding Mode Control	Different control laws can be adopted corresponding to the changes of system trajectories Controller performance is insensitive to modelling errors and parameter uncertainties	Chattering is induced by frequent controller switches Highly nonlinear sliding mode surface results in difficulties of analysing system stability and reachability
Backstepping Control	The exponential stability of dynamic errors guarantees asymptotic tracking of the desired command	Calculating the derivative of pseudo-control inputs results in very large computational efforts
MPC	External constraints are incorporated into the design process naturally Improved transient response is achieved using prediction models	Close-loop property depends on the performance of reference model On-line optimization is time-consuming

Control Allocation of a Compound Coaxial Rotorcraft

In a compound coaxial helicopter, there are more actuators than controlled degrees of freedom. This brings forth the need of control allocation, and is discussed in this chapter. Various control allocation techniques, such as the pseudo-inverse and weighted-pseudo-inverse, cascaded generalized inverse, and incremental nonlinear control allocation method are discussed in Section 7.1. Hereafter, various considerations in order to implement control allocation to a compound coaxial helicopter are discussed, together with various techniques and algorithms, in Section 7.2.

7.1. Control Allocation Techniques

In this section, a review on several control allocation techniques applicable to aircraft systems is given. These include (weighted) pseudo-inverse, cascaded generalized inverse, and incremental nonlinear control allocation (INCA). Note that a multitude of other control allocation and optimization schemes exist, although these will not be covered in this review due to the scope of this literature study and thesis research.

7.1.1. The Control Allocation Problem

In general, a control allocator solves an underdetermined and often constrained system of equations. It maps the desired control effort, the virtual control input $\nu(t)$ (as featured in Figure 6.2 and Figure 6.4), to the commanded actuator deflection (the true control input) $u(t)$ such that:

$$f[u(t)] = \nu(t) \quad (7.1)$$

here, f is a function that maps the virtual control input $\nu(t)$ to the true control input $u(t)$, for the general, nonlinear case. In linear cases, this can be simplified to:

$$B(x)u(t) = \nu(t) \quad (7.2)$$

where $B(x)$ is the control effectiveness matrix, which in an overactuated case is a wide matrix where $m > k$ (more actuators than controlled degrees of freedom). The true control input is subject to both position and rate constraints:

$$\begin{aligned} u_{min} &\leq u(t) \leq u_{max} \\ \dot{u}_{min} &\leq \dot{u}(t) \leq \dot{u}_{max} \end{aligned} \quad (7.3)$$

where the rate of the actuator $\dot{u}(t)$ can be approximated by the flight controller as:

$$\dot{u}(t) = \frac{u(t) - u(t-T)}{T} \quad (7.4)$$

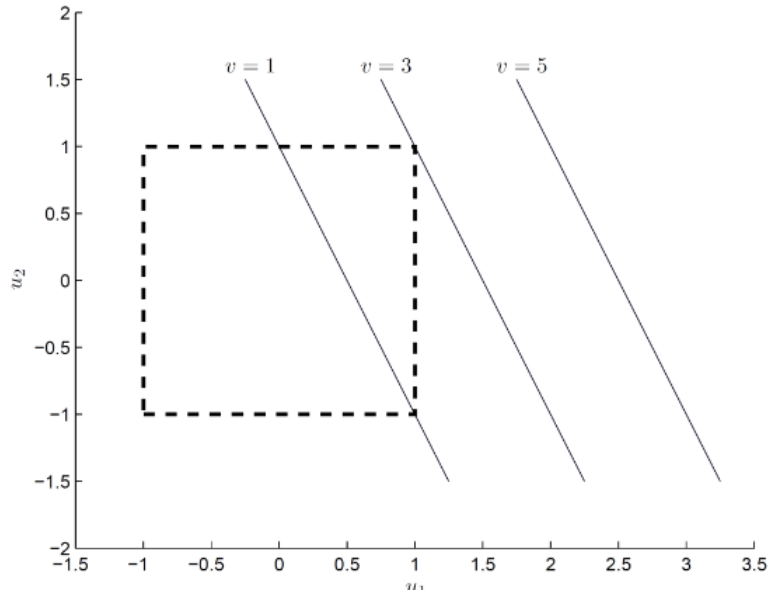


Figure 7.1: Solution domain for the desired control effort $2u_1 + u_2 = \nu$.

The position and rate constraints can then be rewritten into one position constraint:

$$\underline{u} \leq u(t) \leq \bar{u} \quad (7.5)$$

where

$$\begin{aligned} \underline{u} &= \max \{u_{min}, u(t-T) + T\dot{u}_{min}\} \\ \bar{u} &= \min \{u_{max}, u(t-T) + T\dot{u}_{max}\} \end{aligned} \quad (7.6)$$

Not that the approximation of the actuator rate is not very precise. However, for most cases, it performs well. By combining Equation 7.2 and Equation 7.5, we find the most common notation of the linear control allocation problem:

$$\begin{aligned} Bu &= v \\ \underline{u} &\leq u(t) \leq \bar{u} \end{aligned} \quad (7.7)$$

The downside of this simple representation is that it ignores all state-effector and effector-effector interactions. In later techniques, we will incorporate these effects. A visual example of the set of solutions formed by a desired control effort, e.g. $2u_1 + u_2 = \nu$ is shown in Figure 7.1. Here, the line $\nu = 1$ represents a case of unlimited solutions, in which case a 'best' solution has to be chosen, $\nu = 3$ represents the case of only 1 (optimal) solution, and $\nu = 5$ a case where no solutions are possible within the domain, meaning there is no possible combination of actuator deflections which can results in the desired control input.

As previously mentioned, the 'best' flight control allocation can be found within the solution space of the control allocation problem. The solution can therefore be optimized for several objectives such as minimum rotor loading, minimum control surface deflection, minimum radar signature, minimum drag, rapid reconfigurability for fault tolerance, etc. [49] A conclusion from Johansen [49] is that optimization-based methods tend to outperform the alternative methods proposed in literature, mainly in terms of avoiding unnecessary infeasibility and minimizing the use of control effort. Therefore, a focus is put on optimization-based control.

As a measure of quality to determine the 'best' solution, the l_p norm is often used, defined by:

$$\|u\|_p = \left(\sum_{i=1}^m |u_i|^p \right)^{1/p}, \quad 1 \leq p \leq \infty \quad (7.8)$$



where m is the number of actuators, i the index of the actuator, and p the version of the norm used. The l_2 -norm (quadratic) is often implemented in favour of the l_1 -norm since the solutions tends to combine the use of all control effectors, rather than just a few. [49] The optimal solution can be found using the following equations in two steps:

$$u = \arg \min_{u \in \Omega} \|W_u (u - u_d)\|_p \quad (7.9)$$

$$\Omega = \arg \min_{\underline{u} \leq u \leq \bar{u}} \|W_v (Bu - v)\|_p \quad (7.10)$$

where W_u is the actuator weighting matrix, W_v the virtual control weighting matrix, and u_d the preferred steady state actuator deflection. Equation 7.10 determines the set of solutions for which $Bu = v$. If the set is empty, no feasible solutions are possible, as depicted in Figure 7.1, and the most feasible solution which minimizes the l_p norm of the weighted difference between virtual control input and produced moments is chosen. Equation 7.9 then determines which of the solutions produced by Equation 7.10 is optimal, based on the weighted difference between the steady state actuator deflections and true control input.

7.1.2. Pseudo-Inverse Method

The pseudo-inverse method is the most basic method of optimization-based control allocation. It minimizes the l_2 -norm and has an explicit solution. However, it does not take into account actuator constraints and weights, i.e. $W_u = W_v = I$. The resulting solution for the pseudo-inverse control allocation is:

$$u = B^T (BB^T)^{-1} v = B^* v \quad (7.11)$$

Note that the pseudo-inverse and its following, more in-depth methods, allows one to analytically represent the control allocator in a robustness analysis of the system that is valid as long as the control acceleration command is feasible and no single axis is saturated. [49]

7.1.3. Weighted Pseudo-Inverse Method

The weighted pseudo-inverse method initially solves the control allocation problem without constraints. However, the various control effector weights are now included, resulting in the reduced l_2 -optimal control allocation problem:

$$\begin{aligned} \min_u \|W_u (u - u_d)\|_2 \\ \text{subject to } Bu = v \end{aligned} \quad (7.12)$$

which, after a derivation, results in the following solution for the real control deflections:

$$u = [I - GB]u_d + Gv \quad (7.13)$$

where

$$G = W_u^{-1} (BW_u^{-1})^* \quad (7.14)$$

where G denotes the weighted pseudo-inverse of B in which an $*$ indicating the pseudo-inverse of the matrix under the asterix. Even though the amount of infeasible solutions is reduced with the inclusion of control input weights, some infeasible solutions can still be produced according to actuator saturation. These effects can be included by clipping the controls such that the controls are saturated at their limits, producing the best result they can. This is done according to:

$$\text{sat}_i(u) = \begin{cases} \underline{u}_i, & u_i < \underline{u}_i \\ u_i, & \underline{u}_i \leq u_i < \bar{u}_i, \\ \bar{u}_i, & u_i > \bar{u}_i \end{cases} \quad i = 1, \dots, m \quad (7.15)$$



7.1.4. Cascaded Generalized Inverse

In weighted pseudo-inverse, the control actuator position constraints are not actually taken into account, rather, the actuators are just saturated and the result is clipped for mathematical inclusion of this effect in the control allocation solution algorithm. Therefore, weighted pseudo-inverse does not account for the possibility of compensating for the saturated actuators with the remaining free actuators that effect the controlled degree of freedom. This is what the cascaded generalized inverse method tries to achieve.

In the cascaded generalized inverse method, the first step is to compute an initial solution as in the weighted pseudo-inverse method, using:

$$u_1 = [I - G_1 B] u_d + G_1 v \quad (7.16)$$

if u_1 does not violate any constraints, this is the solution. Otherwise, all actuators that violate their constraint are saturated according to Equation 7.15. Subsequently, a new control effectiveness matrix B_2 is computed that only includes those columns that correspond to the remaining free actuators. The problem then becomes:

$$B_2 u_2 = v - B u_1 \quad (7.17)$$

which can be solved by:

$$u_2 = (I - G_2 B_2) u_d + G_2 (v - B u_1) \quad (7.18)$$

If $u = u_1 + u_2$ does not violate any constraints, this is the solution, otherwise, this procedure is repeated until a feasible solution is found.

7.1.5. Incremental Nonlinear Control Allocation

Incremental nonlinear control allocation, referred to as INCA, is a nonlinear dynamic control allocation approach, hence not based on an optimization scheme. In INCA, not only the actuator position constraints are taken into account, but also the actuator rate constraints. Additionally, INCA exploits the nonlinear interactions between effectors, which is not possible with linear control allocation approaches.

The nonlinear control effector model is defined as:

$$\tau_u = \phi(x, u) \quad (7.19)$$

using which the general nonlinear dynamics of the system can be written as:

$$\dot{x} = f(x) + g(x)\phi(x, u) \quad (7.20)$$

with $f(x)$ denoting the non-control related aerodynamic model terms. Using Taylor series expansion around the current state x_0 and actuator positions u_0 , the following approximation can be made:

$$\dot{x} \approx \dot{x}_0 + \frac{\partial}{\partial x} [f(x) + g(x)\phi(x, u)] \Big|_{\substack{u=u_0 \\ x=x_0}} (x - x_0) + \frac{\partial}{\partial u} [f(x) + g(x)\phi(x, u)] \Big|_{\substack{u=u_0 \\ x=x_0}} (u - u_0) \quad (7.21)$$

The term $(x - x_0)$ can be neglected for sufficiently high sampling rates, due to the time scale separation principle. A control increment can be defined as $\Delta u = (u - u_0)$, from which a virtual control law can be introduced:

$$v(x) = \dot{x} \approx \dot{x}_0 + g(x_0) \frac{\partial \phi(x_0, u_0)}{\partial u} \Delta u \quad (7.22)$$

Here, the 'Control Effectiveness Jacobian' (CEJ) is defined as:



$$\nabla_u \phi(x_0, u_0) = \frac{\partial \phi(x_0, u_0)}{\partial u} \quad (7.23)$$

The commanded incremental force and moment vectors are also defined, according to:

$$\Delta \tau_c = g(x_0)^{-1} (v(x) - \dot{x}_0) \quad (7.24)$$

Using these equations, the INCA problem can be stated as follows: given the current state x_0 , current control input u_0 and incremental commanded force and moment vector $\Delta \tau_c$, determine the incremental control input Δu such that:

$$\begin{aligned} \nabla_u \phi(x_0, u_0) \Delta u &= \Delta \tau_c \\ \text{subject to } \underline{\Delta u} &\leq \Delta u \leq \overline{\Delta u} \end{aligned} \quad (7.25)$$

When ignoring the actuator constraints, the simplest INCA control law is found by solving this equation using the standard pseudo-inverse method. In order to solve the INCA problem with actuator constraints, weighted pseudo-inverse or cascaded generalised inverse methods can be used. However, using quadratic programming, multiple other actuator and additional other constraints such as power constraints etc. can be added in the optimization as per:

$$\begin{aligned} \Delta u_{QP-INCA} &= \arg \min_{\Delta u} \underbrace{\|W_Q (\nabla_u \phi(x_0, u_0) \Delta u - \Delta \tau_c)\|_2^2}_{\text{allocation problem}} + \underbrace{\|W_S (\Delta u - \Delta u_p)\|_2^2}_{\text{secondary objective}} \\ \text{subject to } \underline{\Delta u} &\leq \Delta u \leq \overline{\Delta u} \end{aligned} \quad (7.26)$$

The solutions of the INCA method will not be further discussed due to the scope of the literature study and thesis due to its in-depth nature. However, future work based on this thesis subject may include the use of an INCA-based controller, and compare its results with the results that will be obtained from the thesis following this literature study. A noteworthy application of the INCA controller is that on the Lockheed ICE aircraft by Matamoros, De Visser et al. [50] at the TU Delft.

7.2. Implementation Considerations in Compound Coaxial Rotorcraft

In a compound coaxial ABC rotor rotorcraft, there are several redundant flight controls. The control inputs are: symmetric lateral cyclic (θ_{1c}), differential lateral cyclic ($\Delta \theta_{1c}$), symmetric longitudinal cyclic (θ_{1s}), differential lateral cyclic ($\Delta \theta_{1c}$), symmetric collective (θ_0), differential collective ($\Delta \theta_0$), pusher propeller collective (θ_p), elevator δ_e , and rudder δ_r . The general transition between the control inputs during low speed, transitional speed, and high-speed is shown in Figure 7.2 below.

Flight mode	Control method				
	Roll	Pitch	Yaw	Height	Longitudinal velocity
Helicopter mode (0 ~ 20 m/s)	θ_{1c}	θ_{1s}	θ_d	θ_0	θ
Transition mode (20 ~ 60 m/s)	θ_{1c}	$\theta_{1s} \rightarrow \delta_e$	$\theta_d \rightarrow \delta_r$	$\theta_0 \rightarrow \theta$	$\theta \rightarrow \theta_p$
Fixed-wing mode (60 ~ 120 m/s)	θ_{1c}	δ_e	δ_r	θ	θ_p

* θ denotes the pitch angle or pitch channel.

Figure 7.2: Control strategy for a compound coaxial helicopter. [26]

7.2.1. Rotor Speed Control Strategy

Firstly, the implementation of a varying rotor speed is discussed. The rotor speed is scheduled as a function of airspeed in order to mitigate compressibility effects [6] [41] which can significantly increase drag and thus limit the performance of the rotorcraft. Yuan [41] provided the following rotor speed scheduling:



$$\Omega = \begin{cases} 35.9, & V_f < 70 \text{ m/s} \\ 35.9 - \frac{3.59(V_f - 70)}{30}, & V_f \geq 70 \text{ m/s} \end{cases} \quad (7.27)$$

7.2.2. LOS Control Strategy

Secondly, the lift offset (LOS) of the ABC rotors is scheduled in function of airspeed by using the differential lateral cyclic $\Delta\theta_{1c}$ according to Ferguson [28]. It is set to be a trim variable for the LOS, which is given by:

$$LOS = 0.0002V^2 \quad (7.28)$$

7.2.3. Swashplate, Elevator and Rudder Control Strategy

Thirdly, the weights for e.g. a weighted pseudo-inverse method can be allocated as done by Yuqing [26] using Equation 7.29 for the allocation between the longitudinal cyclic θ'_{1s} and the elevator δ_e , and Equation 7.30 for the allocation between differential collective $\Delta\theta_0$ and rudder δ_r .

$$\rho_{\theta_{1s}} = \begin{cases} 1, & V \leq 20 \text{ m/s} \\ 1 - \frac{1}{40}(V - 20), & 20 < V < 60 \text{ m/s}, \\ \epsilon, & V \geq 60 \text{ m/s} \end{cases} \quad (7.29)$$

$$\rho_{\delta_e} = \begin{cases} \epsilon, & V \leq 20 \text{ m/s} \\ \frac{1}{40}(V - 20), & 20 < V < 60 \text{ m/s} \\ 1, & V \geq 60 \text{ m/s} \end{cases}$$

$$\rho_{\theta_d} = \begin{cases} 1, & V \leq 20 \text{ m/s} \\ 1 - \frac{1}{20}(V - 20), & 20 < V < 40 \text{ m/s}, \\ \epsilon, & V \geq 40 \text{ m/s} \end{cases} \quad (7.30)$$

$$\rho_{\delta_r} = \begin{cases} \epsilon, & V \leq 20 \text{ m/s} \\ \frac{1}{20}(V - 20), & 20 < V < 40 \text{ m/s} \\ 1, & V \geq 40 \text{ m/s} \end{cases}$$

where $\rho_{\theta_{1s}}$, ρ_{δ_e} , $\rho_{\Delta\theta_0}$, and ρ_{δ_r} are the control weights of the longitudinal cyclic, elevator (pitch channel), collective and rudder (yaw channel) respectively. V indicates the airspeed and ϵ a small constant with $\epsilon > 0$. The speed regions where the transition occurs are determined by Yuqing in a control efficiency analysis, resulting in the results presented in Figure 7.3. In the XH-59A ABC demonstrator helicopter, a 0% to 100% washout between 40 and 80 kts was used. [6] Depending on the results for the compound coaxial rotorcraft in the thesis following this literature study, proper speed ranges should be used.

7.2.4. Propeller Control Strategy

Lastly, the propeller control strategy proposed by Yuan [41] is discussed. Define a factor a which equals the control allocation between the propeller and the longitudinal cyclic. The factor a is calculated by Equation 7.31 where X_P is the axial thrust provided by the propeller, and X_R the axial thrust provided by the coaxial rotor. This value is larger than 0 but can be larger than 1, indicating that the main rotor is providing backwards thrust. If the propeller would be able to have negative cyclic, it is also possible to have negative values for a .

$$a = \frac{X_P}{X_R + X_P} \quad (7.31)$$

The factor a could also represent the allocation of the longitudinal controller between rotor and propeller as per:

$$\Delta\theta_{I,l} = a \cdot \Delta\theta_p + (1 - a)\Delta\theta_{1s} \quad (7.32)$$

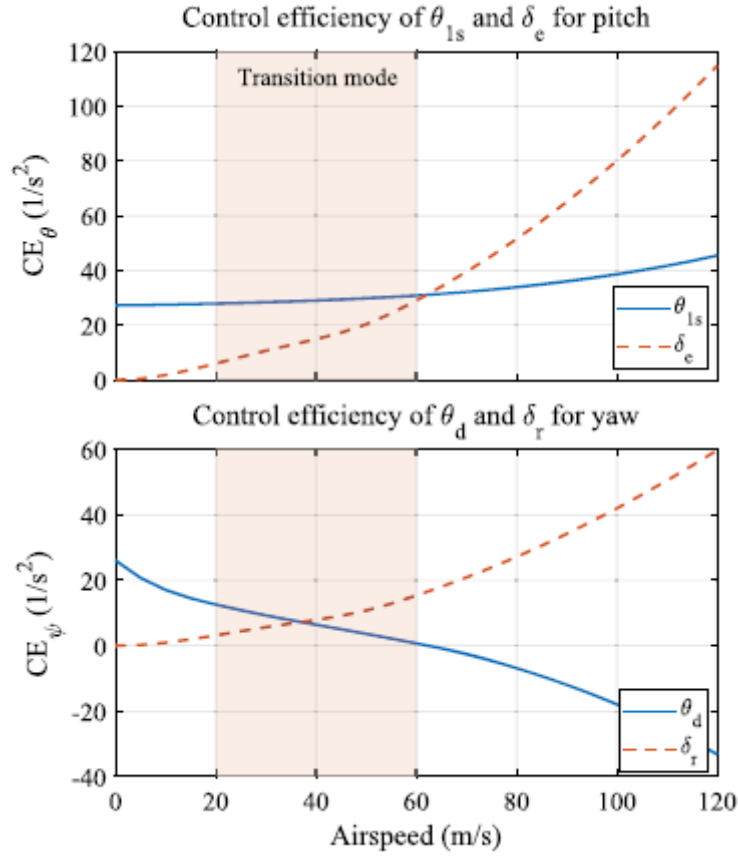


Figure 7.3: Control efficiency for pitch and yaw channels. [26]

where $\Delta\theta_{I,l}$ denotes the input increment in longitudinal direction, $\Delta\theta_p$ the propeller collective increment, and $\Delta\theta_{1s}$ the longitudinal cyclic pitch increment. When $a = 0$, the longitudinal control would directly link to the main rotor longitudinal cyclic pitch θ_{1s} .

Yuan analysed the effects of changing the factor a with flight speed on performance, trim and handling qualities. If the propeller strategy is designed to only reduce power consumption, this results in a trim state shown in Figure 7.4. As can be seen, there are severe discontinuities around 45 m/s, right when the propeller is turned on. This is unacceptable for the riding qualities, which affect the handling qualities as well as resulting in sudden inter-axis coupling.

The proposed propeller control strategy by Yuan [41] uses the objection function:

$$M_{ob,1} = P_{a,v_f=100 \text{ m/s}}, \quad \text{or}, \quad P_{a,v_f=70 \text{ m/s}} \quad (7.33)$$

where $M_{ob,1}$ is the key target point, and sets the key target speed points to 100m/s and 70m/s. These are related to the point of high speed performance, and improved flight range respectively. In order to account for continuity in the trim results, and for reduced inter-axis coupling, boundary conditions are applied. The boundary conditions for the trim characteristics are as follows

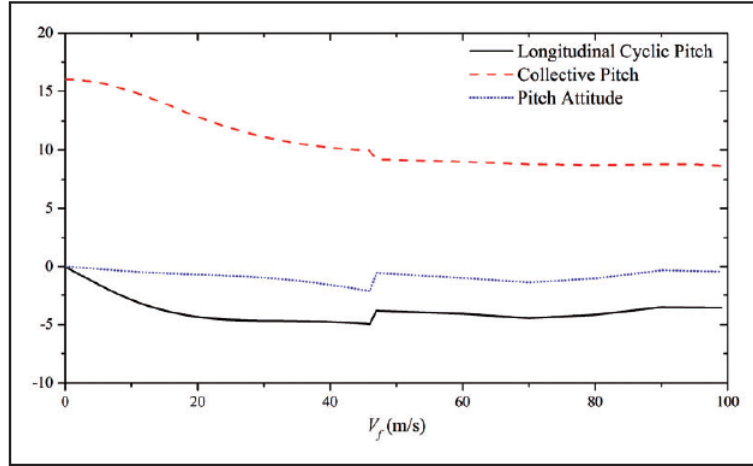


Figure 7.4: Trim results with propeller allocation strategy only accounting for minimum power requirements. [41]

$$\begin{aligned}
 \left| \frac{d\theta_{0, \text{trim}}}{dV_f} \right| &\leq 0.01(\text{rad} \cdot \text{s})/\text{m} \\
 \left| \frac{d\theta_{1c, \text{trim}}}{dV_f} \right| &\leq 0.01(\text{rad} \cdot \text{s})/\text{m} \\
 \left| \frac{d\theta_{1s, \text{trim}}}{dV_f} \right| &\leq 0.01(\text{rad} \cdot \text{s})/\text{m} \\
 \left| \frac{d\theta_{d0, \text{trim}}}{dV_f} \right| &\leq 0.01(\text{rad} \cdot \text{s})/\text{m} \\
 \left| \frac{d\theta_{\text{trim}}}{dV_f} \right| &\leq 0.005(\text{rad} \cdot \text{s})/\text{m} \\
 \left| \frac{d\phi_{\text{trim}}}{dV_f} \right| &\leq 0.005(\text{rad} \cdot \text{s})/\text{m}
 \end{aligned} \tag{7.34}$$

where ϕ_{trim} is the roll attitude in trim. The boundary conditions accounting for proper inter-axis coupling handling qualities are:

$$\begin{aligned}
 \frac{p}{q} &\leq -5 \text{ dB} \\
 \frac{q}{p} &\leq -10 \text{ dB}
 \end{aligned} \tag{7.35}$$

With these objectives and boundary conditions, the propeller trim strategy flowchart as shown in Figure 7.5 is proposed by Yuan, and results in smooth trim characteristics adhering to the boundary conditions, while still performing well in terms of power requirements.

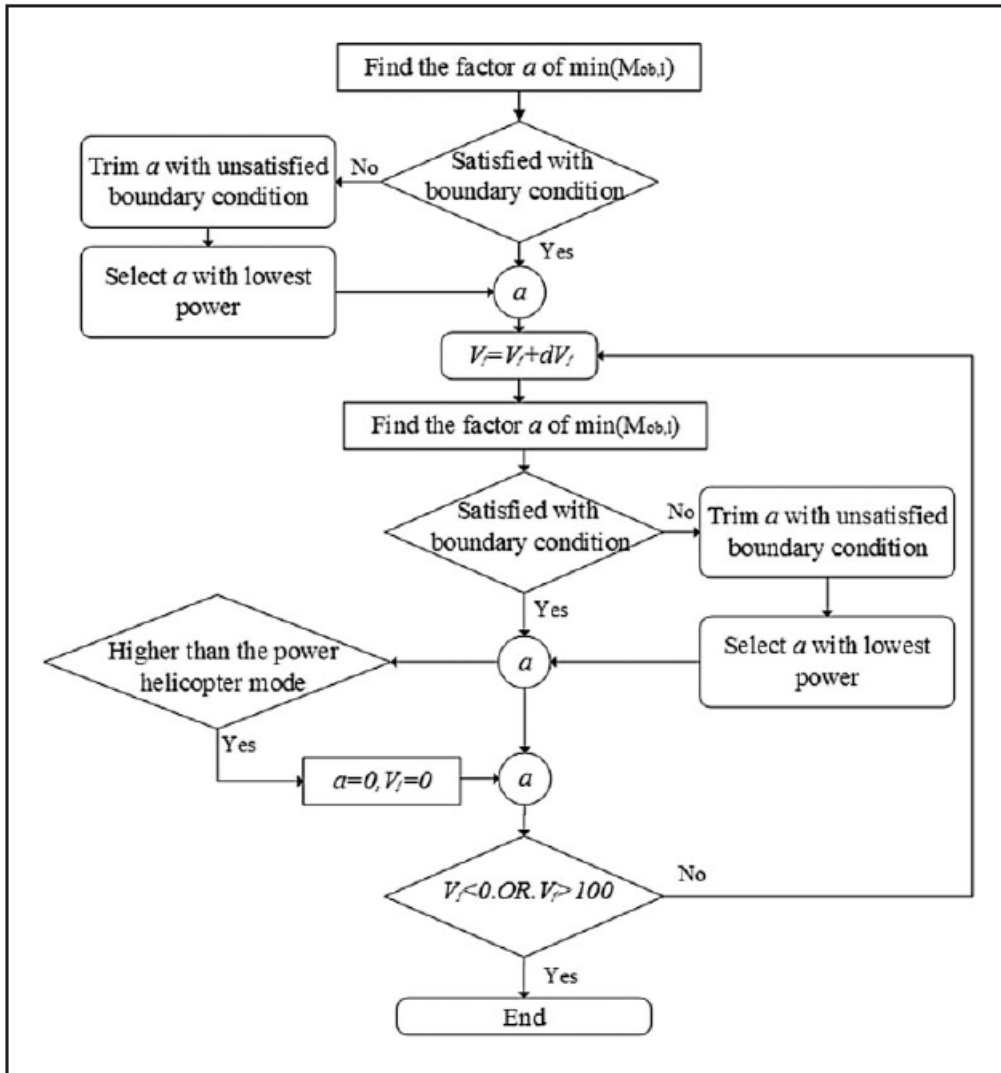
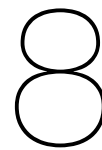


Figure 7.5: Propeller control strategy design flowchart. [41]



Handling Quality Assessment in High-Speed Helicopter Design

Handling Qualities (HQ) are a fundamental aspect in rotorcraft. They determine how well an aircraft flies in terms of safety, and pilot comfort, which gives the pilot more room to perform other mission critical tasks. Inherently, rotorcraft are highly unstable, and therefore benefit immensely from the use of Stability Augmentation Systems (SAS) and autopilots in order to make the helicopter flyable at all, or reduce pilot workload. Often, the reference to 'closed-loop handling qualities' is made, meaning the applied control system (SAS or autopilot) is taken into account. However, assessing these handling qualities is not self-evident, especially for military applications. Significant design and/or control efforts may be required in order to make the handling qualities acceptable. An industry standard for handling quality assessment is the Aeronautical Design Standard, ADS-33E-PRF. [51] Efforts have been taken to improve and update these design standards to a new ADS-33F-PRF [51] standard, which includes revisions to the ADS-33E-PRF and includes several additions to the existing handling quality evaluation metrics. These metrics can mainly be split into two parts: objective and subjective handling quality assessment metrics, which will each be discussed shortly, applied to a compound coaxial high-speed rotorcraft.

8.1. Objective Handling Quality Metrics

In modern approaches for assessing handling qualities, quantitative criteria that characterize desirable handling qualities based on flight test or simulation data are used. [52] In these assessments, regional bounds are defined which indicate Level 1 (desirable), Level 2 (adequate) and Level 3 (undesirable) handling qualities. The goal of this predictive qualitative assessment is to quickly and iteratively determine the handling qualities of the compound helicopter during early design stages, when only low or moderate fidelity models are available. [18] These criteria hence typically use parameters obtained from frequency response analysis or simple step-input commands. Objective handling criteria are often complemented by the calculation of stability margins to ensure proper flying qualities and aircraft stability.

Stability margins in roll, pitch and yaw are important to fall within certain confidence bounds. Berger [46] uses a stability margin of 6 dB and 45 deg, visualized in Figure 8.1 (standard ADS-33E-PRF values) throughout the entire envelope, and relaxes these requirements to 4.5 dB and 40 deg for speeds >260 kts. Apart from the stability margins, adequate response behaviour for phugoid, short period and dutch roll provide increased handling qualities.

In HQ assessment, bandwidth and phase delay are often assessed, as shown in Figure 8.2. Phase delay is calculated using Equation 8.1 with the parameters shown in Figure 8.1. Numerically, it is the slope of the phase curve between ω_{180} and $2 * \omega_{180}$. Physically, it corresponds to the system resonance to change in pilot gain. It can also be considered the initial delay to a pilot step input. [52]

$$\tau_p = \frac{\Delta\Phi_{2\omega_{180}}}{57.3(2 * \omega_{180})} \quad (8.1)$$

In order to quantify the cross-coupling effects, the pitch-to-roll q/p and roll-to-pitch p/q cross-couplings are plotted as shown in Figure 8.3. The average response ratios are derived from the amplitude of the

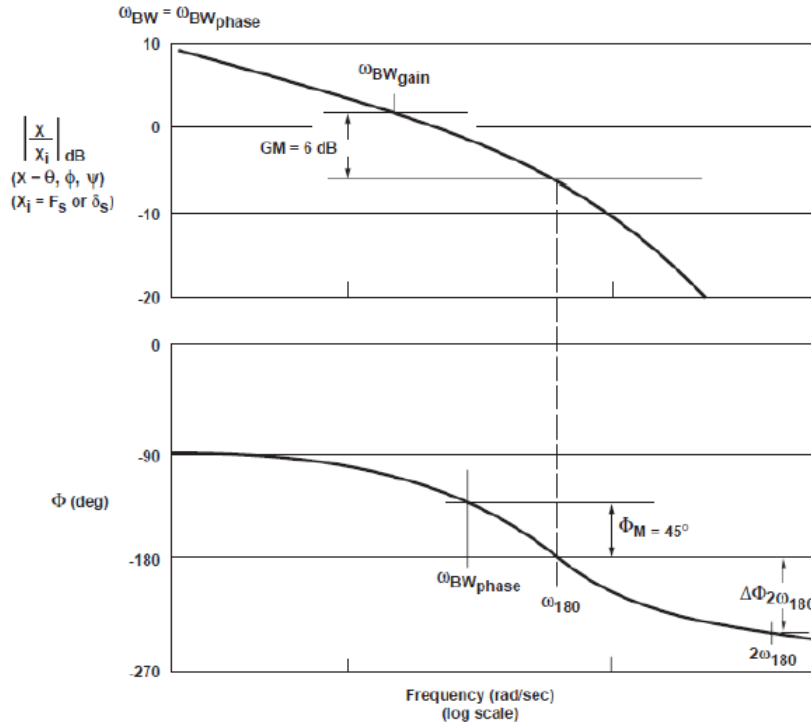


Figure 8.1: ADS-33E-PRF definitions for frequency response gain and phase stability margins. [51]

frequency response functions q/δ_{lat} divided by p/δ_{lat} and p/δ_{lon} divided by q/δ_{lon} , averaged between the bandwidth frequency ω_{bw} and the -180 degrees phase bandwidth ω_{180} . [18]

Bandwidth frequency, phase delay, and cross-coupling metrics are useful for small amplitude and/or high frequency manoeuvres. However, in large amplitude and/or low to moderate frequency response characteristics, other metrics are useful, such as the attitude quickness test. The attitude quickness is defined as the peak rate of change to the peak attitude change for roll ($\frac{p_{pk}}{\Delta\phi_{pk}}$), pitch ($\frac{q_{pk}}{\Delta\theta_{pk}}$), and yaw ($\frac{r_{pk}}{\Delta\psi_{pk}}$). The ADS-33E criteria for the attitude quickness are shown in Figure 8.4 for roll only, for sake of brevity. Note that the requirements are different for target acquisition and tracking MTEs compared to other MTEs. The definitions of the parameters used for attitude quickness are depicted in Figure 8.5, which is a response for a step-input. Note that for different step sizes, this response will be different. Therefore, multiple step-size inputs will be performed, and a trend with increasing changes in attitude will be established.

In order to ensure proper handling qualities, the designer can either manually tweak the SAS control parameters and/or the aircraft parameters, or can employ the use of engineering software. One of these software packages is CONDUIT [53], in which the user can specify a list of tier 1 (very important) and tier 2 (favourable) objective handling quality metrics. CONDUIT will then try and tweak the control parameters in order to achieve Level 1 performance in all Tier 1 metrics, and try to get as high scores as possible for the Tier 2 metrics. NLR uses the CONDUIT package frequently, and chances of it being used throughout this thesis are high.

8.2. Subjective Handling Quality Metrics

Apart from the objective metrics to determine handling quality ratings, subjective handling qualities can be assessed. This is done using a series of experiments, called Mission Task Elements (MTEs), which are either flown in a simulation by the pilot, or tracked using principles such as inverse simulation [54]. Manoeuvres flown by a pilot are usually assessed using the Cooper-Harper rating scale, depicted in Figure 8.6, for which the results are then plotted on level 1-3 scales. Often, Cooper-Harper ratings of 1-3.5 indicate Level 1 handling qualities, 3.5-6.5 Level 2, and 6.5-8.5 Level 3. [51]

Various undertakings have been done in order to establish new MTEs for high-speed helicopters. These

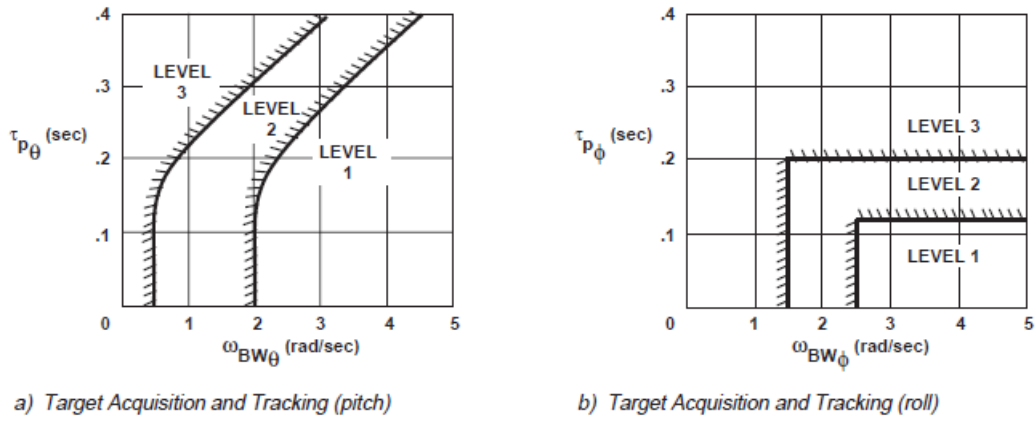


Figure 8.2: ADS-33E-PRF bandwidth/phase delay handling quality criteria for pitch (right) and roll (left). [51]

encompass the further development on the combat break turn [55], high-speed tracking [56], high-speed acceleration/deceleration [57], and high-speed capture-and-hold [58].

Since the conduction of MTE experiments in a simulator such as the SIMONA is beyond the scope of the thesis accompanying this literature study, further detail on subjective handling quality metrics will not be discussed. However, the implementation of a flyable model of the high-speed compound coaxial helicopter in a simulator such as the SIMONA would be a logical and highly interesting expansion upon this thesis.

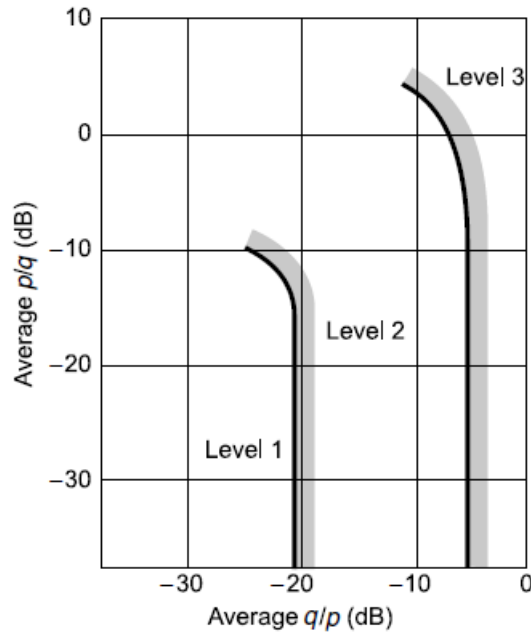


Figure 8.3: Pitch-roll cross-coupling requirements for aggressive agility according to ADS-33E standards. [18] [51]

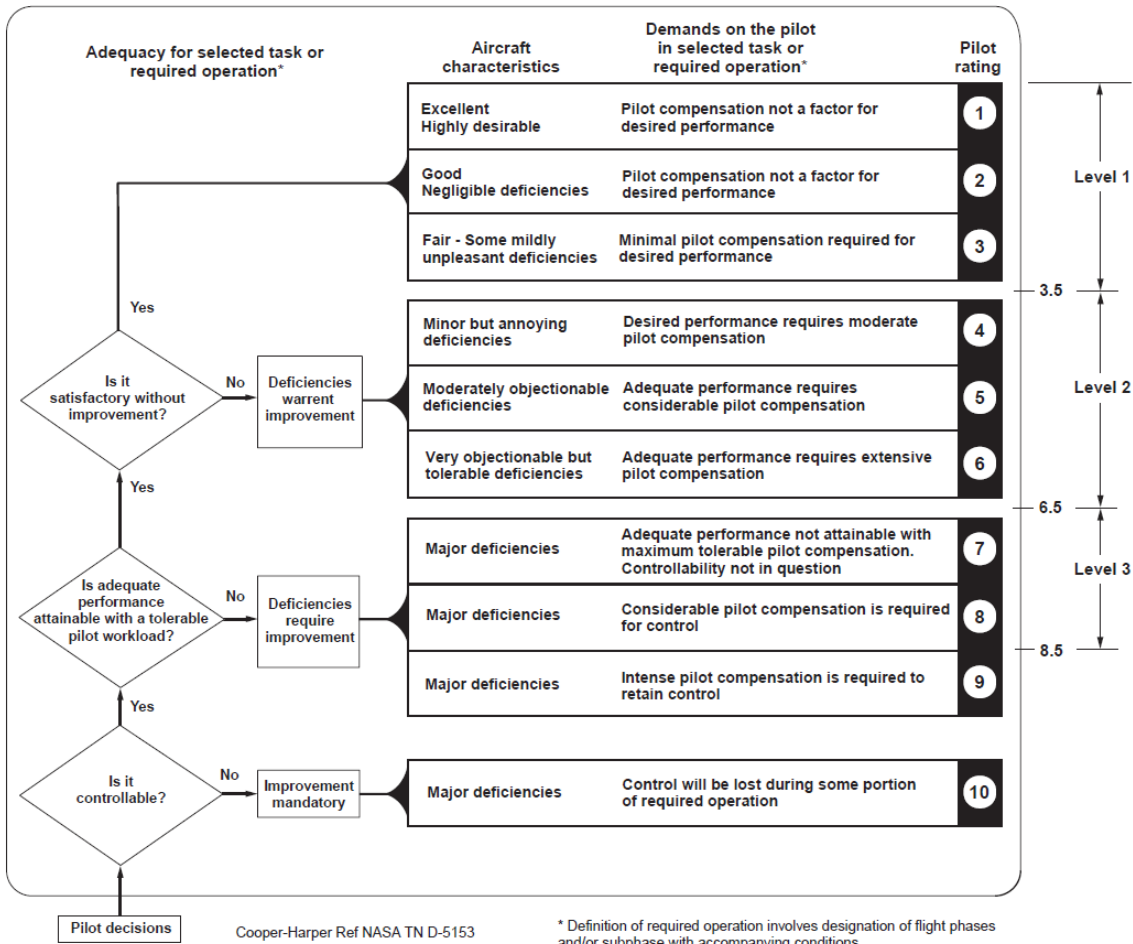


Figure 8.6: Cooper-Harper rating scale definition. [51]

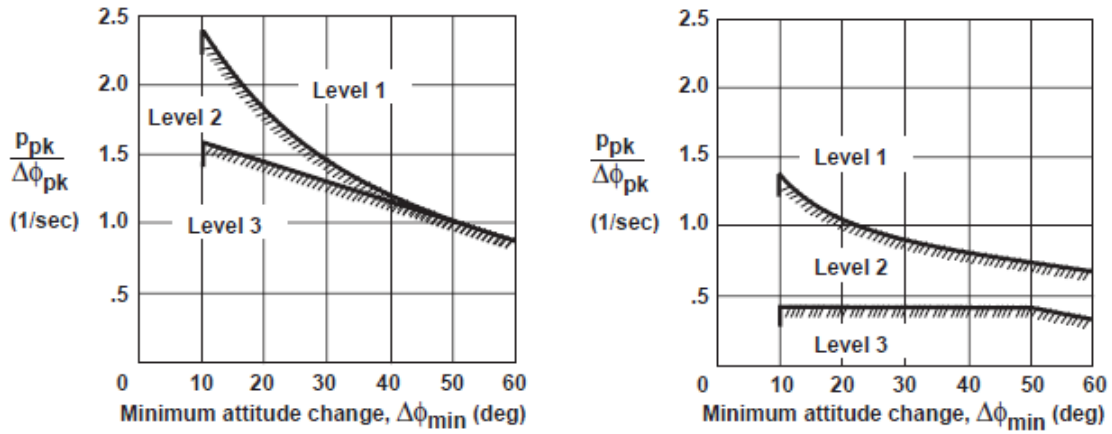


Figure 8.4: Attitude quickness requirements according to ADS-33E for target acquisition and tracking (left) and all other MTEs (right). [51]

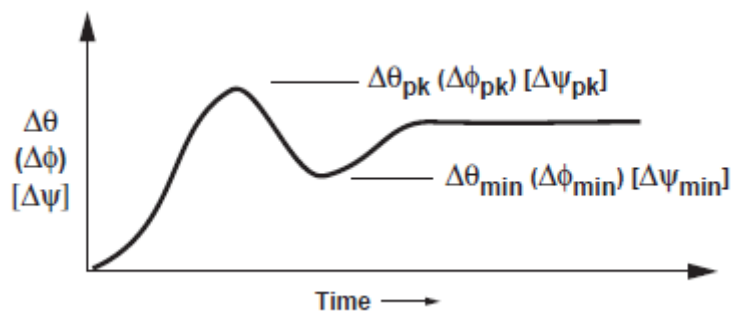


Figure 8.5: Definition of quickness criterion parameters. [51]

Results and Discussion

The goal of this literature study was to gain an understanding of the background on the project and pinpoint several state-of-the-art methods in the modelling, control and handling quality assessment of compound coaxial helicopters. This literature study serves as a basis for the thesis project itself, and provides a baseline for the work that has to be done. The conclusion of this literature study starts in Section 9.1, where the research gap is defined based on an analysis of the most relevant papers, followed by Section 9.2, where answers to the research questions posed in Section 1.3 are formulated, and concluded by a summary of the document in Section 9.3.

9.1. Research Gap

Throughout this literature study, various papers deemed as industry-leading have been identified. These are listed in Table 9.1 and aim to map the existing literature applicable to the research topic at hand. Each paper is assessed based on the inclusion of the following criteria: (i) the use of a compound coaxial rotorcraft utilizing Advancing Blade Concept (ABC) rotors, (ii) the inclusion of a Stability Augmentation System (SAS) and/or Control Augmentation System (CAS), (iii) control allocation (CA) scheme, and (iv) handling quality assessment (HQA), (v) the incorporation of Matlab as main simulation and evaluation tool, and (vi) the research investigation being focused on the conceptual design phase. ✓, ✗, ?, and ∅ indicate the inclusion, exclusion, unidentified inclusion, and partial inclusion of the criteria respectively.

Table 9.1: Main research paper domain exploration applicable to research topic.

	Compound Coaxial ABC	SAS/CAS	CA	HQA	Matlab	Conceptual Design
Zhao et al. (2023)	✓		✓	✓	?	
Qiu et al. (2023)	✓	✓	✓		?	
Berger et al. (2022)	✓	✓	✓	✓		
Berger et al. (2020)	✓		✓			
Gerosa et al. (2019)		✓		✓		✓
Yuan et al. (2019)	✓		✓	✓	?	
Yuan et al. (2019) (2)	✓		✓	✓	?	
Conti (2018)		✓	✓	✓		✓
Ferguson (2015)	✓			✓		

It can be concluded that although each subtopic has been addressed separately, there is no research covering the combination of these areas. Therefore, it can be stated that there is a gap in existing literature concerning the physics-based modelling of a high-speed compound coaxial helicopter in Matlab, which leverages the use of control allocation and stability and control augmentation systems in order to achieve desirable handling qualities during the conceptual design phase.



9.2. Research Questions Results

In Section 1.3.2, several research questions were posed regarding: (i) modelling, (ii) control, and (iii) handling quality assessment, to be addressed during this literature study. Although the individual questions were all discussed throughout this study, the following aims to provide a concise summary of the obtained conclusions/results. Note that if the conclusions from this literature study result to be infeasible or inadequate, they will be changed during the thesis.

Modelling

Research Question M.1

What model fidelity-level is required for the design of a helicopter controller during conceptual design?

Level 1 fidelity according to Padfield's [18] fidelity levels.

Research Question M.2

How will the rotor inflow, rotor interference, wake contraction, pusher propeller, fuselage, and empennage be modelled for a compound coaxial rotorcraft?

The rotor inflow can be modelled using a local momentum theory approach based on the works of Pitt-Peters can be followed, utilizing a linear non-uniform inflow approximation for the lower rotor, and a uniform inflow approximation for the upper rotor. Wake contraction effects can be accounted for depending on the main rotor dimensions. Rotor interference effects are accounted for using a linear approximation for upper and lower rotor interference factors in function of advance ratio. The blade flapping dynamics can be modelled using a hinge-offset spring equivalent flapping model. The fuselage and empennage can be modelled using open access look-up tables.

Research Question M.3

How will the control law architecture interface with the NLR Flightlab model, and how can this serve as a validation source?

The applicability and role of the NLR Flightlab models during this thesis project is still a topic of discussion, and may change throughout the thesis duration. Therefore, no definite answer can be provided to this question.

Research Question M.4

What amendments have to be made to the existing coaxial helicopter model in order to develop a compound coaxial helicopter model?

The ABC rotors have to be added, and a pusher propeller should be added. The addition of an extra trim variable demands the use of an additional trim target, which can be provided by the LOS parameter. The existing model will therefore require a different trim approach.



Research Question M.5

What trim strategy will be employed in order to trim the compound coaxial helicopter model?

As stated in the conclusion of Research Question M.4, the LOS parameter will be used as an additional trim target. The exploration of various trim strategy algorithms was not yet conducted during this literature study, and will therefore be an extra objective to be completed during the thesis itself.

Control

Research Question C.1

What control architectures are most suitable for the design of a high-level controller of a compound coaxial helicopter during the conceptual design phase in order to attain desirable handling qualities?

During the initial control design phase, a PID controller will be used. Depending on the performance of the PID controller, and EMF controller might be implemented, and its effects analysed. Depending on these results, pseudo-control hedging might be implemented, and its effects analysed.

Research Question C.2

What methods are most suitable for the control allocation of a compound coaxial helicopter during the conceptual design phase?

Weighted pseudo-inverse will be used as the control allocation algorithm.

Research Question C.3

How are the control actuators for a compound coaxial helicopter allocated during the various flight phases?

Linear scheduling weights will be applied to the longitudinal cyclic, elevator, differential collective, and rudder. The propeller will first use a linear schedule in order to minimize force provided by the propeller, and can be extended by the strategy proposed by Yuan [41]. Differential lateral cyclic is allocated to control the LOS parameter according to a predefined function. Differential longitudinal cyclic allocation will have to be further explored, based on the conclusions presented in Zhao et al. [yanqin2023influence].

Handling Quality Assessment

Research Question HQ.1

What objective handling quality assessment criteria should be considered during the conceptual design of a compound coaxial helicopter?

Bandwidth and phase delay, cross-coupling effects, and attitude quickness tests will be analysed. Additionally, a selection from the objective handling quality parameters presented in Berger et al. [46] will be made, taking into account MIL-STD-1797B fixed wing handling quality parameters during high-speed flight.

Research Question HQ.2

How will the selected handling quality criteria be enforced such that they have desirable results in the compound coaxial helicopter configuration?

Using software optimisation solutions such as the controller tuner in Matlab/Simulink, or CON-DUIT.

9.3. Summary

In Chapter 1, a motivation on the research topic was given, in light of recent events promoting the development of advanced helicopters, such as the FVL program. Several research objectives and questions have been posed, with the overarching goal being to provide a model update for a compound coaxial helicopter, develop a practically implementable control architecture with suitable control allocation, and perform a handling quality assessment.

In Chapter 3, a brief overview of early coaxial helicopter techniques was provided. This provided insight in the challenges that came with designing coaxial, and specifically rigid coaxial helicopters. Due to these challenges, several new concepts such as the ABC rotor were developed, which were discussed in Chapter 4. Several Sikorsky helicopters utilized this novel technique which shows promising results and shall be used in the thesis project as well. The mechanical details of how such a rotor is controlled were also provided in this chapter, giving insights in the control ganging and differential collective and cyclic controls which are utilized to achieve yaw control and achieve the most benefit out of the ABC rotor respectively.

The modelling approach was discussed in Chapter 5. From this, it could be concluded that a local momentum theory approach based on the works of Pitt-Peters could be followed, utilizing a linear non-uniform inflow approximation. The upper and lower rotor interference effects can be accounted for by an inflow interference factor, which is a linear function of advance ratio. Wake contraction effects were also concluded to be accounted for, although this fact may change depending on the final rotor parameters used in the helicopter design. Regarding blade dynamics, only blade flapping motion is taken into account by means of a hinge-offset spring equivalent flapping model. The blade feathering motion is a function of the differential collective, differential lateral and longitudinal cyclic, blade twist and control phase angle, controlled by the LOS discussed in Section 4.1. After this, it was concluded that the pusher propeller can be modelled by means of conventional blade element theory, disregarding flapping motions due to the high rotational speeds and high blade stiffness. The fuselage and empennage modelling is done by means of open-access, TU Delft or NLR look-up tables.

Various control strategies were discussed in Chapter 6. Most attention was paid to PID and EMF, although several other control strategies were discussed as well. In the initial control design, a PID controller shall be implemented. Depending on time constraints and results from the PID controller, an EMF controller can be implemented due to its promising results in literature. The controller could be augmented by pseudo-control hedging.

The control allocation problem, pseudo-inverse, weighted pseudo-inverse, cascaded generalized inverse and INCA methods were covered in Chapter 7. In the thesis control allocation implementation, a weighted pseudo-inverse method will be utilized due to the accounting of actuator saturation. Various control allocation considerations on the rotor speed, LOS control, swashplate, elevator, and rudder control, and pusher propeller control were discussed as well. Existing algorithms from literature have been covered, and their viability in the compound-coaxial helicopter will be tested.

Finally, in Chapter 8, the handling quality assessment for a high-speed helicopter design was covered. It was concluded that for objective handling quality metrics, bandwidth and phase delay, cross-coupling effects, and attitude quickness tests will be analysed. The use of subjective handling quality metrics was briefly discussed too, but falls beyond the scope of this thesis due to the requirement of piloted simulation or inverse simulation methods.

It can already be stated that this thesis aims to provide a solid foundation for future work to be based on. For example, various efforts in order to provide a more complex control architecture (using e.g. INDI, H_∞ ,



...), control allocation techniques (cascaded generalized inverse, INCA,...), handling quality assessments (using MTEs) and piloted flight simulation (in the SIMONA) could be undertaken.

Part III

Main Analysis

Compound Coaxial Helicopter Modelling – Nonlinear Model

The first part of the thesis is to model the aerodynamic behaviour of the compound coaxial helicopter. The goal of this modelling is to mathematically describe a parametric nonlinear model which is able to provide a fidelity suitable for that of flight dynamics analysis. In subsequent chapters, this model will provide the foundation for linearisation, which will then be used for controller design followed by handling quality assessment.

In Section 10.1, a top-level architecture of the model is discussed and its components is described, and the full equations of motion are discussed. The 3-view drawing which the model geometric parameters are based upon, together with a definition of the body axes and planes are discussed in Section 10.2. Then, the most complex part of the model is described in Section 10.3: the coaxial rotor. This is followed by the pusher propeller model in Section 10.4, empennage model in Section 10.5, and finally the fuselage model in Section 10.6.

10.1. General Modelling Overview

In order to start modelling the full compound coaxial helicopter, a general overview of the modelling approach will be discussed. The top-level model architecture is visualised in Figure 10.1.

Several explanatory notes can be made about the model architecture:

1. Inputs: The model uses a total of 8 control inputs: the average collective θ_0 , differential collective θ_d , longitudinal cyclic θ_{1s} , lateral cyclic θ_{1c} , differential lateral cyclic $\Delta\theta_{1c}$, propeller collective θ_p , elevator deflection δ_e , and rudder deflection δ_r . Note that the differential longitudinal cyclic $\Delta\theta_{1s}$ and a potential pusher propeller monocyclic θ_{1c_p} are not included in the final model.
2. Rotor Dynamics: These encompass the flapping dynamics of both the upper and lower rotor, and output the coning angle a_0 , first harmonic longitudinal flapping coefficient a_1 , and first harmonic lateral flapping coefficient b_1 for both the upper and lower rotor separately. The flapping dynamics are explained in detail in Section 10.3.3.
3. Model Components: The modelling of the various helicopter components. These are, and are respectively described in: the coaxial rotor (Section 10.3), the pusher propeller (Section 10.4), the fuselage (Section 10.6) and the horizontal and vertical tail, together forming the empennage (Section 10.6).
4. Inflow Dynamics: The inflow dynamics require careful consideration in a coaxial rotor configuration. The calculation for the inflow dynamics consist of the inflow physics of the individual rotor, the interference effects between the two rotors, and the wake contraction effects. This last aspect, as explained in Section 10.3.4, is omitted in the final model. The final inflow parameters are modelled as quasi-dynamic states, and comprise of the upper rotor inflow λ_{0_u} , lower rotor inflow λ_{0_l} , and pusher propeller inflow λ_{0_p} .

Also visualised in Figure 10.1 is the summation of the total moments and forced in the body reference frame which mathematically is shown by Equation 10.1.

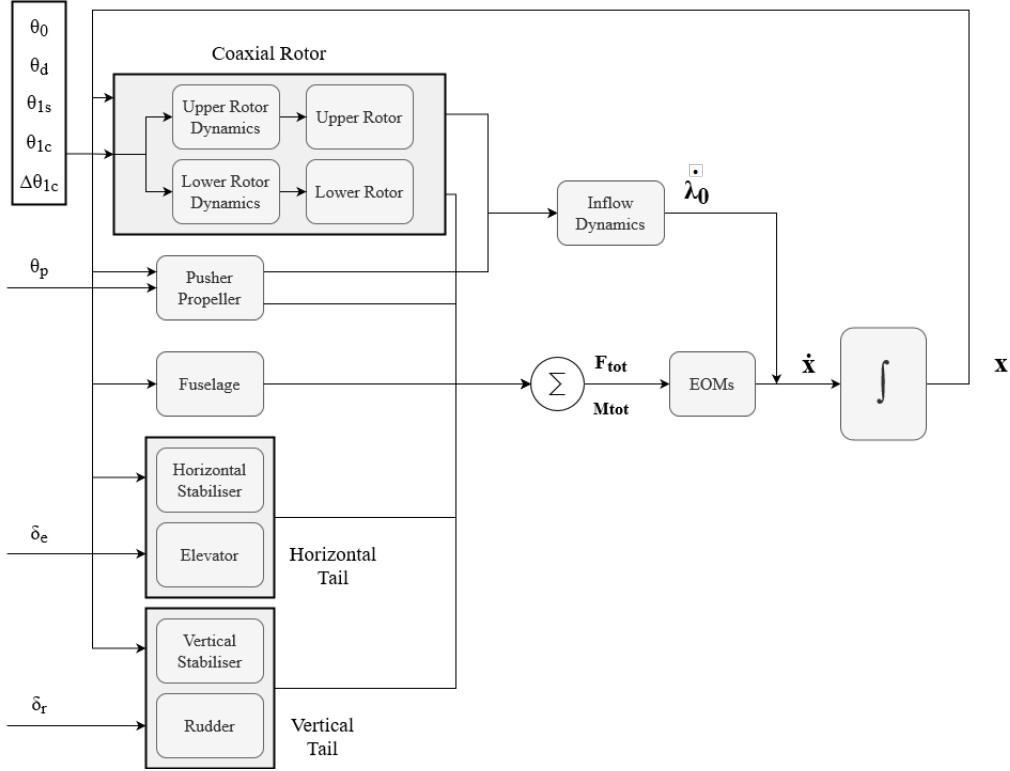


Figure 10.1: Top-level model architecture diagram.

$$\begin{cases} \vec{F}_{tot} = \vec{F}_{mr_{tot}} + \vec{F}_p + \vec{F}_{emp} + \vec{F}_{fus} \\ \vec{M}_{tot} = \vec{M}_{mr_{tot}} + \vec{M}_p + \vec{M}_{emp} + \vec{M}_{fus} \end{cases} \quad (10.1)$$

A total of 9 states are part of the model's system of equations:

- The body velocities: $\vec{u} = [u \ v \ w]^T$
- The body angular velocities: $\vec{\omega} = [p \ q \ r]^T$
- The quasi-dynamic inflow states of the upper rotor, lower rotor and pusher propeller: $\vec{\lambda}_0 = [\lambda_{0_u} \ \lambda_{0_l} \ \lambda_{0_p}]^T$

Note that the positional vector $[x \ y \ z]^T$ and the Euler angles $[\phi \ \theta \ \psi]^T$ are not part of the system states. Rather, when used in the control system detailed in Chapter 13, their values are calculated by time integration of the body velocities and angular velocities respectively, with their initial position as starting condition. The generalised notation of the body velocity and angular velocity states is stated in Equation 10.2 and are well known throughout literature. Here, J denotes the moment of inertia matrix, M the helicopter mass, $\vec{u} = [u, v, w]^T$ the body-fixed linear velocity, $\vec{\omega} = [p, q, r]^T$ the body-fixed angular velocity, and \mathbb{T}_n^b the transformation matrix from the navigational to the body frame.

$$\begin{aligned} \dot{\vec{u}} &= \frac{1}{M} F_{tot} + \mathbb{T}_n^b [0 \ 0 \ g]^T - \vec{\omega} \times \vec{u} \\ \dot{\vec{\omega}} &= J^{-1} [M_{tot} - \vec{\omega} \times J \vec{\omega}] \end{aligned} \quad (10.2)$$

Expanding these equations, we find the total system equations of motion using the default 6-dof equations of motion, joined by the quasi-dynamic inflow states [59]:



$$\begin{aligned}
 \dot{u} &= \frac{X_{tot}}{m} - g \sin \theta - qw + rv \\
 \dot{v} &= \frac{Y_{tot}}{m} - g \cos \theta \sin \phi - ru + pw \\
 \dot{w} &= \frac{Z_{tot}}{m} - g \cos \theta \cos \phi - pv + qu
 \end{aligned} \tag{10.3}$$

$$\begin{aligned}
 \dot{p} &= \frac{(I_{yy}I_{zz} - I_{zz}^2 - I_{xz}^2)r + (I_{xx} - I_{yy} + I_{zz})I_{xz}pq + I_{zz}L_{tot} + I_{xz}N_{tot}}{I_{xx}I_{zz} - I_{xz}^2} \\
 \dot{q} &= \frac{M_{tot} + (I_{zz} - I_{xx})pr - I_{xz}(r^2 - p^2)}{I_{yy}} \\
 \dot{r} &= \frac{(I_{xx}^2 - I_{xx}I_{yy} + I_{xz}^2)pq - (I_{xx} - I_{yy} + I_{zz})I_{xz}qr + I_{xz}L_{tot} + I_{xx}N_{tot}}{I_{xx}I_{zz} - I_{xz}^2}
 \end{aligned} \tag{10.4}$$

$$\begin{aligned}
 \dot{\lambda}_{0_u} &= \frac{C_{T_u}^{BEM} - C_{T_u}^{Gl}}{\tau_{\lambda_0}} \\
 \dot{\lambda}_{0_l} &= \frac{C_{T_l}^{BEM} - C_{T_l}^{Gl}}{\tau_{\lambda_0}} \\
 \dot{\lambda}_{0_p} &= \frac{C_{T_p}^{BEM} - C_{T_p}^{Gl}}{\tau_{\lambda_0}}
 \end{aligned} \tag{10.5}$$

These differential equations can be solved by numerical integration routines such as the Runge-Kutta integration scheme used in the *ode45* function inside MATLAB. Another option is to use simple discrete time-step integration: $x[i+1] = x[i] + dt \cdot \dot{x}[i]$.

10.1.1. Model Assumptions

Throughout the modelling procedure, several vital assumptions are made:

- Wake contraction is not accounted for,
- The inflow model utilises a quasi-dynamic uniform inflow,

10.2. Body Axes and Forces Definitions

In order to properly understand the sign conventions of the axes and forces, the 3-view drawings of the helicopter are depicted in Figure 10.3-Figure 10.4. In these figures, the main helicopter dimensions are also defined, and their values listed in Table 10.1.

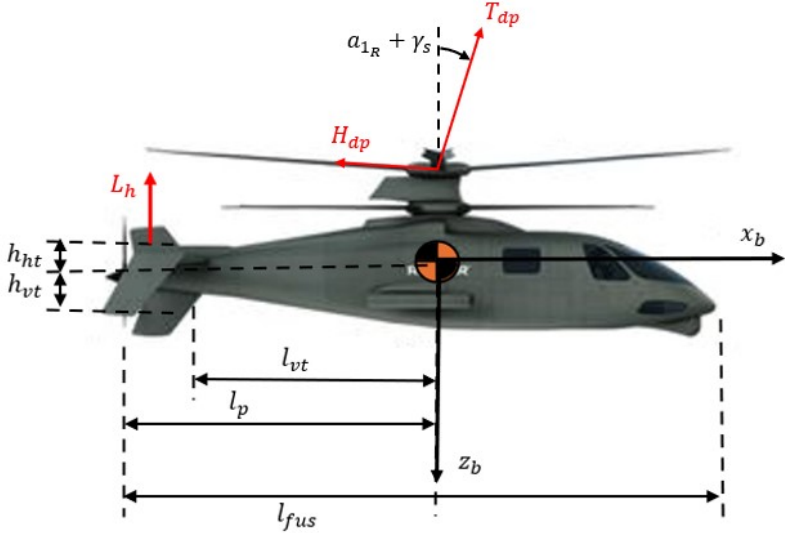


Figure 10.2: Right view of the compound coaxial helicopter.

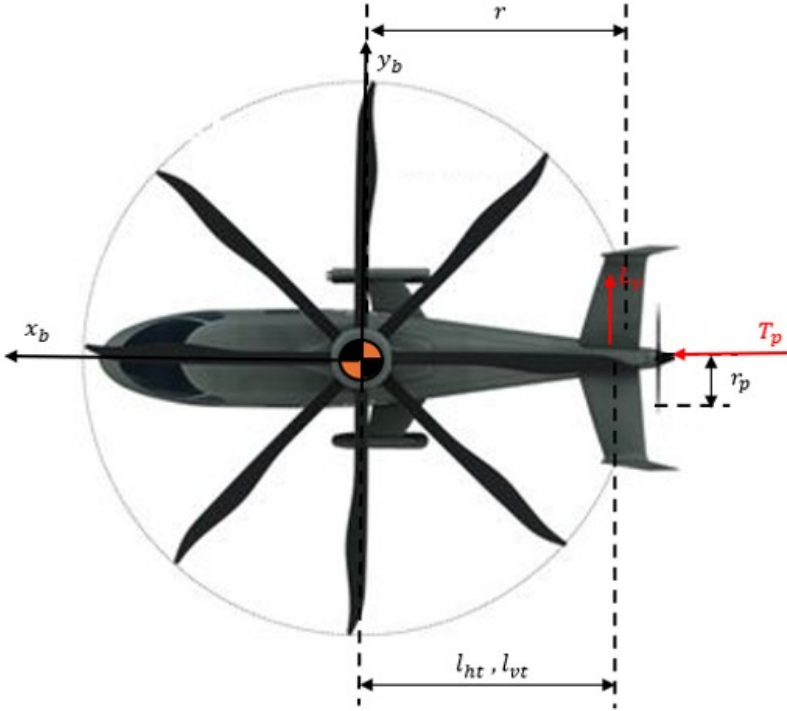
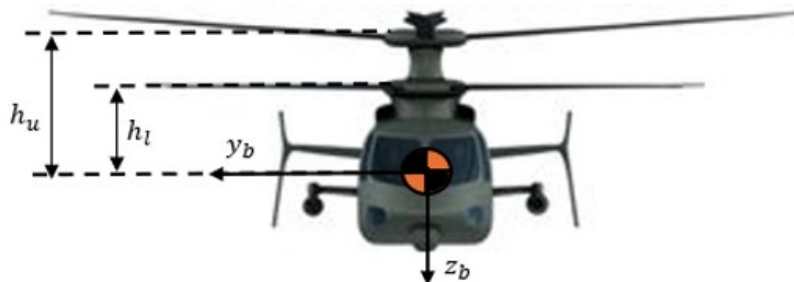


Figure 10.3: Top view of the compound coaxial helicopter.

**Table 10.1:** Main airframe parameters.

Dimension	Symbol	Value	Unit
Length Fuselage	l_{fus}	12.2	m
MOI X-axis	I_x	6800	$kg \cdot m^2$
MOI Y-axis	I_y	40000	$kg \cdot m^2$
MOI Z-axis	I_z	12000	$kg \cdot m^2$
Product MOI XZ	I_{xz}	5000	$kg \cdot m^2$
X-pos. Propeller	l_p	7.66	m
X-pos. Vertical Tail	l_{vt}	6.8	m
X-pos. Horizontal Tail	l_{ht}	6.8	m
Height Upper Rotor	h_u	1.66	m
Height Lower Rotor	h_l	0.89	m
Height Vertical Tail	h_{vt}	0.5	m
Height Horizontal Tail	h_{ht}	0	m
Main Rotor Radius	r	5.49	m

**Figure 10.4:** Front view of the compound coaxial helicopter.

10.3. Coaxial Rotor Modelling

The rotor is the most important and complex aspect of any helicopter model, especially that of an unconventional type such as a coaxial rotor. The analysis and description of how the modelling of the coaxial rotor is described in this section.

Firstly, the rotor axes, planes and angles are defined in Section 10.3.1, followed by a description of general rotor parameters in Section 10.3.2, often used throughout the analysis. Thirdly, the blade flapping dynamics are discussed in Section 10.3.3. Extra attention is spent on the rotor inflows modelling in Section 10.3.4 due to the effects taking place in a coaxial configuration. Lastly, the forces and moments of the rotors are calculated in Section 10.3.5 and transformed to the body frame where their contributions are summarised in Section 10.3.6.

10.3.1. Rotor Axes, Planes and Angle Definitions

In the analysis of rotor dynamics and construction of a corresponding model, it is useful to define the various planes and axes of reference. There are three reference planes of interest, described hereafter, and depicted in Figure 10.5.

- Shaft Plane (SP): Also known as hub plane, has its axis perpendicular to the rotor shaft. This plane is the most convenient with respect to the equations of motion, since it only requires a transformation using the rotor shaft angle(s), if there are any.
- Disk Plane (DP): Or tip-path plane, is defined by the plane that the tips of the rotorblades produce.

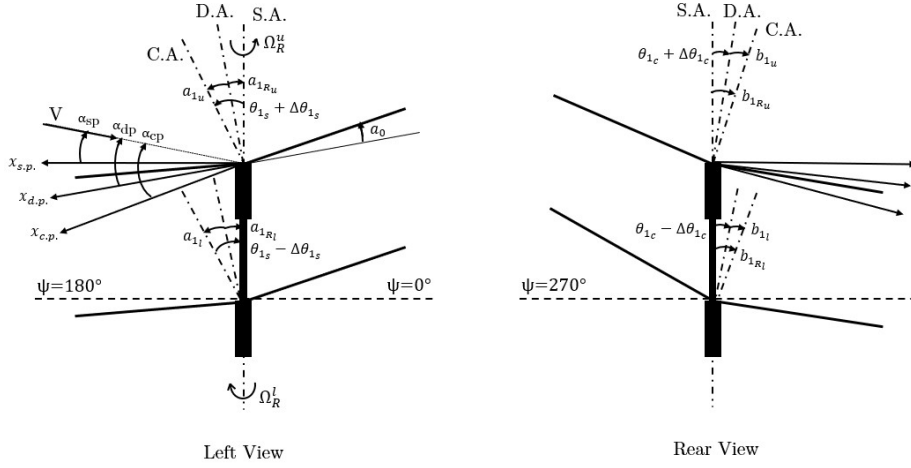


Figure 10.5: Rotor system depicting reference planes and definition of angles.

The thrust vector generated by the rotor is defined to be perpendicular to the disk-plane.

- Control Plane (CP): Also called the no-feathering plane, is a fictive one in flight. It is defined as the plane which would exist if no rotor flapping would occur. Therefore, it is used to define the flapping angles β relative to it.

Note that in hovering flight these planes coincide. Another remark can be made for a coaxial rotorcraft, since each plane is defined separately for the upper and lower rotor, producing a total of 6 reference planes.

In order to transform the rotor frame of reference, starting from the control plane, to the body frame, for proper analysis within the equations of motion. Firstly, the flapping angles are to be considered, inside the control plane. Although most helicopter blades are flexible, the ABC rotor is characterised by its stiff, yet not infinitely stiff, rotor blades. It is however customary to derive the flapping motion from the assumption of the blades being rigid bodies. This results in a periodic motion around the azimuth angle Ψ during steady-state operation, described by the following Fourier series:

$$\beta(\Psi) = a_0 - a_1 \cos \Psi - b_1 \sin \Psi - a_2 \cos 2\Psi - b_2 \sin 2\Psi - \dots \quad (10.6)$$

Here, β denotes the flapping angle, a_0 the mean of the flapping angle, known as the coning angle, the first and second longitudinal harmonics a_1 and a_2 , and lateral harmonics b_1 and b_2 . Throughout most flight dynamics analyses, the second order harmonics are omitted, except when elastic blade modes are being considered. [18] For consistency with the rigid body assumption made before, the second order harmonics are thus omitted from the model used in this thesis.

By means of common rotation matrices [18], the transformation matrix from the control plane to the disk plane \mathbb{T}_{dp}^{cp} can be calculated, resulting in:

$$\mathbb{T}_{dp}^{cp} = \mathbb{R}_y(a_1) \mathbb{R}_x(b_1) = \begin{bmatrix} \cos a_1 & \sin a_1 \sin b_1 & -\sin a_1 \cos b_1 \\ 0 & \cos b_1 & \sin b_1 \\ \sin a_1 & -\cos a_1 \sin b_1 & \cos a_1 \cos b_1 \end{bmatrix} \quad (10.7)$$

In order to transform the disk plane angle representation to the body plane, another transformation is required. This transformation requires the definition of the cyclic pitch angles a_{1R} and b_{1R} . These are calculated using the following equations:

$$\begin{aligned} a_{1R_u} &= \theta_{1s} + \Delta\theta_{1s} - a_{1u} & , & & a_{1R_l} &= \theta_{1s} - \Delta\theta_{1s} - a_{1l} \\ b_{1R_u} &= \theta_{1c} + \Delta\theta_{1c} + b_{1u} & , & & b_{1R_l} &= \theta_{1c} - \Delta\theta_{1c} + b_{1l} \end{aligned} \quad (10.8)$$



Note the distinction between upper and lower rotors in this case, since it becomes important to distinguish them due to the use of differential longitudinal cyclic $\Delta\theta_{1s}$ and differential lateral cyclic $\Delta\theta_{1c}$. Apart from the cyclic pitch angles, the rotor shaft angle γ_s is used in the transformation. Although it is theoretically possible to have a lateral rotor shaft angle, or separate shaft angles for upper and lower rotors, this is rarely done on real (coaxial) helicopters [18]. Therefore, this thesis will limit itself to the longitudinal rotor shaft angle γ_s .

Using the same rotation matrix definitions as before, the transformation matrix from the disk plane to the body plane \mathbb{T}_b^{dp} can be calculated, resulting in:

$$\begin{aligned} \mathbb{T}_b^{dp} &= \underline{R}_y(-a_{1R} - \gamma_s) \underline{R}_x(-b_{1R}) = \\ &= \begin{bmatrix} \cos(a_{1R} + \gamma_s) & \sin(a_{1R} + \gamma_s) \sin b_{1R} & \sin(a_{1R} + \gamma_s) \cos b_{1R} \\ 0 & \cos b_{1R} & -\sin b_{1R} \\ -\sin(a_{1R} + \gamma_s) & \cos(a_{1R} + \gamma_s) \sin b_{1R} & \cos(a_{1R} + \gamma_s) \cos b_{1R} \end{bmatrix} \end{aligned} \quad (10.9)$$

These rotation matrices can be used for both the upper and the lower rotor separately. Note that the lagging and feathering motion of the rotor blades is omitted in this study. For one, this is beyond the scope of this thesis, focusing on flight dynamics behaviour of the helicopter, and for two, since these motions are very small to non-existing in ABC-type rotors, justifying the assumption. [18]

10.3.2. General Rotor Parameters

Throughout future calculations, such as those described in Figure 10.13 in order to calculate thrust coefficients, several other parameters such as the local rotor angles of attack, the normalised airspeed components along the control plane, and the rotor permeability are used. These will be explained in the following paragraph.

Firstly, as can be seen in Figure 10.5, several rotor angles of attack are defined. The shaft plane angle of attack α_{sp} can directly be derived from the longitudinal and vertical airspeed components, u and w . The control plane angle of attack α_{cp} is then calculated by addition of the longitudinal cyclic control θ_{1s} and the consideration of the differential longitudinal cyclic $\Delta\theta_{1s}$, resulting in separate values for the upper and lower rotor. All these angles, including the angle relative to the disk plane, are given by Equation 10.10:

$$\begin{aligned} \alpha_{sp} &= \arctan\left(\frac{u}{w}\right) \\ \alpha_{cp_u} &= \alpha_{sp} + \theta_{1s} + \Delta\theta_{1s} \quad , \quad \alpha_{cp_l} = \alpha_{sp} + \theta_{1s} - \Delta\theta_{1s} \\ \alpha_{dp_u} &= \alpha_{cp_u} + a_{1u} \quad , \quad \alpha_{dp_l} = \alpha_{cp_l} + a_{1l} \end{aligned} \quad (10.10)$$

Secondly, there are several velocity components often used throughout the upcoming analyses. These are the advance ratio's μ_x and μ_z and the rotor permeability λ . The advance ratio's are in fact the airspeed components relative to the control plane, normalised by the rotor tip speed ΩR , and calculated by the following equation for the parallel and perpendicular components respectively.

$$\mu_x = \frac{V \cos \alpha_{cp}}{\Omega R} \quad , \quad \mu_z = \frac{V \sin \alpha_{cp}}{\Omega R} \quad (10.11)$$

The perpendicular advance ratio component μ_z is of high importance when calculating the airflow passing through the rotor disk when creating lift during forward flight.

Lastly, several geometric parameters of the rotors have to be discussed. These include the rotor disc area A , the rotor solidity σ , and the Lock number γ . The rotor disc area A is simply calculated by means of the area of a full circle

$$A = \pi \cdot R^2 \quad (10.12)$$

The rotor solidity σ describes how 'full' the rotor blade is. A higher solidity number signifies a disc which has more coverage of the inscribed circle than a lower solidity number. It can be calculated using

$$\sigma = \frac{Nc_e}{\pi R} \quad (10.13)$$



Where N are the number of blades in the rotor and c_e the equivalent chord area, defined by the chord of a rectangular blade with the same aerodynamic properties of the real blade.

Lastly, the Lock number represents the ratio of inertial and aerodynamic properties of the blade and is calculated using

$$\gamma = \frac{\rho C_{L\alpha} c_e R^4}{I_\beta} \quad (10.14)$$

Where ρ denotes the air density, $C_{L\alpha}$ the lift curve slope of the airfoil, and I_β the blade moment of inertia about its flapping hinge.

10.3.3. Blade Flapping Dynamics

The helicopter blade flapping motion is of paramount importance in any helicopter configuration and is highly dependent on the type of rotors used. It severely dictates the agility and stability of the helicopter bare airframe characteristics. In case of an ABC rotor, a hingeless configuration is used, with stiff blades. Throughout literature, this rotor tends to be modelled using an equivalent hinge-offset and spring-stiffness model, as depicted in Figure 10.6.

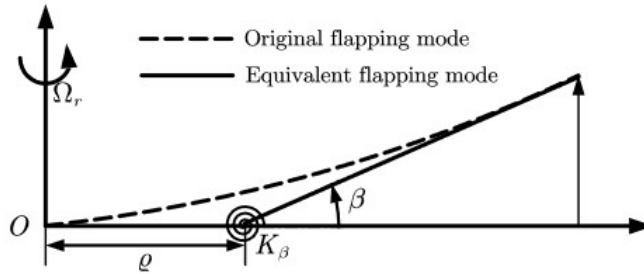


Figure 10.6: Equivalent blade flapping model using equivalent hinge-offset and spring-stiffness. [26]

In this model, K_β denotes the equivalent spring stiffness of the blade, which in the case of an ABC rotor is very high. ρ denotes the equivalent hinge-offset. Note that there is a very large difference between the equivalent hinge-offset ρ and the real hinge-offset e_b as used later in this section. ρ is merely used for the simulation of the blade flapping motion, in order to create a representable system.

In order to find the correct simulation parameters for the equivalent flapping model, the blade flapping frequency ω_f is calculated using Equation 10.15 and compared to values used in literature at the nominal rotor speed operating point. For example, Berger [60] calculated his ABC rotor to have a normalised flapping of 1.49/rev at a normalised rotor speed of 1. Note that compared to usual normalised flapping frequencies, ranging between 1.08-1.17 [18], this is a very high value. This indicates the high responsiveness of the ABC rotor.

$$\omega_f = \sqrt{1 + \frac{\rho M_\beta}{I_\beta} + \frac{K_\beta}{I_\beta \Omega^2}} \cdot \Omega \quad (10.15)$$

Here, the new variable M_β denotes the mass moment of inertia of the blade. In order to find the correct parameters for M_β and K_β , similar rotors throughout literature, such as Ferguson [28] and Padfield [18] have been studied, and tuned in order to find a similar value to that of Berger [60]. I_β was calculated using the moment of inertia for a rod approximation, as per Equation 10.16. Here, m_{bl} is the blade mass.

$$I_\beta = \frac{1}{3} m_{bl} R^2 \quad (10.16)$$

The resulting blade mode fan diagram is shown in Figure 10.7, where it can be seen that the 'Hinge and Spring' line corresponds nicely with the plot by Berger [60]. The corresponding parameters are listed in Table 10.2.

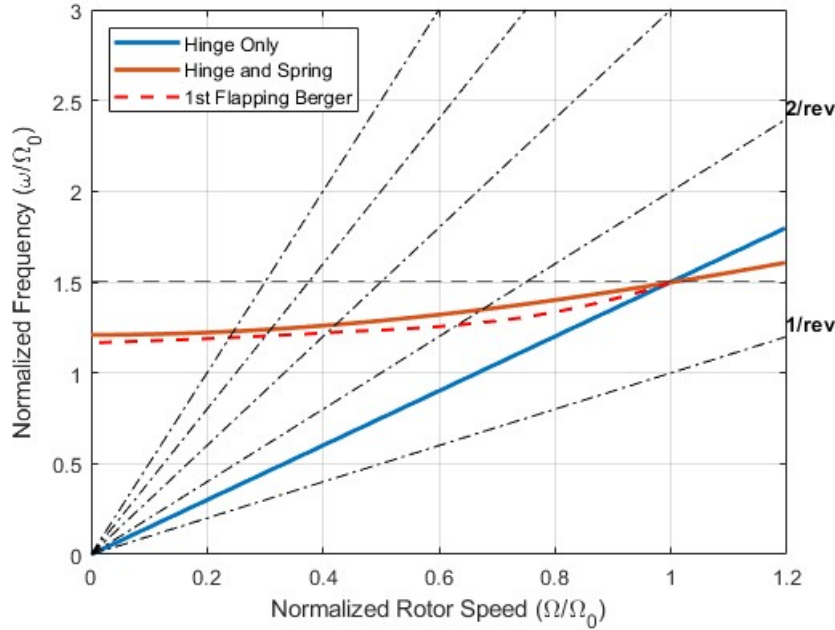


Figure 10.7: Blade mode fan diagram depicting the hinge and spring model, hinge only model, and validation data from Berger [60].

Table 10.2: Blade Flapping Model Parameters.

Parameter	Value	Unit
K_β	900 000	[N/m]
M_β	500	[kg m ²]
I_β	502	[kg m ²]
ϱ	0.04	[-]

Using the equivalent flapping model parameters, the flapping coefficients a_0 , a_1 and b_1 can be calculated. First, starting at the general differential equation for flapping motion [18]:

$$\ddot{\beta} + \beta = \frac{M_a}{I\Omega^2} \quad (10.17)$$

where M_a denotes the flapping aerodynamic moment, which is the heart of the flapping equation and can comprise out of many terms, depending on the aerodynamics and higher-order dynamics considered.

Due to the inherently difficult nature of solving this equation no equations showing the solution to the flapping coefficients have been found for the 6 degrees of freedom, forward flight, equivalent hinge-offset and spring stiffness model have been found in literature. It was also deemed beyond the scope of this thesis to derive these equations in these works. Therefore, it has been opted for to use the Bramwell flapping coefficients [61], for a 6 degrees of freedom, forward flight, hinge-offset with no spring stiffness model. However, as discussed before, there are large differences between the behaviour of these rotor types. Therefore, for the sake of the flapping coefficients calculation only, this model will be used. This assumption is only justifiable when the natural flapping frequencies at nominal rotor-speed are equal for the two models, which is shown to be true in Figure 10.7, looking at the 'hinge only' fan diagram. This frequency can be achieved using an equivalent hinge offset of 0.455. The natural frequency for an equivalent hinge-offset rotor with no spring can be calculated using Equation 10.18.



$$\omega_f = \sqrt{\left(1 + \frac{3e}{2(1-e)}\right)} \quad (10.18)$$

Several notes have to be made on how to solve the flapping differential equation, as per Equation 10.17:

- The fidelity of the equation can achieve high levels of complexity, depending on factors such as how high the order of derivatives are considered, and the fidelity of the underlying aerodynamics of the rotor blade elements. For this analysis, only up to the first derivative of the angles will be considered, as mentioned before, and steady aerodynamics are considered in the rotor lift modelling.
- For simulation-purposes, only the steady-state responses of the blades due to helicopter speed variations are considered. Faster motions, corresponding to blade motions due to control inputs, or fast motions corresponding to transients associated to eigenfrequencies are deemed beyond the scope of a flight-dynamics related thesis.
- It must be emphasised that the hinge-only flapping representation will only be used for the flapping angle calculation. For the rotor forces and moments, the actual equivalent spring stiffness and hinge offset values as listed in Table 10.2 will be used.

The derivation of how to solve the flapping equation will be omitted from this thesis, since it has been covered numerous times in the works of e.g. Simplicio [59], Aalst and Pavel [62], Pavel [61] and many others. The resulting 'Bramwell flapping angles' are one of the most simple and most used solutions to express the disc-tilt angles:

$$\begin{aligned} a_0 &= \frac{\gamma}{8} \left[\theta_0 (1 + \mu_x^2) + \frac{4}{3} \lambda + \frac{2}{3} \mu_x \bar{p} \right] \\ a_1 &= \frac{\frac{8}{3} \mu_x \theta_0 + 2 \mu_x \lambda + \bar{p} - \frac{16}{\gamma} \bar{q}}{1 - \frac{1}{2} \mu_x^2} \\ b_1 &= \frac{\frac{4}{3} \mu_x a_0 + \bar{q} - \frac{16}{\gamma} \bar{p}}{1 + \frac{1}{2} \mu_x^2} \end{aligned} \quad (10.19)$$

As can be seen, these equations still do not include the hinge-offset. Pavel [61] therefore uses the following set of equations, overcoming this shortcoming:

$$\begin{aligned} a_0 &= \frac{\gamma}{8\nu_\beta^2} \left[\theta_0 (1 + \mu_x^2) + \frac{4}{3} \lambda + \frac{2}{3} \mu_x \bar{p} + \theta_{tw} \left(\frac{4}{5} + \frac{2}{3} \mu_x^2 \right) - \frac{4}{3} \mu_x \theta_{1s} \right] \\ a_1 &= \frac{8}{\gamma} \frac{\nu_\beta^2 - 1}{1 - \frac{1}{2} \mu_x^2} b_1 + \frac{\frac{8}{3} \mu_x \theta_0 + 2 \mu_x \lambda + \bar{p} - \frac{16}{\gamma} \bar{q} + 2 \theta_{tw} \mu_x - \left(1 + \frac{3}{2} \mu_x^2\right) \theta_{1s}}{1 - \frac{1}{2} \mu_x^2} \\ b_1 &= -\frac{8}{\gamma} \frac{\nu_\beta^2 - 1}{1 + \frac{1}{2} \mu_x^2} a_1 + \frac{\frac{4}{3} \mu_x a_0 + \bar{q} - \frac{16}{\gamma} \bar{p} + \left(1 + \frac{1}{2} \mu_x^2\right) \theta_{1c}}{1 + \frac{1}{2} \mu_x^2} \end{aligned} \quad (10.20)$$

Many other, higher fidelity sets of equations are derived throughout literature, using many higher-order coupling terms. However, these are beyond the scope of this thesis, and only contribute a relatively small overall steady-state effect on the disc-tilt angles. However, in order to at least get some correction for these small discrepancies, a correction factor can be applied [61]:

$$K_{\text{corr}} = \frac{1.33 \mu_x / |\lambda|}{1.2 + \mu_x / |\lambda|} \quad (10.21)$$

This correction factor K_{corr} takes into account non-uniformity effects of the induced velocity over the rotor disc. This correction is often implemented in the lateral disc-tilt angle b_1 , resulting in:

$$b_1 = -\frac{8}{\gamma} \frac{\nu_\beta^2 - 1}{1 + \frac{1}{2} \mu_x^2} a_1 + \frac{\frac{4}{3} \mu_x a_0 + \bar{q} - \frac{16}{\gamma} \bar{p} + \left(1 + \frac{1}{2} \mu_x^2\right) \theta_{1c} + K_{\text{corr}} \lambda_0}{1 + \frac{1}{2} \mu_x^2} \quad (10.22)$$



10.3.4. Inflow Modelling

As mentioned before, the calculation of the inflow ratio λ_0 is of utmost importance for the thrust calculation of a rotor. An outline of the inflow calculation scheme, resulting in the rotor forces which are calculated in Section 10.3.5, is visualised in Figure 10.8 below:

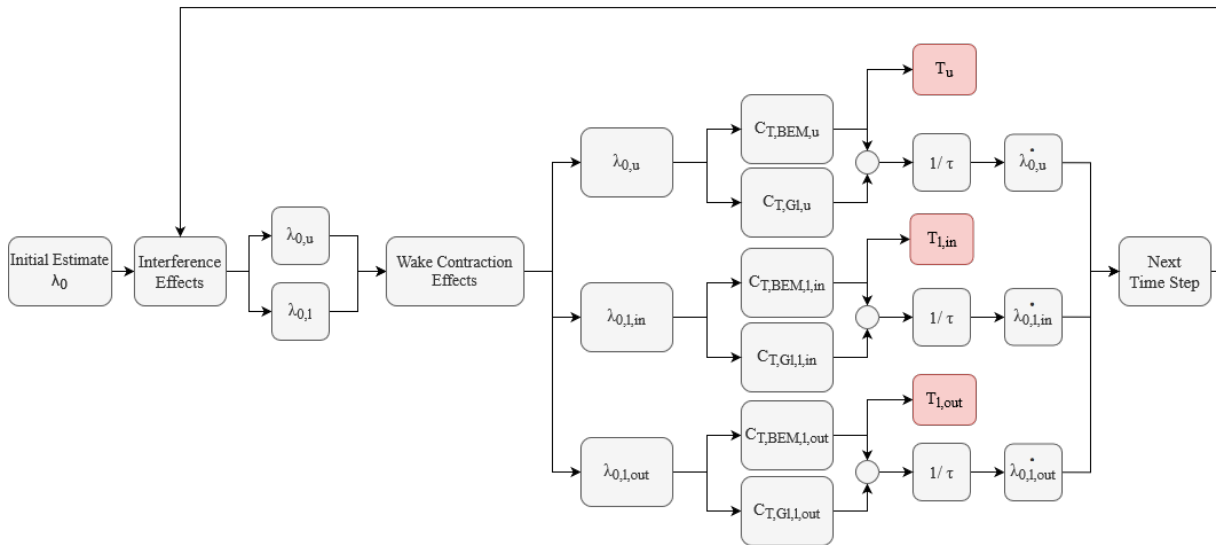


Figure 10.8: Flow-diagram of the discrete time-step inflow calculation.

Glauert’s Actuator Disk Theory

As explained in Chapter 5 in the literature study, use will be made of the simple momentum theory, which is based on the actuator-disc concept. A synopsis on this theory will be given in the following, followed by the implementation description.

Although the real flow over helicopter rotor blades can be of nonlinear and unsteady nature in real conditions, it is more than satisfactory to assume a steady, linearly varying inflow, or even constant (mean) inflow over the rotor blades for the purpose of flight dynamics analysis. [18] Glauert proposed an analysis based on momentum theory in order to calculate the inflow in this way, using the actuator disc concept, as visualised in Figure 10.9. An actuator disc is a disc with an infinitesimally thin thickness which can produce an instantaneous pressure difference in order to accelerate air through it. The ‘disc’ assumes an infinite number of blades.

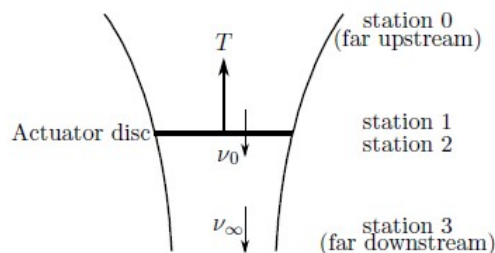


Figure 10.9: Actuator disk theory model during hover.

Using the conservation of mass theory, it can be stated that the mass flow along the wake is constant and equal to $\dot{m} = \rho A \nu_0$ where A is the disc area and ν_0 the velocity over the disc. Applying the conservation of momentum theory, and understanding that the flow is at rest far upstream the disc, the momentum theory can provide the formula for the thrust T over the disc:

$$T = \dot{m} \nu_\infty = \rho A \nu_0 \nu_\infty \tag{10.23}$$



where ν_∞ is the flow velocity far downstream the disc. When applying Bernoulli's equation to the system between station 0 and 1 and 2 and 3 respectively, we find:

$$p_0 = p_1 + \frac{1}{2}\rho\nu_0^2 \quad p_2 + \frac{1}{2}\rho\nu_0^2 = p_0 + \frac{1}{2}\rho\nu_\infty^2 \quad (10.24)$$

combining these results in:

$$p_2 - p_1 = \frac{1}{2}\rho\nu_\infty^2 \quad (10.25)$$

The increase in pressure between stations 1 and 2 can be said to come from the disc loading T/A , resulting in:

$$p_2 - p_1 = \frac{T}{A} \Leftrightarrow \frac{1}{2}\rho\nu_\infty^2 = \rho\nu_0\nu_\infty \Leftrightarrow \nu_\infty = 2\nu_0 \quad (10.26)$$

If this result is applied in the equation for thrust, Equation 10.23, it can be found that:

$$T = 2\rho A\nu_0^2 \quad (10.27)$$

A well known result from the actuator-disc theory. When considering the actuator disc at a certain flight velocity V , under a specific disc plane angle of attack α_{dp} , as illustrated in Figure 10.10, we can find that instead of the flow upstream simply being equal to ν_0 , it now becomes $\sqrt{(V \cos \alpha_{dp})^2 + (V \sin \alpha_{dp} + \nu_0)^2}$. Applying the momentum conservation thrust equation, we get:

$$T = \dot{m}\nu_\infty = 2\rho A\nu_0\sqrt{(V \cos \alpha_{dp})^2 + (V \sin \alpha_{dp} + \nu_0)^2} \quad (10.28)$$

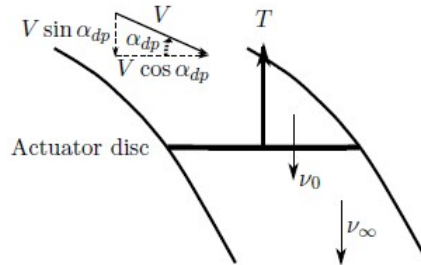


Figure 10.10: Actuator disk theory model during forward flight.

Non-dimensionalising this result, we find the thrust coefficient C_T^{Gl} , where the superscript Gl denotes that the thrust calculation is based on the Glauert actuator-disc momentum theory:

$$C_T^{Gl} = 2\lambda_0\sqrt{(\mu \cos \alpha_{dp})^2 + (\mu \sin \alpha_{dp} + \lambda_0)^2} \quad (10.29)$$

where μ is the dimensionless velocity and equal to $\mu = V/\Omega R$ and $\lambda_0 = \nu_0/\Omega R$ the dimensionless inflow velocity, better known as the inflow ratio.

Quasi-Dynamic Inflow

However, Equation 10.29 still holds 2 unknowns, the inflow ratio and the thrust coefficient. In order to be able to solve this, use is made of the quasi-dynamic inflow method. The quasi-dynamic inflow method uses a time constant τ_{λ_0} and the dynamic change in time of the inflow ratio, $\dot{\lambda}_0$. It calculates the difference between the blade element method thrust calculation and the Glauert thrust calculation using an initial

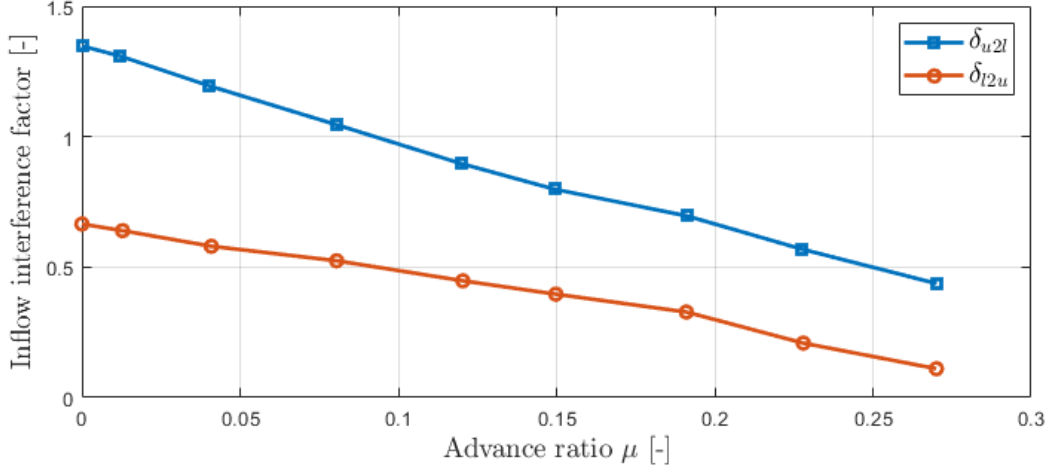


Figure 10.11: Variation of inflow interference with advance ratio from the CFD simulation results by Zhou et al. [37]

value for the inflow. If this value is off, it corrects itself in the next timestep of the discrete simulation. The change in mean inflow can then be calculated using:

$$\dot{\lambda}_0 = \frac{C_T^{BEM} - C_T^{CI}}{\tau_{\lambda_0}} \quad (10.30)$$

Note that a separate inflow parameter is used for the upper and lower rotor respectively.

In the literature study, a method describing the modelling of a linearly-varying inflow has been described using Glauert's approach [35]. This model makes it possible to provide a longitudinal and lateral linear distribution of the inflow along the rotor, and provides the possibility for spanwise analysis of the thrust and lift-coefficients of the rotor disc. This can prove useful when analysing effects such as mach effects along the rotor, and the local effects of differential lateral and longitudinal cyclic inputs. However, in the flight dynamics model used in this thesis, it was provided redundant and beyond the thesis scope, since only the mean inflow and thrust are used. It is however also implemented in the accompanying thesis MATLAB code, and can thus be used in future iterations of this work.

Rotor Interference

Since the model under analysis is a coaxial model, the upper and lower rotor's wakes influence each others inflow significantly. These effects can be accounted for using an attenuation factor δ_{l2u} and δ_{u2l} for the influence from the lower to upper rotor and upper to lower rotor respectively, which result in the inflow ratios:

$$\begin{cases} \lambda_{0_u} = \lambda'_{0_u} + \delta_{l2u} \lambda'_{0_l} \\ \lambda_{0_l} = \lambda'_{0_l} + \delta_{u2l} \lambda'_{0_u} \end{cases} \quad (10.31)$$

where λ_0 denotes the inflow after interference effects, and λ'_0 the mean inflow before interference effects, resulting from the quasi-dynamic inflow, for the upper and lower rotor respectively.

Several approaches to calculating the attenuation factors δ_{l2u} and δ_{u2l} have been proposed by Zhou et al. [37] and Saito and Azuma [22], which have been discussed extensively in the literature study.

The pragmatic approach used in this work is based on that of Zhou et al. [37], in which the variation of the attenuation, or interference factors, changes with advance ratio due to the shift in wake skew angle χ . Zhou et al's CFD analysis resulted in the interference effects depicted in Figure 10.11.

These results are then linearly approximated using Equation 10.32, using the fact that the interference goes to 0 with increasing advance ratio:



$$\begin{cases} \delta_{l2u} = -2.15\mu + 0.68 & \text{for } 0 \leq \mu \leq 0.316 \\ \delta_{l2u} = 0 & \text{for } \mu > 0.316 \\ \delta_{u2l} = -3.81\mu + 1.45 & \text{for } 0 \leq \mu \leq 0.381 \\ \delta_{u2l} = 0 & \text{for } \mu > 0.381 \end{cases} \quad (10.32)$$

An important note must be made on the numerical implementation of the rotor interference. During linearisation and trimming of the model, the interference factor from the upper to lower rotor is set to a constant value of 1, and that of the lower to upper to a value of 0. This further approximation was made due to the abrupt change from the linear function in Equation 10.32 at the point from where the interference factors become 0 with higher advance ratio. The abrupt change in slope of the graph resulted in numerical discrepancies, which led to the shift in sign of the slope of the stability derivatives, at this specific point, which is physically inaccurate. Therefore, the models were trimmed and linearised using the values 1 and 0 for the interference factors, while the original interference coefficients are used throughout simulation examples. It is recommended that this issue receives further investigation if the user desires an improved fidelity of the rotor interference effects.

An important difference between a single-rotor and a coaxial rotor has to be distinguished. In the coaxial rotor configuration, the Glauert thrust coefficient should take into account the rotor interference as defined above, which changes Equation 10.30 to the following pair of equations:

$$\begin{aligned} C_{T_u}^{Gl} &= 2\lambda_0^u \sqrt{\left(\mu \cos \alpha_u^{dp}\right)^2 + \left(\mu \sin \alpha_u^{dp} + \lambda_0^u + \delta_{l2u} \lambda_0^l\right)^2} \\ C_{T_l}^{Gl} &= 2\lambda_0^l \sqrt{\left(\mu \cos \alpha_l^{dp}\right)^2 + \left(\mu \sin \alpha_l^{dp} + \lambda_0^l + \delta_{u2l} \lambda_0^u\right)^2} \end{aligned} \quad (10.33)$$

Using the separate inflows of the upper and lower rotors, the rotor permeability in the disk plane, λ_{dp_u} and λ_{dp_l} , and the inflow ratio's λ_u and λ_l can be calculated using Equation 10.34 and Equation 10.35 respectively.

$$\begin{aligned} \lambda_{dp_u} &= \frac{V}{\Omega R} \sin \alpha_{dp_u} - \lambda_{0_u} \\ \lambda_{dp_l} &= \frac{V}{\Omega R} \sin \alpha_{dp_l} - \lambda_{0_l} \end{aligned} \quad (10.34)$$

$$\begin{aligned} \lambda_u &= \frac{\mu_z - \lambda_{0_u}}{2} \\ \lambda_l &= \frac{\mu_z - \lambda_{0_l}}{2} \end{aligned} \quad (10.35)$$

Wake Contraction

In the literature study, a formal assessment of whether or not the wake contraction should be taken into account was made. A calculation was made based on the XH-59A's rotor parameters, and resulted in the fact that 76% of the lower rotor was influenced by the upper rotor's wake, and that this proved some accuracy gain to be made when modelling these effects. This calculation was redone for a helicopter similar to the SB-1 Defiant, from which the values were reverse engineered from 3-view drawings, resulting in a wake contraction of only 13%, causing 87% of the lower rotor to be affected by the upper rotor. This effect is visualised more closely in Figure 10.12.

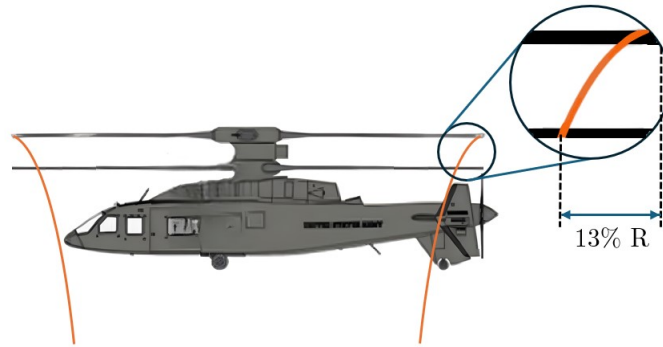


Figure 10.12: Wake contraction from upper to lower rotor in an ABC rotor configuration.

However, various other researchers such as Ferguson [28], Berger [60], and Yuqing Qiu [26] all stated that due to the ABC rotor's stiff blades, the rotors could be placed closer together than conventional coaxial rotor configuration such as those used in the Kamov-series. [5] Due to this small rotor-spacing, they assumed that the wake would not contract enough for it to be taken into account.

Therefore, it was decided that wake contraction effects will not be taken into account in the modelling of the rotor inflow. Further iterations trying to increase the inflow fidelity of the rotor could make use of the theory described in the literature study in order to implement it. Arguments can be made that the value of 87% is significant enough to model these effects. If one would choose to model the wake contraction, the lower rotor inflow would be split into 2 factors, that including interference effects λ_{0_i} , and that excluding interference effects λ'_{0_i} . Note that this area of influence of the interference also shifts with increasing advance ratio, up to the point where the wake is detached from the upper rotor due to the wake skew angle χ . This would also have to be accounted for.

10.3.5. Rotor Forces and Torque

The rotor forces can be split up into 3 forces for the 6 degrees of freedom model: the thrust force T , the longitudinal drag-force component, also known as H-force H , and the accompanying lateral drag force component, the S-force S , as shown in Figure 10.13. Note that the rotor is assumed to be in a small flapping angle β which allows the small angle approximation, resulting in a purely vertically aligned (in the Y-Z plane) thrust vector of the rotor blade. This in turn results in the drag force being perpendicular to the blade, which can be decomposed into H and S . Alongside this, a rotor torque Q is present. All of these forces and torques are present for both the upper and lower rotor separately.

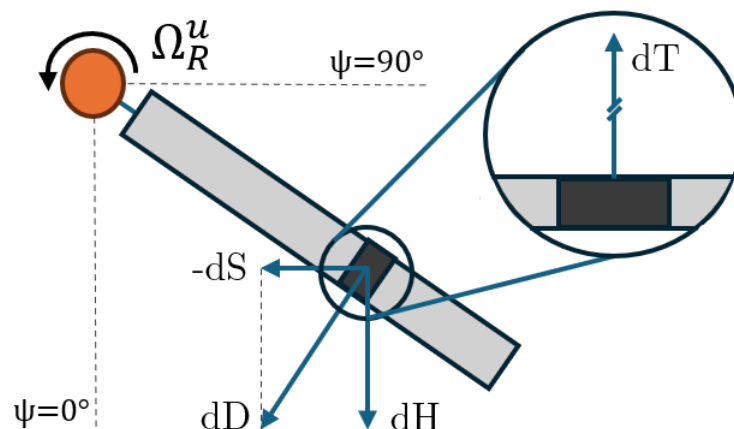


Figure 10.13: Forces acting on the rotor blade. (Illustrated for the upper rotor, same principle applies to lower rotor)



Using blade-element theory, these forces can be calculated with respect to the control-plane. The derivation of these equations is omitted from this scripture due to ample literature being available to describe it, such as those available in Padfield [18] or Leishman [19]. The forces can be transformed from the control plane to the disc plane using the following transformation [59]:

$$\underline{f}_{mr,dp} = \underline{T}_{dp}^{cp} \underline{f}_{mr,cp} \Leftrightarrow \begin{bmatrix} H_{dp} \\ S_{dp} \\ T_{dp} \end{bmatrix} = \begin{bmatrix} \cos a_1 & \sin a_1 \sin b_1 & -\sin a_1 \cos b_1 \\ 0 & \cos b_1 & \sin b_1 \\ \sin a_1 & -\cos a_1 \sin b_1 & \cos a_1 \cos b_1 \end{bmatrix} \begin{bmatrix} H \\ S \\ T \end{bmatrix} \quad (10.36)$$

Using a small angle approximation, which is viable due to the small flapping coefficients and the fact that normally $T \gg S, H$, the following approximations hold:

$$\begin{aligned} C_{T_{dp}} &\approx C_T \\ C_{H_{dp}} &\approx C_H - C_T a_1 \\ C_{S_{dp}} &\approx C_S - C_T b_1 \end{aligned} \quad (10.37)$$

Likewise, the torque coefficient in the control axis corresponds approximately to that in the disc axis, giving:

$$C_{Q_{dp}} \approx C_Q \quad (10.38)$$

The resulting blade-element analysis for the rotor-forces and torque result in the following set of equations, which was simplified by Pavel [61], and appended in order to suit the extra controls for differential collective:

$$C_{T_{dp}} = \frac{\sigma C_{L\alpha}}{2} \left[\left(\frac{1}{3} + \frac{\mu_x^2}{2} \right) (\theta_0 \pm \Delta\theta_0) + \frac{1 + \mu_x^2}{8} \theta_{tw} + \frac{\mu_x \bar{p}}{4} + \frac{\lambda}{2} \right] \quad (10.39)$$

$$\begin{aligned} C_{H_{dp}} &= \sigma C_D \frac{\mu_x}{4} + \frac{\sigma C_{L\alpha}}{4} \left[\left(a_1 \frac{\mu_x^2}{2} + \mu_x \lambda \right) (\theta_0 \pm \Delta\theta_0) + \frac{\mu_x \lambda}{2} \theta_{tw} + \right. \\ &\quad \left. + \bar{q} \left(\frac{b_1 \mu_x}{4} - \frac{a_0}{3} \right) - \frac{a_0 b_1}{3} + (a_0^2 + a_1^2) \frac{\mu_x}{2} + \frac{\bar{p} \lambda}{2} \right] \end{aligned} \quad (10.40)$$

$$\begin{aligned} C_{S_{dp}} &= \frac{\sigma C_{L\alpha}}{4} \left[-\frac{1}{2} \mu_x a_0 (\theta_0 \pm \Delta\theta_0) + \left(-a_0 \frac{\mu_x}{3} + b_1 \frac{\mu_x^2}{4} - \frac{\bar{q}}{4} \right) \theta_{tw} - \right. \\ &\quad \left. - 3a_0 \mu_x (\mu_x a_1 - \lambda) + b_1 \frac{\mu_x a_1 - \lambda}{2} + a_0 a_1 \frac{\mu_x^2 + 1}{3} \right] \end{aligned} \quad (10.41)$$

$$C_{Q_{dp}} = \sigma \left[\frac{C_D}{8} (1 + 4.7\mu_x^2) - C_{T_{dp}} \lambda_{dp} - C_{H_{dp}} \mu_x \right] \quad (10.42)$$

The final forces and torque can then be dimensionalised by $T = \rho A (\Omega R)^2 C_T$, $H = \rho A (\Omega R)^2 C_H$, $S = \rho A (\Omega R)^2 C_S$ and $Q = \rho A (\Omega R)^2 R C_Q$. Note that the sign of Q for the lower rotor is opposite to that of the upper rotor.

10.3.6. Global Contribution

The contribution of the rotor forces to the overall system can be calculated by using the transformation matrix from the disc plane to the body plane \mathbb{T}_b^{dp} , as described in Equation 10.9. Applied to the rotor forces, this results in:

$$\begin{aligned} \underline{f}_{mr} &= \begin{bmatrix} X_{mr} \\ Y_{mr} \\ Z_{mr} \end{bmatrix} = \underline{T}_b^{dp} \underline{f}_{mr,dp} = \\ &= \begin{bmatrix} \cos(a_{1R} + \gamma_s) & \sin(a_{1R} + \gamma_s) \sin b_{1R} & \sin(a_{1R} + \gamma_s) \cos b_{1R} \\ 0 & \cos b_{1R} & -\sin b_{1R} \\ -\sin(a_{1R} + \gamma_s) & \cos(a_{1R} + \gamma_s) \sin b_{1R} & \cos(a_{1R} + \gamma_s) \cos b_{1R} \end{bmatrix} \begin{bmatrix} -H_{dp} \\ S_{dp} \\ -T_{dp} \end{bmatrix} \end{aligned} \quad (10.43)$$



this transformation has to be applied to the upper and lower rotor separately, for its own forces and flapping coefficients respectively, summing the totals:

$$\vec{F}_{mr_{tot}} = \begin{bmatrix} X_{mr_{tot}} \\ Y_{mr_{tot}} \\ Z_{mr_{tot}} \end{bmatrix} = \begin{bmatrix} X_{mr_u} \\ Y_{mr_u} \\ Z_{mr_u} \end{bmatrix} + \begin{bmatrix} X_{mr_l} \\ Y_{mr_l} \\ Z_{mr_l} \end{bmatrix} \quad (10.44)$$

For the moments, the forces times their moment arm has to be taken into account, supplemented by the rotor torque $C_{Q_{dp}}$, the hinge-offset moments in pitch and roll axis L_e and M_e , and the spring-stiffness moments L_k and M_k . This results in the total rotor moment contribution:

$$\vec{M}_{mr} = \begin{bmatrix} L_{mr} \\ M_{mr} \\ N_{mr} \end{bmatrix} = \begin{bmatrix} L_e + L_k \\ M_e + M_k \\ Q_{dp} \end{bmatrix} + \begin{bmatrix} -l \\ -l_1 \\ -h \end{bmatrix} \times \vec{F}_{mr_{tot}} = \begin{bmatrix} L_e + L_k + hY_{mr} - l_1Z_{mr} \\ M_e + M_k - hX_{mr} + lZ_{mr} \\ Q_{dp} + l_1X_{mr} - lY_{mr} \end{bmatrix} \quad (10.45)$$

Again, summing the contributions of the separate rotors gives the total resulting moment set:

$$\vec{M}_{mr_{tot}} = \begin{bmatrix} L_{mr_{tot}} \\ M_{mr_{tot}} \\ N_{mr_{tot}} \end{bmatrix} = \begin{bmatrix} L_{mr_u} \\ M_{mr_u} \\ N_{mr_u} \end{bmatrix} + \begin{bmatrix} L_{mr_l} \\ M_{mr_l} \\ N_{mr_l} \end{bmatrix} \quad (10.46)$$

The hinge-offset moments L_e and M_e are described by Pavel [63] and calculated by:

$$\begin{aligned} L_e &= (\Omega R)^2 \varepsilon_{\beta} m_{bl} \sin b_{1r} \\ M_e &= (\Omega R)^2 \varepsilon_{\beta} m_{bl} \sin (a_{1r} + \gamma_s) \end{aligned} \quad (10.47)$$

and the spring-stiffness moments L_k and M_k by [63]:

$$\begin{aligned} L_k &= \frac{1}{2} N K_b \sin(b_{1r}) \\ M_k &= \frac{1}{2} N K_b \sin(a_{1r} + \gamma_s) \end{aligned} \quad (10.48)$$

The parameters for the main rotors are summarised in the following table:

Table 10.3: Upper and lower rotor planform parameters.

Main Rotor Parameters	Symbol	Value	Unit
Lift curve slope	$c_{l_{\alpha}}$	5.7	-
Blade chord	c	0.257	m
Rotational velocity	ω	207	rad/s
Radius	R	1.1	m
Amount of blades - Upper, lower	N_u, N_l	4, 4	-
Lock number	γ	6.57	-
Solidity Ratio	σ_p	0.153	-
Aerodynamic Interference Factor	K_p	0.4	-
X-distance from C.G. - Upper, lower	l_u, l_l	0, 0	m
Z-distance from C.G. - Upper, lower	h_u, h_l	1.66, 0.77	m
Y-distance from C.G. - Upper, lower	d_u, d_l	0, 0	m
Blade twist	θ_{twist}^p	-10	deg
Shaft angle	γ_s	0	deg



10.3.7. Rotor RPM Scheduling

One last aspect of the rotor modelling that should be discussed is the use of RPM scheduling. In order to make sure the rotor tip speed stays below the drag divergence limits, the rotor RPM can be throttled down at high flight speeds.

However, due to numerical issues encountered during the implementation of this effect, it was decided to be left out of the thesis. The RPM scheduling caused a sudden change in slope for the control and stability derivatives, causing sudden spikes in the values which did not make physical sense.

Altogether, omitting the RPM scheduling should not impact the flight dynamics results much, especially since the focus of this thesis is in the transition region.

10.4. Pusher Propeller Modelling

The pusher propeller aims to provide the rotorcraft with extra thrust during high-speed flight to reach higher speeds while offloading the main rotors and overcome fuselage drag. While modelling the pusher propeller, several aspects allow for simplifications:

- Due to the stiff blades and high rotational speeds, ranging between 2000-2500 RPM [26], the blade dynamics can be neglected.
- While it is possible to model 2D cyclic pitches in order to aid control in pitch and yaw, it is chosen not to implement this in the model. Various studies have analysed the effects of implementing pitch and/or yaw [41] effects of the pusher propeller. While marginal gains in power curves can be made with proper scheduling of the controls, these only range between 2-3%. It is also not the main focus of a general analysis of a compound coaxial rotorcraft, hence it is omitted. It might however be interesting to study these effects in a future iteration of this work.
- The effect of the main rotor wake passing over the pusher propeller in certain flight speed ranges has not been modelled. Although correction factors have been used.

10.4.1. Inflow and Thrust Modelling

The inflow of the pusher propeller is done in a similar manner to that of the main rotor. It is based on quasi-dynamic inflow, according to:

$$\dot{\lambda}_{0_p} = \frac{C_{T_p}^{BEM} - C_{T_p}^{GI}}{\tau \lambda_{0_p}} \quad (10.49)$$

The advance ratio of the pusher propeller, μ_x^p is influenced by all 3 airspeed components, the inflow λ_0^p , pitch rate q and the correcting factor $K_p \Omega R (\delta_{l2u} \lambda_0^u + \delta_{u2l} \lambda_0^l)$ for the wake passing over the pusher propeller, affecting the vertical velocity component along the propeller disc, and can be calculated using Equation 10.50. The effect of the aerodynamic interference, accounted for by K_p is visualised in Figure 10.14.

$$\mu_x^p = \frac{\sqrt{v^2 + (w + K_p \Omega R (\delta_{l2u} \lambda_0^u + \delta_{u2l} \lambda_0^l) + ql_p)^2}}{\Omega_p R_p} \quad (10.50)$$

The permeability of the pusher propeller is given by Equation 10.51, in which it can be seen that the airflow also adjusts the permeability by means of the angular rates and corresponding moment arms.

$$\lambda_p = -\frac{u + qh_p - rd_p}{\Omega_p R_p} - \lambda_0^p \quad (10.51)$$

The thrust coefficient for the pusher propeller according to the blade element theory, and Glauert theory, $C_{T_p}^{BEM}$ and $C_{T_p}^{GI}$ respectively, can then be calculated according to:

$$C_{T_p}^{BEM} = \frac{\sigma_p c_{l\alpha_p}}{2} \left(\left(\frac{1}{3} + \frac{\mu_x^{p2}}{2} \right) \theta_p + \frac{1 + \mu_x^{p2}}{8} \theta_{twist}^p + \frac{\lambda_p}{2} \right) \quad (10.52)$$

$$C_{T_p}^{GI} = 2\lambda_0^p \sqrt{\mu_x^p \sin \alpha_p^{sp2} + \mu_x^p \cos \alpha_p^{sp} + \lambda_0^{p2}}$$

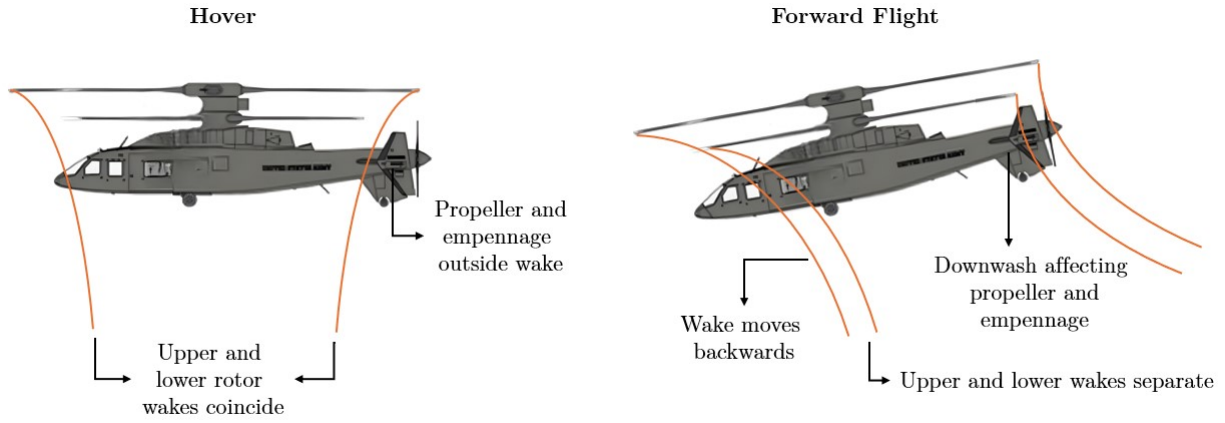


Figure 10.14: Aerodynamic interference over the propeller and empennage caused by rotor wakes.

where $\alpha_p^{sp} = \arctan(w/u)$ is the shaft plane angle of attack of the pusher propeller,

The thrust of the pusher propeller can then be calculated by $T_p = C_{T_p}^{BEM} \rho (\Omega_p R_p)^2 \pi R_p^2$.

10.4.2. Global Contribution

The total contribution of the pusher propeller in terms of forces and moments can be summed as follows. In fact, the pusher propeller is modelled as such, that it only produces an X-force component, which goes right through the origin, and thus not contribute to any moments besides it's torque moment.

$$\vec{F}_p = \begin{bmatrix} X_p \\ Y_p \\ Z_p \end{bmatrix} = \begin{bmatrix} T_p \\ 0 \\ 0 \end{bmatrix} \quad (10.53)$$

$$\vec{M}_p = \begin{bmatrix} L_p \\ M_p \\ N_p \end{bmatrix} = \begin{bmatrix} Q_p \\ T_p h_p \\ T_p d_p \end{bmatrix} \quad (10.54)$$

The torque moment Q_p can be calculated by $Q_p = \rho A (\Omega R)^2 R C_{Q_p}$ for which C_{Q_p} is calculated in a similar manner to that of the rotor in Equation 10.42.

The final pusher propeller parameters used in this thesis are summarized in the table below:

**Table 10.4:** Pusher propeller planform parameters.

Pusher Propeller Parameters	Symbol	Value	Unit
Lift curve slope	$c_{l_{\alpha_p}}$	5.7	-
Drag coefficient	c_{d_p}	0.19	-
Rotational velocity	ω_p	207	rad/s
Radius	R_p	1.1	m
Amount of blades	N_p	6	-
Blade chord	c_p	0.2	m
Solidity Ratio	σ_p	0.142	-
Aerodynamic Interference Factor	K_p	0.4	-
Location on x-axis	l_p	7.66	m
Location on z-axis	h_p	0	m
Location on y-axis	d_p	0	m
Blade twist	θ_{twist}^p	-30	deg

10.5. Empennage Modelling

Another special feature of this type of compound helicopter is the usage of a full empennage. This includes a horizontal and vertical stabiliser, with partly moving elevator and rudder. Note that the parameters can easily be changed in order to get e.g. a full moving elevator. A separate fixed horizontal and vertical tail, and elevator and rudder has been opted for in the model for increased flexibility for future usage, and for stability and control derivative validation purposes.

10.5.1. Lift Calculation Horizontal, Vertical, Elevator and Rudder

Both the horizontal and vertical tail are modelled by means of the simple lift equation as shown in Equation 10.55. Here, V_h and V_v are the local airspeed as seen by the surface, S_h and S_v the surface area's, and C_{l_h} and C_{l_v} the lift coefficients.

$$\begin{aligned} L_h &= \frac{1}{2} \rho V_h^2 S_h C_{l_h} \\ L_v &= \frac{1}{2} \rho V_v^2 S_v C_{l_v} \end{aligned} \quad (10.55)$$

The airspeed components V_h and V_v are influenced by the body dynamics of the helicopter, and the accompanying location of the tail surfaces. It's effect can be accounted for by using kinematics in the calculation of the airspeed components:

$$\begin{aligned} V_h &= \sqrt{u^2 + (w + ql_h)^2} \\ V_v &= \sqrt{u^2 + (v + ph_v - rl_v)^2} \end{aligned} \quad (10.56)$$

The lift curve slopes are normally assumed to have a constant value for stabilisers. However, due to the addition of the elevator and rudder, this changes. An elevator or rudder deflection, can in fact be seen in the same principle in which flaps work in a fixed-wing aircraft, as depicted in Figure 10.15. They alter the chord line for the airfoil, increasing the effective angle of attack, and thereby causing a vertical translation of the lift curve slope. This translation is positive for positive air surface deflections, and negative for negative deflections. Note that this also depends on the type of slot that is used in the elevator and rudder. It is assumed that a slotted flap is used. If a plain flap were to be used, the effects of decreased stall angle of attack might also be modelled. Mathematically, this can modelled by Equation 10.57. $dC_{l_{\alpha_h}}/d\delta_e$ is the lift curve factor of the elevator, and $dC_{l_{\beta_h}}/d\delta_r$ that of the rudder.

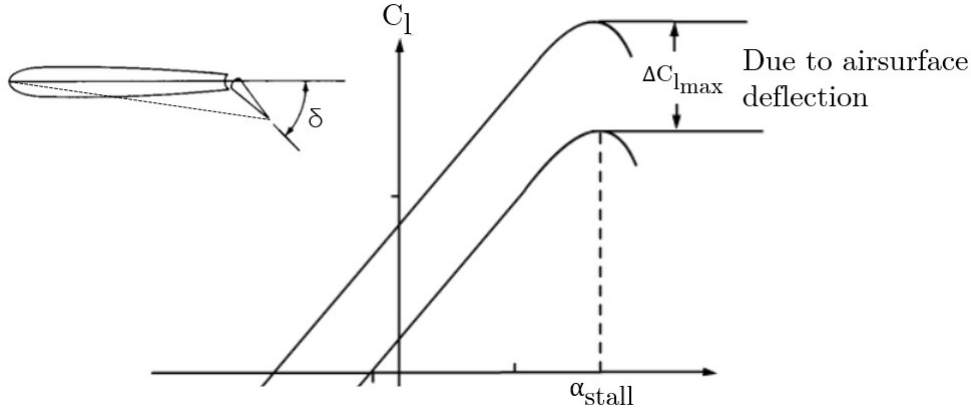


Figure 10.15: Upward shift in lift curve with positive airsurface deflection.

$$C_{l_h} = C_{l_{\alpha_h}}(\alpha_h) + \frac{dC_{l_{\alpha_h}}}{d\delta_e} \delta_e \quad (10.57)$$

$$C_{l_h} = C_{l_{\beta_v}}(\beta_v) + \frac{dC_{l_{\beta_v}}}{d\delta_r} \delta_r$$

Lastly, the angle of attack as seen by the aerosurfaces are calculated in Equation 10.58. α_{h_0} and β_{v_0} are the tail incidence angles. Note the factor $K_h \epsilon_0$ which is used in the calculation for α_h . This is the average downwash angle over the horizontal tail, for which K_h is a constant, and $\epsilon_0 = \nu_0/V$. Here ν_0 is the inflow velocity, which is the dimensionalised inflow ratio. This is modelled as the sum of the inflows of the upper and lower rotor, λ_u and λ_l .¹ In reality, a separate correction factor K_h should be used for the upper and lower rotor, since the rotors are spaced vertically, and their wakes thus do not impede the horizontal tail at the same velocities. However, due to their close spacing, it is assumed that they are co-planar.

$$\alpha_h = \tan^{-1} \left(\frac{w + ql_h}{u} \right) + \alpha_{h_0} - K_h \epsilon_0 \quad (10.58)$$

$$\beta_v = \tan^{-1} \left(\frac{v + ph_v - rl_v}{u} \right) + \beta_{v_0}$$

A note should be made about the calculation of the lift coefficients C_{l_h} and C_{l_v} of the stabilisers. During more extreme manoeuvring, the angle of attack as seen by the airfoil can become quite large. In reality, this causes airflow separation and thus stall. This stall is pragmatically modelled by truncating the lift coefficients at a specific angle of attack, setting the lift coefficient to 0 beyond this value, as depicted in Figure 10.16. Note that when flying in conditions where the elevator is used (see Section 13.2 on control allocation), combined with airspeed conditions which cause a fluctuation around this stall point, the abrupt loss of lift might cause degraded handling qualities. One might solve this by refining the stall modelling, or by for example causing a more gradual descent to 0 for the lift coefficient. The angle of attack is then linearly interpolated for a specific angle of attack α_h or β_v to the corresponding lift coefficient value C_{l_h} or C_{l_v} using the lookup-table as plotted in Figure 10.16.

¹In order to avoid common confusion, this is the inflow after correction for vertical advance ratio, $\lambda = \frac{\mu_z - \lambda_0}{2}$ as per Equation 10.35.

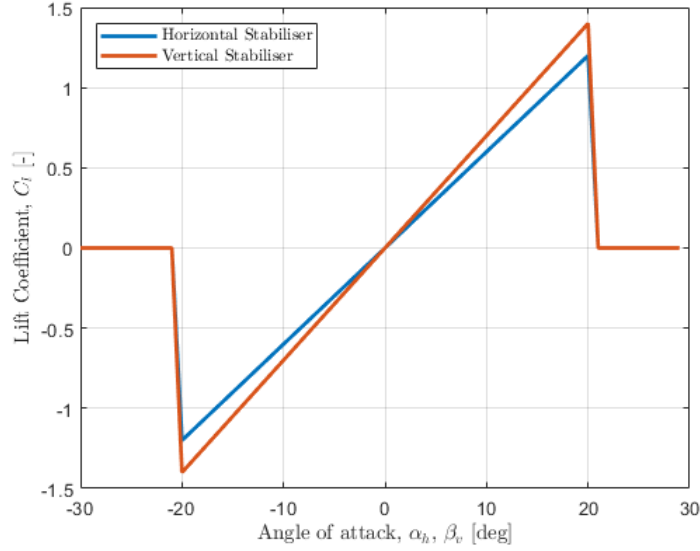


Figure 10.16: Lookup table used for lift coefficient calculation for horizontal and vertical tail, including stall effect.

10.5.2. Global Contribution

The total contribution of the empennage in terms of forces and moments can be summed as follows. Note that the model does not directly include the drag produced by the empennage, rather, it is included in the total fuselage drag, described in the next section. Small angles α_h and β_v are assumed, simplifying the calculation for the total body dynamics.

$$\vec{F}_{emp} = \begin{bmatrix} X_{emp} \\ Y_{emp} \\ Z_{emp} \end{bmatrix} = \begin{bmatrix} X_h + X_v \\ Y_h + Y_v \\ Z_h + Z_v \end{bmatrix} = \begin{bmatrix} -L_h * \sin(\alpha_h + \alpha_{h0}) \\ 0 \\ -L_h * \cos(\alpha_h + \alpha_{h0}) \end{bmatrix} + \begin{bmatrix} -L_v * \cos(\beta_v + \beta_{v0}) \\ L_v * \cos(\beta_v + \beta_{v0}) \\ 0 \end{bmatrix} \quad (10.59)$$

$$\vec{M}_{emp} = \begin{bmatrix} L_{emp} \\ M_{emp} \\ N_{emp} \end{bmatrix} = \begin{bmatrix} L_h + L_v \\ M_h + M_v \\ N_h + N_v \end{bmatrix} = \begin{bmatrix} Z_h * d_h + Y_h * h_h \\ Z_h * l_h - X_h * h_h \\ -Y_h * l_h - X_h * d_h \end{bmatrix} + \begin{bmatrix} Z_v * d_v + Y_v * h_v \\ Z_v * l_v - X_v * h_v \\ -Y_v * l_v - X_v * d_v \end{bmatrix} \quad (10.60)$$

The final parameters used in the empennage model are listed in Table 10.5 below:

**Table 10.5:** Empennage parameters.

Empennage Parameters	Symbol	Value	Unit
<i>Horizontal Tail</i>			
Lift curve slope	$dC_{l_{\alpha_h}}$	3.4	-
Lift elevator slope	$dC_{l_{\alpha_h}}/d\delta_e$	0.7	rad^{-1}
Incidence angle	α_{h0}	0	deg
Surface Area	S_h	5	m^2
Downwash factor	K_h	1.5	-
X-distance from C.G.	l_h	6.8	m
Y-distance from C.G.	d_h	0	m
Z-distance from C.G.	h_h	0	m
<i>Vertical Tail</i>			
Lift curve slope	$dC_{l_{\beta_v}}$	4	-
Lift elevator slope	$dC_{l_{\beta_v}}/d\delta_r$	0.3	rad^{-1}
Incidence angle	β_{v0}	0	deg
Surface Area	S_v	1.197	m^2
X-distance from C.G.	l_v	6.8	m
Y-distance from C.G.	d_v	0	m
Z-distance from C.G.	h_v	0.5	m

10.6. Fuselage Modelling

Lastly, the fuselage aerodynamic effects will be modelled. It's model is split into 3 main aspects: the drag model, pitching moment and rolling moment. The fuselage is assumed to be symmetrical around the x-z plane, and thus not create a yawing moment. Moreover, it is assumed that the fuselage does not produce any significant lift, as it is a bluff body.

The drag model used for the aircraft is based on the basic drag equation as per Equation 10.61, where $\alpha_{fus} = \tan^{-1}(w/u)$ Note the parameter $\sum(C_D S)_S$, which comes from the total equivalent flat plate area. This flat plate is a mathematical description of a flat plate with a specific surface area which produces the same total drag as the aircraft. An approximation of this value can be made from Figure 10.17, from which it can be deduced that $\sum(C_D S)_S = 2.5$.

$$D_{fus} = \frac{1}{2} \rho V^2 \sum(C_D S)_S \cos(\alpha_{fus}) \quad (10.61)$$

The fuselage pitching moment can be calculated using the pitch moment coefficient $C_{M_{fus}}$:

$$C_{M_{fus}} = \left(\frac{V}{\Omega R} \right)^2 \frac{1}{AR} K_{fus} V_{fus} (\alpha_{fus} - \alpha_{fus_{M=0}} - \epsilon_0) \quad (10.62)$$

where A is the fuselage cross-sectional area, assumed to be a perfect circle, and thus equal to πR^2 , R the radius of that circle, K_{fus} a correction factor for the assumed fuselage volume V_{fus} , α_{fus} the fuselage angle of attack, calculated by $-\tan^{-1}(w/u)$, and $\alpha_{fus_{M=0}}$ the angle of attack for which the fuselage pitching moment coefficient is zero. Lastly, ϵ_0 equals the same wake correction factor as for the empennage, this time assumed to be central on the fuselage, and thus not needing a correction factor.

The fuselage rolling moment can be calculated using the rolling moment coefficient $C_{N_{fus}}$:

$$C_{N_{fus}} = \left(\frac{V}{\Omega R} \right)^2 \frac{1}{AR} K_{fus} V_{fusN} \beta_{fus} \quad (10.63)$$

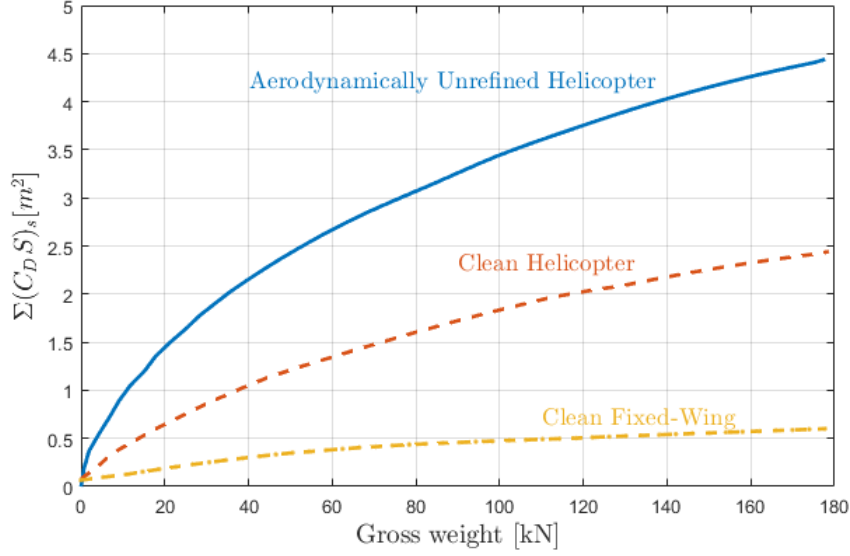


Figure 10.17: Summed equivalent flat plate coefficient $\Sigma(C_D S)_s$ in function of gross weight. [19]

where β_{fus} equals the sideslip angle of the fuselage, equal to $\sin^{-1}(v/V)$

The resulting forces from the fuselage still have to be expressed in the body-fixed reference frame, and thus transformed using α_{fus} and β_{fus}

$$\vec{F}_{fus} = \begin{bmatrix} X_{fus} \\ Y_{fus} \\ Z_{fus} \end{bmatrix} = \mathbb{R}_y(\alpha_{fus}) \mathbb{R}_z(-\beta_{fus}) \begin{bmatrix} -D_{fus} \\ 0 \\ 0 \end{bmatrix} = -D_{fus} \begin{bmatrix} \cos \beta_{fus} \cos \alpha_{fus} \\ \sin \beta_{fus} \\ \cos \beta_{fus} \sin \alpha_{fus} \end{bmatrix} \quad (10.64)$$

The fuselage moments can simply be calculated using:

$$\vec{M}_{fus} = \begin{bmatrix} L_{fus} \\ M_{fus} \\ N_{fus} \end{bmatrix} = \rho A (\Omega R)^2 R \begin{bmatrix} 0 \\ C_{M_{fus}} \\ C_{N_{fus}} \end{bmatrix} \quad (10.65)$$

The fuselage parameters used in the model are summarised in Table 10.6 below:

Table 10.6: Fuselage parameters.

Fuselage Parameters	Symbol	Value	Unit
Equivalent flat plate drag	$dC_{l_{\alpha_h}}$	2.5	m^2
Volume correction factor	K_{fus}	0.7	-
Fuselage radius	R	4	m
Zero moment fuselage angle of attack	$\alpha_{fus \ M=0}$	-1	deg



10.7. Lateral Lift-Offset Considerations

In a coaxial rotor configuration using an ABC-rotor, high-speed flight is enabled by use of the lateral lift-offset. As discussed in the literature study, the lateral-lift offset is a measure of how far outward the lift vector is 'pushed' in order to achieve a lateral moment equilibrium between upper and lower rotor, as visualised in Figure 10.18. As can be seen, most of the lift (if not all) in an ABC-type rotor is produced on the advancing blade side (hence the name). This enables the feature that once retreating blade stall occurs, it does not affect lift production of the rotors at all, omitting any drawbacks caused by retreating blade stall. This in turn allows the helicopter to achieve much higher speeds, especially when augmented by the pusher propeller.

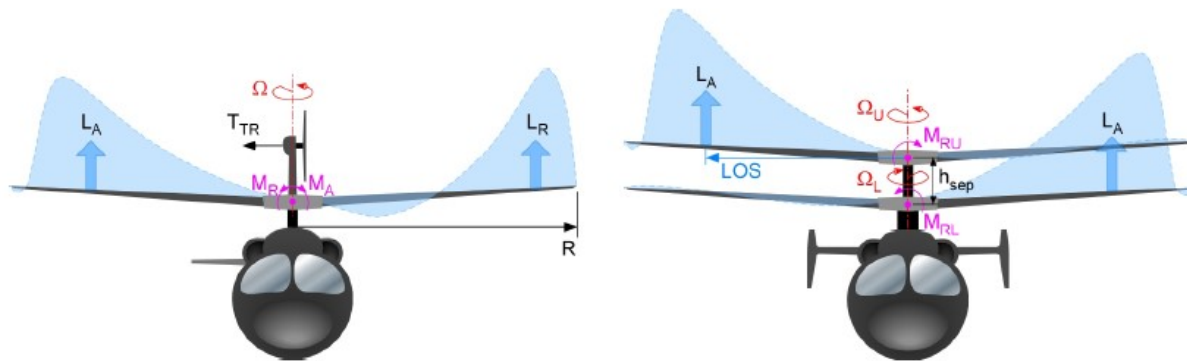


Figure 10.18: Lateral moment equilibrium comparison between a single main rotor (left) and the ABC concept (right). [33]

However, in order to model this effect, one has to have access to the lateral components of the lift produced by each rotor. This in turn requires the modelling of spanwise inflow and a corresponding calculation of spanwise thrust. As was clear from the thrust and inflow modelling in Section 10.3, only the mean inflow across the upper and lower rotor have been calculated in this model. This results in the thrust vector going right through the rotor hub, which removes the opportunity to 'push' the lift distribution outwards, in order to properly model lift-offset. This demonstrates a disadvantage of the inflow and thrust calculation approach used during modelling.

However, lift-offset does not impact the flight dynamics characteristics in any significant way. Since there is still a lateral moment equilibrium, and the total forces remain the same, there is no difference on the complete aircraft system between a model that includes lift-offset, and one that does not. It can therefore be stated that this 'shortcoming' of the model is deemed justified for the scope of this thesis.

In an effort to guide future iterations of this project, which might be more focused on the aerodynamics of the coaxial rotor configuration, a brief discussion on the modelling of local inflow, thrust, and computation of lateral-lift offset and accompanying differential lateral cyclic $\Delta\theta_{1c}$ in trim is given.

10.7.1. LOS Model Considerations

In order to be able to model a lateral lift distribution, several aspects have to be taken into account:

- **Inflow modelling:** A lateral (and possibly longitudinal) inflow distribution should be modelled. This can be done using a linear inflow approximation such as that discussed in the literature study, based on Glauert's linear inflow approach in local momentum theory. [35] If the user were to opt for a non-linear distribution, other, more advanced methods such as vortex wake models [31], should be used. This however significantly increases complexity of the inflow model, especially in a coaxial setting, with inter-rotor effects.
- **Thrust computation:** Using the spanwise inflow calculated during the inflow modelling stage, the spanwise forces can be calculated. However, instead of using a simplified equation as done in Section 10.3, each blade element should be modelled separately. This introduces more complexity to



the system, while gaining fidelity. One main aspect of this blade-element modelling approach is the blade pitch, which can be calculated using:

$$\begin{aligned}\theta_u(y, \psi, \Gamma) &= (\theta_0 + \theta_d) + (\theta_{1c} + \Delta\theta_{1c}) \cos(\psi_u - \Gamma) + (\theta_{1s} + \Delta\theta_{1s}) \sin(\psi_u - \Gamma) + \frac{\theta_{twist}y}{R} \\ \theta_l(y, \psi, \Gamma) &= (\theta_0 - \theta_d) - (\theta_{1c} - \Delta\theta_{1c}) \cos(\psi_l - \Gamma) + (\theta_{1s} - \Delta\theta_{1s}) \sin(\psi_l - \Gamma) + \frac{\theta_{twist}y}{R}\end{aligned}\quad (10.66)$$

Where the blade pitch is calculated in function of the lateral position y , azimuthal position ψ and phase lag Γ . As can be seen, the differential lateral cyclic $\Delta\theta_{1c}$ is a direct component of this blade pitch. Note that other factors such as the differential collective also effect the blade pitch, affecting differential collective, which will be explained later.

Significant steps thus have to be taken in order to be able to model the lateral lift distribution, depending on the targeted fidelity level.

10.7.2. Differential Lateral Cyclic Calculation Algorithm

With the lateral lift distribution now available, it is possible to calculate the required $\Delta\theta_{1c}$ for a specific LOS. As described in the literature study, Ferguson concluded that the lateral-lift-offset LOS follows a quadratic distribution in function of flight velocity V , calculated using Equation 10.67 and visualised in Figure 10.19. It is clear that in hover, there is no LOS, since the advancing and retreating blades produce and equal amount of lift.

$$LOS = 0.00002V^2 \quad (10.67)$$

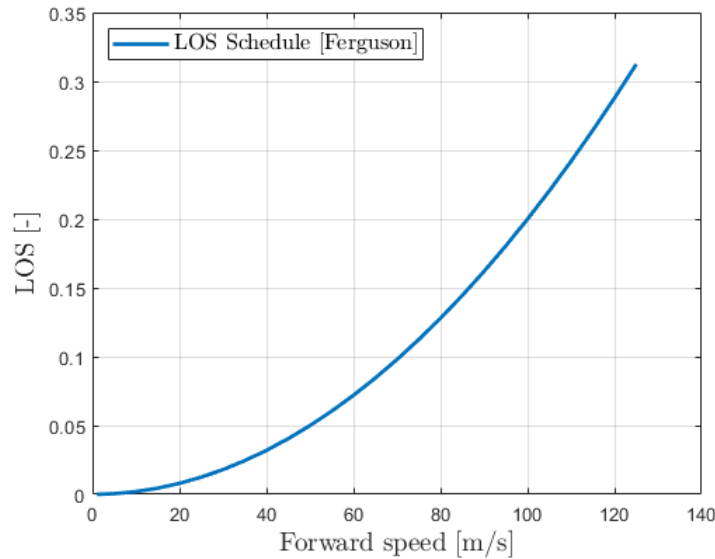


Figure 10.19: LOS in function of flight velocity as per Ferguson. [28]

In order to calculate the differential lateral cyclic $\Delta\theta_{1c}$ required to acquire the correct lift offset, 2 approaches are recommended. Firstly, one could introduce $\Delta\theta_{1c}$ as a trim variable, and include it in a trim routine with the LOS equation as an extra trim target. This is the approach adopted by Ferguson [28]. Secondly, $\Delta\theta_{1c}$ can be calculated by means of a Regula-Falsi procedure which is implemented during each trim step. An example algorithm is depicted in the algorithm below. Here, $LOSparams$ contain the required parameters for the LOS calculation, which is calculated as shown in line 3. [42]



```

1  T_tot(i) = abs(LOSparams(1,i));
2  L_MR_u(i) = LOSparams(2,i);
3  LOS(i) = L_MR_u(i)/(T_tot(i)*R);
4  LOSdes(i) = 0.00002*V(i)^2;
5  LOSdiff(i) = LOSdes(i) - LOS(i);
6
7  while abs(LOSdiff(i)) > 0.001
8      theta_cdifff(i) = theta_cdifff(i) + deg2rad(0.01);
9      [f(:,i), LOSparams(:,i)] = ...
10         f_xk6(vel(:,i), x_k(:,i), p(i), q(i), r(i), theta_f(i), delta_e(i),
11             delta_r(i), theta_cdifff(i));
12
13     T_tot(i) = abs(LOSparams(1,i));
14     L_MR_u(i) = LOSparams(2,i);
15     LOS(i) = L_MR_u(i)/(T_tot(i)*R);
16     LOSdes(i) = 0.00002*V(i)^2;
17     LOSdiff(i) = LOSdes(i) - LOS(i);
18 end

```

10.7.3. Differential Collective Cross-Coupling Effects

If this approach were to be adopted, one other phenomenon should be accounted for: that of the effect of differential collective θ_d on the LOS. In Equation 10.66 it was clear that θ_d affects the blade pitch. In terms of LOS, Figure 10.20 visualises the effect of positive collective differential on the LOS (exaggerated). It can be seen that the lift of the upper rotor increases, and that of the lower decreases, as intended by the differential collective to produce a torque difference. However, due to the alteration of the blade pitch, a coupling effect on the LOS appears. The differential collective shifts the lower rotor lift vector inwards, and that of the upper rotor outwards, causing significant rolling moment effects. This cross-coupling would have to be accounted for during trim and control strategies.

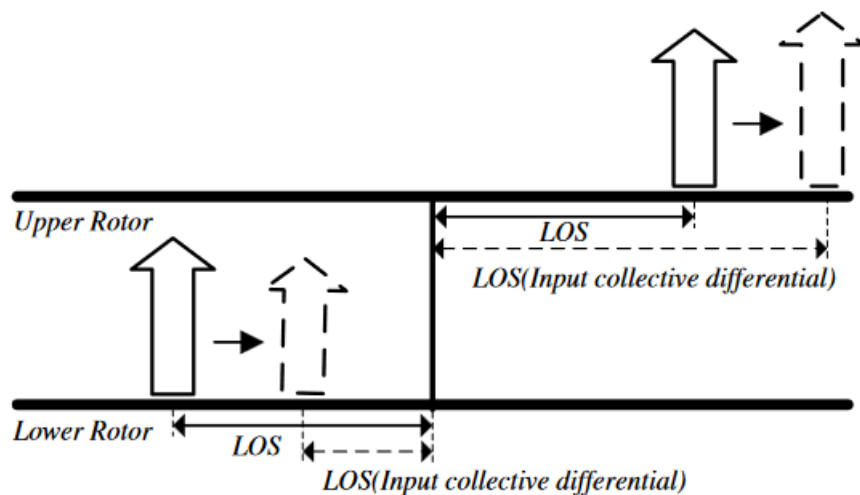


Figure 10.20: Effect on LOS due to differential collective input. [17]

Trimming the Model

In any meaningful helicopter model, a trim analysis is conducted. The trim analysis forms the basis for dynamic stability analysis, open-loop system response, handling qualities, calculating trim points for control systems, etc. Therefore, this chapter aims to provide the trim analysis of the model constructed in the previous chapter. Firstly, in Section 11.1, the general trim problem is outlined, and the choice of the trim variables is discussed. Due to the complex nonlinear nature of the helicopter, the Newton-Raphson numerical trim-routine will be used, which is discussed in Section 11.2. Lastly, the trim results are plotted, discussed, and compared with validation data in Figure 11.3.

11.1. Trim Problem and Choice of Trim Variables

The trim problem states that we would like to find the correct combination of control angles to hold the helicopter in a specific state. Trimming can be achieved in turning, climbing, descending or level flight. In this thesis, a simple level flight with an increasing forward speed u as trim speed is opted for, as it is the starting point for any meaningful analysis, and has the most validation data available.

In steady flight conditions, the aircraft angular velocities and body accelerations equal zero. This results in the aircraft being in steady flight conditions when the Euler rigid body equations are 0, as equated below:

$$\begin{aligned}
 \frac{X_{tot}}{m} - g \sin \theta &= 0 \\
 \frac{Y_{tot}}{m} - g \cos \theta \sin \psi &= 0 \\
 \frac{Z_{tot}}{m} - g \cos \theta \cos \psi &= 0 \\
 L_{tot} &= 0 \\
 M_{tot} &= 0 \\
 N_{tot} &= 0
 \end{aligned}
 \tag{11.1}$$

It is evident that in total, 6 equations have to equal zero. In order to calculate the correct combination of controls, the numerical Newton-Raphson trim-algorithm [28] is used, for which a brief discussion is held in Section 11.2 below.

Because the aircraft has a total of 8 controls and only 6 equations, special attention has to be payed on the controls. As is done in most literature available, such as Berger [60], Qiu [26] and Ferguson [28], the elevator deflection δ_e , rudder deflection δ_r are set to 0 throughout the trim range, which leaves 6 controls.¹ However, the differential lateral cyclic $\Delta\theta_{1c}$ is calculated in function of LOS as mentioned in Section 10.7, and thus also has a pre-set, value, leaving only 5 trim targets, or controls. Therefore, an extra trim target has to be chosen. It was chosen to make this extra trim target the fuselage roll angle ϕ_f . Some literature opts for the extra trim target to be the fuselage pitch angle θ_f . However, this creates higher drag compared to fixing it at 0. An advantage of this would be that the pusher propeller becomes slightly offloaded.

¹The elevator and rudder deflections will not be used as trim variables since they are only 'activated' from a certain flight speed, according to control allocation principles, as discussed in Section 13.2, and for consistency with validation data.



However, from later analysis, as shown in Figure 11.3, it is clear that the pusher propeller stays within limits. An optimisation analysis could be done to see what the most advantageous configuration would be in terms of power, assessing the influence of θ_f and ϕ_f . This is however beyond the scope of this thesis.

Due to the quasi-dynamic inflow states, 3 extra equations have to be satisfied, namely those in Equation 11.2. However, these can simply be satisfied by making use of the inflow states λ_{0_u} , λ_{0_l} and λ_{0_p} as extra trim targets.

$$\begin{aligned}\dot{\lambda}_{0_u} &= 0 \\ \dot{\lambda}_{0_l} &= 0 \\ \dot{\lambda}_{0_p} &= 0\end{aligned}\tag{11.2}$$

In total, there are thus 9 equations which have to be satisfied, and 9 controls which are used as trim variables, depicted in the trim state vector x below:

$$x = [\theta_0 \quad \Delta\theta_0 \quad \theta_{1s} \quad \theta_{1c} \quad \theta_p \quad \phi_f \quad \lambda_{0_u} \quad \lambda_{0_l} \quad \lambda_{0_p}]^T\tag{11.3}$$

11.2. Newton-Raphson Trim Algorithm

As mentioned before, use will be made of the Newton-Raphson trim algorithm, which will be outlined in the following. The procedure in order to find the minimum of the sum of f_i , as expressed in Equation 11.5, is outlined in Figure 11.1.

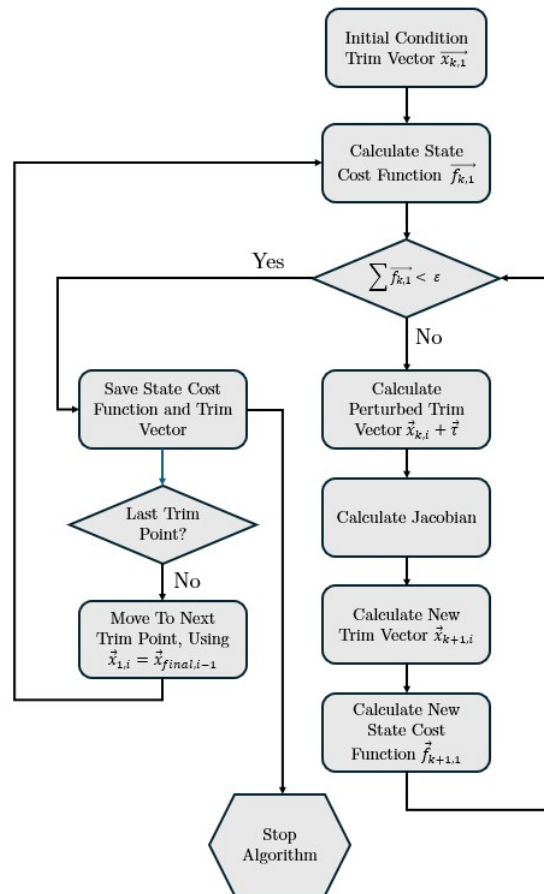


Figure 11.1: Newton-Raphson trim algorithm flowchart.

In essence, the Newton-Raphson algorithm is a minimisation problem, in which the sum of all the state derivatives has to be as close to 0 as possible. This is expressed in Equation 11.4, where f_i denotes the



cost function (in this case equal to the state derivatives) of the corresponding state derivative, and x_i denote the unknown variables, or inputs. i ranges from 1 to N , where N is the number of states (equal to the number of unknown variables).

$$f_i(x_1, x_2, \dots, x_N) = 0 \quad i = 1, 2, \dots, N \quad (11.4)$$

$$\sum_{n=1}^9 f_i = 0 \quad (11.5)$$

Firstly, an initial input vector $x_{k,1}^{\vec{}}$, which is comprised of the individual components $x_{1,1}$ to $x_{9,1}$. For the very first trim point, the initial guess for the collective angle, $x_{1,1}$, is 10 deg, while the other angles, $x_{2,1}$ to $x_{6,1}$ have an initial guess of 0. The initial guess for the upper and lower rotor inflow, $x_{7,1}$ and $x_{8,1}$, are both calculated by $\sqrt{\frac{m}{2} * g / (2A\rho)} / (\Omega * R)$. The inflow of the pusher propeller $x_{9,1}$ has an initial guess of 0. The initial estimates of the first trim point are all listed in Table 11.1.

Table 11.1: Initial guesses of the trim variables at the first trim point.

Trim Variable	Symbol	Unknown Variable	Initial Guess
Mean Collective	θ_0	x_1	10 [deg]
Differential Collective	θ_d	x_2	0
Longitudinal Cyclic	θ_{1s}	x_3	0
Lateral Cyclic	θ_{1c}	x_4	0
Propeller Collective	θ_p	x_5	0
Fuselage Roll Angle	ϕ	x_6	0
Upper Rotor Inflow	λ_{0u}	x_7	$\sqrt{\frac{m}{2} g / (2A\rho)} / (\Omega R)$
Lower Rotor Inflow	λ_{0l}	x_8	$\sqrt{\frac{m}{2} g / (2A\rho)} / (\Omega R)$
Propeller Inflow	λ_{0p}	x_9	0

After the initial guess, the state derivatives are calculated in function of the trim variables, by means of the nonlinear function from Chapter 10, resulting in $f_{x_{k,1}}^{\vec{}}$.

Most likely, the resulting total of the sum of the state derivative components, $f_{x_{k,1}}^{\vec{}}$, is not 0. Therefore, an update to the trim state using the Jacobian matrix is made according to:

$$x_{k+1,i}^{\vec{}} = x_{k,i}^{\vec{}} - \left. \frac{f_i^{\vec{}}}{x_i^{\vec{}}} \right|_{x_i^{\vec{}}=x_{k,i}^{\vec{}}}^{-1} f_{x_{k,i}}^{\vec{}} \quad (11.6)$$

The Jacobian matrix can be approximated numerically using:

$$J = \left. \frac{f_i^{\vec{}}}{x_i^{\vec{}}} \right|_{x_i^{\vec{}}=x_{k,i}^{\vec{}}}^{-1} \approx \frac{f_{i x_{k,i}^{\vec{}}+\vec{\tau}}^{\vec{}} - f_{x_{k,i}}^{\vec{}}}{\tau} \quad (11.7)$$

Here, τ equals a small disturbance constant³. $f_{x_{k,i}^{\vec{}}+\vec{\tau}}^{\vec{}}$ denotes the state derivative vector evaluated at the input vector $x_{k,i}^{\vec{}}$ added by the disturbance vector $\vec{\tau}$.

The disturbance vector $\vec{\tau}$ only has a non-zero value in 1 row, corresponding to the trim variable that is

²The first subscript denotes the trim vector component (1 to 9), and the second the trim point number

³The choice of the disturbance constant was chosen based on a sensitivity analysis in order to find where a convergence of state excitations after the disturbance was found. Making the constant too small or too large can lower accuracy or cause divergence.



being disturbed at the moment. This is best illustrated by example. Assume that we want to calculate the influence of the lateral cyclic θ_{1c} on the complete system dynamics \vec{f} . Since θ_{1c} corresponds to the unknown variable x_4 , the disturbance vector $\vec{\tau}$ now becomes:

$$\vec{\tau} = [0 \ 0 \ 0 \ \tau \ 0 \ 0 \ 0 \ 0 \ 0]^T \quad (11.8)$$

where τ is a small constant. This disturbance vector $\vec{\tau}$ then gets added to the trim vector \vec{x}_k , resulting in:

$$\vec{x}_k + \vec{\tau} = [x_1 \ x_2 \ x_3 \ x_4 + \tau \ x_5 \ x_6 \ x_7 \ x_8 \ x_9]^T \quad (11.9)$$

$\vec{f}(\vec{x}_k + \vec{\tau})$ can then be evaluated. Applying the disturbance to every trim variable, the effect of each trim variable x_k on each state derivative f_i can be assessed and assembled in a Jacobian matrix, resulting in a 9x9 matrix, where each column represents the change of state derivatives f_i due to a certain input x_k :

$$J = \begin{bmatrix} \frac{\partial f_1}{\partial \theta_0} & \frac{\partial f_1}{\partial \theta_d} & \dots & \frac{\partial f_1}{\partial \lambda_{0p}} \\ \frac{\partial f_2}{\partial \theta_0} & \frac{\partial f_2}{\partial \theta_d} & \dots & \frac{\partial f_2}{\partial \lambda_{0p}} \\ \vdots & \vdots & \ddots & \vdots \\ \frac{\partial f_9}{\partial \theta_0} & \frac{\partial f_9}{\partial \theta_d} & \dots & \frac{\partial f_9}{\partial \lambda_{0p}} \end{bmatrix} \quad (11.10)$$

After evaluating the state derivatives \vec{f} using the new input $x_{k+1,i}$, it can be checked whether or not the sum of the elements is smaller than a pre-defined small constant ϵ . If not, a new input vector $x_{k+1,i}$ is calculated, and re-assessed. Convergence of the Newton-Raphson algorithm is achieved due to the use of the Jacobian matrix, and is often only takes a few iterations, as shown in Figure 11.2.

After the threshold of ϵ has been reached, the trim algorithm can move on to the next trim point. In order to decrease iterations needed to find a converged solution with a cost function sum smaller than ϵ , the final input vector \vec{x}_k of the previous trim point is used. This makes sense when thinking about the physical system. When the forward speed has only been increased by a small amount, the aerodynamic forces do not change drastically compared to the trim point before. The decrease in iterations required using this approach is also visualised in Figure 11.2. Generally, about 1-2 (and sometimes even 4 if trim point density is increased), indicating a percentage decrease in iterations from 0% (0 iterations saved) to 57% (4 iterations saved).

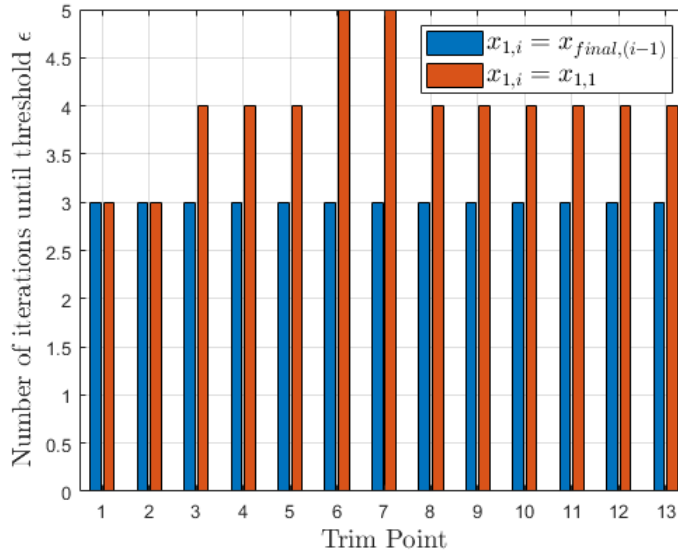


Figure 11.2: Number of iterations until threshold ϵ has been reached, using the last trim point's trim vector, or starting from the very first initial conditions respectively.



11.3. Trim Results

Using the Newton-Raphson algorithm, all trim states are calculated in the trim state vector \vec{x} , as per Equation 11.3, for each trim point. These results are plotted in Figure 11.3 in function of the forward velocity associated to each trim point. The aircraft has been trimmed for 26 trim points between 1 and 120 m/s⁴. These trim plots are compared with the results from Qiu [26] and Berger [46] respectively, where-ever possible⁵. These papers have been chosen specifically since the helicopter parameters and modelling approach was based significantly on a combination of both.

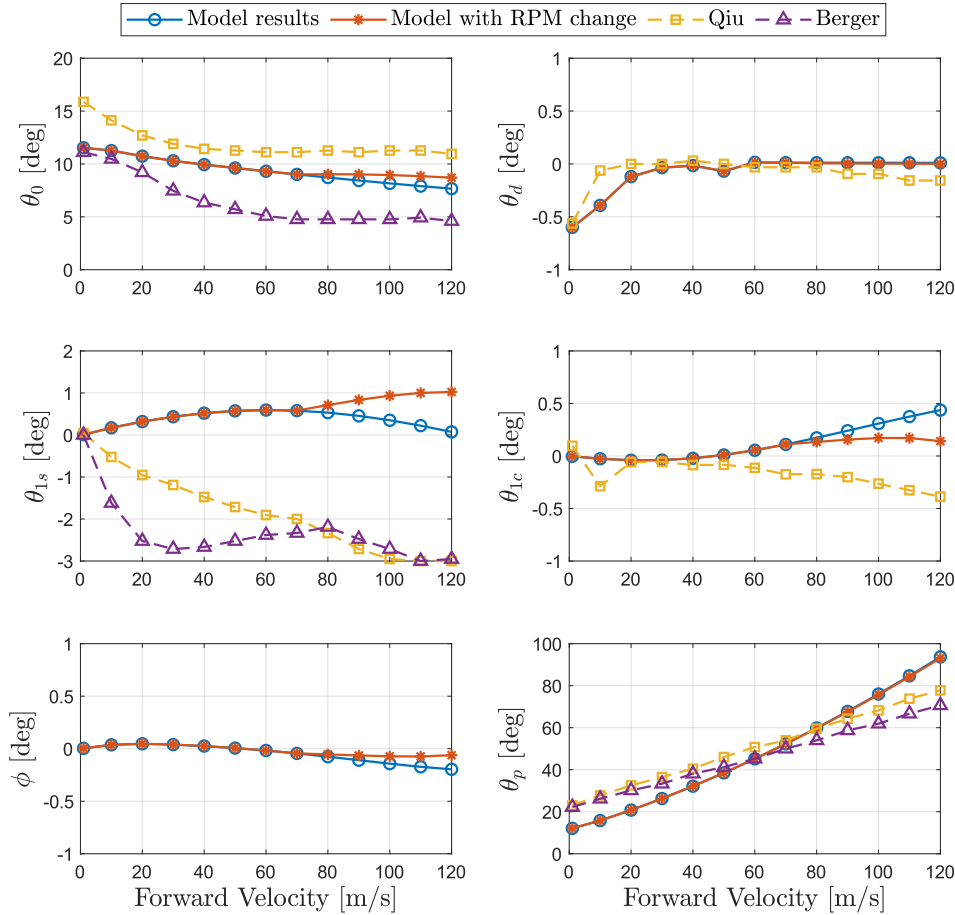


Figure 11.3: Trim results for the compound coaxial model without and with RPM scheduling, with validation from Qiu [26] and Berger [46] respectively.

When comparing the model results with validation results, several aspects can be noted:

- **Mean collective θ_0 :** In a conventional helicopter, the trim collective reaches a minimum at the minimum power required curve and increases with increasing flight velocity due to the fuselage pitch angle (needed for forward velocity), which affects the vertical contribution of the thrust from the main rotor. It can be seen that the model correctly captures the unloading effect of the collective, since forward velocity is now provided by the pusher propeller θ_p and because the fuselage pitch θ_f is fixed at 0 for all flight speeds.

Next, a less pronounced curving of the collective can be seen compared to validation data. This is most likely due to discrepancies between inflow dynamics, and can indicate that the inflow calculation

⁴Note that only 13 trim points are plotted for a less cluttered graph, and for consistency with validation.

⁵Berger does not discuss the differential collective and lateral cyclic deflection for some reason, and Qiu uses θ as a trim variable instead of ϕ .



might need improvement.

Lastly, it can be seen that with the model including the RPM rotor scheduling, the model shows a 'flattening out' of the collective required, in line with the validation data. This is due to the lowering of the rotor RPM, causing a slight increase in collective required for the same thrust generation.

- **Differential collective θ_d :** The differential collective follows the validation very well, proving the implementation accuracy of the control.

One interesting remark that was seen throughout analysis was that care has to be taken with the definition of θ_d . The control in this paper is defined as the deflection of one rotor compared to the mean, or: $\theta_d = \frac{\theta_u - \theta_l}{2}$. In earlier versions of the model, the total difference between the upper and lower rotor pitch was taken as θ_d , causing double the trim value.

- **Longitudinal forward cyclic θ_{1s} :** The longitudinal forward cyclic shows the most discrepancy with literature.

Firstly, it can be seen that the sign is opposite throughout the entire trim regime, this however, is simply due to a difference in sign convention for the forward cyclic.

Secondly, it can be seen that the curve and magnitude is significantly different to that of both validation datasets. This is most likely to be attributed to the difference in flapping angle calculation, since during trim, θ_{1s} is used to trim out the flapping angle. This is confirmed in Figure 11.4, where it can be seen that the longitudinal cyclic tries to alter the control plane angle of attack α_{cp} such that it compensates for the first harmonics of the longitudinal flapping coefficients a_{1u} and a_{1l} .

When further analysis was conducted, the main attribution to this unconventional was found to be the rotor blade twist angle θ_{tw} , altering the blade geometry and thus the effect on the flapping angle coefficients. When decreasing the blade twist to -3 deg, a more conventional curve for a_{1u} and a_{1l} was obtained, as visualised in Figure 11.5. However, it can be seen that around $40 - 45$ m/s some numerical discrepancies are amplified, which are also visible, to a far lesser extent, in Figure 11.4. It is thought that this is due to the sudden decoupling of the upper rotor's wake on the lower rotor's wake, hence altering the inflow values quite significantly from one trim point to another. One solution could be to increase trim point density around this airspeed. This numerical instability could also be seen in the trim variable plots. Another possible solution could be to re-assess how the flapping angles are calculated.

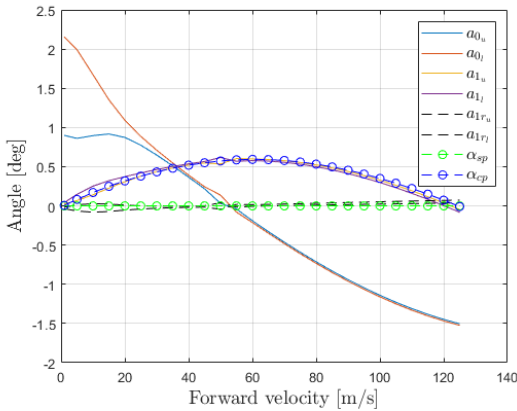


Figure 11.4: Rotor angles throughout the trim regime using a rotor blade twist angle $\theta_{tw} = -10$ deg for both rotors.

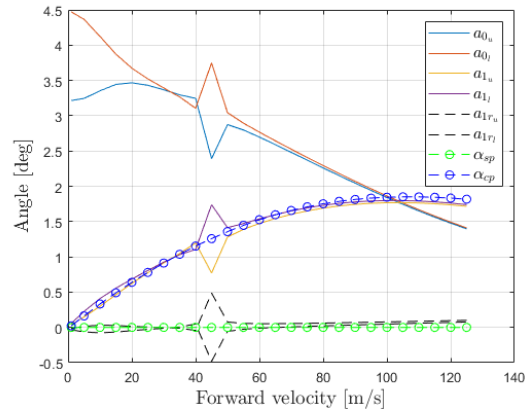


Figure 11.5: Rotor angles throughout the trim regime using a rotor blade twist angle $\theta_{tw} = -3$ deg for both rotors.

- **Lateral cyclic θ_{1c} and propeller collective θ_p :** The lateral cyclic and propeller collective both show good agreement with validation. The slight discrepancies could be attributed to differences in planform data which lead to different stability and control derivatives, and a slight difference in modelling approaches.
- **Fuselage roll angle ϕ :** Due to the unique trim solution in which ϕ is used as a trim variable, no validation data was found in the 2 validation papers. However, the small values and gentle curve make sense with roll-coupling behaviours seen in most helicopters.

Stability Analysis of the Compound Coaxial Helicopter

In order to verify the dynamic behaviour of the modelled compound coaxial helicopter, a stability analysis is performed. This will give a general insight of the effects of thrust and lift compounding on the dynamic characteristics of the helicopter.

The first step in this analysis is to linearise the nonlinear model, which can be done in two ways. The first method is by using a numerical linearisation algorithm, in which the states are perturbed around the trim state and the forces and moments evaluated. This allows for the calculation of stability and control derivatives by numerical differentiation. The second approach is by means of system identification techniques, in which the stability and control derivatives are modelled to fit a linear simulation model in order to find a fit to the nonlinear model. This can be done by various techniques such as least squares regression, machine learning, splines, etc.¹ In this thesis however, the first approach will be adopted due to its broad coverage in literature [28] and is a less intense process. It must be noted that the system identification method can provide very interesting results and analysis, especially in practical flight test settings, and might provide a very interesting alternative to future iterations of this project.

The main aim of this chapter is thus to assess the dynamic stability characteristics of the compound coaxial helicopter, and identify the control derivatives which will be of key importance during control allocation efforts in Section 13.2. Firstly, the linearisation algorithm and construction of a linear model are discussed in Section 12.1, followed by a discussion of the calculated stability and control derivatives in Section 12.2 and Section 12.3 respectively. After the calculation of these derivatives, which form the linear model, an open-loop response for both the nonlinear and linear models are evaluated qualitatively in Section 12.4. The stability discussion is closed off in Section 12.5, where a quantitative analysis of the longitudinal natural modes of motion is presented.

12.1. Linearisation Algorithm

One of the main assumptions of a numerically linearised system is that the forces and moments of the system can be expressed as Taylor-series expansions. For example, the X-body force can be expressed as:

$$X \approx X_e + \frac{\partial X}{\partial u} \delta u + \frac{\partial X}{\partial w} \delta w + \dots \quad (12.1)$$

the other forces and moments can be expanded in a similar manner. In this equation, δ term denotes a small perturbation to the system of the respective state, such as u , w , or any other state. In fact, in order to calculate the linearised system matrix A , the response to the equations of motion, in function of the states and inputs $F(\vec{x}, \vec{u})$, is calculated by perturbing all states \vec{x} . The perturbed system dynamics can be expressed as:

¹The reader is encouraged to research the course of System Identification for more information and very interesting applications on this matter.



$$\dot{\vec{x}} + \delta\dot{\vec{x}} = \vec{F}(\vec{x}, \vec{u}) + \frac{\partial \vec{F}}{\partial \vec{x}} \delta\vec{x} + \frac{\partial \vec{F}}{\partial \vec{u}} \delta\vec{u} + \dots \quad (12.2)$$

The linearised control matrix B can be calculated by perturbing the control inputs instead of the states. Note that the linear system is expressed around the trim state, therefore, it can be stated that:

$$\dot{x} = \vec{F}(\vec{x}, \vec{u}) = 0 \quad (12.3)$$

The Taylor-series expansion of the equations of motion can thus be simplified, by linearising around the trim point, as:

$$\delta\dot{\vec{x}} = \frac{\partial \vec{F}}{\partial \vec{x}} \delta\vec{x} + \frac{\partial \vec{F}}{\partial \vec{u}} \delta\vec{u} \quad (12.4)$$

or, by dropping the perturbation expression, more commonly expressed as:

$$\dot{\vec{x}} = A\vec{x} + B\vec{u} \quad (12.5)$$

For the states and controls:

$$\begin{aligned} \vec{x} &= [u, v, w, p, q, r] \\ \vec{u} &= [\theta_0, \theta_d, \theta_{1s}, \theta_{1c}, \Delta\theta_{1c}, \theta_p, \delta_e, \delta_r] \end{aligned} \quad (12.6)$$

The final derivatives that are the entries of the system matrix A and control matrix B are estimated by means of a central-difference numerical approximation. This calculation is best shown by means of an example. Suppose we want to calculate the stability derivative X_u . This is calculated by perturbing the equation of motion of \dot{u} by u . Where \dot{u} is:

$$\dot{u} = -(qw - rv) + \frac{X}{m} - g \sin \theta \quad (12.7)$$

For simplicity, let's call this equation F_1 . As can be seen, this equation is dependent on the helicopter's states and controls. By means of the central-difference approximation, as depicted in Equation 12.8, we can calculate the stability derivative X_u . This is done by perturbing F_1 by δu around the trim state U_e .

$$X_u \approx \frac{F_1(U_e + \delta u) - F_1(U_e - \delta u)}{2\delta u} \quad (12.8)$$

Here, δu is a small perturbation value, which is chosen based upon the same convergence reasoning for the perturbation constant as discussed in the previous chapter on model trimming.

12.2. Stability Derivatives

The stability derivatives are essential to evaluating the behaviour of the helicopter to external disturbances, and to analyse cross-coupling between states. By analysing these derivatives, an understanding of the correctness and the behaviour of the system can be found.

In total, 36 stability derivatives are computed (6 equations and 6 states). However, they do not all share the same relative importance for the simulations that will be performed in Section 13.6. The main stability derivatives of importance are the speed stability derivative M_u , the dihedral effect derivative L_v (whose name is derived from fixed wing dihedral angle principles), longitudinal static stability derivative M_w , damping derivatives L_p and M_q , roll due to pitch coupling L_q , drag damping X_u , heave damping Z_w , and yaw due to roll coupling N_p :

It is important to note that when assessing the moment stability derivatives, the force stability derivatives are in essence also assessed. This is because the moments are in essence a direct result of the forces and

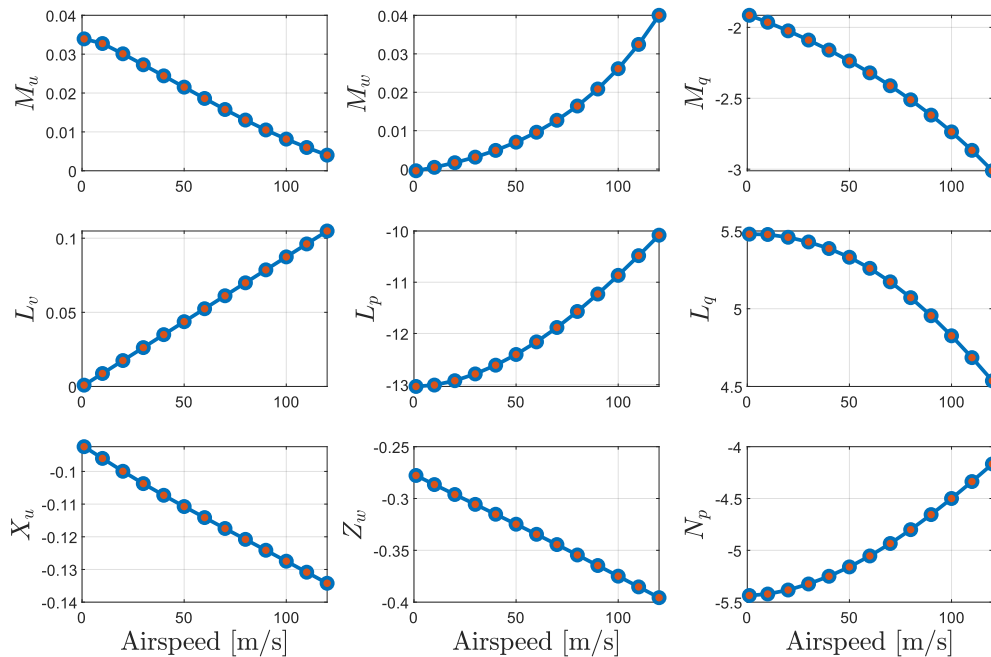


Figure 12.1: Main stability derivatives under analysis.

arms. The moments also dictate the general vehicle dynamics. Since the yawing moment results are in general quite small, their stability derivatives are not formally assessed, apart from the yaw-to-roll coupling N_p .

From Figure 12.1, several interesting remarks concerning the stability derivatives can be made:

- **Speed stability derivative M_u :** This stability derivative is mainly attributed due to rotor blowback. When a frontal airspeed disturbance is subject to the helicopter, the rotor tends to 'blow back', causing a pitch-up moment, which decelerates the aircraft. Hence, when this value is positive, it is speed stable, which is the case. This blowback effect decreases with increasing airspeed, usually approaching 0, similar to fixed-wing aircraft.
- **Dihedral effect derivative L_v :** This derivative finds its main origin in the same effect as M_u , namely that due to rotor blowback. Now however in the lateral plane. It can be seen that this value is positive, indicating lateral speed instability. This however is atypical compared to normal helicopter behaviour, and is not attributed to the coaxial configuration. It is therefore suspected that there might be an error in the calculation of the lateral rotor forces and/or angles, and inflow calculation (a uniform inflow was used for these results). Attempts were made unsuccessfully thus far to solve this error, however, due to the longitudinal manoeuvres that will be performed, and small value of the stability derivative, it was decided to leave it as is, since it will influence the simulation results only slightly.²
- **Longitudinal static stability derivative M_w :** The derivative starts at $M_w \approx 0$ around hover, and increases with flight speed. Since $M_w > 0$, using the body-axes definitions of the helicopter, it indicates instability. This is in-line with literature results. [60] [28]
However, M_w is highly dependent on the rotor flapping dynamics and flapping mechanism (rigid, fully articulated, ...), and tail sizing. The individual effects of each component contributing to the M -moment, as calculated in Section 10.3.5, is shown in Figure 12.2. It can be seen that both the fuselage and rotor cause destabilising moments, while the horizontal stabiliser tries to compensate for this. However, this appears to be insufficient. Note that the M_w derivative is highly dependent on

²It is suggested that any future iteration looks at this stability derivative by first performing sign-checks in the modelling, followed by a parametric sizing study, evaluating how all relevant parameters effect L_v .



the tail sizing, and rotor spring stiffness and hinge offset.³

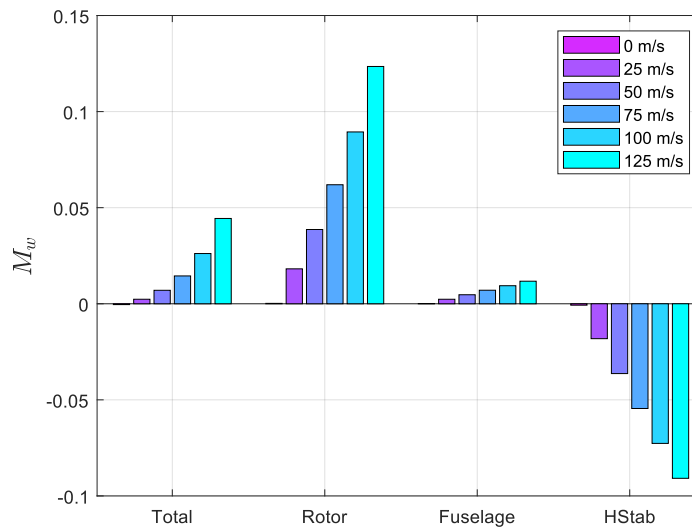


Figure 12.2: Component contribution to M_w .

It can be seen that there is a very large destabilising influence of spring moment caused by the modelled spring-stiffness of the rotor blades. Apart from this, it can be seen that the elevator size also heavily influences the stability, in a stabilising manner.

- **Damping derivatives L_p and M_q :** These derivatives indicate the respective damping derivatives of the rolling and pitching axes, indicating whether or not they dampen their own movement (i.e. a positive rate causing a negative moment). This is the case for both L_p and M_q , although it can be seen that L_p becomes less stable with increasing airspeed, which is contradictory with trends throughout literature [60] [28]. This might again indicate a possible error within the L -moment calculation. M_q does become more stable with increasing flight speed, as expected.
- **Cross-coupling stability derivatives L_q and N_p :** Lastly, the roll due to pitch and yaw due to roll stability derivatives L_q and N_p are discussed. It can be seen that L_q is largest at low-speed, and decreases with increasing speed. However, when comparing with literature, the sign is opposite, the values large, and the value not converging to 0, as is common with helicopters. The high initial value is thought to be attributed to the coaxial configuration, which causes twice the effect (twice the rotors). The other discrepancies are most likely attributed to a similar error (if not the same) as in the other L -derivatives. N_p can be seen to be quite small and decreasing with increasing flight speed.
- **Drag damping derivative X_u :** The drag damping derivative consists mainly of the increased drag produced by the fuselage with a positive disturbance u . Due to the decrease in angle of attack of the pusher propeller, the amount of forward thrust generated by the propeller also decreases. It is mainly associated with the stabilisation of the phugoid. However, it will prove to be insufficient to stabilise it as will be discussed in Section 12.5. In fixed-wing or tilt-wing aircraft, X_u tends to be much larger due to the presence of wings, which often stabilises the phugoid.
- **Heave damping derivative Z_w :** The heave damping derivative is predominantly defined by the change of rotor thrust with a disturbance in vertical velocity w . With an increase in w , the angle of attack of the rotor blades increases, and more thrust is generated. Since w is defined positive downwards, this value is negative. The magnitude of the derivative is dependent on the blade loading, i.e. the ratio between the aircraft mass and disc area.

Compared to conventional helicopters, the coaxial configuration seems to be more responsive to disturbances. This is to be expected and in-line with results from literature. Ferguson [28] especially, gives a very clear

³Various parameters have been tested, and indeed showed to be able to stabilise the aircraft. However the current parameters were chosen for the derivatives to be in-line with literature.



and detailed explanation on the stability derivatives, and how these differ from a coaxial to a conventional helicopter.

It can be said that the aircraft stability derivatives are of satisfactory quality. The longitudinal and cross-coupling derivatives show promising results. However, the dynamics in the roll-axis seem to be slightly erroneous, and should be re-evaluated in the future.

One promising result from derivatives such as X_u and Z_w is that compared to conventional helicopters with hingeless rotor designs, such as the Bo105, their values are around twice that of the single rotor conventional helicopter. [18] This is to be attributed to the coaxial design and is a good indicator that the higher responsiveness of a coaxial configuration is captured in the model.

12.3. Control Derivatives

The control derivatives are essential in understanding the behaviour of the controls on the helicopter dynamics. By analysing the response of each state due to a disturbance in a control input, an understanding of the behaviour, and assessment of the correctness of the model controls can be made.

The control derivatives are assessed in the same manner as the stability derivative, although now the change in state derivatives is assessed by a perturbation in a specific control relative to the trim value of that control. There are a total of 48 control derivatives, namely the 8 controls: θ_0 , θ_d , θ_s , θ_c , $\Delta\theta_c$, θ_p , δ_e , δ_r , times the 6 main states: u , v , w , L , M , and N . These will be discussed in the this subsection.

Firstly, the collective θ_0 control derivatives are depicted in Figure B.5. It can clearly be seen that the main control effect is on the Z-force, which is to be expected for the collective. However, it can also be seen that there is an X-force caused by the collective, which is 0 at hover, but increases with flight speed. This is to be attributed due to tilting of the disc-plane throughout the flight regime, tilting the thrust vector of the rotors, which increases in amplitude with increasing collective setting. This X-force in turn causes the moment associated with the collective. A similar analogy can be held for the lateral Y-force and rolling moment (and associated cross-coupling rolling moment), due to the lateral rotor disc tilt.

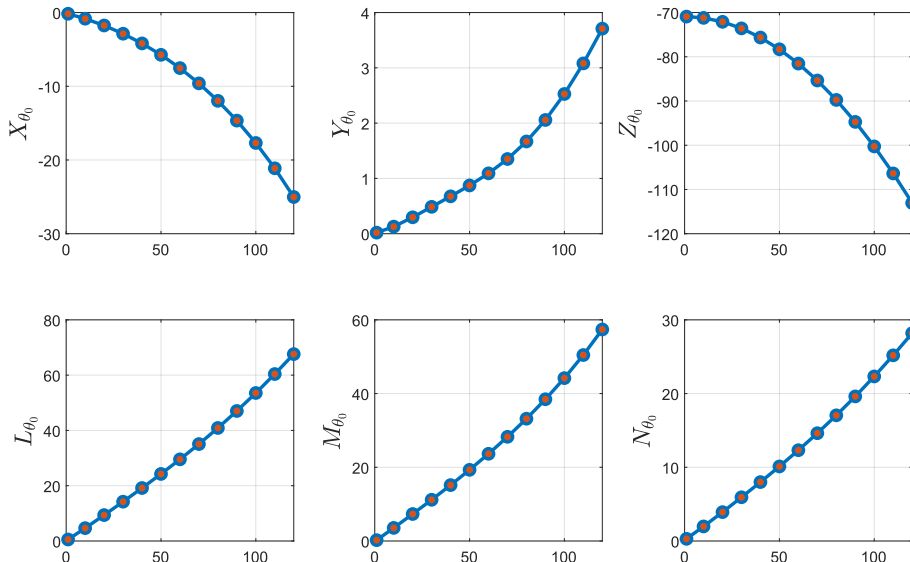


Figure 12.3: Control derivatives - collective.

Secondly, the differential collective θ_d is assessed and visualised in Figure B.6. It can be seen that the differential collective produces very little forces. It can be seen that it's main use, producing a yawing moment is achieved. However, it can be seen that this effect becomes negative after a certain flight speed, while it is expected to tend towards 0 for increasing flight speed. This however, might be attributed to the fact that the stall effects are not modelled in the rotor blades and that a sign switch occurs due to



the relation between tangential and lateral blade element velocity. The moment caused by the differential collective is most likely caused by a slight difference in longitudinal flapping angles between the 2 rotors and cross-coupling effects

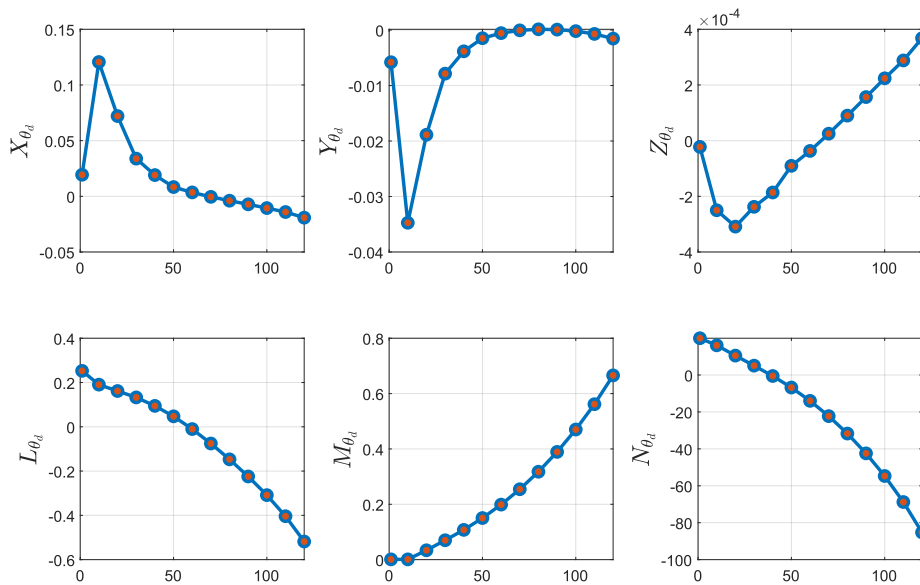


Figure 12.4: Control derivatives - differential collective.

Thirdly, the longitudinal cyclic control derivatives are plotted in Figure B.7. Clearly, an increase in X-force, and a decreasing in Z-force is caused by longitudinal cyclic stick input, which is exactly as expected. Increasing longitudinal cyclic tilts the disc plane forwards, tilting the thrust vector. It can be seen that this effect becomes more pronounced as flight speed increases. The X-force component mainly causes an M-moment, which also increases with increasing flight velocity, indicating that the cyclic becomes more effective at higher velocities. This comes paired with a cross-coupling on both the roll- and yaw-axes.

Fourthly, the lateral cyclic control derivative is visualised in Figure B.8. It can clearly be seen that there is no effect on the X- and Z-forces by the lateral cyclic. The main effect is in the Y-force, and rolling moment, which has slight (but not insignificant) cross-coupling with the yaw axis.

Fifthly, the differential lateral cyclic input is plotted in Figure B.9. Here, the same effects as for the lateral cyclic can be seen, to a far lesser extent. This is a good sign since the goal of lateral cyclic is not to control the aircraft, but rather create lift offset such that the helicopter is enabled to fly at high speeds.

Next, the pusher propeller collective control derivative can be seen in Figure B.10. The pusher propeller very simply only results in a pure X-force generating control, causing no unwanted effects, and is practically constant throughout the flight regime.

Second-to-last, the elevator control derivative is shown in Figure 12.9. It can be seen that the elevator X-force component is not modelled when using any elevator deflection, due to the small angle approximation. Hence, the elevator becomes a pure Z-force and M-moment generator, and becomes drastically more effective at higher flight speeds.

Lastly, the rudder control derivative is plotted in Figure 12.10. It can be seen that the rudder purely generates a Y-force, also omitting the X-force component due to the small angle approximation during modelling. The rudder then causes a yawing moment, which also drastically increases in effectiveness with flight speed. It can be seen that the yawing causes a cross-coupling in the roll axis, which is quite significantly, almost half the effectiveness of the yawing moment. This is an undesirable feat which can be altered by a design study, by e.g. changing the vertical placement of the rudder (0.5m in this model). Note

⁴Even in fixed wing aircraft, the yawing moment causes roll, and oppositely, better known as dutch roll.

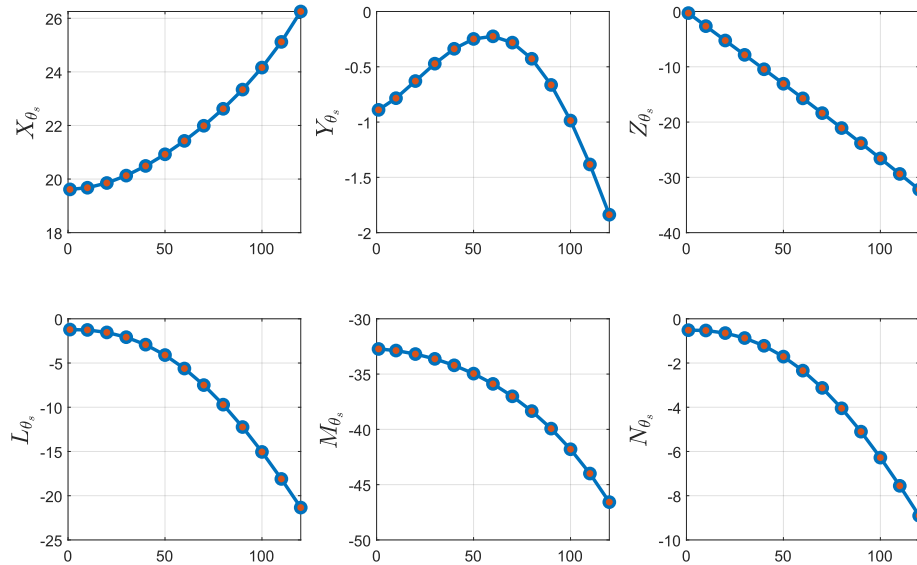


Figure 12.5: Control derivatives - longitudinal cyclic.

that some cross-coupling is inevitable in a helicopter system.⁴

Overall, it can be seen that the controls work as intended, meaning that they are implemented correctly for the intended purposes. However, there are multiple situations where certain aerodynamic effects are expected to have an effect, but do not, which is due to the modelling simplifications made in Chapter 10. Apart from this, it can be seen that there is still a significant cross-coupling in some controls, especially those correlated to the rotor system. This is something that should be considered when designing a control system, and assessing handling quality criteria.

In general, it has been found that the derivatives can be very sensitive to modelling errors. One such example was that at some point throughout the analysis, the angle b_{1_u} was mistakenly used in the calculation of the Y-force instead of $b_{1_{R_u}}$, resulting in an extreme roll due to pitch coupling.

Realistically speaking, there are most likely still several (smaller) errors in the model which affect the behaviour of the aircraft in linear simulation (resulting from the linear state-space model).

It also has to be noted that every assumption and non-modelled effect throughout the modelling chapter also affects the linear results, which is a direct effect of the model fidelity.

However, it can confidently be said that the model is able of capturing the main flight dynamics of the aircraft and is thus suitable for continued analysis. One remark to be given to future iterations of this model, is to have a close look at the required model fidelity, assessing if the assumptions made are justifiable, and if the stability and control derivatives are suitable for the analysis.

12.4. Open-Loop System Response

Now that the compound coaxial helicopter has been modelled, trimmed, and linearised, a final test on all of the previous steps can be performed, namely that of an open-loop response. In an open-loop response, a small disturbance is given to the helicopter, possibly at several speeds, around the trim state, and its behaviour is simulated and compared to what is physically expected.

In order to verify the nonlinear and linear model, open-loop responses are simulated for both cases at hover, 40 m/s, 80 m/s and 100 m/s in Section 12.4.1 and Section 12.4.2 respectively. These speeds have been chosen specifically since hover is a default interesting behaviour case, 40 m/s lies around the middle of the transition region between longitudinal cyclic and elevator (discussed in detail in Section 13.2, 80 m/s is the speed at which the longitudinal cyclic and elevator have the same control effectiveness (also discussed in detail in Section 13.2), and 100 m/s indicating high-speed flight, where the elevator is more effective than the longitudinal cyclic.

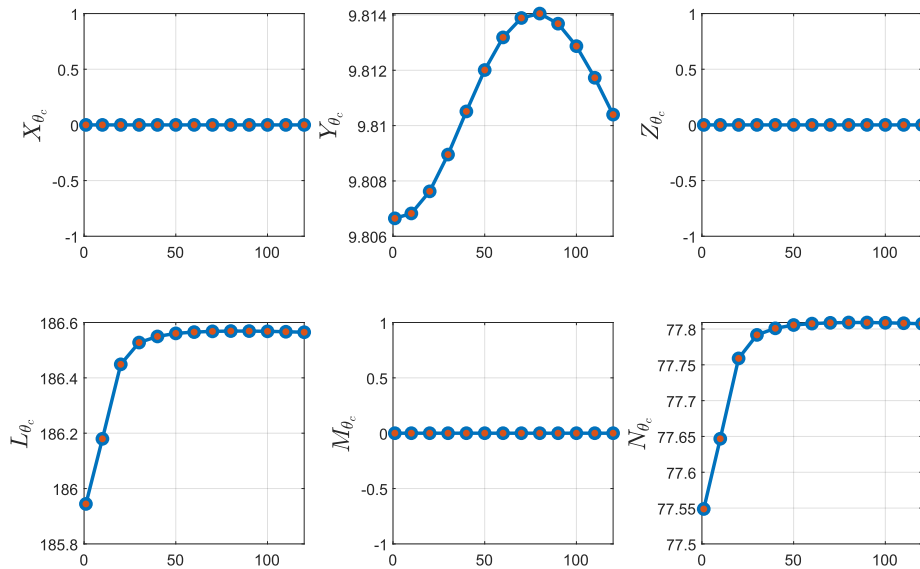


Figure 12.6: Control derivatives - lateral cyclic.

Throughout the simulations (also in subsequent chapters), the trim point is selected with a resolution of 5 m/s (the trim resolution from Chapter 11). The corresponding trim state selected during simulation is taken as the closest trim point to the current airspeed. In future iterations, an interpolation scheme, or more elaborated methods such as T-S fuzzy models. [26]

12.4.1. Nonlinear Model Open-Loop Response

In order to simulate the nonlinear response, a simple discrete time simulation has been set up in MATLAB. This function houses the entire nonlinear model, and outputs the states of the model using the velocity, trim state vector, angular accelerations, fuselage pitch angle, and other control inputs as inputs. The state vector in the next discrete time step is calculated using simple Euler integration based on the equations of motion described in Section 10.1.

This program was then ran for both a longitudinal cyclic and an elevator deflection of 1 deg separately, at hover, 40 m/s, 65 m/s and 100 m/s. The results are depicted in Figure 12.11-Figure 12.14. The full lines indicate the response due to longitudinal cyclic, and the dashed due to elevator. Several aspects are noteworthy:

- Hover:** The aircraft is slightly off trim which causes a slight drift in speeds, and thus also influences the response of the helicopter. The elevator has no effect, as there is no pitch rate caused by the elevator deflection, which is confirmed by the elevator control derivative M_{δ_e} in Figure 12.9. The longitudinal cyclic on the other hand can be seen to have quite a large peak pitch rate of around 18 deg/s. This is to be attributed to the coaxial configuration being more agile, especially in a stiff-bladed hingeless rotor such as the ABC-rotor. It has to be noted that some modelling errors cause this pitch rate to be too large, making the cyclic too sensitive. It can be seen that the helicopter is slightly stable at hover, with a long oscillation period and low damping. This will be inspected more closely in Section 12.5.
- 40 m/s:** The longitudinal cyclic has become slightly more effective, while the elevator has become effective as well, but still less than the longitudinal cyclic. The helicopter has now seem to become slightly unstable.
- 80 m/s:** At this speed, the longitudinal cyclic and elevator are equally effective, which can be seen since the 2 plots are exactly on top of each other. The helicopter is now clearly unstable, rapidly diverging from its original condition after around 10 seconds.

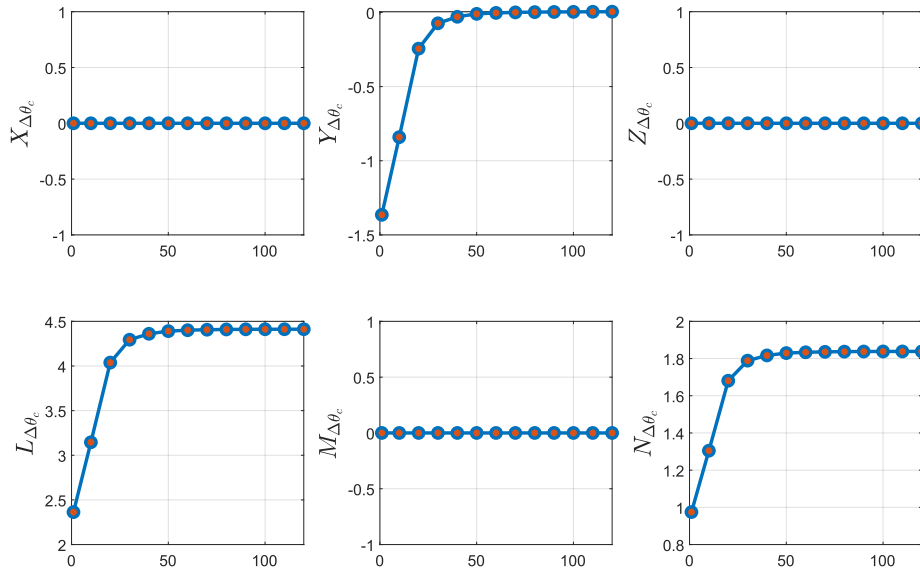


Figure 12.7: Control derivatives - differential lateral cyclic.

- **100 m/s:** The pitch rate caused by the elevator is now larger than that of the cyclic, meaning it is now more effective. The helicopter is now very unstable and rapidly diverges. Note that when large angles are reached by the model, it becomes inaccurate, since the model does not take into account large angles (e.g. around 90 degrees pitch, roll, etc..).

It can clearly be seen that the helicopter can benefit from a control augmentation system in order to create more desirable damping characteristics and handling qualities, especially at mid-to-high speed flight. This will be the focus of Chapter 13, which will aim to stabilise the system and track several manoeuvres.

12.4.2. Linear Model Open-Loop Response

In order to gain the same understanding for the linear system as for the nonlinear system, the same disturbances were given to the linear system. The linear system simulation was modelled in MATLAB Simulink, for which the responses are shown in Figure 12.15 - Figure 12.18. Note that the input signals are with respect to the trim state.

It can be seen that the linear response closely follows that of the nonlinear system, apart from a few differences. The effectiveness difference between the longitudinal cyclic and elevator is visible in the linear responses as well, while achieving similar maximum pitch rates with similar dynamic instability.

However, it can be seen that the linear model seems to be slightly less dynamic, and even a bit more stable compared to the nonlinear system, indicating that it captures less of the nonlinearities of the system. It can also be seen that the response to the velocities is smaller than that of the nonlinear response.

Lastly, the hover response shows an almost perfectly damped (not perfect, as will be shown in Section 12.5) response, which is different than the nonlinear response. However, due to the nonlinear model being off-trim, this is most likely the cause of the difference between the responses.

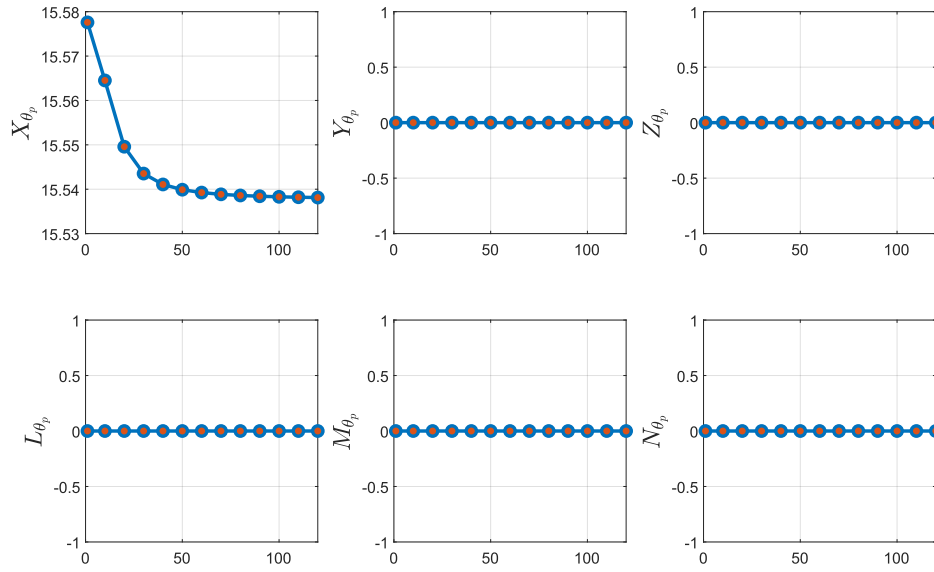


Figure 12.8: Control derivatives - pusher propeller collective.

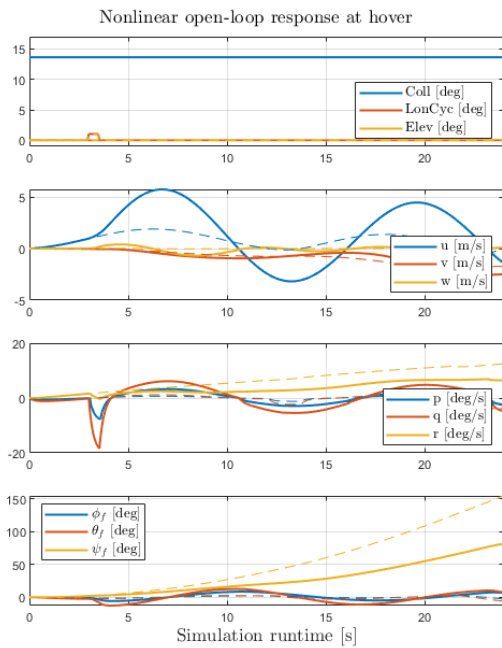


Figure 12.11: Nonlinear response at hover.

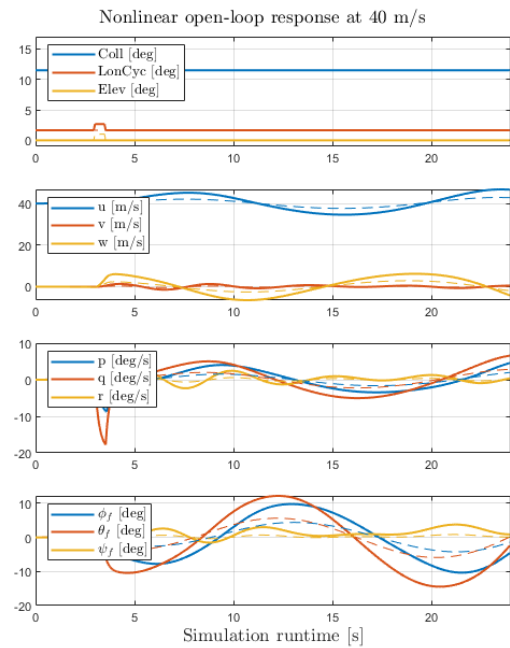


Figure 12.12: Nonlinear response at 40 m/s.

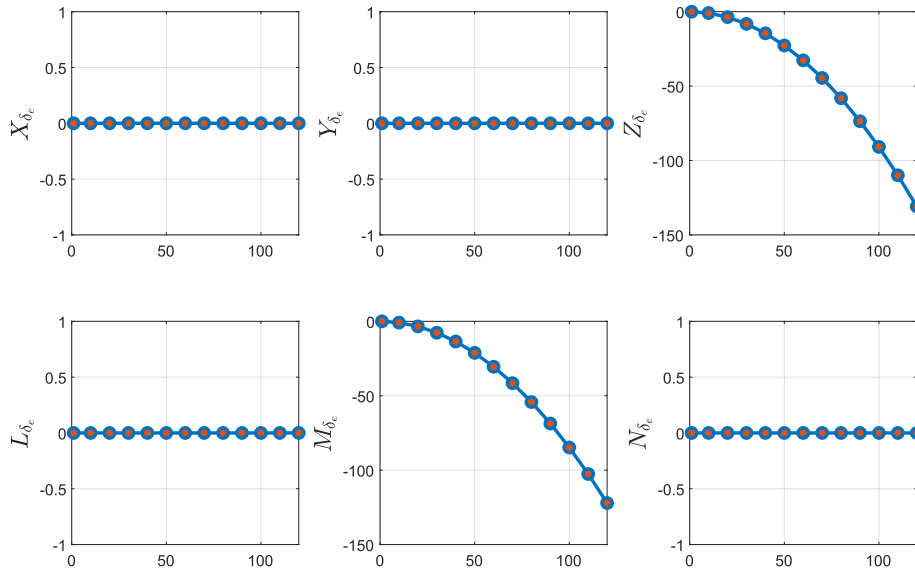


Figure 12.9: Control derivatives - elevator.

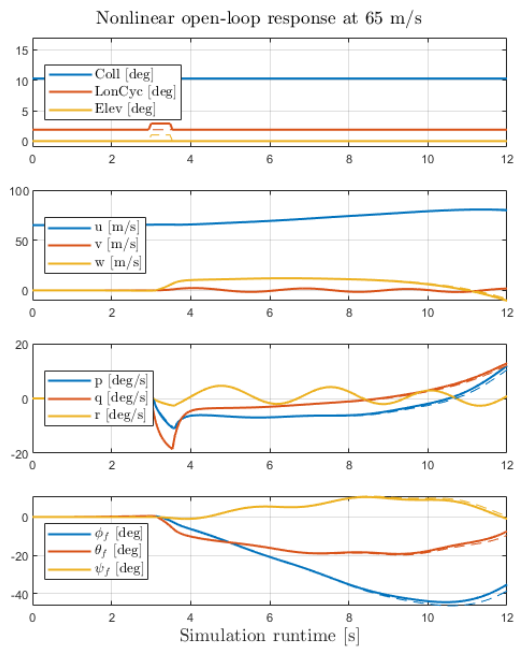


Figure 12.13: Nonlinear response at 65 m/s.

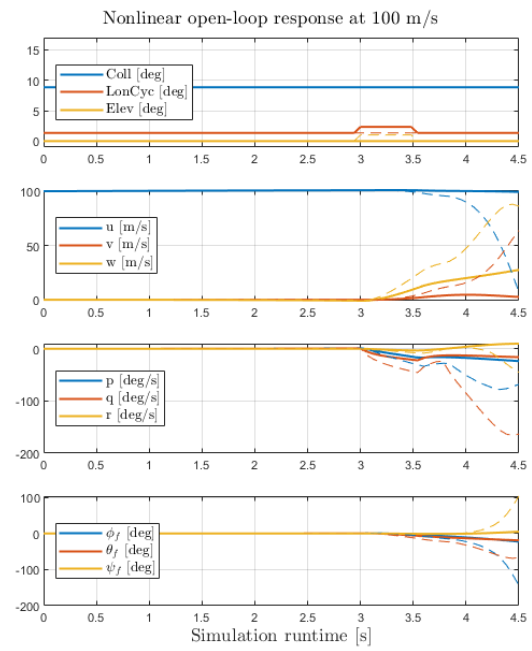


Figure 12.14: Nonlinear response at 100 m/s.

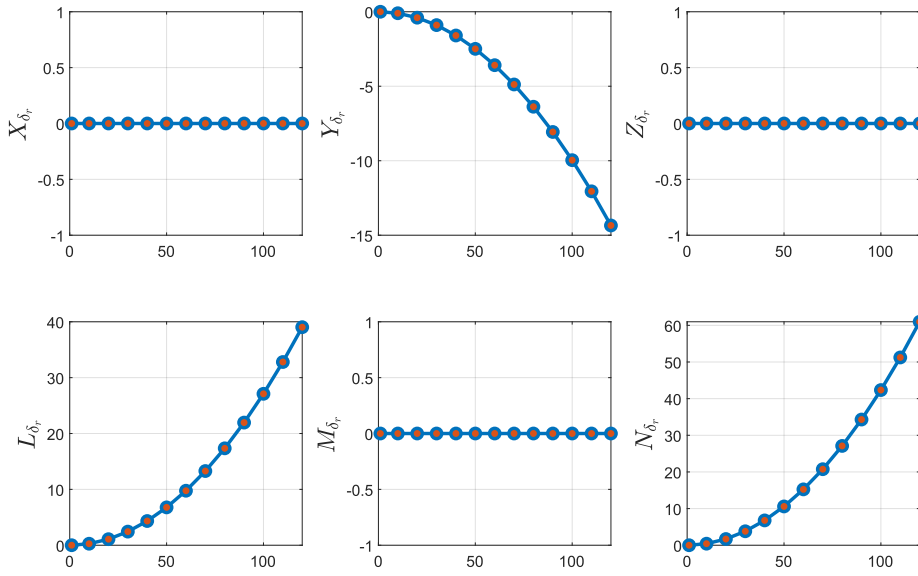


Figure 12.10: Control derivatives - rudder.

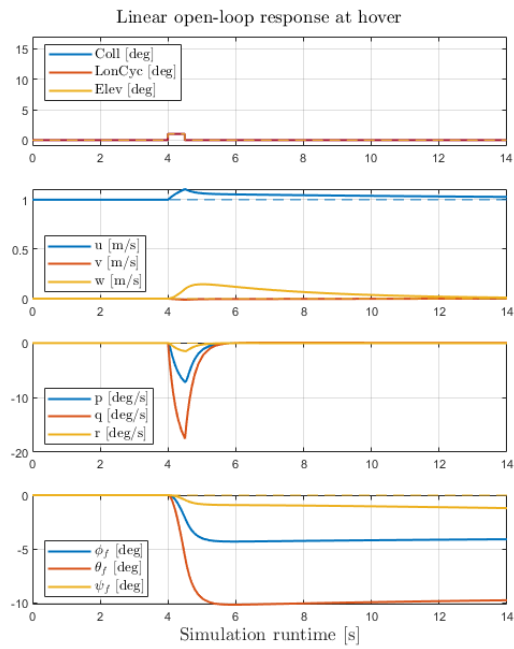


Figure 12.15: Linear response at hover.

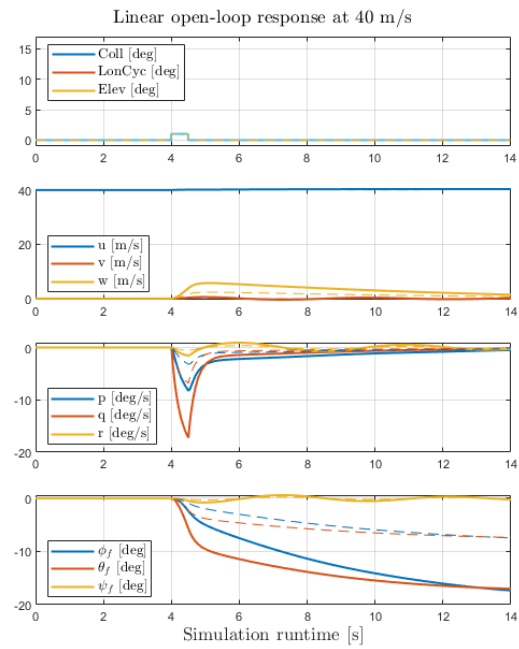


Figure 12.16: Linear response at 40 m/s.

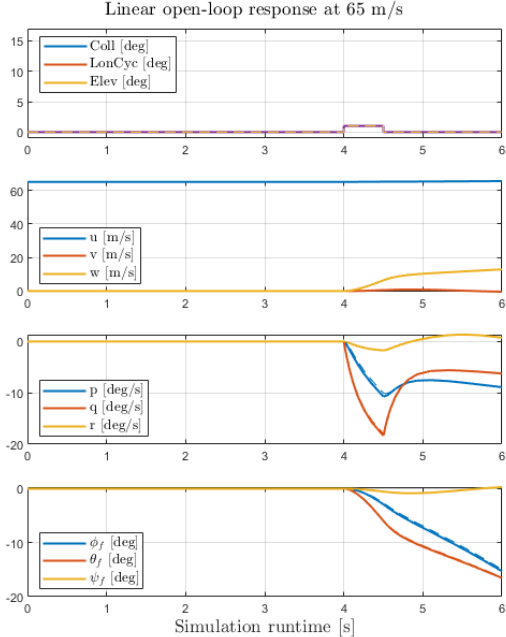


Figure 12.17: Linear response at 65 m/s.

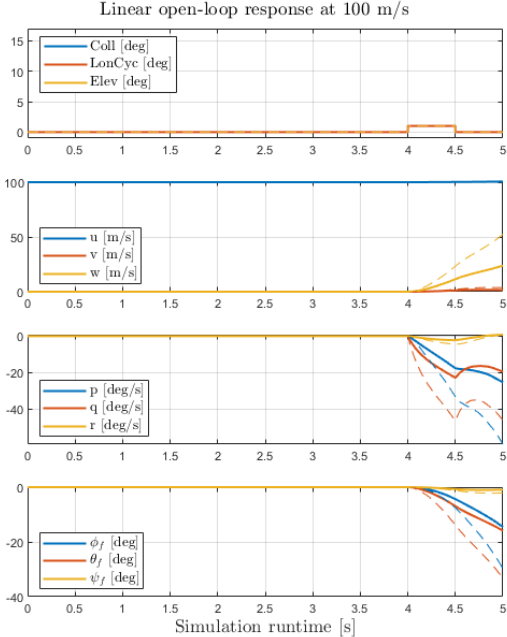


Figure 12.18: Linear response at 100 m/s.



12.5. Longitudinal Natural Modes of Motion

In order to get a quantitative understanding of the stability characteristics, the next following step from the stability and control derivatives are the natural modes of motion. Since the helicopter manoeuvring will be limited to the longitudinal axis, only the longitudinal modes will be studied. These encompass the phugoid, short period, pitch subsidence and heave subsidence.

The pitch and heave subsidence are simply the stability derivatives M_q and Z_w respectively. They indicate the pitch damping and heave damping of the aircraft, and are negative throughout the entire flight regime, with increased damping.

The eigenvalues of the phugoid and short-period modes can be calculated by means of the approximating characteristic equation for low-frequency oscillation, resulting in the quadratic equation's as outlined by Equation 12.9 and Equation 12.10 respectively. [18]

$$\lambda^2 - \left(X_u + g \frac{M_u}{M_q^2} \right) \lambda - g \frac{M_u}{M_q} = 0 \quad (12.9)$$

$$\lambda_{sp}^2 - (Z_w + M_q) \lambda_{sp} + Z_w M_q - M_w (Z_q + U_e) = 0 \quad (12.10)$$

Solving these quadratic equation provides the eigenvalues for the modes of motion, and can be plotted on a $\omega - \mu$ graph, as in Figure 12.19. Here, ω is the imaginary part of the eigenvalue, indicating the oscillation, and μ the real part of the eigenvalue, indicating the damping. The plots range from dark blue to dark red, indicating an increase in speed.

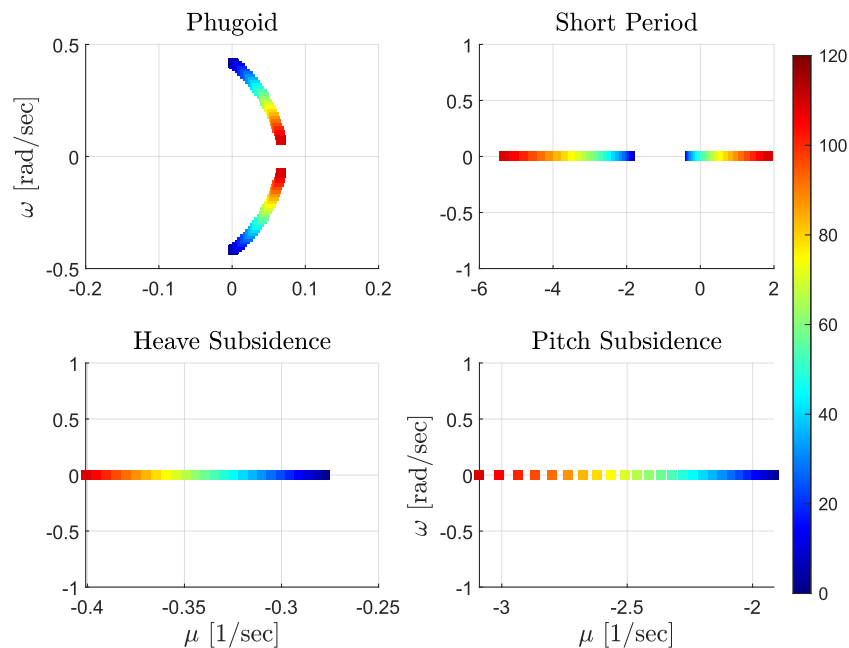


Figure 12.19: Longitudinal natural modes of motion.

It can be seen that the phugoid is close to 0 at low speed flight, with the real part of the eigenvalue still positive, indicating slight instability. The imaginary part of the eigenvalue at low speeds indicates high oscillatory behaviour. Throughout the flight speed, the phugoid becomes slightly more unstable and much less oscillatory. This is in line with results from Ferguson [28]. The main reason for this instability is the use of a hingeless rotor, where the stiff rotors create large moments around the rotor hub due to the large hinge-offset and spring-stiffness moments. When the coaxial rotor system is perturbed in forward speed, there is a pitch-up moment due to the rotor blades flapping back, which is confirmed by the positive M_u derivative. As the fuselage pitches up, the main rotors provide a pitch down moment due to the negative M_q



value, causing an oscillatory motion which steadily increases in magnitude. Due to a similar perturbation in forward speed, the blade incidence of the rotor reduces, providing an extra drag force [28], decreasing X_u . However, this appears to be insufficient to stabilise the aircraft. Note that the model behaviour, and consequently its derivatives and open-loop behaviour, highly depend on the rotor characteristics such as hinge offset and spring stiffness.

The short period can be seen to be non-oscillatory and stable at low speeds, while decreasing with increasing speed. This is the result of the spring term $Z_w M_q - M_w(Z_q + U_e)$, which greatly impacts the short period stability. [28] The term is required to be positive for stability, and when plotted in Figure 12.20 can be seen to become negative around 40 m/s, which is verified by the nonlinear plots, where it can be seen that the aircraft becomes unstable. The term $-(Z_w + M_q)$ is always positive since the lift force due to a vertical disturbance and the aircraft response due to a pitch rate are stabilising.

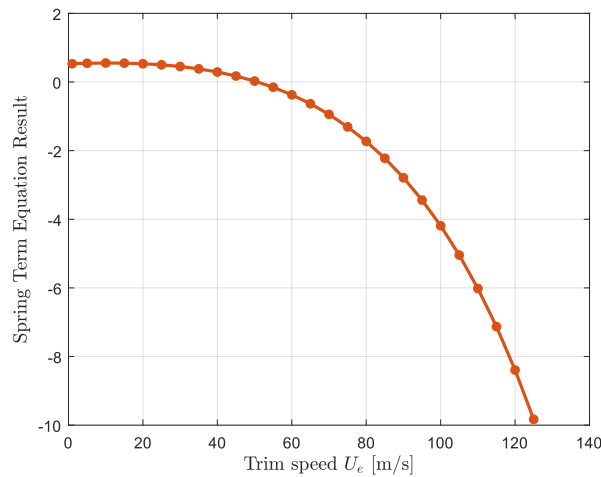


Figure 12.20: Spring term result of Equation 12.10.

Both the pitch and heave subsidence are non-oscillatory and damped throughout the entire flight envelope, which was clear from their longitudinal stability derivative values M_q and Z_w .

The eigenvalues at intervals of 25 m/s are listed in Table 12.1. It can be concluded that although there is a large negative eigenvalue (pitch subsidence), there is still a dominant eigenvalue in the right half plane (phugoid), causing instability. of the system. This gives rise to the requirement of a control system, for which special attention has to be given to the overactuation problem.

Table 12.1: Longitudinal eigenvectors throughout the trim range.

V (m/s)	Phugoid	Short Period	Heave Subsidence	Pitch Subsidence
1	$0.0008 \pm 0.4169i$	-0.2783	-0.2778	-1.9148
25	$0.0177 \pm 0.3649i$	-0.2364	-0.3009	-2.0563
50	$0.0343 \pm 0.3052i$	-0.0107	-0.3248	-2.2369
75	$0.0479 \pm 0.2346i$	0.4065	-0.3494	-2.4601
100	$0.0584 \pm 0.1605i$	1.0149	-0.3749	-2.7370
125	$0.0664 \pm 0.0739i$	1.8434	-0.4009	-3.0891

Flight Controller Design

In this chapter, the control strategies essential for enhancing the performance and handling quality of compound coaxial helicopters will be discussed. It begins by exploring the controller architecture in Section 13.1, which forms the backbone of the control system, followed by a detailed examination of multi-stage control allocation to ensure optimal distribution of control efforts in Section 13.2. The chapter then addresses the inner loop attitude controller in Section 13.3, crucial for maintaining the helicopter's desired orientation, and the outer loop velocity controller in Section 13.4, which governs the aircraft's speed and trajectory. Additionally, it covers the critical aspects of controller tuning to achieve desired performance metrics in Section 13.5. The chapter concludes with a comprehensive simulation analysis of two specific manoeuvres in Section 13.6: the 3-2-1-1 input and bob-up/down with acceleration and deceleration, demonstrating the effectiveness of the proposed control strategies in real-world scenarios.

13.1. Controller Architecture

From previous analysis in Section 12.5, it became clear that the helicopter could benefit greatly from a control system. However, several challenges arise when designing this controller. Firstly, there is cross-channel coupling, as in any helicopter, additionally to this, there is cross-coupling between the different control surfaces, which has to be accounted for during tuning. Secondly, there are a greater number of controls than states, causing redundant controls. These will have to be scheduled and their changing effectiveness accounted for.

The top-level controller architecture, based on that of Qiu [26] is visualised in Figure 13.1. The controller consists of an inner- and outer-loop controller, each making use of control allocation to deal with the overactuated system, and the nonlinear coaxial model. The outer-loop controller in essence controls the velocity $[u, v, w]^T$, and consequently position, while the inner-loop controls the helicopter attitude. Both the outer- and inner-loop controllers will feature an Explicit-Model-Following (EMF) based control, with both control allocation algorithms based on the weighted pseudo-inverse method.

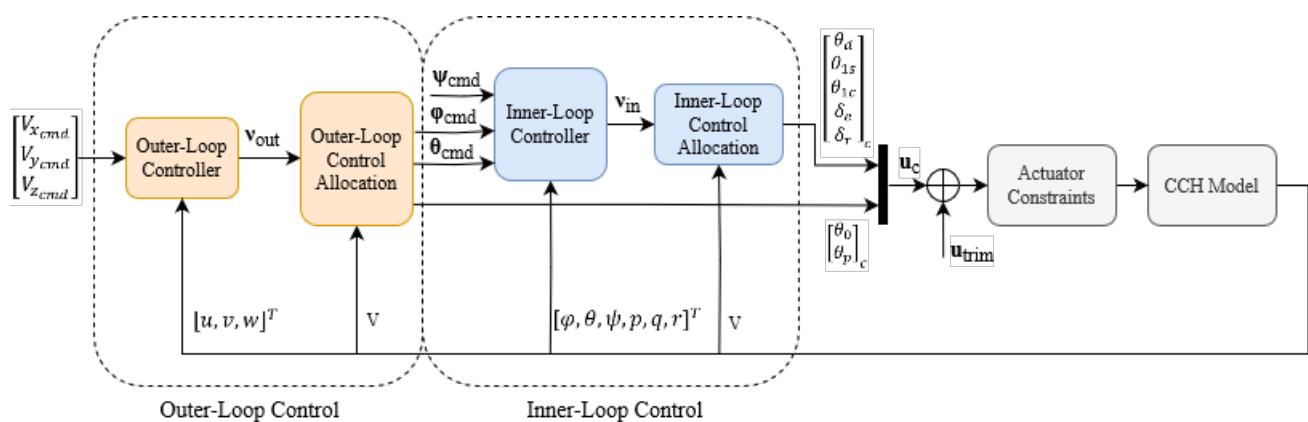


Figure 13.1: Top-level controller architecture.



Firstly, the velocity commands $[V_{x_{cmd}}, V_{y_{cmd}}, V_{z_{cmd}}]^T$ are processed by the outer-loop controller, finding the outer-loop virtual control ν_{in} which is fed into the outer-loop control allocation, producing the commanded attitudes $[\psi_{cmd}, \phi_{cmd}, \theta_{cmd}]^T$. These are in turn used by the inner-loop controller to produce the virtual control ν_{out} , which is then processed by the inner loop control allocation algorithm to produce the inner and outer loop controls $[\theta_d, \theta_{1s}, \theta_{1c}, \delta_e, \delta_r]^T$ and $[\theta_0, \theta_p]^T$ respectively. The sum of these controls form $\mathbf{u}_c = [\theta_d, \theta_{1s}, \theta_{1c}, \delta_e, \delta_r, \theta_0, \theta_p]^T$, which are added to the trim state inputs \mathbf{u}_{trim} . The trim inputs are calculated in the same manner as during the open-loop response, finding the nearest trim point velocity and using those variables, which were stored during the trimming routine. Note that due to the decoupling of the outer and inner loop, the inner loop controls $[\theta_d, \theta_{1s}, \theta_{1c}, \delta_e, \delta_r]^T$ and outer loop controls $[\theta_0, \theta_p]^T$ are decoupled. This reduces the influence of the inner loop on altitude and velocity control.

13.2. Multi-Stage Control Allocation

To address the control redundancy and clear control coupling discussed in Chapter 12, a multi-stage control allocation algorithm will be developed. Given the drastic changes in actuator effectiveness throughout the flight envelope, these must be considered during the allocation process. The allocation procedure will be based on the weighted pseudo-inverse method and is designed to compute the seven actuator commands (excluding the differential lateral cyclic $\Delta\theta_{1c}$) using inner- and outer-loop virtual control laws.

13.2.1. Inner-Loop Control Allocation

The first stage of the algorithm design is the inner loop allocation, which controls the aircraft's attitude angles: pitch θ , roll ϕ , and yaw ψ . Pitch will be controlled using the longitudinal cyclic θ_{1s} and elevator δ_e . Roll is controlled solely by the lateral cyclic θ_{1c} and thus does not require allocation. Yaw is controlled by the differential collective θ_d and rudder δ_r . V denotes airspeed, and ϵ is a small constant greater than zero.

The control effectiveness of the actuators varies significantly throughout the flight range, as illustrated in Figure 13.2. The intersections indicate where one control becomes more effective than another, marking the transition region for this channel, which occurs at 65 m/s. The transition region begins at 20 m/s, indicating the gradual activation of the rudder and elevator, as commonly referenced in literature [26]. This gradual activation makes sure that when the elevator is activated, it prevents suddenly causing any large deflections and moments, especially around the start of the transition region, where the control is almost only slightly effective.

Using the transition regions, a linear distribution for the control weights can be established. This distribution linearly decreases the usage of θ_{1s} and $\Delta\theta_d$ and linearly increases the usage of δ_e and δ_r . The control weights for pitch and yaw are calculated by Equation 13.1 and Equation 13.2, respectively. Here, $\rho_{\theta_{1s}}$ and ρ_{δ_e} are the control weights for the longitudinal cyclic θ_{1s} and elevator δ_e in the pitch channel. Similarly, ρ_{θ_d} and ρ_{δ_r} denote the control weights for differential collective θ_d and rudder δ_r in the yaw channel. These are visualised in Figure 13.3 for pitch; the yaw-channel distribution follows the same trend. [26] It can be seen however, that there is a region around 40 m/s, in which there is very little yaw authority, since both control derivatives of the differential collective, and the rudder, are very small.

$$\rho_{\theta_{1s}} = \begin{cases} 1, & V \leq 20 \text{ m/s} \\ 1 - \frac{1}{40}(V - 20), & 20 < V < 65 \text{ m/s} \\ \epsilon, & V \geq 65 \text{ m/s} \end{cases} \quad (13.1)$$

$$\rho_{\delta_e} = \begin{cases} \epsilon, & V \leq 20 \text{ m/s} \\ \frac{1}{40}(V - 20), & 20 < V < 65 \text{ m/s} \\ 1, & V \geq 65 \text{ m/s} \end{cases}$$

$$\rho_{\theta_d} = \begin{cases} 1, & V \leq 20 \text{ m/s} \\ 1 - \frac{1}{40}(V - 20), & 20 < V < 65 \text{ m/s}, \\ \epsilon, & V \geq 65 \text{ m/s} \end{cases} \quad (13.2)$$

$$\rho_{\delta_r} = \begin{cases} \epsilon, & V \leq 20 \text{ m/s} \\ \frac{1}{40}(V - 20), & 20 < V < 65 \text{ m/s} \\ 1, & V \geq 65 \text{ m/s} \end{cases}$$

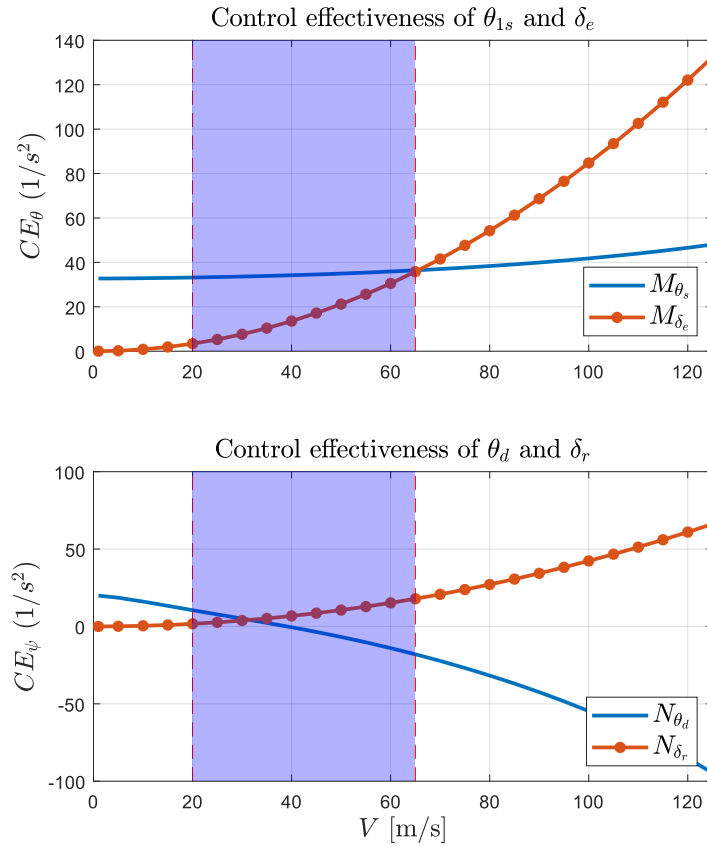


Figure 13.2: Control effectiveness for pitch and yaw throughout flight range.

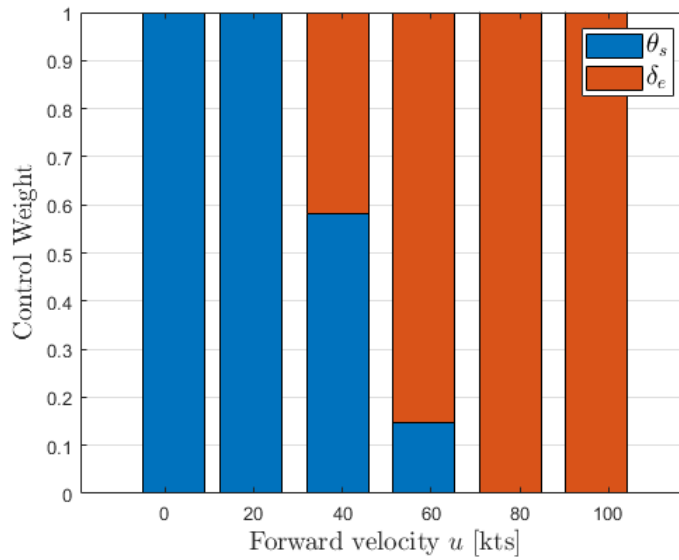


Figure 13.3: Control allocation weights for the pitch channel.

Next, using the inner-loop virtual control $\nu_{in} = [\nu_\phi, \nu_\theta, \nu_\psi]^T$, a pseudo-inverse allocation algorithm can be applied, resulting in the allocation for roll, pitch, and yaw as follows [26]:



$$\left\{ \begin{array}{l} \text{Roll angle } \phi: [\theta_{1c}]_c = \frac{\nu_\phi}{L_{\theta_{1c}}} \\ \text{Pitch angle } \theta: [\theta_{1s}, \delta_e]_c^T = \mathbf{W}_\theta^{-1} \mathbf{B}_\theta^T (\mathbf{B}_\theta \mathbf{W}_\theta^{-1} \mathbf{B}_\theta^T)^{-1} \nu_\theta, \\ \quad \mathbf{W}_\theta = \text{diag} \left[\frac{1}{\rho_{\theta_{1s}}}, \frac{1}{\rho_{\delta_e}} \right], \mathbf{B}_\theta = [L_{\theta_{1s}}, M_{\delta_e}] \\ \text{Yaw angle } \psi: [\theta_d, \delta_r]_c^T = \mathbf{W}_r^{-1} \mathbf{B}_r^T (\mathbf{B}_r \mathbf{W}_r^{-1} \mathbf{B}_r^T)^{-1} \nu_r, \\ \quad \mathbf{W}_r = \text{diag} \left[\frac{1}{\rho_{\theta_d}}, \frac{1}{\rho_{\delta_r}} \right], \mathbf{B}_r = [N_{\theta_d}, N_{\delta_r}] \end{array} \right. \quad (13.3)$$

Here, $L_{\theta_{1s}}$, M_{δ_e} , N_{θ_d} , and N_{δ_r} are the control derivatives calculated in Section 12.3.

Notably, a significant advantage of this design is its inherent ability to account for cross-coupling between the primary control axes of the helicopter.

13.2.2. Outer-Loop Control Allocation

The second stage of the allocation process is the outer loop, which manages airspeed tracking. The longitudinal velocity V_x is controlled by the pitch angle θ_{cmd} and pusher propeller θ_p , vertical velocity V_z by collective θ_0 and pitch angle θ , and lateral velocity by the roll angle ϕ . This allocation process is based on the transition from hover (helicopter) mode to high-speed (fixed wing) mode.

The transition region will also range from 20-65 m/s, similar to the inner-loop control allocation. This leads to the same formula for the control weights for the outer loop, shown below.

$$\rho_{\theta_{cmd}^x} = \begin{cases} 1, & V \leq 20 \text{ m/s} \\ 1 - \frac{1}{40}(V - 20), & 20 < V < 65 \text{ m/s} \\ \epsilon, & V \geq 65 \text{ m/s} \end{cases} \quad (13.4)$$

$$\rho_{\theta_p} = \begin{cases} \epsilon, & V \leq 20 \text{ m/s} \\ \frac{1}{40}(V - 20), & 20 < V < 65 \text{ m/s} \\ 1, & V \geq 65 \text{ m/s} \end{cases}$$

$$\rho_{\theta_0} = \begin{cases} 1, & V \leq 20 \text{ m/s} \\ 1 - \frac{1}{40}(V - 20), & 20 < V < 65 \text{ m/s}, \\ \epsilon, & V \geq 65 \text{ m/s} \end{cases} \quad (13.5)$$

$$\rho_{\theta_{cmd}^z} = \begin{cases} \epsilon, & V \leq 20 \text{ m/s} \\ \frac{1}{40}(V - 20), & 20 < V < 65 \text{ m/s} \\ 1, & V \geq 65 \text{ m/s} \end{cases}$$

Here, ρ_{θ_x} , ρ_{θ_p} , ρ_{θ_0} , ρ_{θ_z} indicate the control weights, θ_{cmd}^x the commanded pitch for longitudinal velocity V_x , and θ_{cmd}^z for vertical velocity V_z . The total commanded pitch angle is then:

$$\theta_{cmd} = \theta_{cmd}^x + \theta_{cmd}^z \quad (13.6)$$

Next, using the inner-loop virtual control $v_{in} = [v_\phi, v_\theta, v_r]^T$, a pseudo-inverse allocation algorithm can be applied, resulting in the allocation for roll, pitch, and yaw as follows [26]:

Similarly to the inner-loop, the outer loop control $\nu_{out} = [\nu_x, \nu_y, \nu_z]^T$ can be used in a pseudo-inverse algorithm, resulting in the outer-loop control outputs θ_{cmd} , θ_p , θ_0 , and ϕ :



$$\left\{ \begin{array}{l} \text{Longitudinal velocity } V_x: [\theta_{\text{cmd}}^x, \theta_p]^T = \mathbf{W}_x^{-1} \mathbf{B}_x^T (\mathbf{B}_x \mathbf{W}_x^{-1} \mathbf{B}_x^T)^{-1} \nu_x \\ \qquad \qquad \qquad \mathbf{W}_x = \text{diag} \left[\frac{1}{\rho_{\theta_{\text{cmd}}^x}}, \frac{1}{\rho_{\theta_p}} \right], \mathbf{B}_x = [-1, 1] \\ \text{Lateral velocity } V_y: \phi_{\text{cmd}} = \nu_y \\ \text{Vertical velocity } V_z: [\theta_0, \theta_{\text{cmd}}^z]^T = \mathbf{W}_z^{-1} \mathbf{B}_z^T (\mathbf{B}_z \mathbf{W}_z^{-1} \mathbf{B}_z^T)^{-1} \nu_z \\ \qquad \qquad \qquad \mathbf{W}_z = \text{diag} \left[\frac{1}{\rho_{\theta_0}}, \frac{1}{\rho_{\theta_{\text{cmd}}^z}} \right], \mathbf{B}_z = [1, 1] \end{array} \right. \quad (13.7)$$

13.2.3. Control Strategy

Due to the demonstrated changing control effectiveness, and by implementing the control allocation procedure outlined before, a control strategy throughout the flight regime can be constructed, and is outlined in Table 13.1.

Table 13.1: Compound coaxial helicopter control strategy throughout flight regime. [26]

Flight Mode	Control Method				
	Roll	Pitch	Yaw	Height	Forward Velocity
Helicopter Mode (0-20 m/s)	θ_{1c}	θ_{1s}	θ_d	θ_0	θ
Transition Mode (20-65 m/s)	θ_{1c}	$\theta_{1c} \rightarrow \delta_e$	$\theta_d \rightarrow \delta_r$	$\theta_0 \rightarrow \theta$	$\theta \rightarrow \theta_p$
Fixed Wing Mode (>65 m/s)	θ_{1c}	δ_e	δ_r	θ	θ_p

13.3. Inner-Loop Attitude Controller

As outlined at the start of this chapter, the inner-loop controller controls the aircraft attitude angles $[\psi_{\text{cmd}}, \phi_{\text{cmd}}, \theta_{\text{cmd}}]$ for which ϕ_{cmd} and θ_{cmd} come from the outer-loop control allocation, and where ψ_{cmd} is a pre-defined command value. The chosen architecture for the inner-loop controller is based on an Explicit-Model-Following (EMF) technique [64], and is depicted in Figure 13.4.

The input signals for the inner loop are ϕ_{cmd} , θ_{cmd} , and ψ_{cmd} , which come from the outer-loop control allocation. These are fed into M_θ , and M_ψ , denoting the explicit models, which will be explained in the following paragraph. The output of these explicit models are ϕ_c , θ_c , and ψ_c , which refer to the explicit model control value. Using these relative error between the explicit control value and the aircraft states, a normal PID tuner is used with the parameters $K_{P,\phi}$, $K_{I,\phi}$, $K_{P,p}$, $K_{P,\theta}$, $K_{I,\theta}$, $K_{P,q}$, $K_{P,\psi}$, $K_{I,\psi}$, and $K_{P,r}$, the proportional and integral gains for the roll angle, roll rate, pitch angle, pitch rate, yaw angle and yaw rate respectively. After summation, the virtual controls ν_ϕ , ν_θ , and ν_ψ are fed into the inner-loop control allocation, and processed to output the real aircraft inner-loop controls $[\theta_d, \theta_{1s}, \theta_{1c}, \delta_e, \delta_r]^T$, which are combined with the outer-loop controls $[\theta_0, \theta_p]^T$ to form the total input vector \mathbf{u}_c .

The virtual control laws ν_ϕ , ν_θ , and ν_ψ are based on PID control laws which are shown in Equation 13.8, with accompanying gains explained above.

$$\begin{aligned} \nu_\phi &= K_{P,\phi} (\phi_c - \phi) + K_{I,\phi} \int (\phi_c - \phi) dt - K_{P,pp} \\ \nu_\theta &= K_{P,\theta} (\theta_c - \theta) + K_{I,\theta} \int (\theta_c - \theta) dt - K_{P,qq} \\ \nu_\psi &= K_{P,\psi} (r_c - r) + K_{I,\psi} \int (r_c - r) dt - K_{P,rr} \end{aligned} \quad (13.8)$$

In an EMF controller, the state error is not calculated directly with respect to the command signal e.g. θ_{cmd} , but rather to an explicit model control value θ_c . This control value is calculated by means of using the command signal θ_{cmd} as an input to an explicit model transfer function, e.g. $M_\theta(s)$, which has desirable transient behaviour in terms of rise time, overshoot and settling time. Note that for any aircraft target mission profile, this explicit model may change. For example, a combat helicopter might require more

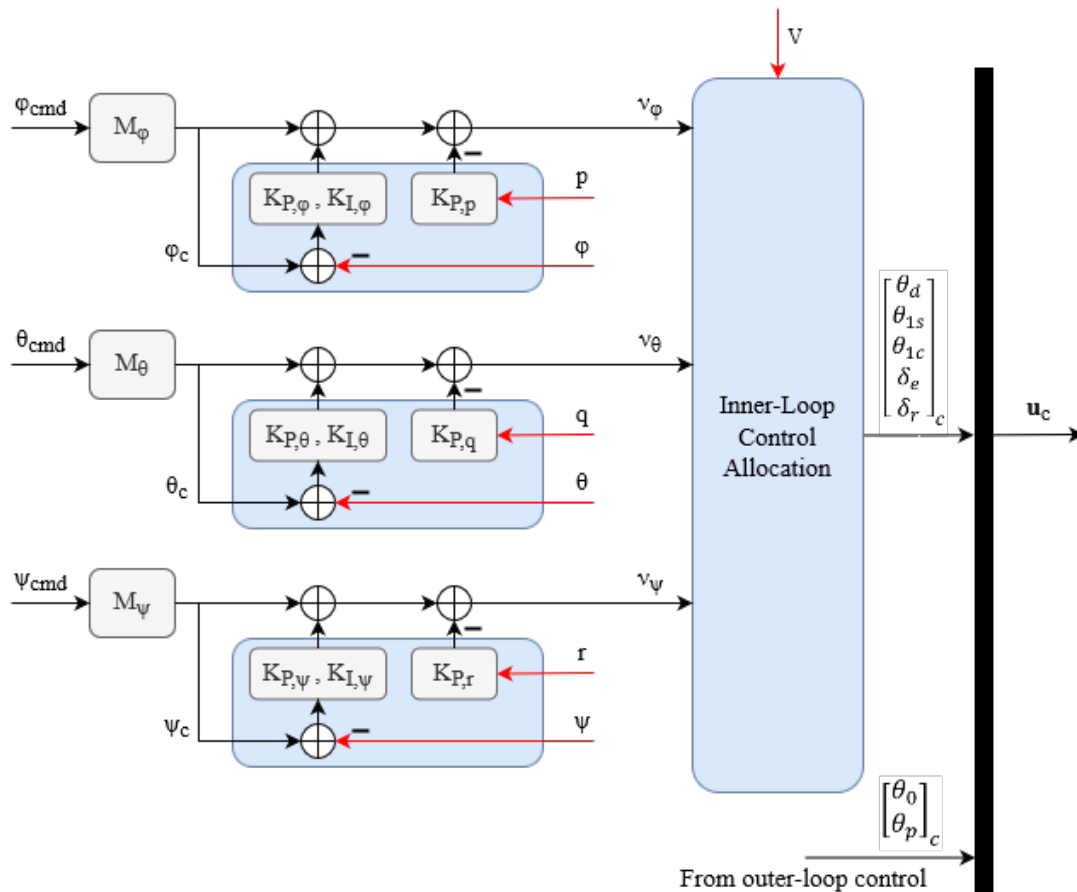


Figure 13.4: Inner loop controller design based on EMF control.

aggressive transient behaviour, requesting smaller rise times, at the cost of more overshoot and/or more oscillatory behaviour. A transport aircraft on the other hand might require very little overshoot, at the cost of rise time. In essence, it is a trade-off between manoeuvrability and stability.

$$M_\phi(s) = M_\theta(s) = M_\psi(s) = \frac{\omega_n^2}{s^2 + 2\zeta\omega_n s + \omega_n^2} \quad (13.9)$$

In this thesis, $M_\phi(s)$, $M_\theta(s)$ and $M_\psi(s)$ are all defined by second degree transfer functions, by means of Equation 13.9. Here, ω_n is the natural frequency, and ζ the damping ratio. The choice of these parameters determine the explicit model behaviour, and can thus be tuned to fit desired manoeuvrability and stability characteristics. The values chosen in this research are listed in Table 13.2, which are based on a critical damping ratio, corresponding to 0.707, which causes the fastest rise time without oscillations. The natural frequency of 4 rad/s causes a good rise-time, with comfortable but responsive agility. The time-domain signal response produced by the command model for an example 5 degree pitch step input, using the previously mentioned model parameters, is visualised in Figure 13.5.

Table 13.2: Explicit model parameters.

Channel	ω_n [rad/s]	ζ
Roll angle, ϕ	4.0	0.707
Pitch angle, θ	4.0	0.707
Yaw angle, ψ	4.0	0.707

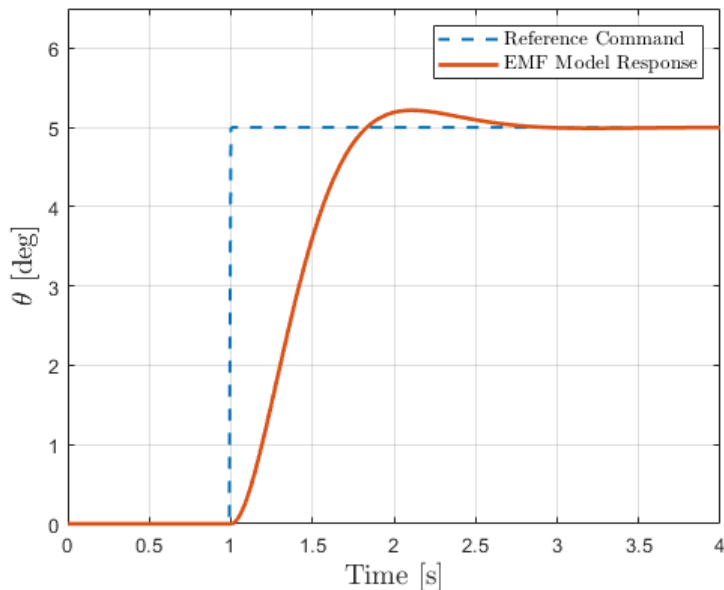


Figure 13.5: Step input reference command and EMF model response.

An extension of the EMF technique is to calculate a deflection δ_{axis} , where the subscript "axis" can be either the longitudinal axis, lateral, or yaw axis, which is then summed up with the gains from the original EMF method. The deflection δ is calculated by means of taking the inverse of a transfer function, e.g. $\frac{\theta}{\delta_{lon}}$, where the transfer function is a fit to the bare-airframe transfer function depicting the frequency domain behaviour of $\frac{\theta}{\delta_{lon}}$, where δ_{lon} is a combination of the longitudinal cyclic θ_{1s} and the elevator δ_e . The fit is done between 1-10 rad/s, which is where most of the pilot inputs in the frequency domain happen. [65] Note that at every change of stability and/or control derivatives, this transfer function may need to change, and thus an automated implementation is recommended. An example of this system is discussed in Qiu et al. [26]. Using this strategy, a more robust flight controller can be established, by using the PID controller merely as a stabiliser to account for the discrepancies between the lower-order inverse models and the actual bare-airframe dynamics.

13.3.1. Actuator Limit and Rate Constraints

In an effort to constrain the actuators to resemble real-life limits, their maximal and minimal limits, and rates are implemented after the controller calculates a certain desired input. The limits that are used are listed in Table 13.3, based on the works of Vayalali et al. [66]. Note that other more detailed analysis in aspects such as the rotor spacing might constrain the actuators more. A more elaborate way to incorporate the actuator saturation would be by means of Pseudo-Control Hedging, however, this is beyond the scope of this work.

Table 13.3: Actuator limit and rate constraints.

Actuator	Limit [deg]	Rate Constraint [deg/s]
Longitudinal Cyclic θ_{1s}	± 12	± 28
Lateral Cyclic θ_{1c}	± 6	± 28
Collective θ_0	$0 \rightarrow 20$	± 16
Propeller Collective θ_p	$-10 \rightarrow 100$	± 16
Elevator δ_e	± 20	± 28
Rudder δ_r	± 20	± 28



13.4. Outer-Loop Velocity Controller

In order to calculate the required attitude commands ϕ_{cmd} , θ_{cmd} , and ψ_{cmd} for the inner-loop controller, and to be able to track command velocities $V_{x_{cmd}}$, $V_{y_{cmd}}$, and $V_{z_{cmd}}$, the outer-loop controller must be designed. Similarly to the inner-loop controller, the outer-loop controller is based on EMF principles, featuring the same transient behaviour parameters ω_n and ζ as the inner loop. The outer-loop controller is depicted in Figure 13.6 below.

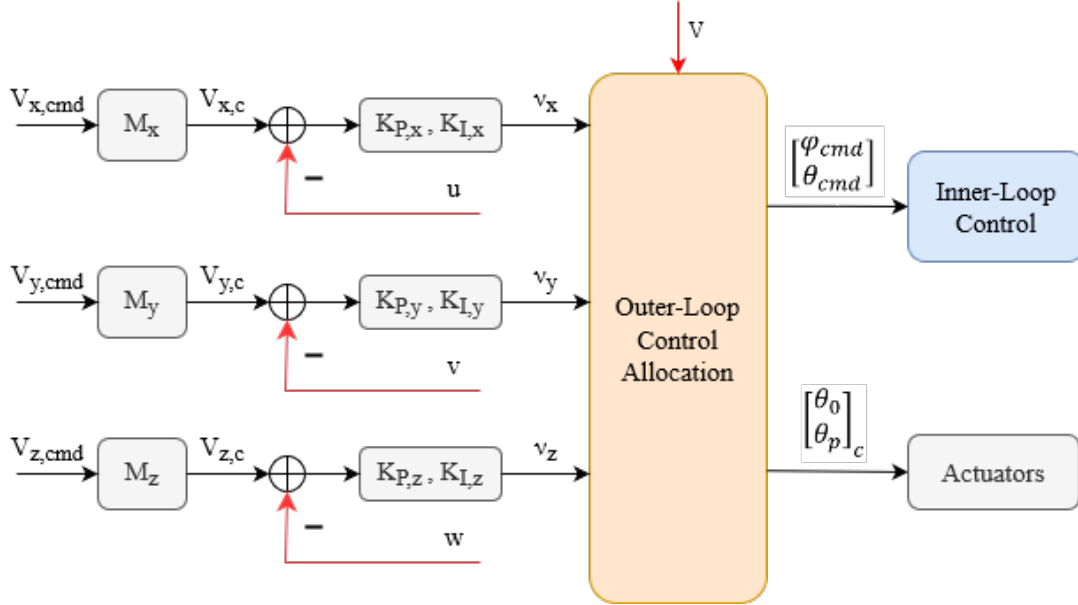


Figure 13.6: Outer loop controller design based on EMF control. [26]

Here, $V_{x_{cmd}}$, $V_{y_{cmd}}$, and $V_{z_{cmd}}$ denote the commanded velocities, which after the EMF model get transformed into the EMF control commands V_{x_c} , V_{y_c} , and V_{z_c} . These EMF commands then get compared to the actual airspeed u , v , and w , and compensated for using traditional PID control. K_{P_x} , K_{I_x} , K_{P_y} , K_{I_y} , K_{P_z} , and K_{I_z} , denote the proportional and integral gains for each respective flight velocity. The PID stabilisation produce the virtual controls ν_x , ν_y , and ν_z which are fed into the outer-loop control allocation (Section 13.2.2), and produce the necessary inputs for the inner-loop control, and the collective and pusher propeller inputs θ_0 and θ_p . Note that similarly to the inner-loop, no use is made of the differential control, since it did not improve controller performance.

Similar to the inner-loop controller, the outer-loop virtual control laws ν_x , ν_y , and ν_z can be calculated using Equation 13.10, which is also based on classical control theory.

$$\begin{aligned}
 \nu_x &= K_{P,x} (V_{x_c} - V_x) + K_{I,x} \int (V_{x_c} - V_x) dt \\
 \nu_y &= K_{P,y} (V_{y_c} - V_y) + K_{I,y} \int (V_{y_c} - V_y) dt \\
 \nu_z &= K_{P,z} (V_{z_c} - V_z) + K_{I,z} \int (V_{z_c} - V_z) dt
 \end{aligned} \tag{13.10}$$

13.5. Controller Tuning

Using the EMF-based controller design now covered, the gains have to be tuned in order to get a desirable response in both states and required control inputs. This section deals with the selected performance criteria, tuning method and recommendations, and an overview of the final gain set.



13.5.1. Model-Following Performance Criterion

In order to define the controller performance, a quantitative performance parameter has to be defined. Using the approach by Hilbert and Bouwer [64], the model following performance Q is defined by:

$$Q = 1 - |\bar{e}| \quad (13.11)$$

where \bar{e} is the mean value of the error vector during the simulation time, and is calculated by:

$$|\bar{e}| = \frac{1}{T} \sum_{i=1}^T |e_i| \quad (13.12)$$

where T is the simulation time, and e_i the error between the measured state and the EMF model command. Take for example a 3-2-1-1 input in the pitch channel, at 40 m/s, which is inside the transition region then, $e_i = \theta_c - \theta$. When plotted, the control system gives the following results:

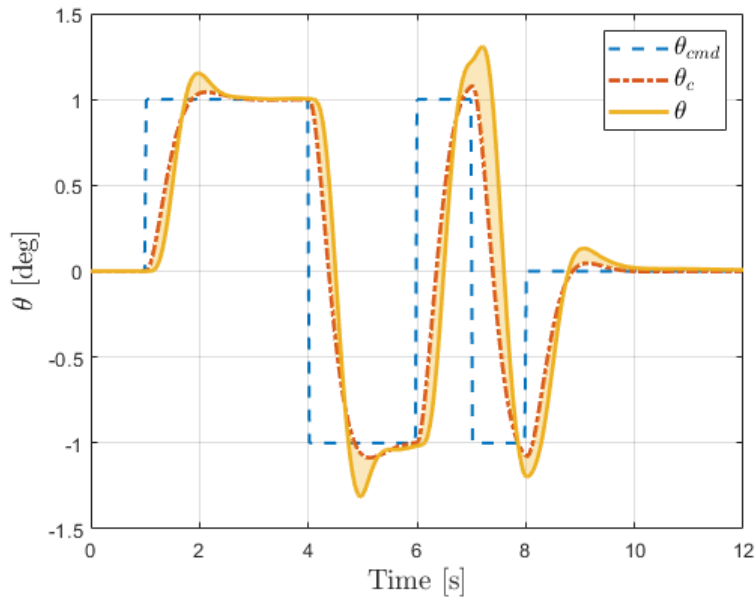


Figure 13.7: Pitch attitude tracking performance at 40 m/s.

The error e_i is visualised by the shaded yellow area. Using Equation 13.11, the pitch tracking performance Q_θ can be calculated and results in 0.9309. Note that with longer simulation times, this value automatically increases, hence attention must be paid. A simulation time of 12s and a start of the manoeuvre at 1s is deemed suitable for the particular 3-2-1-1 manoeuvre.

13.5.2. Tuning Approach

Using the model following performance variable Q , and by qualitative inspection of both states and inputs, the control system was tuned manually for an airspeed of 40 m/s. This was deemed the most interesting flight region to focus on in this thesis due to it being in the middle of the transition region, which in turn effectively demonstrates the use of the control allocation algorithm. Informal tuning has been performed for hover and high-speed flight (100 m/s), but these results are not final and will thus not be presented in this thesis and are beyond the scope of the topic. For the interested reader, these gains can be found in the *EMFController6dof.mat* MATLAB file in the GitHub repository.

However, there are a total of 15 gains to be tuned, and tuning each of them manually for the final desired manoeuvre response would be an interesting endeavour to say the least.¹ Therefore, a more elegant manual tuning approach was developed, for which a flowchart is depicted in Figure 13.8.

¹I tried.

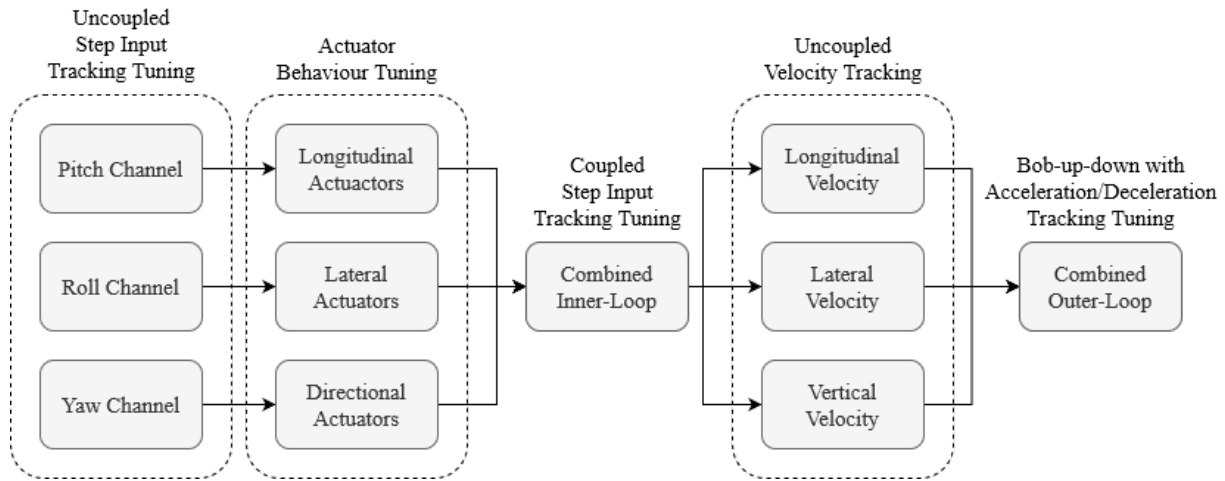


Figure 13.8: Decoupled manual gain tuning approach for the CCH control system.

Firstly, the inner-loop channels were tuned separately, assuming they are uncoupled. For each channel, a 3-2-1-1 input similar to Figure 13.7 was tuned in order to get a performance tracking parameter $Q > 0.9$. This initial uncoupled 3-2-1-1 tuning was done in MATLAB Simulink, using the PID Tuner function, which gave a good initial starting point for the gains to further be tuned. After adequate 3-2-1-1 inputs are produced, a closer look was given to the actuator behaviour. In case of sudden spikes in the controllers, or large oscillations, which were sometimes not visible in the attitudes, further tuning was required. After the uncoupled tuning was complete, a step input for each attitude, with a delay of 2s between each, was commanded and tuned in order to again meet the same performance parameters threshold $Q > 0.9$. This result is visualised in Figure 13.9 for an airspeed of 40 m/s.

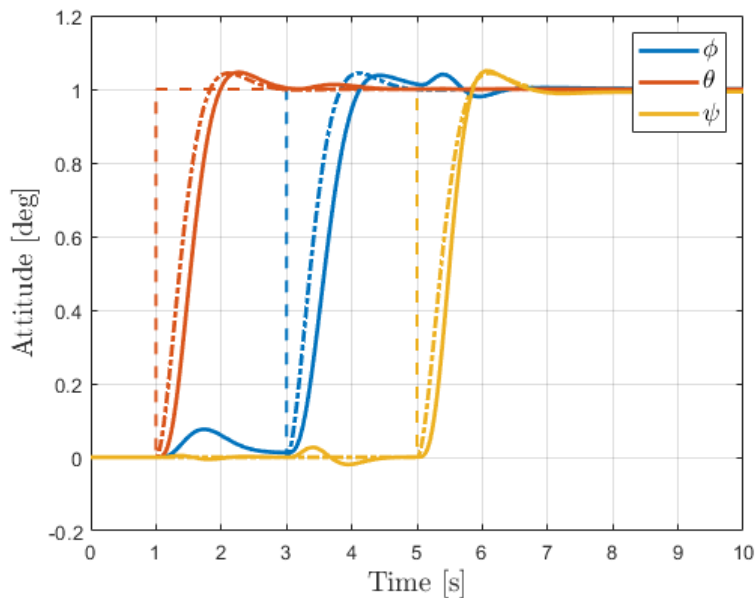


Figure 13.9: Coupled attitude step input tuning results at 40 m/s.

Note that the dashed lines indicate the reference command, the dotted dashed lines the model result, and the full lines the actual helicopter states after tuning. The cross-coupling effects are clearly visible in the plot, but the controller takes good care of removing these upsets. The Q -values for this specific manoeuvre are listed in Table 13.4.

**Table 13.4:** Performance values for the pitch, roll and yaw channels after coupled inner-loop tuning.

Channel	Performance Value Q
Roll angle, ϕ	0.9824
Pitch angle, θ	0.9748
Yaw angle, ψ	0.9895

With the inner-loop tuned, the focus could be shifted towards the outer-loop. Firstly, the outer-loop gains were again tuned separately, as if uncoupled, with the same performance criterion threshold. After this uncoupled tuning, a bob-up-down with acceleration and deceleration manoeuvre was set up, which will be further discussed in Section 13.6.2, and the controller was implemented and further tuned to give similar tracking results, while also assessing the actuator behaviour. The final selected gains at 40m/s for both the inner- and outer-loop are listed in Table 13.5.

Table 13.5: Final controller gains used in the inner- and outer- loop at 40m/s.

Channel	Outer-Loop	Gain	Channel	Inner-Loop	Gain
Roll ϕ	K_{P_ϕ}	120	Longitudinal Velocity u	K_{P_x}	-0.9
	K_{I_ϕ}	0.8		K_{I_x}	0
	K_{P_p}	2.8			
Pitch θ	K_{P_θ}	80	Lateral Velocity v	K_{P_y}	-0.0262
	K_{I_θ}	15		K_{I_y}	0
	K_{P_q}	20			
Yaw ψ	K_{P_ψ}	50	Vertical Velocity w	K_{P_z}	5
	K_{I_ψ}	0.1		K_{I_z}	0.1
	K_{P_r}	8			

All in all, this manual tuning approach still deemed cumbersome and time-intensive. Therefore, much improvement can be made by using different, more elegant tuning methods. One option considered and explored during the work of this thesis was the MATLAB Simulink Control System Tuner app. In this application, it is possible to tune the complete linearised system for specific tuning targets, such as closed-loop pole placement, command signal tracking, gain and phase margin constraints, and much more. However, no success was reached using this method. It is thought that either there was a mistake in the Simulink block diagram, or the system proved to be too complex for the Control System Tuner app to handle. A second option which is recommended for industry users such as NLR, is to make use control tuning software such as the Control Designers Unified Interface, or, CONDUIT[®] [53], developed by the U.S. Army Combat Capabilities Development Command (DEVCOM). This tuning software allows the user to select an extremely broad range of tuning goals, such as handling qualities from ADS-33 or MIL-STD, for a specific model, select critical requirements, and tune the system accordingly.

13.6. Manoeuvre Simulation

In order to demonstrate the performance of the helicopter control system, several manoeuvres are simulated and evaluated. These encompass the 3-2-1-1 manoeuvre, a common input combination for system identification purposes and dynamic excitation of the aircraft, and the bob-up/bob-down with acceleration and deceleration, a limited agility, precise manoeuvring mission task element from ADS-33. [51]

13.6.1. 3-2-1-1 Input

The 3-2-1-1 input is, as previously stated, a common flight test technique in order to excite the dynamic modes of the aircraft, often performed in system identification experiments. The purpose of simulating this specific manoeuvre in this thesis however, is to analyse the performance of the controller in each respective



attitude angle ϕ , θ , and ψ .

The 3-2-1-1 input sequence involves setting a specific target attitude angle and subsequently adjusting it through a series of defined steps. Initially, the attitude angle is set to the target value and held for 3 seconds. Following this, the angle is deflected to the opposite side and maintained for 2 seconds. The angle is then returned to the initial direction for 1 second, flipped again for an additional 1 second, and finally reset to 0. This sequence is visualised in Figure 13.10.

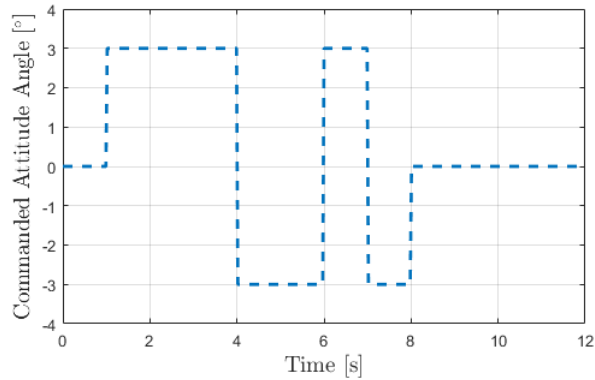


Figure 13.10: Reference 3-2-1-1 signal with an attitude command of 3 degrees.

In order to assess the cross-coupling behaviour in terms of attitudes and inputs for the 3-2-1-1 manoeuvre, each attitude is evaluated separately. Firstly, the roll is analysed. In Figure 13.11 - Figure 13.12 it can be seen that the controller is able to track the roll well. A strong cross-coupling can be seen in the yaw axis too, requiring yaw compensation. At some point, some cyclic input is also required which in turn requires some compensation of collective in order to remain in level flight.

Secondly, the pitch command is analysed in Figure 13.13 - Figure 13.14. Again, the controller is able to track the command well with both longitudinal cyclic and elevator, and the necessary compensation for level flight with the collective. Some cross-coupling to the yaw and roll axis is also visible, although to a far lesser extent.

Lastly, the yaw command is seen in Figure 13.15 - Figure 13.16. Again a similar pitch compensation as in roll can be seen, with some cross-coupling in the roll axis as well.

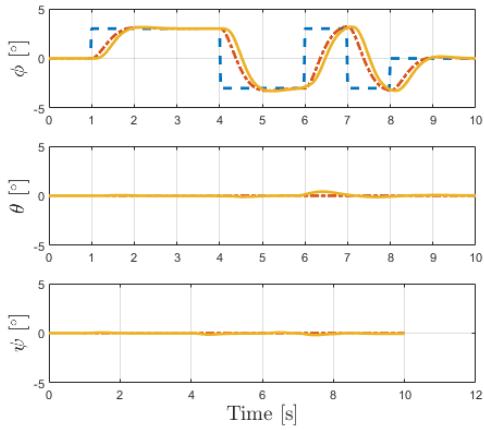


Figure 13.11: Tracked attitude commands during the 3-2-1-1 roll manoeuvre.

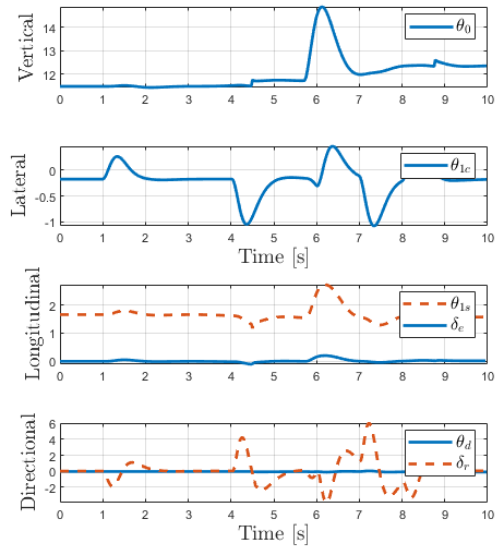


Figure 13.12: Inputs commands during the 3-2-1-1 roll manoeuvre.

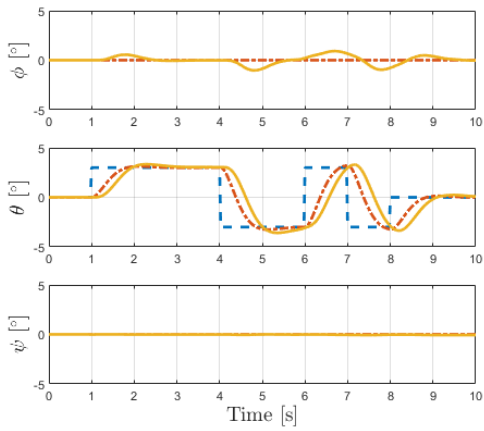


Figure 13.13: Tracked attitude commands during the 3-2-1-1 pitch manoeuvre.

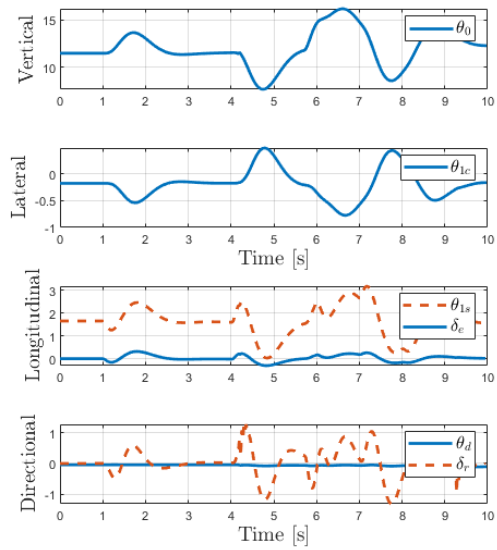


Figure 13.14: Inputs commands during the 3-2-1-1 pitch manoeuvre.

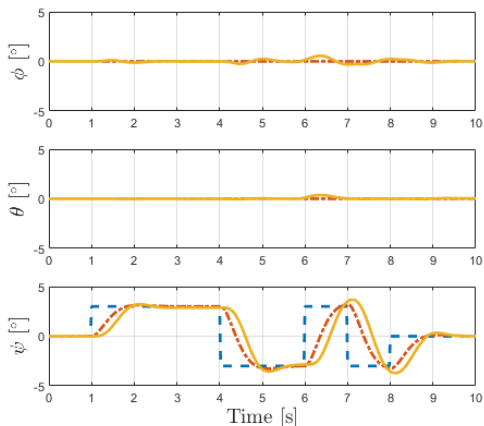


Figure 13.15: Tracked attitude commands during the 3-2-1 yaw manoeuvre.

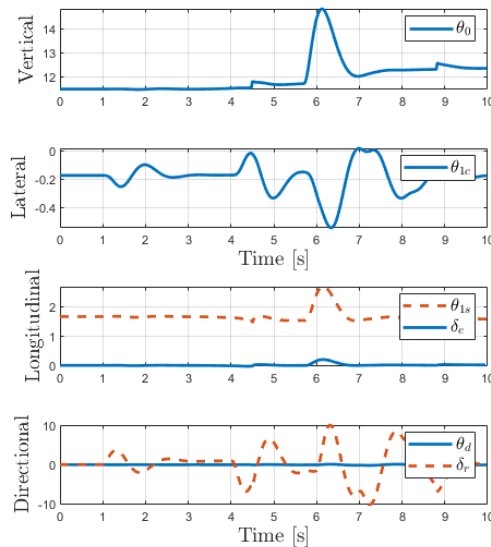


Figure 13.16: Inputs commands during the 3-2-1 yaw manoeuvre.

13.6.2. Bob-Up/Bob-Down with Acceleration and Deceleration

The bob-up/bob-down manoeuvre is a precise manoeuvring task with limited agility from the ADS-33 mission task elements.[51] It combines the commands of both vertical and horizontal velocities which serves as an evaluation for the developed outer- and inner-loop control allocation.

The bob-up starts at an altitude of 100m with a flight velocity of 40m/s and is then commanded to decelerate to 30m/s, climb at a constant rate of 2m/s for 10 seconds, continue at level flight, accelerate to 40m/s again, decelerate to 30 m/s, descend at a constant rate of 2m/s for 10 seconds, and continue level flight at 30m/s. This manoeuvring sequence is graphically depicted in Figure 13.17 together with the EMF commands.

Using the previously established gains, for which this manoeuvre constituted to finalising the values, the simulated results depicted in Figure 13.18, with corresponding control as depicted in Figure 13.19, are found. Note that V_z is defined positive upwards in this plot.

These findings offer valuable insights into the overall model, control system, and control allocation. The discussion will focus on the forward velocity command, vertical velocity command, and cross-coupling effects, with the corresponding control mechanisms forming the basis of this analysis:

- Forward velocity:** It can be seen that the forward velocity is very nicely tracked with respect to the commanded signal. During the transition region, a combination of the aircraft pitch and pusher propeller setting set the forward velocity. The pitch is allocated in the inner-loop to both to longitudinal cyclic and elevator. From Figure 13.19, it can be seen that the pusher propeller setting θ_p changes in the same manner as the forward velocity, with altering trim values. It first assertively decelerates/accelerates, to then stabilise at the new trim setting. It does this with very little oscillations. In Figure 13.18 it becomes clear that the control system commands a pitch up with deceleration, and a pitch down with acceleration, as expected. Looking again at Figure 13.19, the allocation to θ_{1s} and δ_e can be seen. It can be seen that there is some jittery behaviour for the longitudinal cyclic, which is due to the a combination of the limitation of the PID controller and imperfect tuning. It should also be noted that there is an unexpected use of the longitudinal cyclic during the pitch commanding, instead of pulling the longitudinal cyclic backwards, to raise the noise, the controller momentarily pitches nose up, quickly followed by nose down. It appears that the combination with the elevator results in a proper pitch angle. Most likely, this is the result due to the pitch coupling of the collective and lateral cyclic. It appears that the EMF controller with PID has a tough time with the highly coupled, simultaneous control requests.

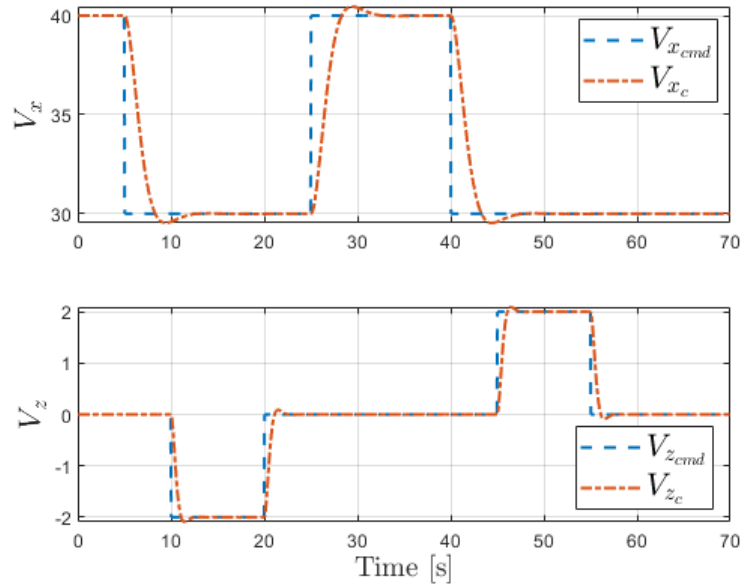


Figure 13.17: Commanded velocities V_x and V_y during the ADS-33 bob-up/bob-down with acceleration and deceleration manoeuvre.

- Vertical Velocity:** The vertical velocity is also tracked well as soon as the command is given. However, a clear coupling between the pitch angle and the vertical velocity can be seen. The vertical velocity can be seen to be controlled by the collective and the pitch angle. However, since collective is much more dominant at this speed than the pitch angle, it can be seen that almost solely the collective is used. One can observe the cross-coupling effect of the loss of lift due to a cyclic input, requiring a compensation in collective, and the altering low/high state of the collective, depending on the required vertical velocity.
- Cross-Coupling Effects:** These encompass the lateral axis states, such as the roll and yaw. It can be seen that there is a clear cross-coupling between pitch and roll, which the lateral cyclic is able to compensate for. The yaw on the other hand is observed to have a slight drift, with the rudder and differential collective being only very slightly active. It is thought that this is a combination between a modelling discrepancy and the chosen control law for yaw. Upon closer analysis, it was seen that there was a very small steady-state error of the yaw rate r , which a yaw-rate controller might be able to solve, instead of a yaw-angle controller.

As can be seen, the controller is able to track the commanded velocities and attitudes well, with exception of the yaw angle ψ . However, it becomes clear from the control inputs that the simultaneous usage of the control inputs due to the multidimensional control commands and highly coupled dynamics results in slightly jittery and coupled results. This is a limitation of the PID controller and could be solved by the earlier proposed inverse transfer function and more elaborate tuning methods.

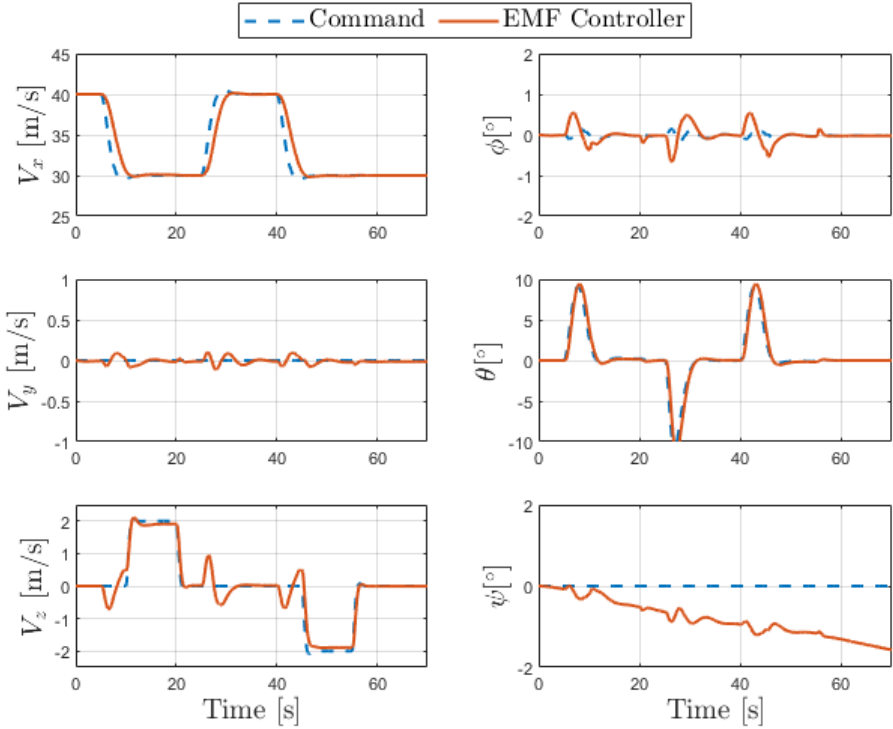


Figure 13.18: State results comparing the commanded values and EMF values during the bob-up/bob-down with acceleration and deceleration manoeuvre.

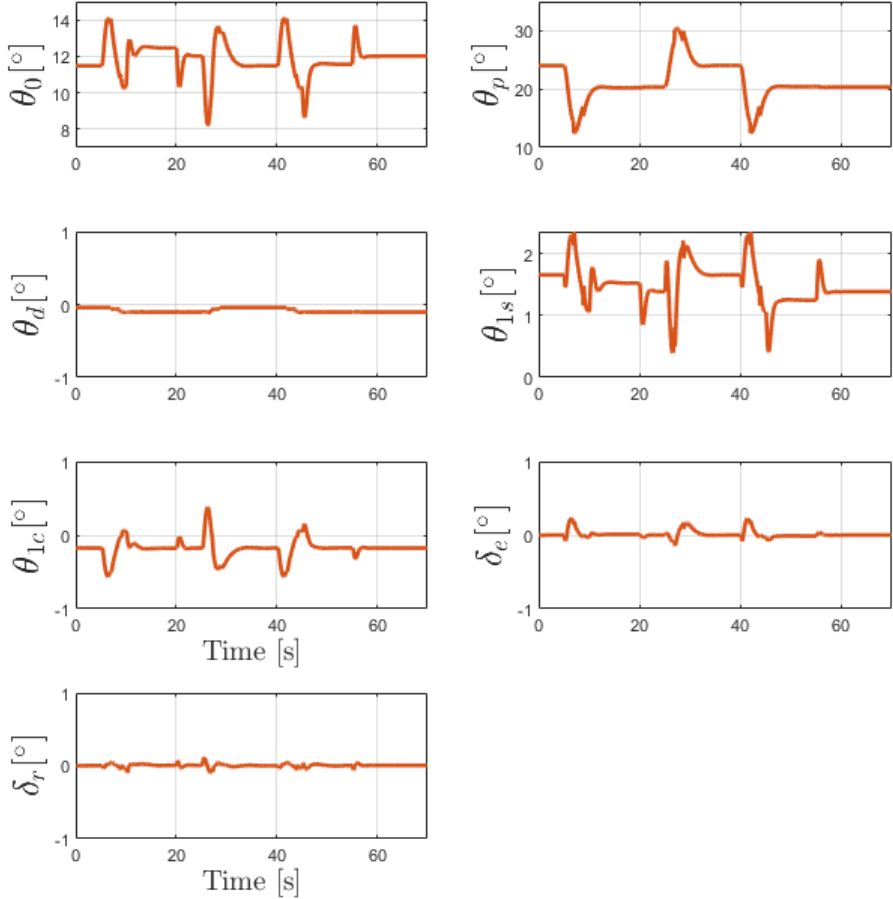


Figure 13.19: Control inputs results resulting from the EMF controller during the bob-up/bob-down with acceleration and deceleration manoeuvre.

Objective Handling Quality Assessment

In this chapter, the objective assessment of handling qualities for the compound coaxial rotorcraft is discussed, with a focus on key parameters such as bandwidth and phase delay, as well as attitude quickness in Section 14.1 and Section 14.2 respectively. These metrics play a crucial role in determining the responsiveness and stability of the aircraft, directly impacting pilot workload and operational efficiency. By analysing the dynamic response characteristics and comparing them to established standards such as the ADS-33E-PRF, an initial evaluation of the helicopter's handling performance is established. In Section 14.3, a brief discussion is given upon the selection of handling quality criteria depending on the mission profile of the helicopter, and high-speed flight characteristics.

14.1. Bandwidth and Phase Delay

The dynamic response characteristics of helicopters, in particular bandwidth and phase delay, have a significant impact on how well they handle. These variables have a direct bearing on the workload of pilots and the efficiency of operations by defining the aircraft's responsiveness and stability.

The frequency range that the helicopter can successfully respond to control inputs is referred to as its bandwidth. A larger bandwidth improves mobility and control precision by allowing the aircraft to respond to pilot commands faster. In actuality, reaching an ideal bandwidth requires striking a balance between aircraft intrinsic stability and responsiveness. While a bandwidth that is too low can cause poor responsiveness and diminished handling qualities, an excessively high bandwidth can cause instability.

Phase delay is the time lag between the helicopter's response and the pilot's control input. The control loop is significantly impacted by this delay, which has an impact on when and how the pilot acts. A minimum phase delay minimises the pilot's cognitive and physical burden by enabling more accurate and timely corrections. Conversely, high phase delays can cause oscillatory behaviour and decreased control accuracy, which makes it difficult for pilots to perform accurate movements.

In the ADS-33E [51] handling quality requirements for military rotorcraft document, the bandwidth ω_{BW} is defined as the the phase-limited bandwidth, as depicted in Figure 14.1. It can be seen that the phase-limited bandwidth is the frequency at which there is a 45 degree phase margin for the system. The phase delay τ_p is calculated as the fit between ω_{180} and $2\omega_{180}$, as calculated in Equation 14.1. The evaluation of the results is done by means of the ADS-33E-PRF defined limitations, visualised graphically in Figure 14.2 and Figure 14.3 for pitch and roll. The yawing motion does not have a standard defined by ADS-33.

$$\tau_p = \frac{\Delta\Phi 2\omega_{180}}{57.3 (2\omega_{180})} \quad (14.1)$$

The calculation of the bandwidth and phase-delay require the bode-plots of the entire closed-loop system. This can be a challenge within MATLAB, since the more complex and multi-layered the control system, the harder it becomes to track the transfer functions. Therefore, in order to analyse the bandwidth and phase delay, the linearised MATLAB Simulink model, with the full controller implementation using the step input tracking was used. Inside Simulink, the 'Control System Tuner' tool was used. Inside this tool, the specific signals that want to be measured can be selected. For example, as shown in Figure 14.1, the

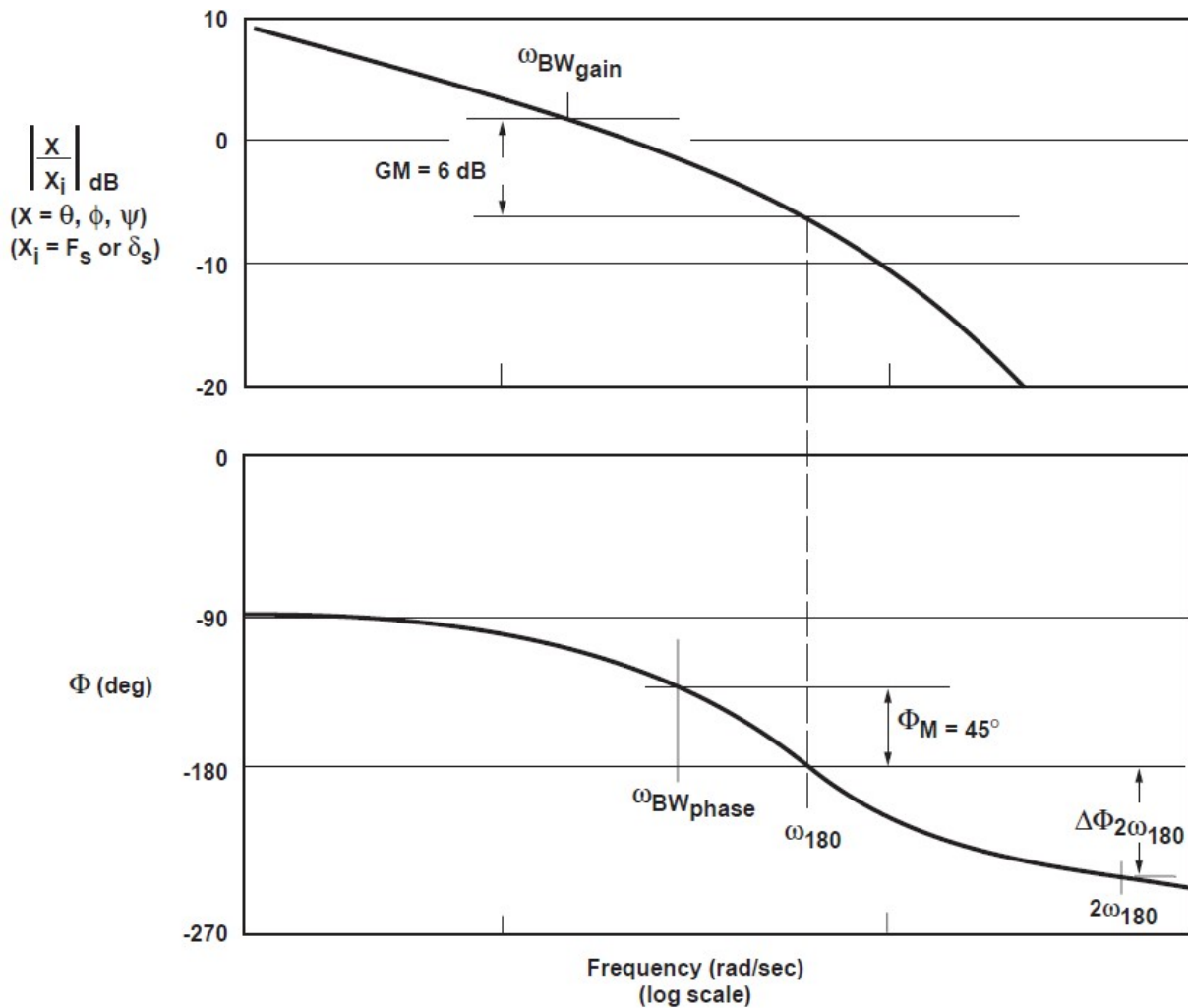


Figure 14.1: Definitions of bandwidth and phase delay as in ADS-33E PRF. [51]

parameter $\frac{x}{x_i}$ is for e.g. pitch equal to $\frac{\theta}{\nu_\theta}$, where ν_θ is the virtual longitudinal control input that goes to the control allocation (as can be seen in Figure 13.4).

Using the Control System Tuner app, the bode plots can be generated for each axis: pitch, roll and yaw, for the airspeeds of interest, which in this case are 20 m/s, 40 m/s, and 65 m/s, since these are the values within the transition region. The results are summarised in Table 14.1, for which it can be seen that throughout the entire transition region, the system achieves level 1 handling qualities by a fair margin, with increasing responsiveness with speed. However, it must be noted that the delays are very small compared to literature, this is most likely to be attributed to the fact that the actuators dynamic are not accounted for, which are the largest source of command delays.

Table 14.1: Bandwidth and phase delay results on the inner-loop control during the transition region for the linear system.

Metric	20 m/s			40 m/s			65 m/s		
	Roll	Pitch	Yaw	Roll	Pitch	Yaw	Roll	Pitch	Yaw
Response Bandwidth [rad/s]	3.52	4.8	5.23	3.72	4.91	5.23	3.91	5.17	5.23
Response Phase Delay [s]	0.02	0.04	0.05	0.02	0.04	0.05	0.02	0.04	0.05
Handling Qualities Level	Level 1			Level 1			Level 1		

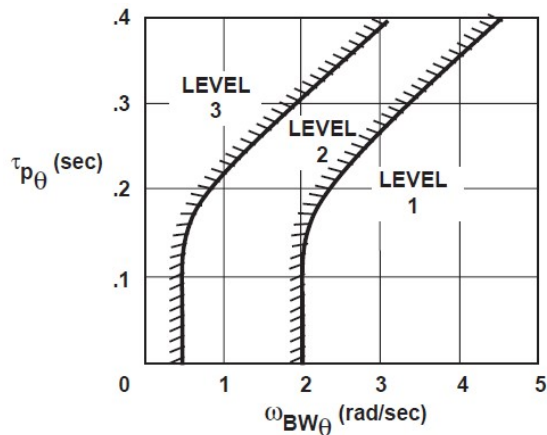


Figure 14.2: ADS-33E-PRF Standards for bandwidth and phase delay during pitch target acquisition and tracking.

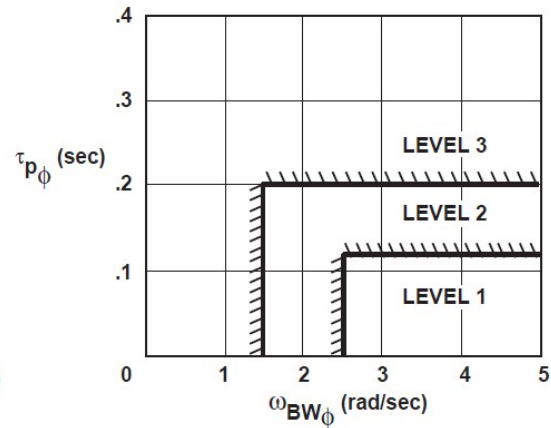


Figure 14.3: ADS-33E-PRF Standards for bandwidth and phase delay during roll target acquisition and tracking.

14.2. Attitude Quickness

The ADS-33E-PRF standards specify attitude quickness requirements for combat helicopters, which are especially interesting to consider in a coaxial helicopter configuration, since they are well known to be more manoeuvrable and agile than their single rotor counterparts. With the added compound features for attitude changes, such as the elevator and the rudder, this quickness is expected to be even more powerful. With the current allocation algorithm however, a maximum moment set is not analysed. However, with the compounding, it is a logical conclusion that this large moment set brings the possibility for some very large attitude rates to be achieved. This analysis however, will focus on the attitude quickness of the compound coaxial helicopter using the currently implemented control system and control allocation, which will provide an initial insight into the performance of the helicopter.

The attitude quickness parameters is split into pitch, roll, and yaw quickness, which will be analysed in Section 14.2.1-Section 14.2.3 respectively for the flight speed of 40 m/s, in order to clearly see the control allocation in action.

14.2.1. Pitch Attitude Quickness

The pitch attitude quickness of the helicopter will be calculated for attitude changes between 5 and 30 degrees, in steps of 5 degrees. Following this, the calculated pitch quickness will be plotted in and compared to the ADS-33 requirements. The pitch quickness Q_{pitch} is calculated by means of Equation 14.2. Here, q_{max} is the maximum pitch rate achieved during the manoeuvre, and $\Delta\theta_{pk}$ the maximum pitch angle throughout the manoeuvre, relative to the initial position (which is 0 in this case).

$$Q_{pitch} = \frac{q_{max}}{\Delta\theta_{pk}} \quad (14.2)$$

The resulting pitch attitude quickness values are plotted in Figure 14.4. It can be seen that the compound coaxial helicopter is able to reach level 1 requirements throughout all attitude changes, with a slight decrease in quickness with increasing attitude change.

To provide a detailed analysis of pitch rate dynamics and input utilisation, Figure 14.5 and Figure 14.6 illustrate the system's response to attitude changes of 5 degrees and 20 degrees, respectively. These figures include red horizontal lines indicating the maximum pitch rate, maximum pitch angle, and minimum pitch angle after the rise time, which are essential for calculating the attitude quickness.

For the 5-degree attitude change, the system requires a maximum longitudinal cyclic input of approximately 9 degrees, coupled with an elevator input peaking at around 4 degrees. These inputs collectively produce a maximum pitch rate of approximately 16 deg/s, resulting in a rapid attitude response.

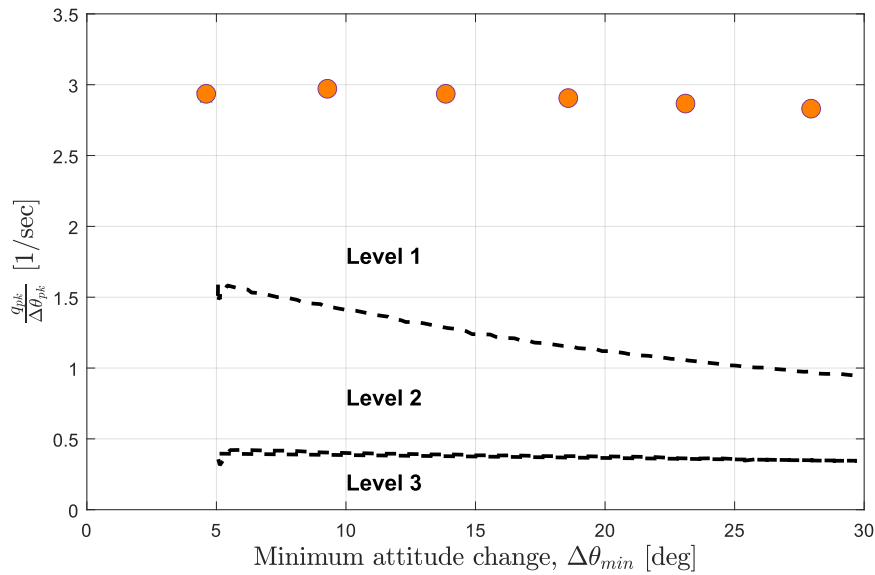


Figure 14.4: Pitch attitude quickness results from 5-30 deg commands, compared to ADS-33 requirements.

However, a distinct phenomenon is observed in the 20-degree attitude change scenario. Although the longitudinal cyclic input reaches its maximum, the elevator input does not. This indicates a limitation within the current control allocation scheme, which prioritises control inputs solely based on current airspeed and their respective effectiveness. This suggests the need for a more sophisticated control allocation algorithm, especially for large attitude manoeuvres, to fully exploit the total possible moment space that can be generated.

It is important to note that due to discrepancies in moment of inertia, rotor/elevator sizing, and aerodynamics, these values may exhibit slight inaccuracies. Additionally, the performance of the PID controller significantly influences the attitude quickness. Nevertheless, since all the attitude commands adhere to the Level 1 category standards, the results are deemed satisfactory. Despite the noted inaccuracies, the overall impact of the compound coaxial rotor system is effectively demonstrated.

14.2.2. Roll Attitude Quickness

The roll attitude quickness will be evaluated for roll attitude changes ranging from 10 to 50 degrees, in accordance with ADS-33 specifications, and calculated in a manner similar to the pitch quickness. As depicted in Figure 14.7, all attitude quickness results fall within Level 1 handling quality criteria, demonstrating sufficient quickness for the ABC rotor type in conjunction with the controller, as anticipated.

Similar to the pitch quickness assessment, the roll response inputs, rate, and attitude can be analysed, as shown in Figure 14.8. The data indicates that the coaxial ABC rotors achieve substantial roll rates, resulting in high quickness. For a 20-degree attitude change, Figure 14.8 reveals that the lateral cyclic input reaches its maximum, signifying the onset of diminishing quickness, as evident in Figure 14.9.

14.2.3. Yaw Attitude Quickness

The yaw attitude quickness is assessed for attitude changes between 10 and 60 degrees, according to ADS-33 standards. Similar to the pitch and roll quickness, the yaw quickness falls within Level 1 standards throughout the entire attitude range. A similar trend of the attitude quickness deteriorating as soon as the maximum deflection has been reached is visible here as well.

An interesting remark to be made for the rudder, since it was evident from Figure 13.2 in Section 13.2 that around 40m/s, which is the speed the attitude quickness is being assessed at, there is very little yaw authority. It was evident that the effectiveness of the differential collective is almost 0, while the rudder is just starting to become somewhat effective. This leads to very large deflections required for the

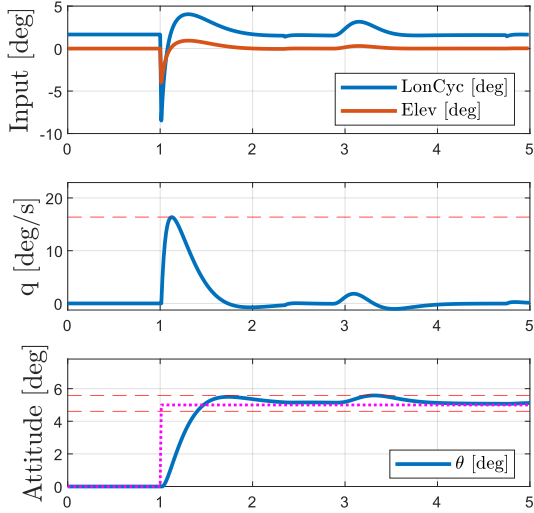


Figure 14.5: Pitch response for $\theta_{cmd} = 5$ deg.

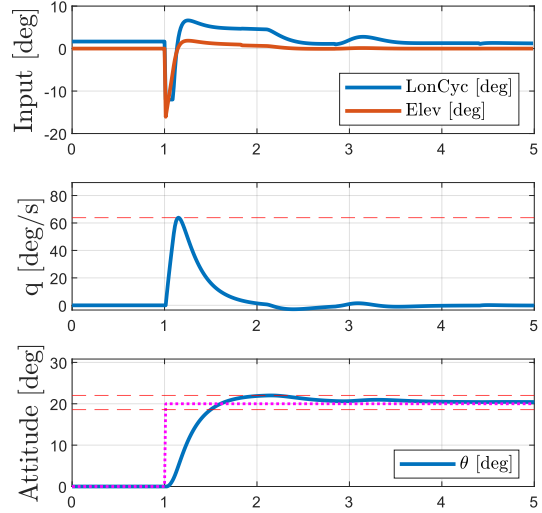


Figure 14.6: Pitch response for $\theta_{cmd} = 20$ deg.

rudder, limiting the attitude quickness. It is therefore expected that with increasing flight velocity, the yaw quickness would increase as well, due to the increasing control effectiveness of the rudder.

The yaw attitude quickness is evaluated for attitude changes between 10 and 60 degrees, in compliance with ADS-33 standards. Similar to the pitch and roll quickness assessments, the yaw quickness remains within Level 1 standards across the entire attitude range, as shown in Figure 14.10. A consistent trend of deteriorating attitude quickness is observed when maximum deflection is reached.

A notable observation regarding the rudder emerges from Figure 13.2 in Section 13.2. At approximately 40 m/s (the speed at which the attitude quickness is assessed) there is minimal yaw authority. The differential collective's effectiveness is nearly zero, while the rudder is just beginning to become somewhat effective. This results in the rudder requiring very large deflections, thereby limiting the attitude quickness, visualised in Figure 14.11 and Figure 14.12. It is anticipated that with increasing flight velocity, the yaw quickness would improve due to the increasing control effectiveness of the rudder.

14.3. Further Handling Quality Considerations

Throughout this handling quality assessment, a limited set of handling quality criteria, namely the bandwidth and phase delay, and the attitude quickness, were assessed. Combined with the flown mission task elements by the controller in Section 13.6, this provides an initial insight in the model and controller objective and subjective handling quality performance.

However, in a formal design setting, where the limitations of a one-man thesis with a set time frame are alleviated, this is not enough. The deciding handling quality criteria is that which is deemed mission critical, and under performing. As stated, the assessed handling quality criteria are 'mission'-critical, indicating that a specific mission has to be established for the aircraft. As stated in the literature review, there is a larger transport variant of the compound coaxial helicopter, such as the SB-1 Defiant, with combat capabilities, or a smaller, more manoeuvrable, scout-variant of the helicopter, such as the Sikorsky S-97 Raider X. It is therefore recommended that a more in-depth handling quality assessment uses the mission profile as a basis for the handling quality selection.

Apart from the mission-specific handling qualities, the high-speed flight characteristics, enabled due to the forward velocity compounding provided by the pusher propeller, in combination with the ABC rotor, increase the handling quality scope of the helicopter. It therefore is essential to go towards fixed-wing handling qualities for the high-speed region. One such author who assessed the high-speed flight handling qualities, is Berger [47].

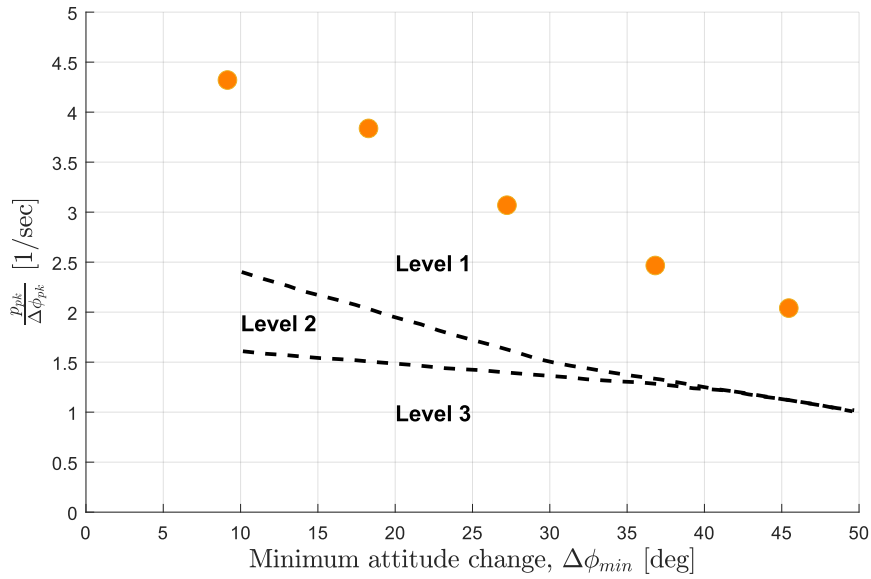


Figure 14.7: Roll attitude quickness results from 10-50 deg commands, compared to ADS-33 requirements.

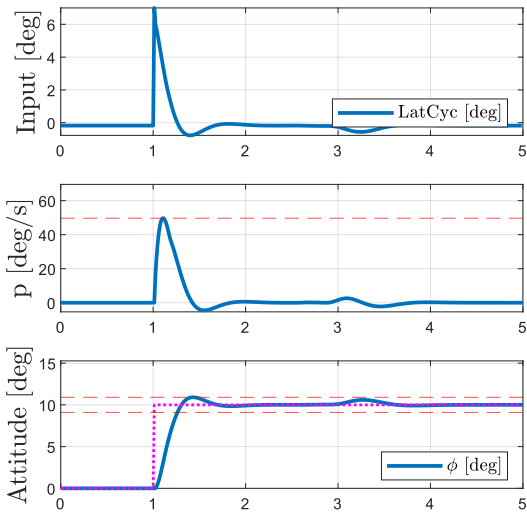


Figure 14.8: Roll response for $\phi_{cmd} = 10$ deg.

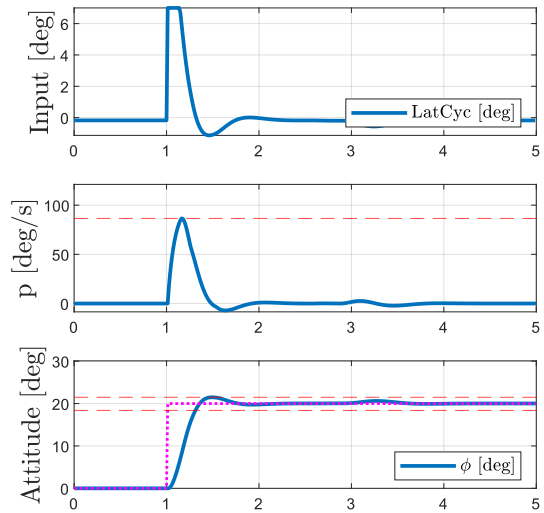


Figure 14.9: Roll response for $\phi_{cmd} = 20$ deg.

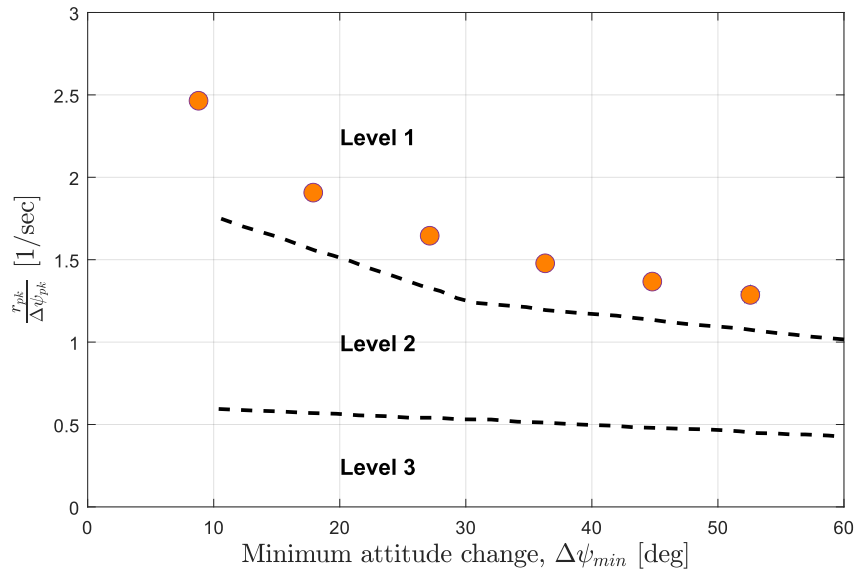


Figure 14.10: Yaw attitude quickness results from 10-60 deg commands, compared to ADS-33 requirements.

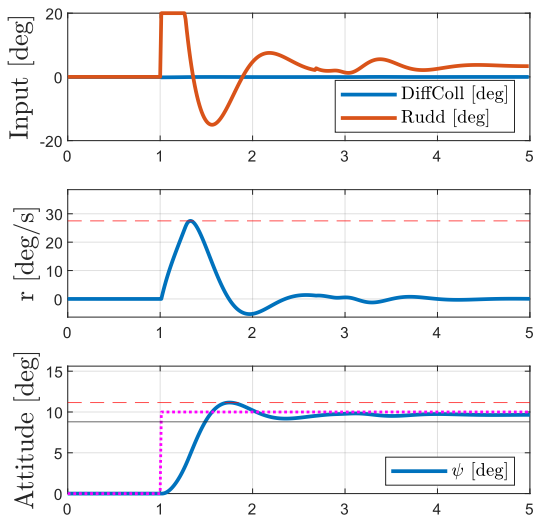


Figure 14.11: Yaw response for $\psi_{cmd} = 10$ deg.

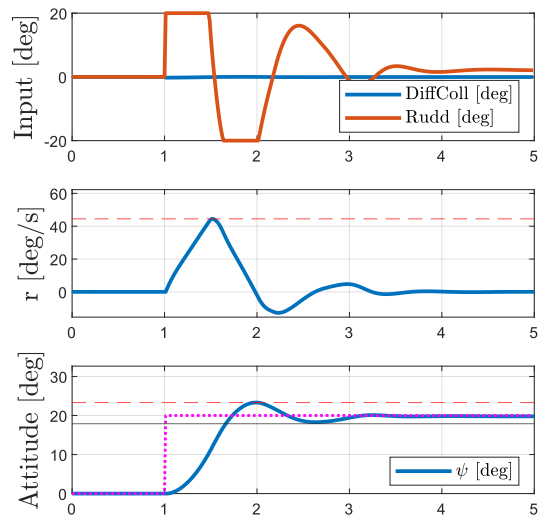


Figure 14.12: Yaw response for $\psi_{cmd} = 20$ deg.

Part IV

Closure

In this final chapter, a brief overview of the research objectives, followed by a description of the conclusions on these objectives is given.

15.1. Research Objectives

The goal of this thesis was threefold:

- Firstly, a 6-dof mathematical model, able to capture the overall flight dynamics of the compound coaxial helicopter, should be developed. This model should be capable of supporting the development of a control system during the conceptual design phase.
- Secondly, a high-level control law, leveraging the use of control allocation, should be developed, in order to perform manoeuvre tracking tasks and be used for an objective handling quality assessment.
- Lastly, suitable handling quality criteria should be identified and implemented for the compound coaxial rotorcraft, with a focus on the transition region velocities.

15.2. Research Conclusions

The conclusions can be formed based on the previous stated objectives: the model (and stability analysis), the control system (with control allocation), and handling quality assessment.

15.2.1. Mathematical Model Development

The first step throughout this research was to develop a nonlinear model which is able to capture the core flight dynamics behaviour of a compound coaxial rotor, with a Level 1 fidelity [18]. In the end, a 9-dof nonlinear compound coaxial helicopter, based on the SB-1 defiant, was modelled, trimmed and linearised. The nonlinear helicopter featured a total of 8 control inputs: the mean collective θ_0 , differential collective θ_d , longitudinal cyclic θ_{1s} , lateral cyclic θ_{1c} , differential lateral cyclic $\Delta\theta_{1c}$, propeller collective θ_p , elevator deflection δ_e , and rudder deflection δ_r . The differential collective and differential lateral cyclic were unique to the ABC rotor configuration, as well as the use of the pusher propeller, elevator and rudder, which allowed for compounding of controls in forward velocity, pitch attitude, and yaw attitude control.

The rotor dynamics were modelled by means of an equivalent blade flapping model, which made use of an equivalent hinge offset and spring stiffness. Both of these parameters were tuned in order to achieve a similar flapping frequency response at nominal rotor speed compared to literature. Rotor dynamics such as lead/lag and feathering were not modelled due to the use of the ABC rotor, for which these dynamics are very small.

The most challenging model aspect was definitely the coaxial rotor inflow dynamics. The final model made use of a uniform inflow distribution with steady and linear aerodynamics, while accounting for the mutual rotor interferences which are variable throughout the flight regime. Wake contraction was deemed to not be modelled, since it only affected 13% of the rotor radius. However, if a higher fidelity is desired, it is advised to account for this, as it will alter the thrust producing characteristics of the lower rotor. The inflow of the rotors was modelled by means of a quasi-dynamic inflow, which produced 2 extra states, one for the upper rotor, and one for the lower rotor. Due to the use of a uniform rotor inflow, a lateral distribution of the rotor lift cannot be modelled. This does not have an effect on the overall body dynamics of the vehicle, but



it does remove the opportunity for closer analysis of the lift on the rotorblades. In turn, this leads to the fact that the differential lateral cyclic control, which would be used for lateral lift-offset control, could not be scheduled.

The pusher propeller was modelled without a monocyclic control, as it was deemed beyond the scope of this thesis. The blade dynamics of the pusher propeller were also not modelled due to the high rotational speed and stiff blades. Therefore, a simple calculation for the thrust could be made based solely on the inflow and pitch setting. The inflow was also based on a quasi-dynamic inflow, creating the 9th degree of freedom of the model.

The fuselage, elevator and rudder were modelled using simple aerodynamic lookup tables and formulae in order to find their contributions to the overall body dynamics.

When trimming the aircraft, it was deemed necessary to have one extra trim target. This was chosen to be the roll angle since the fuselage pitch angle was set to 0 for minimal drag. The overall trim result was comparable to literature, with exception of the longitudinal cyclic due to the large blade twist angle.

15.2.2. Stability Analysis

During the longitudinal stability analysis, it was found that the aircraft is longitudinally unstable starting from a speed around 40m/s. The phugoid mode appeared to be unstable throughout the flight regime, while the short period got unstable after this previously mentioned velocity. It was found that the coaxial rotors were the biggest contributor of different flight dynamics compared to conventional helicopters. The stiff blades also caused a large instability. The use of the elevator stabilised the aircraft but insufficiently so in the current planform with current parameters. It could also be seen that various damping derivatives such as X_u and Z_w were twice as large as their conventional helicopter counterparts, mainly due to the coaxial rotor setup.

It was also noted that the stability is highly dependent on the airframe planform and used parameters, especially that of the rotor hinge offset and spring stiffness. It is very well possible that there are inaccuracies in the estimated values used in this thesis, which cause different dynamic behaviour. However, the dynamics are comparable to literature and the effects of the stiff coaxial rotors and compounding effects are clearly demonstrated.

15.2.3. Control Laws and Control Allocation Design

Due to the poor stability at low speeds, and instability at mid- to high speeds, the need for a control system arised. The chosen flight controller was based on an Explicit Model Following (EMF) type controller which was decoupled into an outer- and inner-loop for the velocities and attitudes respectively. Both loops made use of a control allocation scheme, allocating the pusher propeller and pitch angle for forward speed, collective and pitch for vertical speed, elevator and longitudinal cyclic for pitch, and rudder and differential collective for yaw. It was found that around 40 m/s in the transition region, there is very little yaw authority due to the low control effectiveness of both the rudder and the differential collective. The control allocation was based on a weighted pseudo-inverse algorithm where the weights were a simple function of velocity. However, this could lead to jittery behaviour around the start and end of the transition region, and might not be the most ideal in terms of power consumption. The controller was stabilised using a PID control loop and the actuators were simply modelled by accounting for their deflection and rate limits. Note that the actuator dynamics were not accounted for and thus have an almost instantaneous effect in the control loop. The PID controller was tuned based on an elaborate manual gain tuning approach, with satisfactory results. Improvements can however be made with more elaborate tuning methods such as those provided in CONDUIT.

The 3-2-1-1 manoeuvre simulation at 40m/s revealed a strong cross-coupling between the roll and yaw axis, which could also be seen throughout the control derivatives in the stability analysis. However, the controller was able to properly track the manoeuvre. The second manoeuvre that was simulated aimed to demonstrate a full combination of both inner- and outer-loop by means of a bob-up/bob-down with acceleration and deceleration manoeuvre in the transition region. It was found that the controller was able to track the commands well, with the exception of a small drift in the yaw angle ψ , which is thought to be due to a combination of using the yaw angle as a feedback variable instead of the yaw rate, and due to the low control authority of both yaw controls. A strong cross-coupling between the pitch and vertical velocity, which was not accounted for fast enough by the collective, was also found. During the manoeuvre, the usage of the control allocation was demonstrated very well by the collaboration of the propeller, longitudinal cyclic and elevator in order to control pitch, which was used for both forward and



vertical velocity. The combination of the collective and pitch (again being controlled by the longitudinal cyclic and the elevator) was also demonstrated well.

15.2.4. Handling Quality Assessment

The final objective of this thesis was to perform an initial objective handling quality assessment in order to further demonstrate the behaviour of the helicopter. Firstly, the bandwidth and phase delay were evaluated by use of MATLAB Simulink's control system designer tool. It was found that the aircraft performed within Level 1 criteria. However, due to the actuators not being modelled properly in the control system, there was a very small response phase delay. Modelling these effects might thus reveal slight variations, although it is expected to still fall within Level 1 criteria.

Then, the attitude quickness was evaluated for all 3 attitudes at 40m/s, for which all of them fell within Level 1 criteria. A common trend could be seen that as soon as actuator saturation was reached, the quickness would degrade rapidly. One other aspect that was noticed was the non-ideal usage of the control allocation when actuator saturation was reached. The control allocation algorithm caused one control to be completely saturated for a long time, while the other control was not performing at the full capability, not using the full moment generative capability of the airframe.

Lastly, the low authority of the yaw controls was also clear, requiring almost constant maximal deflections for sustained times in order to track the signals. However, they still performed well.

Lastly, it was concluded that even though this handling quality assessment gave an initial insight into the system, it is far from complete since the limiting factor would be the worst performing handling quality, requiring the evaluation of a large set of handling quality parameters, which was however beyond the time-frame of this thesis. It was also advised to study more closely the high-speed handling qualities, such as the ones used for fixed-wing aircraft.

Recommendations

This chapter provides a brief overview of the primary recommendations for the future continuation of this research project. Firstly, it should be stated that I have a strong belief that this thesis provides a solid foundation for future work to be based off it, if various still existing problems and inaccuracies are solved. The thesis provided a good backbone for a mathematical nonlinear model, which was trimmed and linearised. Then, an initial EMF controller was built including a weighted pseudo-inverse control allocation scheme, featuring usage of the redundant controls. Finally, an initial handling quality assessment was performed. Each one of these three areas can be improved and expanded upon, and will be elaborated upon in the following.

Modelling

- Include a non-uniform inflow distribution, such as a linear inflow distribution (discussed in the literature study), in order to be able to model and schedule for the LOS effects using the differential lateral cyclic.
- Include rotor RPM scheduling, and resolve the issue inside the stability and control derivatives. This will slightly alter the dynamic characteristics, especially at high speeds.
- Include a rotor spacing calculation, such that adequate rotor spacing is maintained throughout the trim regime. Pay special attention to when maximum deflections of actuators are used, since this is most likely limited due to rotor separation.
- Use different flapping coefficient equations which utilise both the hinge offset and spring stiffness, instead of having to rely on the spring frequency values. This would remove some inaccuracies for the flapping angles, which carry through in the resulting rotor angles and thus trim and control.
- Include wake contraction effects, as outlined in Figure 10.8. This will increase the fidelity slightly and result in a slight loss of lift in the lower rotor, altering the total thrust generation.
- Remove small angle approximations wherever applied, in order to widen the range of attitudes covered by the nonlinear model, while making physical sense.
- Include a monocyclic control in the propeller. This would create possibilities for larger moment sets in the yaw direction, possibly removing the low yaw authority around 40 m/s. This would also create extra challenges, but also flexibility in the flight control allocation algorithm.
- Re-iterate the planform sizing parameters, by performing a more detailed sizing study in order to improve the realism of the design. The design parameters now are deduced from comparable helicopters in literature and sometimes roughly estimated by an educated guess. A 3D model was constructed for this thesis, which might be used for mass moment of inertia estimates.

Control

- Include the use of more sophisticated tuning methods besides manual tuning. Several examples could be the options within MATLAB Simulink, although these might provide issues due to the complexity of the control system and dynamics of the 9dof helicopter. A very good industry alternative, also capable of tuning for handling quality requirements, is CONDUIT.
- Include the use of an inverse model, such as done by [26], in order to create more robustness in the



system, and omit the dependence on PID tuning, since the PID will only be used as a stabilisation factor. More elaborate control systems such as NDI control will also be a great alternative for the controller. Attention must however be paid to the complexity and industrial applicability of these more modern types of controllers.

- Provide a more sophisticated control allocation scheme, based on an (multi-objective) optimisation routine. This routine could be based on e.g. minimal power consumption (minimal drag), or by focusing on the start and end of the transition region, where jitter and degraded handling qualities might occur. One other aspect to be included in this control allocation improvement could be the usage of more of the secondary control when one control is saturated, as was shown to happen during high attitude manoeuvres in Section 14.2.
- Implement the use of Pseudo-Control Hedging (PCH) in order to more efficiently account for actuator saturation. PCH often works well in combination with NDI control, but also greatly benefits EMF control (potentially with an inverse model).
- Extend the controller beyond transition mode. The logical and most interesting following domains would be hover and the high-speed flight domain. In the high-speed flight, several new mission-task elements such as the transient turn, combat break turn, and other manoeuvres discussed in the literature exist, and can provide for an excellent study.
- Include actuator dynamics beyond the rate and position constraints.
- Combat the low authority zone for yaw control around 40m/s. This could be done by including an extra control such as monocyclic propeller pitch, but would pose higher design costs and complexity. Different sizing metrics could be studied such that there is always a sufficient control effectiveness throughout the transition region.

Handling Quality Assessment

- Use an engineering software tool such as CONDUIT in order to tune the system for a wider range of handling qualities.
- Widen the range of handling qualities that are assessed, since only the worst performing one matters, if it is deemed crucial to the system.
- For high speed flight, look at fixed-wing handling quality requirements, and perform an appropriate analysis for this. The same goes for the high-speed manoeuvres as discussed in the control recommendations.

References

- [1] J. Gertler. “Army Future Vertical Lift (FVL) Program”. In: *Congressional Research Service* (2020).
- [2] M. Weisgerber. *Army Chooses Bell V-280 to Replace Its Black Hawk Helicopters*. 2022. URL: <https://www.defenseone.com/business/2022/12/army-chooses-bell-v-280-replace-its-black-hawk-helicopters/380487/> (visited on 2023).
- [3] L. Heckmann. *FARA Cancellation Leaves Unfilled Gaps, Army Commander Says*. 2024. URL: <https://www.nationaldefensemagazine.org/articles/2024/4/25/fara-cancellation-leaves-unfilled-gaps-army-commander-says> (visited on 2024).
- [4] G. Leishman. “A History of Helicopter Flight”. In: (2000).
- [5] Airforce Technology. *Ka-52 Alligator Attack Helicopter*. 2022. URL: <https://www.airforce-technology.com/projects/ka52-alligator-attack-helicopter-russia/?cf-view> (visited on 2023).
- [6] J. Ruddell et al. *Advancing Blade Concept (ABC) Technology Demonstrator - Final Report for Period 1972 - June 1980*. Tech. rep. Sikorsky Aircraft Division United Technologies Corporation, 1981.
- [7] R. Prouty et al. “The Lockheed AH-56 Cheyenne - Lessons Learned”. In: *AIAA Aircraft Design Meeting* (1992).
- [8] Raymond L. “Hybrid Helicopters: Compounding the Quest for Speed”. In: *American Helicopter Society* 52.4 (2006), pp. 30–54.
- [9] F. Lombardi. *Breaking Down the Bell 525 Crash Report*. 2018. URL: <https://digitaledition.rotorandwing.com/april-may-2018/breaking-down-the-bell-525-crash-report/> (visited on 2023).
- [10] G. von Kursell. *A pioneer of modern helicopter technology: the BO105 celebrates its 50th birthday*. 2017. URL: <https://www.airbus.com/en/newsroom/press-releases/2017-02-a-pioneer-of-modern-helicopter-technology-the-bo105-celebrates-its> (visited on 2023).
- [11] R. Blackwell et al. “Dynamic Design Characteristics of the Sikorsky X2 Technology Demonstrator Aircraft”. In: *American Helicopter Society Forum* 64 (2008).
- [12] *Sikorsky S-69 / XH-59 1972*. 2008. URL: http://www.aviastar.org/helicopters_eng/sik_s-69.php (visited on 2023).
- [13] A. Bagai. “Aerodynamic Design of the X2 Technology Demonstrator Main Rotor Blade”. In: *American Helicopter Society Forum* 64 (2008).
- [14] E. Eller. “X2 Load Alleviating Controls”. In: *American Helicopter Society Forum* 68 (2012).
- [15] S. Magnuson. *Sikorsky Expects to Fly New Scout Helicopter Next Year*. 2023. URL: <https://www.nationaldefensemagazine.org/articles/2023/10/9/sikorsky-expects-to-fly-new-scout-helicopter-next-year> (visited on 2023).
- [16] D. Parsons. *U.S. Army taps Sikorsky Raider X, Bell Invictus for FARA fly-off*. 2023. URL: <https://verticalmag.com/news/fara-sikorsky-bell/> (visited on 2023).
- [17] Y. Yuan et al. “Investigation of Lift Offset on Flight Dynamics Characteristics for Coaxial Compound Helicopters”. In: *Journal of Aircraft* 56.6 (2019), pp. 2210–2222.
- [18] G. Padfield. “Helicopter Flight Dynamics”. In: *The Theory and Application of Flying Qualities and Simulation Modelling*. Blackwell Publishing, 2013.



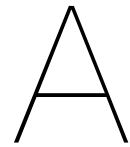
- [19] J. Gordon Leishman. *Principles of Helicopter Aerodynamics, 2nd Ed.* Cambridge University Press, 2006, 2006.
- [20] Renliang Chen et al. “A review of mathematical modelling techniques for advanced rotorcraft configurations”. In: *Progress in Aerospace Sciences* 120 (2021), p. 100681.
- [21] W. Johnson. “Rotorcraft Aeromechanics”. In: Cambridge, 2007.
- [22] S. Saito et al. “A numerical approach to co-axial rotor aerodynamics”. In: (1981).
- [23] R. Chen. *A Survey of Nonuniform Inflow Models for Rotorcraft Flight Dynamics and Control Applications*. Tech. rep. NASA, 1989.
- [24] Robert P Coleman et al. *Evaluation of the induced-velocity field of an idealized helicopter rotor*. NACA Washington, DC, USA, 1945.
- [25] D. Pitt et al. “Theoretical Prediction of Dynamic-Inflow Derivatives”. In: *European Rotorcraft and Powered Lift Aircraft Forum* 16.47 (1980).
- [26] Q. Yuqing et al. “Dynamics analysis and control of coaxial high-speed helicopter in transition flight”. In: *Aerospace Science and Technology* 137 (2023).
- [27] K. Ferguson et al. “Flight Dynamics Investigation of Compound Helicopter Configurations”. In: *Journal of Aircraft* 52.1 (2015).
- [28] K. Ferguson. *Towards a better understanding of the flight mechanics of compound helicopter configurations*. Tech. rep. University of Glasgow, 2015.
- [29] J. Leishman et al. “Figure of Merit Definition for Coaxial Rotors”. In: *Journal of the American Helicopter Society* 53.3 (2008), pp. 290–300.
- [30] J. Leishman et al. “An Optimum Coaxial Rotor System for Axial Flight”. In: *Journal of the American Helicopter Society* 53.4 (2008), pp. 366–381.
- [31] Edward Barocela. “The effect of wake distortion on dynamic inflow for lifting rotors”. PhD thesis. Washington University, 1997.
- [32] Krishnamohan R Krothapalli et al. “Helicopter rotor dynamic inflow modeling for maneuvering flight”. In: *Journal of the American Helicopter Society* 46.2 (2001), pp. 129–139.
- [33] Ashish Bagai et al. “Rotor Free-Wake Modeling Using a Pseudo-Implicit Technique—Including Comparisons with Experimental Data”. In: *Journal of the American Helicopter Society* 40.3 (1995), pp. 29–41.
- [34] C Young. *A note on the velocity induced by a helicopter rotor in the vortex ring state*. RAE, 1978.
- [35] Hermann Glauert. *A general theory of the autogyro*. Tech. rep. HM Stationery Office, 1926.
- [36] J Meijer Drees. “A theory of airflow through rotors and its application to some helicopter problems”. In: *The Journal of the Helicopter Association of Great Britain* 3.2 (1949), pp. 79–104.
- [37] G-Y Zhou et al. “Research on a mathematical model for coaxial helicopter flight dynamics.” In: *Acta Aeronautica et Astronautica Sinica* 24.4 (2003), pp. 293–295.
- [38] Walter Castles Jr et al. *Distribution of normal component of induced velocity in lateral plane of a lifting rotor*. Tech. rep. 1956.
- [39] J. Campfens. *Modeling of a coaxial helicopter. Msc Thesis*. Tech. rep. Technical University of Delft, 2008.
- [40] Anton J Landgrebe. “The wake geometry of a hovering helicopter rotor and its influence on rotor performance”. In: *Journal of the American Helicopter society* 17.4 (1972), pp. 3–15.
- [41] Ye Yuan et al. “Propeller control strategy for coaxial compound helicopters”. In: *Proceedings of the Institution of Mechanical Engineers, Part G: Journal of Aerospace Engineering* 233.10 (2019), pp. 3775–3789.



- [42] Y Yuan et al. “Trim characteristics and verification of coaxial rigid rotor aircraft”. In: *Journal of Nanjing University of Aeronautics & Astronautics* 48.2 (2016), pp. 186–193.
- [43] AE Phelps III et al. *Aerodynamic characteristics of a counter-rotating, coaxial, hingeless rotor helicopter model with auxiliary propulsion*. Tech. rep. 1978.
- [44] Jinshuo Hu et al. “Survey on flight control technology for large-scale helicopter”. In: *International Journal of Aerospace Engineering* 2017 (2017).
- [45] Amil Daraz et al. “Modified PID controller for automatic generation control of multi-source interconnected power system using fitness dependent optimizer algorithm”. In: *PloS one* 15.11 (2020), e0242428.
- [46] Tom Berger et al. “Coaxial-Compound Helicopter Flight Control Design and High-Speed Handling Qualities Assessment”. In: *Journal of the American Helicopter Society* 67.3 (2022), pp. 98–113.
- [47] Tom Berger et al. “Flight control design and simulation handling qualities assessment of high-speed rotorcraft”. In: *Vertical Flight Society’s 75th Annual Forum and Technology Display*. 2019.
- [48] Marilena D Pavel et al. “Incremental nonlinear dynamic inversion for the Apache AH-64 helicopter control”. In: *Journal of the American Helicopter Society* 65.2 (2020), pp. 1–16.
- [49] Tor A Johansen et al. “Control allocation—A survey”. In: *Automatica* 49.5 (2013), pp. 1087–1103.
- [50] Ismael Matamoros et al. “Incremental nonlinear control allocation for a tailless aircraft with innovative control effectors”. In: *2018 AIAA Guidance, Navigation, and Control Conference*. 2018, p. 1116.
- [51] C. Blanken et al. *Proposed Revisions to Aeronautical Design Standard - 33E (ADS-33-E-PRF) Towards ADS-33F-PRF*. Tech. rep. U.S. Army, 2019.
- [52] A. Conti. *Incorporating Flight Handling Qualities Requirements Into the Design of Future High-Speed Compound Rotorcraft*. Tech. rep. Pennsylvania State University, 2018.
- [53] Jason D Colbourne et al. “Control law design and optimization for rotorcraft handling qualities criteria using CONDUIT”. In: *ANNUAL FORUM PROCEEDINGS-AMERICAN HELICOPTER SOCIETY*. Vol. 55. 1. 1999, pp. 1168–1188.
- [54] Douglas G Thomson et al. “The principles and practical application of helicopter inverse simulation”. In: *Simulation Practice and Theory* 6.1 (1998), pp. 47–70.
- [55] Hong Xin et al. “Further Development and Piloted Simulation Evaluation of the Break Turn ADS-33 Mission Task Element”. In: *Journal of the American Helicopter Society* 67.4 (2022), pp. 1–14.
- [56] David H Klyde et al. “Piloted simulation evaluation of tracking mission task elements for the assessment of high-speed handling qualities”. In: *Journal of the American Helicopter Society* 65.3 (2020), pp. 1–23.
- [57] Roy L Brewer et al. “Further development and evaluation of a new high-speed acceleration/deceleration ADS-33 mission task element”. In: *Annual Forum Proceedings-AHS International*. Vol. 2018. American Helicopter Society. 2018.
- [58] David H Klyde et al. “Piloted simulation evaluation of attitude capture and hold MTEs for the assessment of high-speed handling qualities”. In: *Annual Forum Proceedings-AHS International*. Vol. 2018. American Helicopter Society. 2018.
- [59] P Simplício et al. “An acceleration measurements-based approach for helicopter nonlinear flight control using incremental nonlinear dynamic inversion”. In: *Control Engineering Practice* 21.8 (2013), pp. 1065–1077.
- [60] Tom Berger et al. “Modeling and control of lift offset coaxial and tiltrotor rotorcraft”. In: *CEAS Aeronautical Journal* 11.1 (2020), pp. 191–215.
- [61] Marilena Domnica Pavel. “On the necessary degrees of freedom for helicopter and windturbine low-frequency mode modeling”. In: (2001).



- [62] R van Aalst et al. “On the question of adequate modelling of steady-state rotor disc-tilt for helicopter manoeuvring flight”. In: (2002).
- [63] Marilena Pavel. “Memorandum M-756: Six Degrees of Freedom Linear Model for Helicopter Trim and Stability Calculation”. In: (Dec. 1996).
- [64] K HILBERT et al. “The design of a model-following control system for helicopters”. In: *17th Fluid Dynamics, Plasma Dynamics, and Lasers Conference*. 1984, p. 1941.
- [65] Duane McRuer. “Development of pilot-in-the-loop analysis.” In: *Journal of Aircraft* 10.9 (1973), pp. 515–524.
- [66] Praneet Vayalali et al. “Redistributed pseudoinverse control allocation for actuator failure on a compound helicopter”. In: *Conference: The Vertical Flight Society’s 76th Annual Forum & Technology Display*. 2020.



Algorithms

A.1. Nonlinear Simulation

```
1 %% Nonlinear Simulation
2 for i = 1:simN
3     % Speed Definitions
4     V(i) = sqrt(u(i)^2 + v(i)^2 + w(i)^2);
5     vel(:,i) = [u(i); v(i); w(i); 0; 0; 0];
6
7     % Constant Trim Variables from Initial Condition
8     U(1,i) = U(1,1);
9     U(3,i) = U(3,1);
10    U(4,i) = U(4,1);
11    U(5,i) = U(5,1);
12    U(6,i) = U(6,1);
13
14    % FREE RESPONSE after 1 deg lonCyc/Elev input
15    delta_r(i) = 0;
16    theta_cdifff(i) = 0;
17    if distChoice == 1
18        if t(i)<3
19            U(3,i) = U(3,1);
20            delta_e(i) = 0;
21        end
22        if t(i)>3
23            U(3,i) = U(3,1) + deg2rad(1);
24            delta_e(i) = 0;
25        end
26        if t(i)>3.5
27            U(3,i) = U(3,1);
28            delta_e(i) = 0;
29        end
30    else
31        if t(i)<3
32            U(3,i) = U(3,1);
33            delta_e(i) = 0;
34        end
35        if t(i)>3
36            U(3,i) = U(3,1);
37            delta_e(i) = deg2rad(1);
38        end
39        if t(i)>3.5
40            U(3,i) = U(3,1);
41            delta_e(i) = 0;
42        end
43    end
44
```



```
45 % State Update
46 xdot(:,i) = f_xk6(vel(:,i), U(:,i), p(i), q(i), r(i), theta(i), delta_e(i),
47     delta_r(i), theta_cdifff(i));
48
49 % Euler Integration
50 u(i+1) = u(i)+dt*xdot(1,i);
51 v(i+1) = v(i)+dt*xdot(2,i);
52 w(i+1) = w(i)+dt*xdot(3,i);
53 p(i+1) = p(i)+dt*xdot(4,i);
54 q(i+1) = q(i)+dt*xdot(5,i);
55 r(i+1) = r(i)+dt*xdot(6,i);
56 U(7,i+1) = U(7,i)+dt*xdot(7,i);
57 U(8,i+1) = U(8,i)+dt*xdot(8,i);
58
59 psidot(i) = (q(i)*sin(phi(i)) + r(i)*cos(phi(i))) / cos(theta(i));
60 thetadot(i) = q(i)*cos(phi(i)) - r(i)*sin(phi(i));
61 phidot(i) = p(i) + psidot(i)*sin(theta(i));
62
63 phi(i+1) = phi(i)+dt*phidot(i);
64 theta(i+1) = theta(i)+dt*thetadot(i);
65 psi(i+1) = psi(i)+dt*psidot(i);
66
67 t(i+1) = t(i)+dt;
68 end
```

B

Linearisation Results

B.1. Stability Derivatives

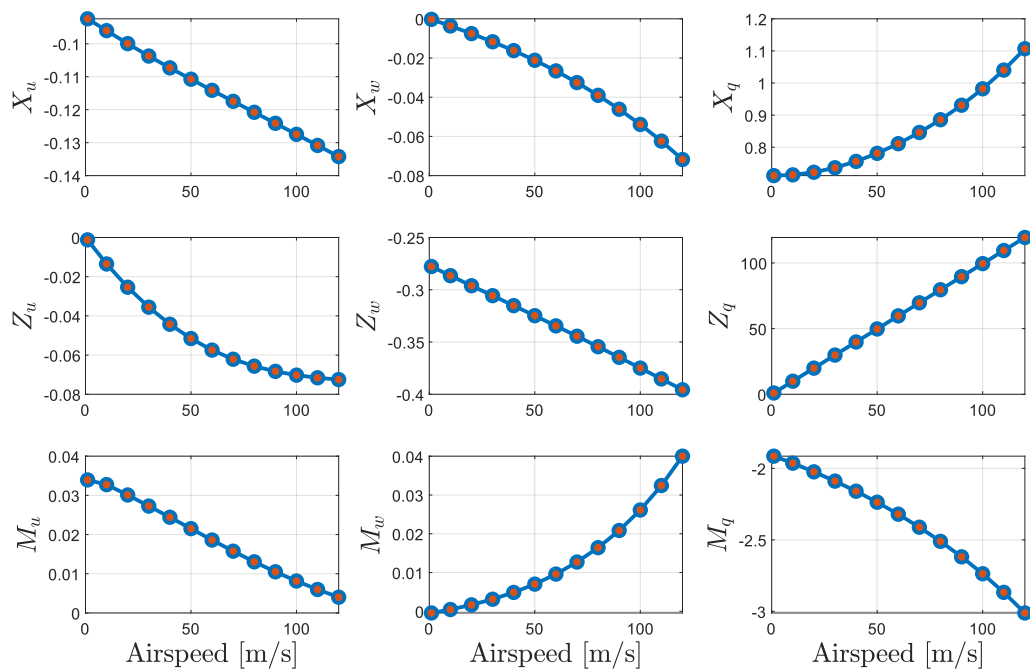


Figure B.1: Stability derivatives - longitudinal.

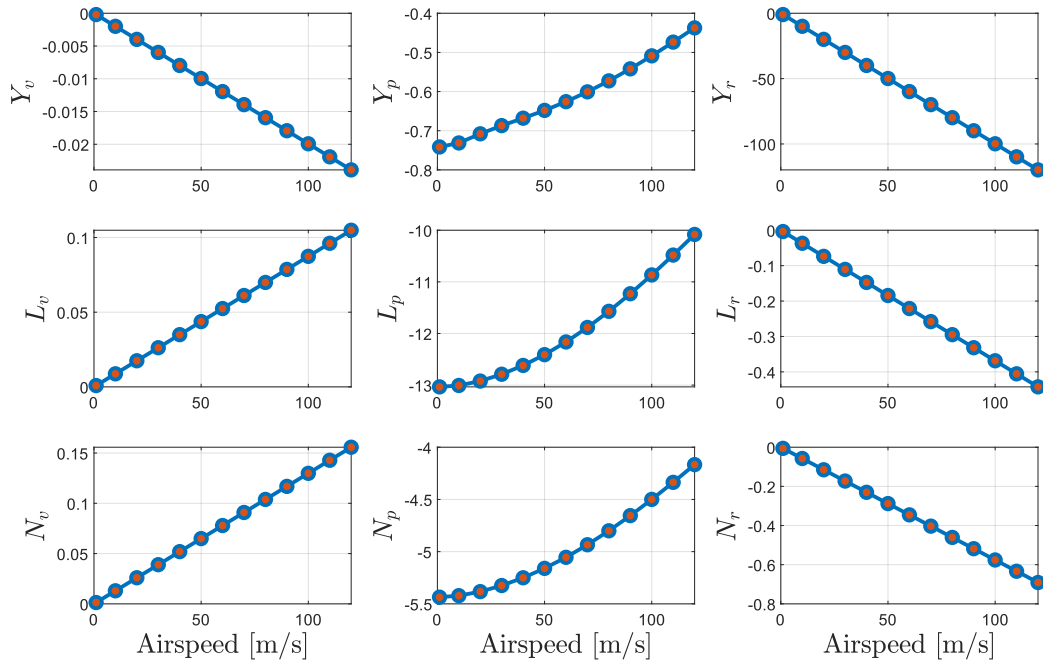


Figure B.2: Stability derivatives - lateral.

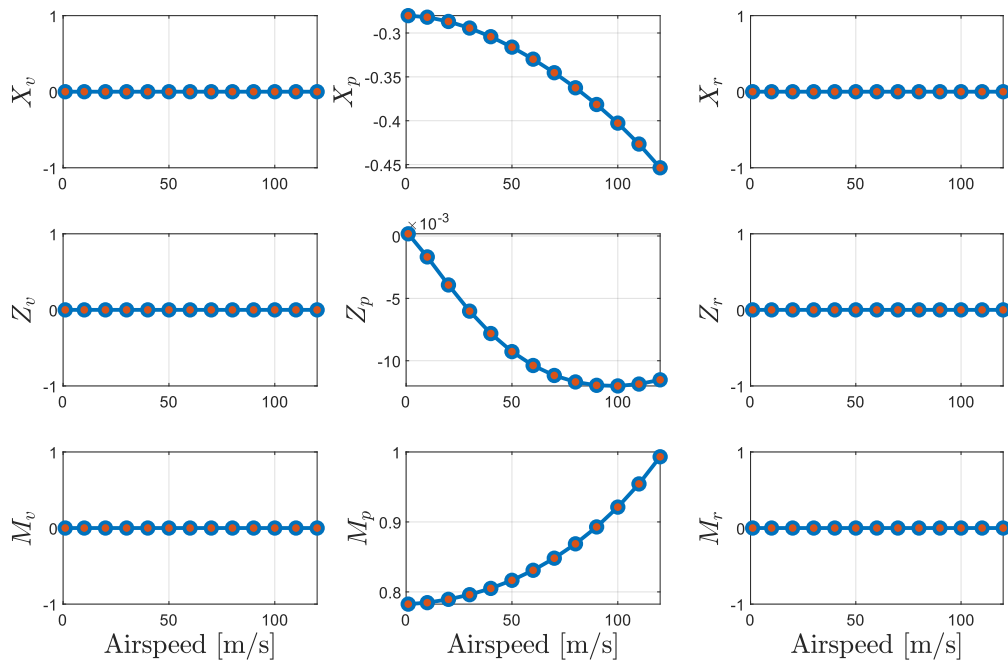


Figure B.3: Stability derivatives - lateral into longitudinal.

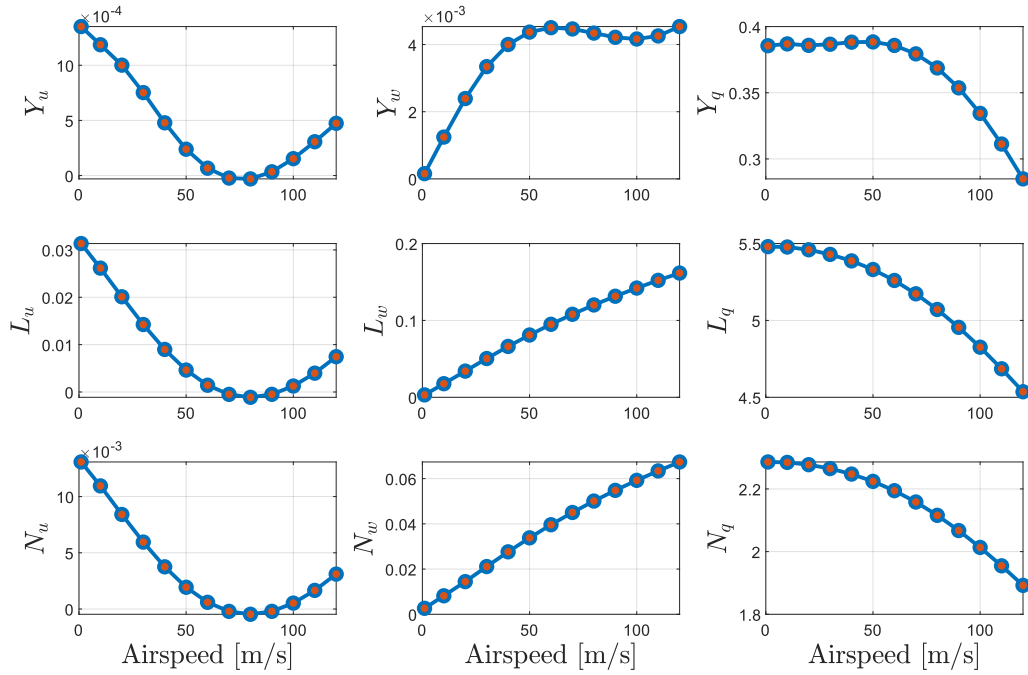


Figure B.4: Stability derivatives - longitudinal into lateral.

B.2. Control Derivatives

B.2.1. Collective Control Derivatives

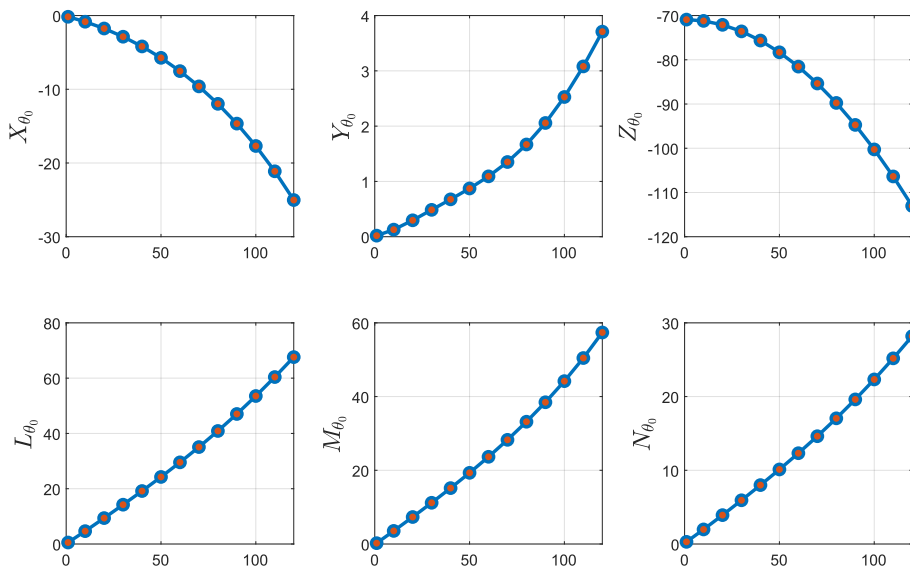


Figure B.5: Control derivatives - collective.



B.2.2. Differential Collective Control Derivatives

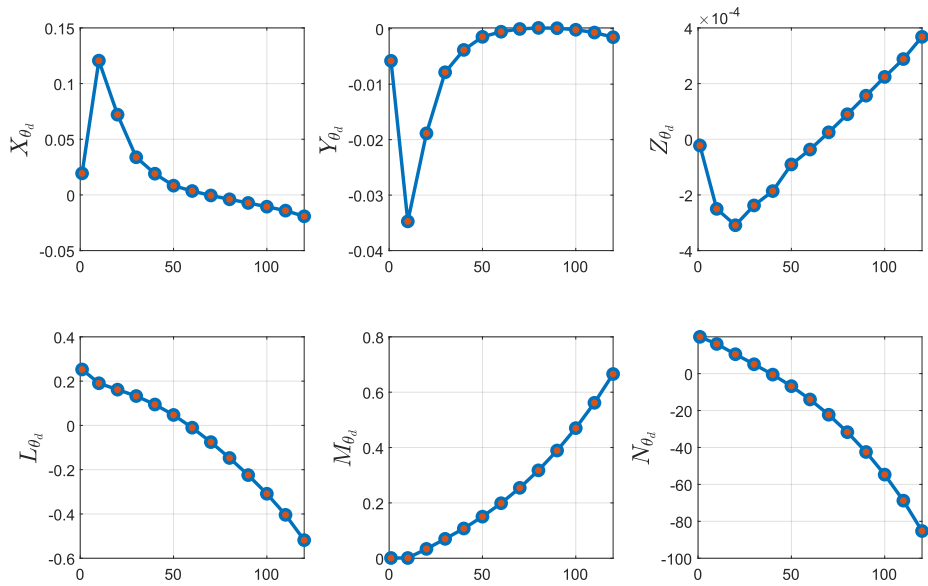


Figure B.6: Control derivatives - differential collective.

B.2.3. Longitudinal Cyclic Control Derivatives

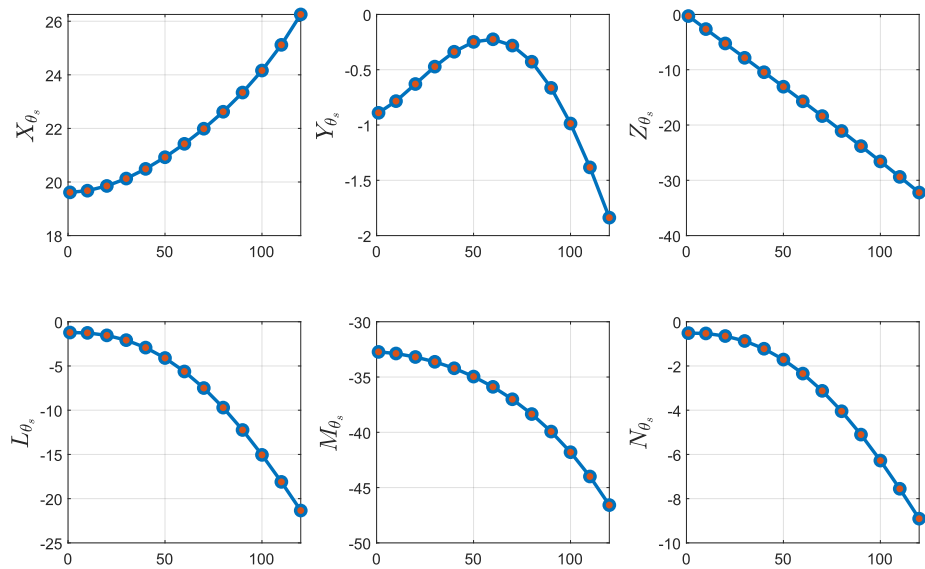


Figure B.7: Control derivatives - longitudinal cyclic.



B.2.4. Lateral Cyclic Control Derivatives

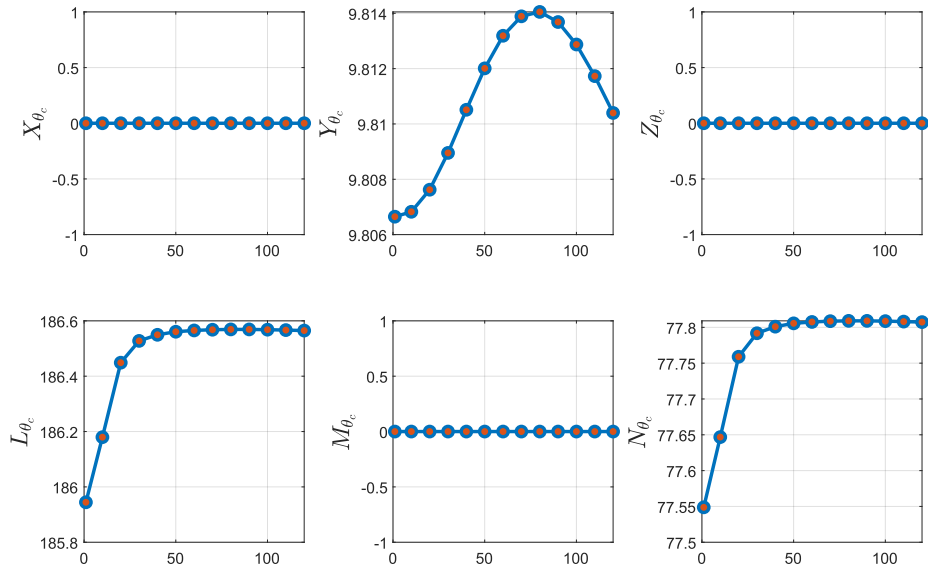


Figure B.8: Control derivatives - lateral cyclic.

B.2.5. Differential Lateral Cyclic Control Derivatives

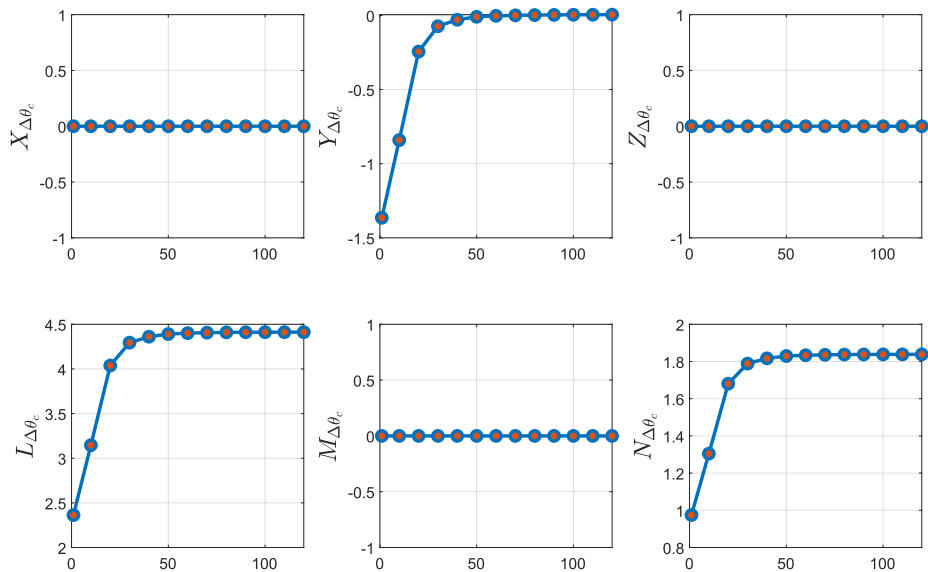


Figure B.9: Control derivatives - differential lateral cyclic.



B.2.6. Pusher Propeller Collective Control Derivatives

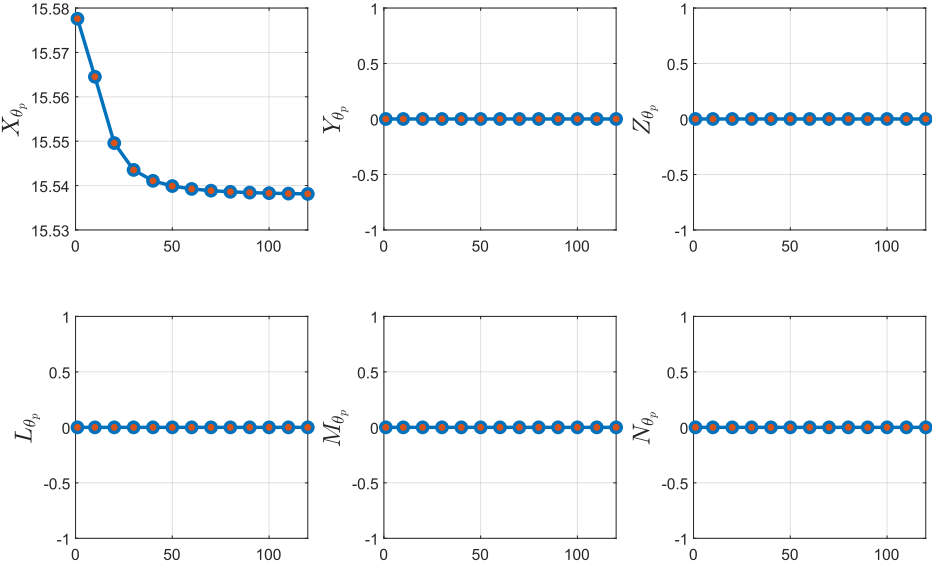


Figure B.10: Control derivatives - pusher propeller collective.